FZD-461

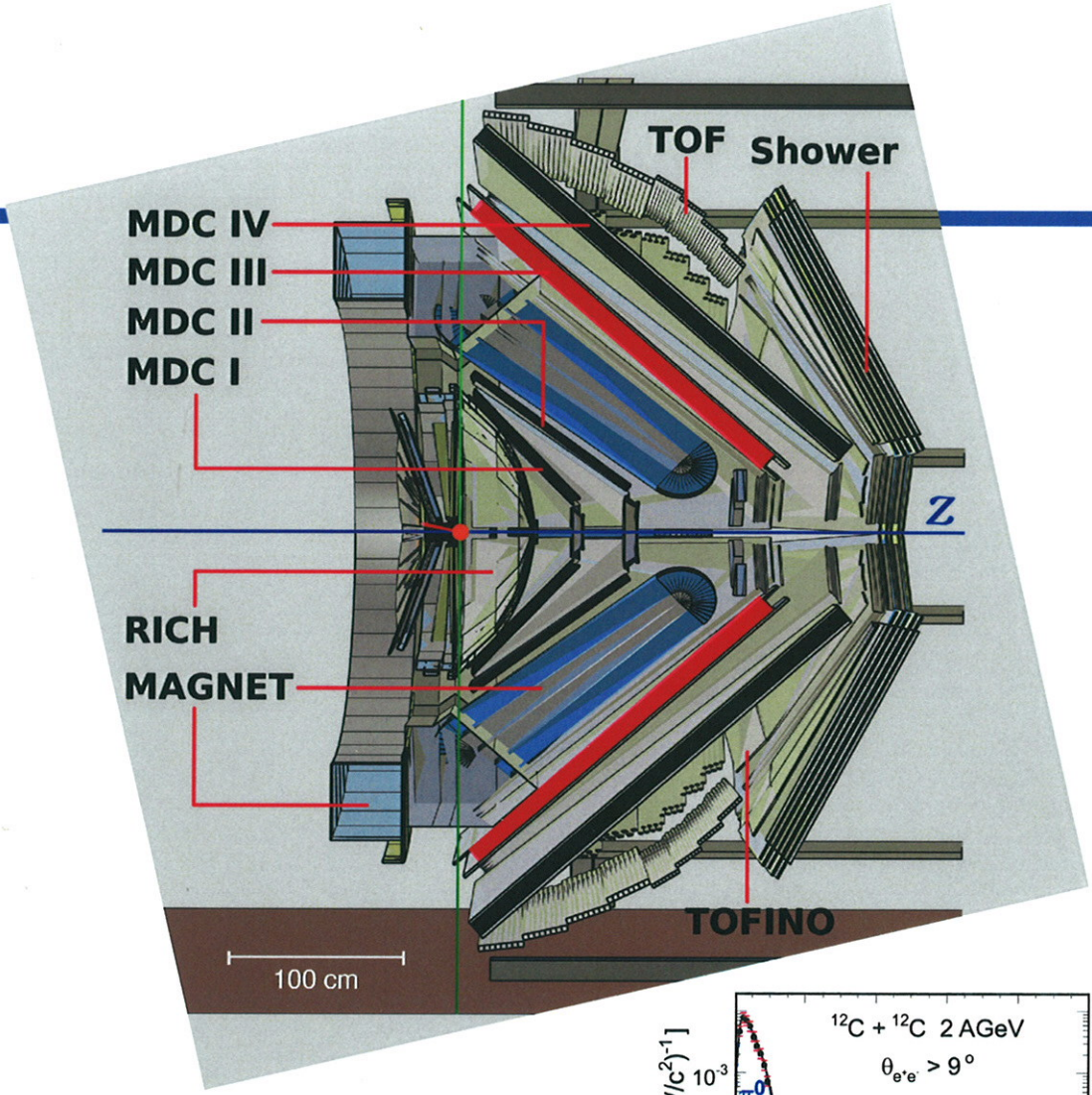

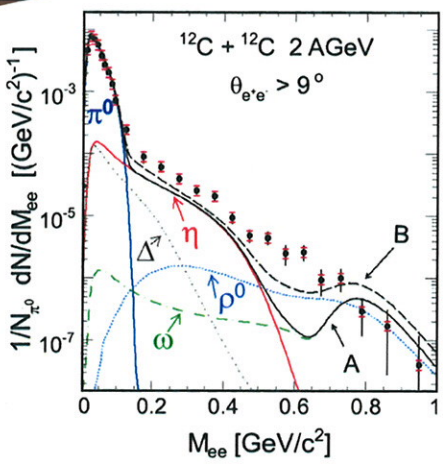

Wissenschaftlich-Technische Berichte
FZD-461 2007 · ISSN 1437-322X

ANNUAL REPORT 2006

INSTITUTE OF RADIATION PHYSICS

Forschungszentrum
Dresden Rossendorf

Wissenschaftlich-Technische Berichte
FZD-461
2007

Annual Report 2006

Institute of Radiation Physics

Editors:
K. Fahmy, E. Grosse, B. Kämpfer,
C. Schneidereit, A. Wagner

Forschungszentrum
Dresden Rossendorf

Cover Picture:

Cross section trough the HADES installation with some acronyms labelling important components (RICH: Ring Imaging Cherenkov, MAGNET: supraconducting magnet coils, MDC I - IV: Multi-wire Drift Chambers, TOF: Time Of Flight wall, Shower: shower detector). MDC III (highlighted in red) is built in FZD. The detector is azimuthally symmetric around the Z-axis (blue horizontal line labelled by Z, which also depicts the beam direction; the red dot indicates the target position). More than 100 scientists from 19 institutions in 10 countries join the HADES Collaboration. HADES operates at the heavy ion synchrotron SIS18 in GSI/Darmstadt.

The graph exhibits a first spectrum of dielectrons measured with HADES in the reaction ^{12}C (2 A GeV) + ^{12}C (for details, see Phys. Rev. Lett. 98 (2007) 052302 and related contributions in this Annual Report). The measurements are aimed at unveiling the origin of masses of selected hadrons.

Explanation of special symbols:

The letters given in parentheses in the following text and used as superscripts in the titles of the scientific contributions do express our grateful acknowledgement to the funding, sponsoring or grants provided by several institutions.

Research projects were funded by the Federal Ministry of Education and Research BMBF (**B**), by the German Research Foundation DFG (**D**), by the European Commission (**E**), by the GSI Darmstadt (**G**), by the FZ Jülich (**J**).

Typeset using TEX ©

Contact:

Forschungszentrum Dresden-Rossendorf
Institut für Strahlenphysik

Postal Address	**Address for visitors**
P.O. Box 51 01 19	Bautzner Landstraße (SW) 128
D-01314 Dresden	D-01328 Dresden
Germany	Germany

Phone: ++49 (0) 351 260 2270
Fax: ++49 (0) 351 260 3700
Email: contact.radiationphysics@fzd.de
http://www.fzd.de/FWK

This report is also available at http://www.fzd.de/FWK

Contents

Page

Preface
and List of Collaborations 1

Scientific Contributions I
Structure of Matter - Subatomic Physics 5

Strongly Interacting Matter in the Early Universe Prior to Confinement
D. Seipt, M. Bluhm, R. Schulze, B. Kämpfer . . . 7

Anti-Matter in Big Bang and Little Bang
H. Schade, B. Kämpfer . . . 8

Dielectron Production in ^{12}C+^{12}C Collisions at 2 AGeV with HADES
G. Agakichiev, F. Dohrmann, R. Kotte, B. Kämpfer for the HADES Collab. . . . 9

HADES Experiment: Di-Lepton Spectroscopy in p+p (2.2 GeV) and C + C (1 and 2 A GeV) Collisions
W. Przygoda, F. Dohrmann, E. Grosse, B. Kämpfer, R. Kotte for the HADES Collaboration . . . 10

Dielectron Detection Capabilities of HADES for Beam Energies accessible at FAIR
B. Bannier, F. Dohrmann, E. Grosse, B. Kämpfer, R. Kotte, L. Naumann, J. Wüstenfeld . . . 11

Validation of HADES-MDC Data
P. Zhou, K. Kanaki, F. Dohrmann, B. Kämpfer for the HADES Collaboration . . . 12

Propagation of Broad Meson Resonances in a BUU Type Transport Model: Application to Di-Electron Production
H.W. Barz, B. Kämpfer, Gy. Wolf, M. Zetenyi . . . 13

Di-Electron Bremsstrahlung in Intermediate-Energy *Dp* Collisions
L.P. Kaptari, B. Kämpfer . . . 14

Di-Electrons from η Meson Dalitz Decay in Proton-Proton Collisions
L.P. Kaptari, B. Kämpfer . . . 15

$\omega - \pi\gamma^*$ Transition Form Factor in Proton-Proton Collisions
L.P. Kaptari, B. Kämpfer . . . 16

K^+ and Λ Production in C + C Collisions at 2 *A*GeV with HADES
K. Kanaki, A. Sadovsky, F. Dohrmann, E. Grosse for the HADES Collaboration . . . 17

In-Medium Effects on Phase Space Distributions of Antikaons Measured in Proton-Nucleus Collisions
W. Scheinast, F. Dohrmann, L. Naumann, E. Grosse, B. Kämpfer for the KaoS Collaboration . . . 18

Production of K^+ and of K^- Mesons in Heavy-Ion Collisions from 0.6 to 2.0 A GeV Incident Energy
F. Dohrmann, E. Grosse, L. Naumann, W. Scheinast, A. Wagner for the KaoS Collaboration . . . 19

Isospin Dependence of Relative Yields of K^+ and K^0 Mesons at 1.528 AGeV
R. Kotte for the FOPI Collaboration . . . 20

Hyperon Production in the Channel $pp \to K^+\Lambda p$ Near the Reaction Threshold
L. Naumann for the COSY-TOF Collaboration . . . 21

Hunting ϕ Mesons in C + C Collisions at 2 *A*GeV
R. Kotte and the HADES Collaboration . . . 22

Coherent Photo-Excitation of Θ^+
A.I. Titov, B. Kämpfer, S. Date, Y. Ohashi 23

Production of Strangeness in Hot and Cold Nuclear Matter induced by both Leptonic and Hadronic Projectiles
F. Dohrmann 24

Systematics of Pion Emission in Heavy Ion Collisions in the 1 AGeV Regime
R. Kotte for the FOPI Collaboration 25

Single-Pion Production in pp Collisions at 0.95 GeV/c (I)
L. Naumann for the COSY-TOF Collaboration 26

Study of Spectator Tagging in the Reaction $np \to pp\pi^-$ with a Deuteron Beam
L. Naumann for the COSY-TOF Collaboration 27

Upper Limits on Resonance Contributions to Proton-Proton Elastic Scattering in the c.m. Mass Range 2.05-2.85 GeV/c^2
F. Dohrmann for the EDDA Collaboration 28

Four-Quark Condensates at Finite Density in Nucleon QCD Sum Rules
R. Thomas, T. Hilger, B. Kämpfer 29

Foundation of the Quasi-Particle Model of Strongly Interacting Matter
M. Bluhm, B. Kämpfer, R. Schulze, D. Seipt 30

Family of QCD Equations of State within a Quasi-Particle Model
M. Bluhm, B. Kämpfer, R. Schulze, D. Seipt 31

QCD Critical End-Point Effects in a Quasi-Particle Model
M. Bluhm, B. Kämpfer 32

Relativistic Approaches to Investigations of Few-Nucleon Systems
S.M. Dorkin, L.P. Kaptari, B. Kämpfer, S.M. Semikh 33

Development of Straw Tubes for High Rate Capability Application
L. Naumann for the CBM-TRT Collab. 34

Radiation Damage of Polypropylene Fiber Targets in Storage Rings
F. Dohrmann for the EDDA Collaboration 35

Determining Beam Parameters in a Storage Ring with a Cylindrical Hodoscope Using Elastic Proton–Proton Scattering
F. Dohrmann for the EDDA Colaboration 36

Studies of a Separator Dipole Magnet for Tagging Experiments for Photon-Induced Transmutation at ELBE
F. Dohrmann, A. Sytcheva, E. Grosse 37

Testing the Performance of Timing MRPC Detectors at ELBE
R. Kotte, F. Dohrmann, L. Naumann, D. Stach 38

Dipole Response of ^{88}Sr up to the Neutron-Separation Energy
R. Schwengner, G. Rusev, N. Benouaret, R. Beyer *et al.* 39

Dipole-Strength Distributions in the Stable Even-Mass Mo Isotopes
G. Rusev, R. Schwengner, M. Erhard, E. Grosse, A. R. Junghans, K. Kosev, K. D. Schilling, A. Wagner . 40

Origin of the Magnetic Dipole Strength in the Stable Even-Mass Mo Isotopes
G. Rusev, R. Schwengner, F. Dönau, M. Erhard *et al.* 41

Effect of Nuclear Deformation on the Electric Dipole Strength in the Particle-Emission-Threshold Region
F. Dönau, G. Rusev, R. Schwengner, A.R. Junghans, K.D. Schilling, A. Wagner 42

Low-Lying $E1$, $M1$, and $E2$ Strengths in ^{124,126,128,129,130,131,132,134,136}Xe: Systematic Photon Scattering Experiments in the Mass Region of a Nuclear Shape or Phase Transition
G. Rusev, K. D. Schilling, R. Schwengner *et al.* 43

Quadrupole Moment of the 8^+ Yrast State in ^{84}Kr
R. Schwengner, S. Mallion,G. Rainovski, G. Rusev *et al.* 44

Beta Decay of ^{101}Sn
R. Schwengner *et al.* 45

Beta Decay of the Proton-Rich Nuclei ^{102}Sn and ^{104}Sn
R. Schwengner *et al.* 46

Photon Scattering Experiments on the Quasistable, Odd-Odd Mass Nucleus ^{176}Lu
G. Rusev, R. Schwengner *et al.* 47

The Two-Step Gamma Cascade Method as a Tool for Studying Photon Strength Functions of Intermediate-Weight and Heavy Nuclei
G. Rusev *et al.* 48

Electromagnetic Excitations in Nuclei: from Photon Scattering to Photodisintegration
M. Erhard, C. Nair, , R. Beyer, E. Grosse, A.R. Junghans, A. Wagner *et al.* 49

Photodisintegration Studies on p-Nuclei: The Case of Sm Isotopes
C. Nair, A.R. Junghans, M. Erhard, E. Grosse *et al.* 50

Commissioning of a Pneumatic Delivery System for Photoactivation Experiments at the Electron Accelerator ELBE
A. Wagner, J. Claussner, M. Erhard, E. Grosse, A. Hartmann *et al.* 51

A CAMAC-Based Data Acquisition System for Photoactivation Experiments at the Electron Accelerator ELBE
M. Fauth, P. Crespo, M. Erhard, A.R. Junghans, C. Nair, K.D. Schilling, A. Wagner 52

Improving the Timing Properties of the Photo-Fission Setup
K. Kosev, N. Nankov, M. Friedrich, A. Hartmann, E. Grosse, *et al.* 53

Low-Threshold Proton-Recoil Detectors for nELBE
R. Beyer, E. Grosse, K. Heidel, J. Hutsch, A.R. Junghans *et al.* 52

A BaF_2 Detector Array for Neutron-Capture γ-Rays
J. Klug, E. Altstadt, C. Beckert, R. Beyer *et al.* 55

A Photo-Neutron Source for Time-of-Flight Measurements at the Radiation Source ELBE
J. Klug, E. Altstadt, C. Beckert, R. Beyer *et al.* 56

Low-Energy Cross Section of the ^{7}Be(p,γ)^{8}B Solar Fusion Reaction from the Coulomb Dissociation of ^{8}B
F. Schümann, S. Typel, F. Hammache, E. Grosse, A. Wagner *et al.* 57

Study of Radiative Proton Capture to the Ground State in ^{15}O
Gy. Gyürky, F. Confortola, H. Costantini, M. Marta, D. Bemmerer *et al.* 58

^{3}He$(\alpha,\gamma)^7$Be cross section at low energies
Gy. Gyürky, F. Confortola, H. Costantini, D. Bemmerer, M. Marta *et al.* 59

Cooling Dynamics in Multi-Fragmentation Processes
T.X. Liu, W.G. Lynch, M.J. van Goethem, X.D. Liu, A. Wagner *et al.* 60

Secondary Structure and $Pd^{(II)}$ Coordination in S-Layer Proteins from *Bacillus Sphaericus* Studied by Infrared and X-Ray Absorption Spectroscopy
K. Fahmy, M. Merroun, K. Pollmann, J. Raff, O. Savchuk *et al.* 63

Linkage between the Intramembrane H-bond Network around Aspartic Acid 83 and the Cytosolic Environment of Helix 8 in Photoactivated Rhodopsin
N. Lehmann, U. Alexiev, K. Fahmy 65

Physical Properties of the Transmembrane Segment 3 of Rhodopsin
S. Madathil, G. Furlinski, K. Fahmy 67

Structure-Function Relationship of Actin-Flavonoid Interactions
S. Madathil, K. Fahmy , M. Böhl, F. Pfennig, H.O. Gutzeit, S. Tietze, A. Sokoll, J. Apostolakis 68

Structural Properties of the Kinesin "Coiled-Coil Break 1" Region
S. Madathil, K. Fahmy , A.H. Crevenna, D.N. Cohen, J. Howard 69

Dynamics of FEL-Light-Induced Changes in Thin DNA Films Observed by Brewster Angle Microscopy
M. Sczepan, G. Furlinski, D. Wohlfarth *et al.* 70

Identification of Actinide Molecule Complexes by Vibrational Photothermal Beam Deflection Spectroscopy
H. Foerstendorf, K. Heim, W. Seidel, G. Bernhard 71

Remote Controlled IR-Diagnostic Station for the Rossendorf FELs
W. Seidel, R. Jainsch, M.Justus *et al.* 72

Extraction of Single FEL Radiation Pulses Using a Laser-Activated Plasma Switch
W. Seidel, S. Winnerl 74

The IR Beam Line from the FELs to the High Magnetic Field Laboratory
W. Seidel, A. Winter, R.. Wünsch, S. Zvyagin 76

Spectral Width and Duration of the IR-Pulses from FELBE
W. Seidel, D. Stehr 78

Influence of the System Matrix on the Quality of the Reconstruction of In-Beam PET Data
G. Shakirin, P. Crespo, W. Enghardt 79

Optimum Voxel Size for Direct Time-of-Flight In-Beam PET
G. Shakirin, P. Crespo, F. Fiedler, W. Enghardt, E. Grosse, A. Wagner 80

In-Beam PET Measurements of Biological Half-Lives of ^{12}C Irradiation Induced β^+-Activity
F. Fiedler, M. Sellesk, P. Crespo *et al.* 81

The Feasibility of In-Beam PET for Therapeutic Beams of ^3He
F. Fiedler, P. Crespo, K. Parodi, M. Sellesk, W. Enghardt 82

In-beam PET at High-Energy Photon Beams: A Feasibility Study
H. Müller, W. Enghardt 83

Results of First Experiments on In-Beam PET at 34 MV Bremsstrahlung Beams
D. Möckel, T. Kluge, J. Pawelke, W. Enghardt 84

Electron Beam Monitoring for Channeling Radiation Measurements
W. Neubert, B. Azadegan, W. Enghardt, K. Heidel, J. Pawelke, W. Wagner 85

Investigation of Planar Channeling Radiation from Different Plane of Quartz
B. Azadegan, W. Wagner, J. Pawelke 86

Dependence of the Linewidth of Planar Electron Channeling Radiation on the Thickness of the Diamond Crystal
B. Azadegan, W. Wagner, J. Pawelke 87

RBE of 25 kV X-Rays for the Survival and Induction of Micronuclei in the Human Mammary Epithelial Cell Line MCF-12A
A. Lehnert, E. Lessmann, J. Pawelke, W. Dörr 88

Repair Kinetics of DNA Double Strand Breaks Induced in Human Mammary Epithelial Cells
E. Beyreuther, W. Dörr, E. Lessmann, J. Pawelke 89

AMOS - An Effective Tool for Adjoint Monte Carlo Photon Transport
D. Gabler, J. Henniger, U. Reichelt 90

Application of Advanced Monte Carlo Methods in Numerical Dosimetry
U. Reichelt, J. Henniger, C. Lange 91

Scientific Activities 93

Publications 95
Proceedings, Reports and Posters 104
Talks at Conferences and other Institutes 109
Talks of Visitors 115
Lectures 116
Theses 117
Meetings organized by the ISP 118

Personnel 119

Departments of the ISP 121
Personnel of the ISP 122
Guest Scientists 123

Index of Authors 124

Preface

The Forschungszentrum Dresden-Rossendorf (FZD) is a multidisciplinary research centre and part of the Wissenschafts-Gemeinschaft G. W. Leibniz (WGL), one of the German agencies for extra-university research. FZD is active in materials research, in the life sciences and in environmental research. The **Institute of Radiation Physics** *(ISP for "Institut für Strahlenphysik") within the FZD avails for its research the coupling of radiation to matter in subatomic dimensions as well as to tissue, to cells, and to their components. Its research in the field of* **Subatomic Physics** *is part of the FZD-program* **Structure of Matter** *and its investigations concerning the interaction of* **Biostructures and Radiation** *contribute to the* **Life Science** *program of the FZD. In this field the ISP exploits possibilities to transfer efforts on experimental and theoretical techniques from particle and nuclear physics to projects in radiobiology and biophysics. Much of this kind of interdisciplinary transfer is connected to the Radiation Source ELBE at the FZD. With its super-conducting accelerator for relativistic electrons this large installation provides photons in the wide wavelength range from fm to mm - i.e. bremsstrahlung for the investigation of photonuclear processes, hard X-rays for radio-biological and other studies and infrared light from FEL's for research on the structural dynamics of bio-molecules. The investigation of radiation-induced processes not only dominates the projects in nuclear astrophysics as pursued at ELBE, it also is a central theme of the experimental and theoretical research performed by the ISP in close connection to the heavy ion synchrotron SIS and the upcoming FAIR facility at Darmstadt. The Annual Report presented here shows last year's progress as obtained at the ISP in these various fields and their interconnections.*

Experiments performed at the high energy heavy-ion accelerators at GSI-FAIR observe the consequences of increasing nuclear density and theoretical concepts based thereon are an important ingredient for the understanding of the Big Bang and other high density cosmic scenarios. This branch of hadron physics is one of the research activities in subatomic physics at the ISP. It studies the strong (nuclear) interaction in the nuclear medium and especially in high density phases of hadronic matter. As partner of the international HADES-CBM project the Institute is heavily involved in respective experiments and also various theoretical research at the ISP relates to these experiments.

The experimental conditions at ELBE are very favourable for photon-induced processes in the excitation energy range characteristic for the environments relevant to the cosmic production of the chemical elements. This holds for the time shortly after the Big Bang when first nuclei are formed and it is especially so for hot scenarios in heavy stars, novae or super-novae where the formation of high-Z elements can take place. As there the "p-process" and thus photodisintegration becomes important, detailed experimental investigations on electro-magnetic dipole strength distributions in various nuclei near $Z = 40$ and $N = 50$ were performed. The analysis is presently ongoing and a reliable parameterization of the strength is in view. It shall establish conclusive extrapolations to exotic nuclei on the paths of the element production processes. Using the photo-activation technique interesting results were obtained for some nuclides with presently unexplained discrepancies to abundance predictions. First studies related to the R^3B-LAND facility open the path towards the electromagnetic disintegration of radioactive nuclei which will be available abundantly at FAIR. Compact bunches of secondary neutrons, i.e. pulsed neutron beams in the MeV-range to be produced at ELBE, will also play a role in this field as well as in basic nuclear physics research dedicated to processes of importance for future nuclear power installations. Initiated by the ISP and the Safety Research Institute (IfS) at FZD, ELBE offers new possibilities for studies related to the removal of radioactive waste by transmutation.

In its second part this Report describes the research in the life sciences, mainly performed using accelerator based technology. Conceptual design studies for the free electron lasers (FEL) at ELBE including detailed investigations on transport and control of the infrared (IR) and THz beams have since long been part of the work in the Institute. The ISP biophysics department has concentrated on the use of IR radiation in the study of bio-molecular dynamics under non-destructive and native-like conditions. Fundamental aspects of the structure and conformational changes of pharmacologically relevant receptor proteins and of DNA play a key role in these investigations. Novel approaches using FEL pump and visible probe beams have been established to study the motion of the DNA backbone. IR-studies on actinide-molecule complexes have been performed together with radio-chemists from the FZD-Institute IRC.
In the past the ISP contributed essentially to the field of tumour-conform radiotherapy by exploring on-line positron emission tomography. The successful operation of a PET scanner simultaneously to the irradiation of tumours with heavy ion beams considerably improved the reliability and reproducibility of the radiation therapy with fast ions. This in-situ PET as developed at the ISP has been shown to also allow the control of irradiations performed with other beams like ^{3}He and even photons, as shown by numerical and first experimental studies. Beams from ELBE have been developed for another interesting field: Quasi-monochromatic X-rays of easily variable energy as produced in electron channeling have been investigated systematically by varying thickness and orientation of the channelling crystal. Thus, the studies of the elementary processes causing radiation-induced cell damage can at ELBE now been transferred from X-ray tubes to a monochromatic source.

The interaction between different scientific fields at the ISP has led to considerable synergy effects, e.g. with respect to hardware for the experimental investigations or in the field of computer simulations needed for their interpretation. The transfer of information and expertise from the large international particle and nuclear physics communities to the life sciences has been continuously promoted by the ISP. Thus the Institute's speciality of combining various areas of research reaching from laboratory studies on cosmic processes to the interaction of radiation with bio-structures has contributed essentially to its progress.

This report documents the progress of the research at the Institute of Radiation Physics mainly through two types of contributions:

1. *Every PhD student (as well as some of the Diploma candidates) has included one or two pages representing the present status of her resp. his thesis work.*
2. *From each publication which appeared – or was submitted – in 2006 one or two figures were combined with some short text from the paper to generate a report.*

By this means the current status of research is demonstrated without producing additional graphs or text.

The scientific activities of the Institute have benefited from various support. We gratefully acknowledge the close and fruitful collaboration with GSI/FAIR Darmstadt and with the Technical University (TU) Dresden. These contacts and those to many other scientific institutions in Germany and abroad are of vital importance for the Institute. Specific investigations were subsidized by the Federal Ministry for Education and Research (BMBF), the Saxon Ministry for Science and Art (SMWK), GSI Darmstadt and Forschungszentrum Jülich. We express our gratitude to them as well as to the Deutsche Forschungs-Gemeinschaft (DFG) and to the European Union (EU) for the support of various research projects initiated by the Institute.

Eckhart Grosse

Collaborations

Hadron Physics

- **HADES and CBM Collaborations:**

GSI Darmstadt	FZD
Univ. Frankfurt	Univ. Giessen
TU München	Univ. Heidelberg
Inst. of Physics Bratislava, Slovakia	LNS Catania, Italy
LPC and Univ. Blaise Pascal Clermont, France	Univ. of Cyprus, Cyprus
Jagellonian Univ. Cracow, Poland	JINR Dubna, Russia
Univ. degli Studi di Milano, Italy	ITEP Moscow, Russia
INR Moscow, Russia	MEPhI Moscow, Russia
Inst. de Physique Nucleaire d'Orsay, France	Nuclear Physics Inst. Rez, Czech Republic
Univ. of Santiago de Compostela, Spain	Univ. of Valencia, Spain

- We still benefit from previous contributions to other hadron experiments like KaoS, FOPI, COSY-TOF and COSY-ANKE, from which interesting results come to publication continuously.

Nuclear Physics

- GSI Darmstadt
- TU Dresden
- TU Darmstadt
- GSI Darmstadt
- Univ. Köln
- Univ. Michigan State
  EFNUDAT Collaboration (EU-I3), USA
- TU Dresden
- INRNE and Univ. Sofia, Bulgaria
- Laboratorio di Gran Sasso, Italy
- Charles Univ. Prague, Czech Republic
- Univ. of Notre Dame, USA
- Univ. of Washington at Seattle, USA

Structural Dynamics of Biomolecules

- Rockefeller Univ., New York, USA
- Univ. Orenburg, Russia
- IITM, Chennai, India
- MPI für Zellbiologie und Genetik, Dresden
- MPI für Molekulare Physiologie, Dortmund
- TU Dresden
- FU Berlin
- LMU München

Cell Radiobiology

- GSI Darmstadt
- TU Dresden
- OncoRay Dresden
- PTB Braunschweig / BESSY II
- Univ. Göttingen
- Humboldt Univ. Berlin
- Marie-Sklodowska-Curie Memorial Center of Oncology, Gliwice, Poland

In-beam PET for Quality Assurance of Charged Hadron Therapy

- DKFZ Heidelberg
- Univ. Heidelberg
- GSI Darmstadt
- Soltan Inst. for Nuclear Studies, Otwock Swierk, Poland
- MedAustron, Wiener Neustadt, Austria
- Atominst. der Österreichischen Univ. an der TU Wien, Austria
- Univ. Claude Bernard Lyon 1, France
- CERN, Genf, Switzerland
- Harvard Medical School, Boston, USA

▷ Structure of Matter - Subatomic Physics

Strongly Interacting Matter in the Early Universe Prior to Confinement [B,E]

D. Seipt, M. Bluhm, R. Schulze, B. Kämpfer

Part of Diploma thesis D. Seipt

Strongly interacting matter (quarks and gluons) dominates the energy density e, pressure p and entropy density s in the early universe all the way from electro-weak transition at temperature $T \sim 100$ GeV down to confinement at $T \sim 170$ MeV. This is evidenced in Fig. 1, where we exhibit the effective numbers of degrees of freedom for energy density, h_{eff} in $e = \frac{\pi^2}{30} h_{eff}(T)\, T^4$, for pressure, f_{eff} in $p = \frac{\pi^2}{90} f_{eff}(T)\, T^4$, and for entropy density, g_{eff} in $s = \frac{2\pi^2}{45} g_{eff}(T)\, T^3$, respectively. The dotted curves depict the electro-weak contributions (photons, leptons, $W^\pm$ and Z^0). The total numbers including the contribution of strongly interacting matter are displayed as solid curves (based on our quasi-particle model adjusted to lattice QCD data at low temperatures; the drop at 170 MeV is due to confinement, where quarks and gluons are converted into hadrons). Below confinement, clearly the electro-weak matter dominates for a long period. The dashed curves are for an ideal gas approximation not containing any interaction effects. Of course, it can not account for the strong correlations build up at confinement and reducing strongly the effective degrees of freedom. Remarkable is the failure of the naive standard perturbation theory below 1 GeV (not shown).

In searching for weakly interacting massive relic particles (WIMPs) one can estimate their cosmic abundance from the freeze-out at about $T \sim m_X/25$. Thus, the freeze-out temperature is in the range from 400 MeV till 40 GeV assuming masses m_X in the range 10 - 1000 GeV. It turns out that the exact relic densities for dark matter candidates (say, sterile neutrinos etc.) depend on two essential functions, $g_{eff}(T)$ and

$$g_*^{1/2}(T) = \frac{h_{eff}}{\sqrt{g_{eff}}} \left(1 + \frac{T}{3} \frac{d \log h_{eff}}{d T}\right). \qquad (1)$$

As pointed out in [1] an uncertainty of 10 % in the strong interaction component for pressure translates into an uncertainty up to 1 % in the corresponding relic densities. WMAP measurements have determined the matter density (including the hitherto unknown dark matter) to an accuracy of better than 10 %. The Planck mission will improve the determination better than 1 % (cf. [1] for references). In this respect the precise determination of the effective degrees of freedom in the early universe in the above quoted temperature range is tempting, in particular for the strong interaction sector. The future direct detection experiments at LHC will further constrain the particle zoo beyond the present standard model of particle physics.

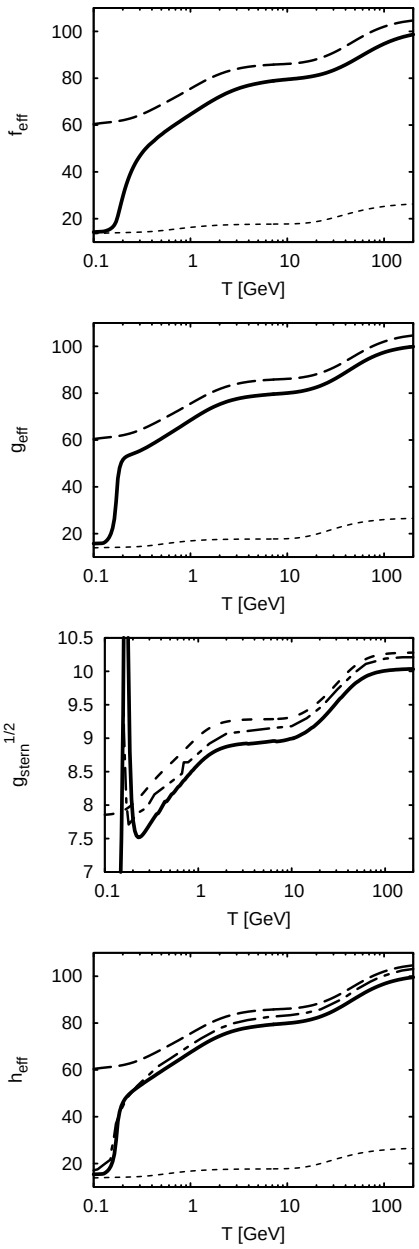

Fig. 1 *The dependence of various parameters quantifying the number of degrees of freedom in the early universe. Solid curves: electro-weakly + strongly interacting matter (the latter one calculated within our quasi-particle model [2]), dotted curves: only electro-weak particles, dashed curves: neglecting any interaction effects. The dot-dashed curves reproduce the assessment in [1].*

[1] M. Hindmarsh, O. Philipsen, Phys. Rev. D 71 (2005) 087302

[2] M. Bluhm, B. Kämpfer, G. Soff, Phys. Lett. B 620 (2005) 131

Anti-Matter in Big Bang and Little Bang [B,E]

H. Schade, B. Kämpfer

Part of PhD thesis H. Schade

The Boltzmann equations for nucleons and anti-nucleons integrated over momentum read

$$\frac{dY_+}{dx} = -\frac{\Lambda}{x^\xi}\left(Y_+(Y_+ - \eta) - Y_{eq}^2\right), \quad (1)$$

$$\frac{dY_-}{dx} = -\frac{\Lambda}{x^\xi}\left(Y_-(Y_- - \eta) - Y_{eq}^2\right), \quad (2)$$

where $Y_\pm = n_\pm/s$ are the baryon densities $n_\pm$ normalized to entropy density $s = \frac{2\pi^2}{45} h_{eff}(T) T^3$. We attribute Y_+, n_+ to baryons (protons) and Y_+-, n_- to anti-baryons (anti-protons). $h_{eff}(T)$ is the effective number of all degrees of freedom in the fireball with comoving volume $V(t)$. We apply the Boltzmann approximation, as for the following $x \equiv m_N/T$ is larger than unity. Therefore, $Y_{eq} = \frac{45}{4\pi^4}\frac{2}{h_{eff}} x^2 K_2(x)$.

In Little Bang, $\Lambda = 3\langle\sigma v\rangle \tau m_N^3 \frac{2\pi^2}{45} h_{eff}$ encodes the thermally averaged annihilation cross section $\langle\sigma v\rangle$. In Big Bang, $\Lambda = \langle\sigma v\rangle\, g_{eff}^{1/2}\, M_{Pl}\, m_N\, (\pi/45)^{1/2}$ holds with g_{eff} determining the effective degrees of freedom relevant for the energy density and M_{Pl} as Planck mass and m_N as nucleon mass.

In deriving eqs. (1, 2) we use adiabaticity of the expanding fireball, i.e. $sV = const$. Both evolution equations are related by baryon conservation, $Y_+ - Y_- = \eta = const$, i.e. $\dot{Y}_+ = \dot{Y}_-$. For the Little Bang in heavy-ion collisions we utilize $V/\dot{V} = \tau$ with τ as characteristic time scale. This allows us to formulate the evolution as a function of x instead as a function of time t. In Big Bang the expansion of the comoving volume is governed by Friedmann's equations. Tab. 1 evidences the huge differences of Little Bang and Big Bang dynamics.

Tab. 1 *Orders of magnitude of the parameter Λ and initial conditions for η, and the power ξ as well.*

	Λ	η	ξ
Little Bang	10^3	10^{-1}	4
Big Bang	10^{21}	10^{-9}	2

The generic features of the Ricatti like eqs. (1, 2) are: For large values of Λ, $Y_\pm$ are dragged by $Y_\pm^{eq}$ for a long time, while for small values of Λ, $Y_\pm$ depart rapidly from $Y_\pm^{eq}$ even when starting at equilibrium, as supposed in the thermo-statistical interpretation of hadron abundances in relativistic heavy-ion collisions, see [1] and Fig. 1. This off-equilibrium evolution causes the ratio of anti-protons to protons to stay roughly constant from chemical freeze-out till kinetic freeze-out. In such way the "anti-proton puzzle" [2] is solved.

In contrast, in the Big Bang the small value of η, represented by the small value of the ration of baryons to photons, causes Y_+ to be frozen in at 45 MeV (Fig. 2), while the anti-baryons are annihilated for long time span yielding at freeze-out an exceedingly small fraction. In particular, the anti-baryon fraction in this homogeneous scenario is so small that the standard primordial nucleosynthesis is not influenced.

While the evolution of $n_\pm$ can be described by such kinetic equations, the origin of the initial conditions remains to be addressed separately and represents a mystery in both Little Bang and Big Bang.

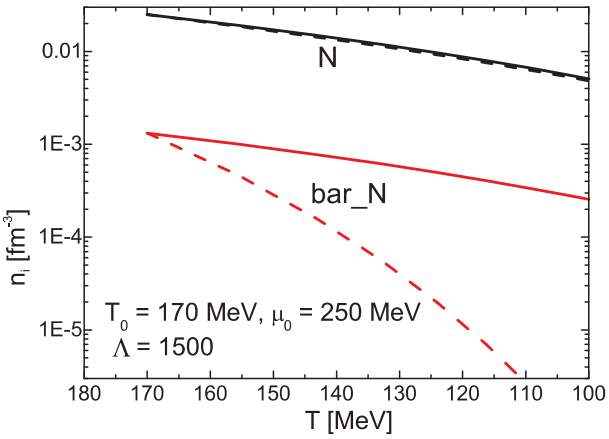

Fig. 1 *The proton density ("N") and anti-proton density ("bar-N") as a function of temperature. Initial conditions for CERN-SPS. Solid curves: actual densities $n_\pm$ for the off-equilibrium evolution, dashed curves: equilibrium densities $n_\pm^{eq}$.*

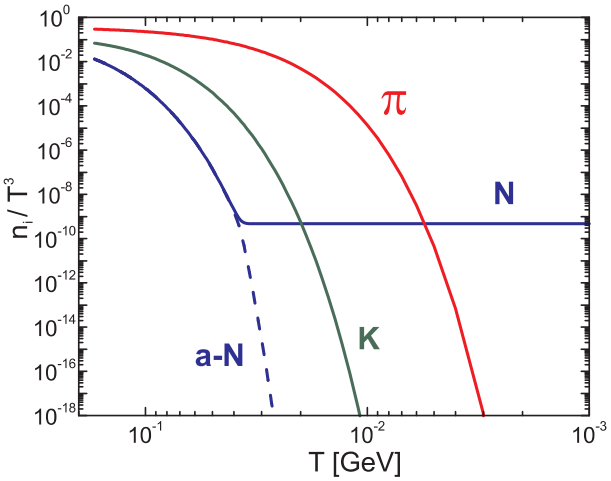

Fig. 2 *Evolution of densities of nucleons (N), anti-nucleons (a-N), pions (π) and kaons (K) as a function of temperature in Big Bang. From [3].*

[1] J. Cleymans, B. Kämpfer, M. Kaneta, S. Wheaton, N. Xu, Phys. Rev. C 71 (2005) 054901

[2] R. Rapp, E.V. Shuryak, Phys. Rev. Lett. 86 (2001) 2980

[3] B. Kämpfer, M. Bluhm, J. Phys. G 31 (2005) S1141

Dielectron Production in ^{12}C+^{12}C Collisions at 2 AGeV with HADES [B,G]

G. Agakichiev, C. Agodi, H. Alvarez-Pol, A. Bałanda, D. Bertini, J. Bielcik, G. Bellia, M. Böhmer, H. Bokemeyer, J.L. Boyard, P. Braun-Munzinger, P. Cabanelas, S. Chernenko, T. Christ, R. Coniglione, L. Cosentino, J. Díaz, **F. Dohrmann**, I. Durán, T. Eberl, **W. Enghardt**, L. Fabbietti, O. Fateev, C. Fernandez, P. Finocchiaro, J. Friese, I. Fröhlich, B. Fuentes, C. Garabatos, J. A. Garzón, R. Gernhäuser, M. Golubeva, D. González-Díaz, **E. Grosse**, F. Guber, T. Hennino, S. Hlavac, R. Holzmann, J. Homolka, A. Ierusalimov, I. Iori, A. Ivashkin, M. Jaskuła, M. Jurkovic, M. Kagarlis, M. Kajetanowicz, **B. Kämpfer**, **K. Kanaki**, T. Karavicheva, A. Kastenmüller, L. Kidoń, P. Kienle, I. Koenig, W. Koenig, H. J. Körner, B. W. Kolb, **R. Kotte**, R. Krücken, A. Kugler, W. Kühn, R. Kulessa, A. Kurepin, S. Lang, S. Lange, J. Lehnert, E. Lins, D. Magestro, C. Maiolino, A. Malarz, J. Markert, V. Metag, J. Mousa, M. Münch, C. Müntz, **L. Naumann**, A. Nekhaev, J. Novotny, J. Otwinowski, Y. C. Pachmayer, V. Pechenov, T. Pérez, P. Piattelli, J. Pietraszko, R. Pleskac, M. Płoskoń, V. Pospísil, W. Prokopowicz, W. Przygoda, B. Ramstein, A. Reshetin, J. Ritman, M. Roy-Stephan, A. Rustamov, **A. Sadovsky**, B. Sailer, P. Salabura, M. Sánchez, P. Sapienza, A. Schmah, H. Schön, W. Schön, C. Schröder, E. Schwab, R. S. Simon, V. Smolyankin, L. Smykov, S. Spataro, B. Spruck, H. Ströbele, J. Stroth, C. Sturm, M. Sudoł, M. Suk, A. Taranenko, P. Tlusty, A. Toia, M. Traxler, H. Tsertos, D. Vassiliev, A. Vázquez, V. Wagner, W. Waluś, M. Wiśniowski, T. Wójcik, **J. Wüstenfeld**, Y. Zanevsky, K. Zeitelhack, D. Zovinec and P. Zumbruch (HADES collaboration)

Published in Phys. Rev. Lett. 98 (2007) 052302, 1-5

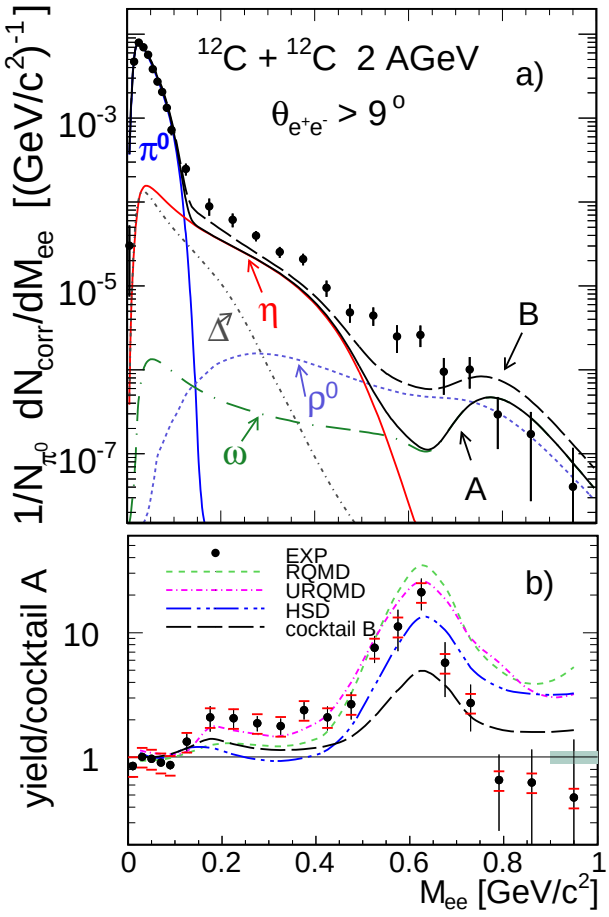

(a) Efficiency- and background-corrected e^+e^- invariant-mass distribution for $\theta_{e+e-} > 9^o$ (symbols) compared to a thermal dielectron cocktail of free π^0, η and ω decays (cocktail A, solid line), as well as including ρ and Δ resonance decays (cocktail B, long-dashed line). Only statistical errors are shown. (b) Ratio of data and cocktail A (dots), compared to ratios of various model calculations and cocktail A. All calculations have been filtered and folded with the HADES [1-4] acceptance and mass resolution. Statistical and systematic errors of the measurement are shown as vertical and horizontal lines, respectively. The overall normalization error of 11% is depicted by the shaded area.

The invariant-mass spectrum of e^+e^- pairs produced in ^{12}C+^{12}C collisions at an incident energy of 2 GeV per nucleon has been measured for the first time. The measured pair production probabilities span over five orders of magnitude from the π^0-Dalitz to the ρ/ω invariant-mass region. Dalitz decays of π^0 and η account for all the yield up to 0.15 GeV/c^2, but for only about 50% above this mass. A comparison with model calculations shows that the excess pair yield is likely due to baryon-resonance and vector-meson decays. Transport calculations based on vacuum spectral functions fail, however, to describe the entire mass region.

[1] R. Schicker et al., Nucl. Instr. Meth. A 380 (1996) 586
[2] J. Friese et al. (HADES collaboration), Prog. Part. Nucl. Phys. 42 (1999) 42
[3] H. Bokemeyer et al., Nucl. Instr. Meth. A 477 (2002) 397
[4] P. Salabura et al. (HADES collaboration), Nucl. Phys. A 749 (2005) 150

HADES Experiment: Di-Lepton Spectroscopy in p+p (2.2 GeV) and C + C (1 and 2 A GeV) Collisions [B,G]

W. Przygoda, G. Agakishiev, C. Agodi, H. Alvarez-Pol, A. Balanda, R. Bassini, G. Bellia, D. Belver, J. Bielcik, A. Blanco, M. Boehmer, C. Boiano, A. Bortolotti, J. Boyard, S. Brambilla, P. Braun-Munzinger, P. Cabanelas, S. Chernenko, T. Christ, R. Coniglione, M. Dahlinger, J. Diaz, R. Djeridi, **F. Dohrmann**, I. Duran, T. Eberl, **W. Enghardt**, L. Fabbietti, O. Fateev, P. Finocchiaro, P. Fonte, J. Friese, I. Froehlich, J. Garzon, R. Gernhaeuser, M. Golubeva, D. Gonzalez-Diaz, **E. Grosse**, F. Guber, T. Heinz, T. Hennino, S. Hlavac, J. Hoffmann, R. Holzmann, A. Ierusalimov, I. Iori, A. Ivashkin, M. Jaskula, M. Jurkovic, M. Kajetanowicz, **B. Kämpfer**, **K. Kanaki**, T. Karavicheva, D. Kirschner, I. Koenig, W. Koenig, B. Kolb, U. Kopf, **R. Kotte**, J. Kotulic-Bunta, R. Kruecken, A. Kugler, W. Kuehn, R. Kulessa, S. Lang, J. Lehnert, L. Maier, P. Maier-Komor, C. Maiolino, J. Marin, J. Markert, V. Metag, N. Montes, E. Moriniere, J. Mousa, M. Muench, C. Müntz, **L. Naumann**, R. Novotny, J. Novotny, W. Ott, J. Otwinowski, Y. Pachmayer, T. Perez, V. Pechenov, J. Pietraszko, J. Pinhao, R. Pleskac, V. Pospisil, A. Pullia, N. Rabin, B. Ramstein, S. Riboldi, J. Ritman, P. Rosier, M. Roy-Stephan, A. Rustamov, **A. Sadovsky**, B. Sailer, P. Salabura, P. Sapienza, A. Schmah, W. Schön, C. Schröder, E. Schwab, P. Senger, R. Simon, V. Smolyankin, L. Smykov, S. Spataro, B. Spruck, H. Ströbele, J. Stroth, C. Sturm, M. Sudol, V. Tiflov, P. Tlusty, A. Toia, M. Traxler, H. Tsertos, I. Turzo, V. Wagner, W. Walus, C. Willmott, S. Winkler, M. Wisniowski, T. Wojcik, **J. Wüstenfeld**, Y. Zanevsky, P. Zumbruch (HADES collaboration)

Published in Acta Phys. Pol. B 37 (2006) 139-151

The HADES (High Acceptance Di-Electron Spectrometer) is a tool designed for lepton pair (e^+e^-) spectroscopy in pion, proton and heavy ion induced reactions in the 1–2 A GeV energy range. One of the goals of the HADES experiment is to study in-medium modifications of hadron properties like effective masses, decay widths, electromagnetic form factors etc. Such effects can be probed with vector mesons (ρ, ω, ϕ) decaying into e^+e^- channel. The identification of vector mesons by means of a HADES spectrometer is based on invariant mass reconstruction of e+e- pairs. The combined information from all spectrometer subdetectors is used to reconstruct the di-lepton signal. The recent results from 2.2 GeV p+p, 1 A GeV and 2 A GeV C + C experiments are presented.

[1] J. Friese et al. (HADES collaboration), Prog. Part. Nucl. Phys. 42 (1999) 42

[2] H. Bokemeyer et al., Nucl. Instr. Meth. A 477 (2002) 397

[3] P. Salabura et al. (HADES collaboration), Nucl. Phys. A 749 (2005) 150

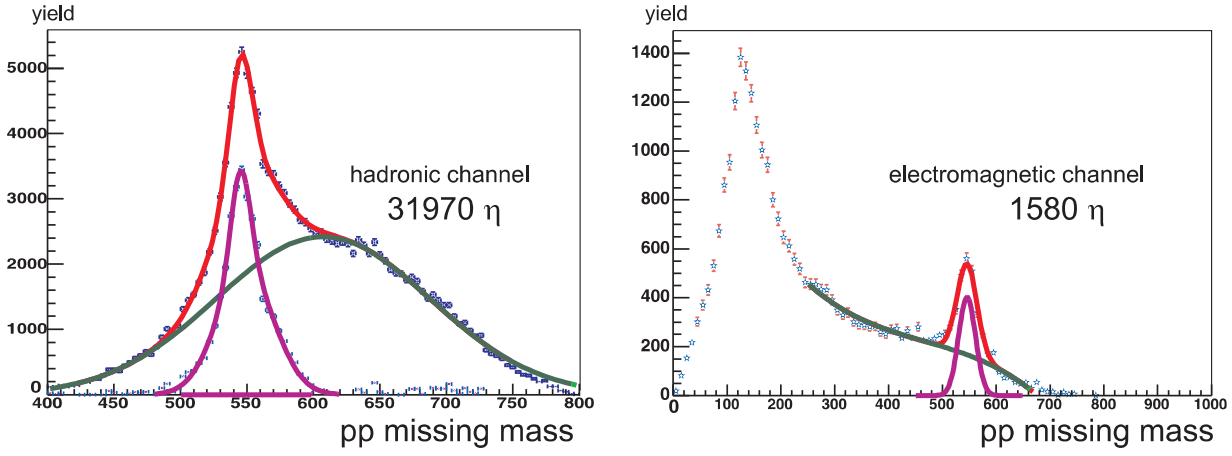

η meson signal retrieved from pp missing mass spectrum for hadronic (left) and electromagnetic (right) channels (no acceptance corrections). For each track the minimization procedure (kinematic fit, varying momentum, polar and azimuthal angles) was performed.

Dielectron Detection Capabilities of HADES for Beam Energies accessible at FAIR [G]

B. Bannier, F. Dohrmann, E. Grosse[1], B. Kämpfer, R. Kotte, L. Naumann, J. Wüstenfeld

Part of diploma thesis B. Bannier

For the FAIR project considerable updates of existing accelerator facilities at the GSI Darmstadt are projected. The available beam energies of the new SIS100 and SIS300 accelerators will be in the range of 2 AGeV to 25 AGeV and above. Experiments with both elementary probes and heavy-ions at beam energies $\leq$ 3.5 AGeV have been performed with the HADES detector at SIS18. The possible dielectron detection capabilities of HADES at the new facilities, focusing on Carbon–Carbon collisions at kinetic beam energies $T = 8 - 25$ AGeV were studied. An event generator based on the state of the art relativistic transport code UrQMDv1.3p1 [1] has been implemented and is available. Based on this event generator dielectron spectra for 8 AGeV and 25 AGeV are shown in Fig. 1 taking into account the geometrical acceptance of the HADES detector as it is currently installed.

For both energies a peak in the ρ, ω mass region is visible, although the background situation at the higher energy deteriorates considerably. The simulations indicate that a determination of the yield of true pairs from particle decays in the $\rho - \omega$ mass region after one week of beam time may be feasible. This study [2] has to be seen in line with other studies [3,4] on this subject.

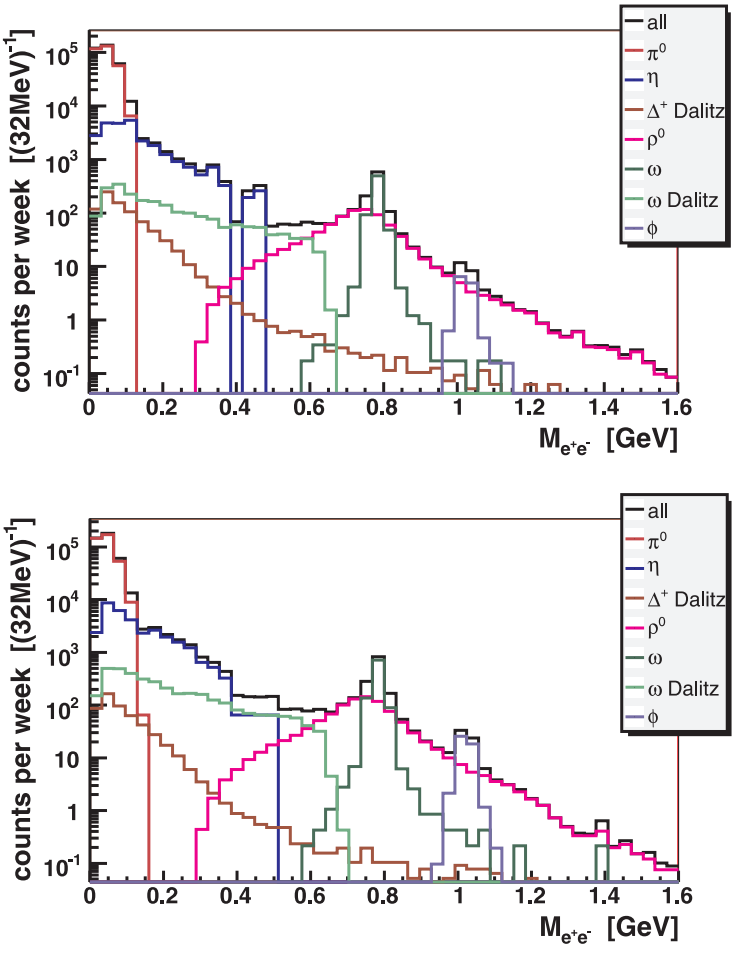

Fig. 1 *Invariant mass spectra for central Carbon-Carbon collisions at beam energies of 8 AGeV (upper panel) and 25 AGeV (lower panel) after one week of beamtime. Pairs are created from all e^+ and e^- emitted into the HADES acceptance with momenta $p >$ 50 MeV. Leptons from pairs with opening angles smaller than 9^o are excluded. Particle momenta have been convolved with a momentum dependent error following the procedure given in [5]. For clarity, the simulated combinatorial background was omitted from these figures. Details on how to subtract combinatorial background using the like-sign method are given in [2].*

[1] http://www.th.physik.uni-frankfurt.de/~urqmd
[2] B. Bannier, Diploma Thesis, Technische Universität Dresden, Sep. 2006
[3] T. Galatyuk and J. Stroth, CBM-PHYS-note-2006-001, internal report, GSI Darmstadt 2006
[4] A. Kugler, Talk at CBM meeting, GSI Darmstadt 2004; Proc. Nucl. Phys. Winter meeting, Bormio 2006
[5] R. Holzmann, HAFT: Hades Acceptance Filter for Theorists, internal report, GSI Darmstadt 2006, http://hades-wiki.gsi.de/cgi-bin/view/SimAna/HadesAcceptanceFilter

[1] *also TU Dresden*

Validation of HADES-MDC Data [B,G]

P. Zhou, F. Dohrmann, B. Kämpfer, K. Kanaki, R. Kotte, L. Naumann, A. Sadovsky, J. Wüstenfeld
for the HADES collaboration

Part of PhD thesis P. Zhou

It is the goal of the HADES (High Acceptance Di-Electron Spectrometer) [1] collaboration to study the properties of mesons which are produced in the nuclear medium, in particular light vector mesons ρ, ω and ϕ. In order to investigate the dielectron elementary production mechanisms in pp reactions at an incident beam energy of 1.25 AGeV, the HADES collaboration performed the experiment in April 2006 at GSI.

Before data analysis, valuing the quality of the raw data taken from DAQ (data acquisition), must be done at first. The procedure of "File Validation" is an indispensable first step of data analysis. During data analysis, tracking of particle is the committed step, which have to use the signals taken from MDC (Multi-Wire Drift Chambers). One important part of the "File Validation" is MDC file selection which is presented here step by step.

1. Monitor Rate of HV (high voltage) changes: To protect the detectors the power supply system can automatically control the HV. Once a short-circuit has happened in one of the detectors, it immediately shuts the HV down slowly. This is a so called HV trip. During the HV trip the output signals of the detector are unusable, thus the first step of data analysis is to find out whether any data was taken during that time and then mark out the file which contains the data. Therefore, it is necessary to plot the rate of HV changes as per 10 minutes for each day. An example plot of one day is given in Fig. 1.

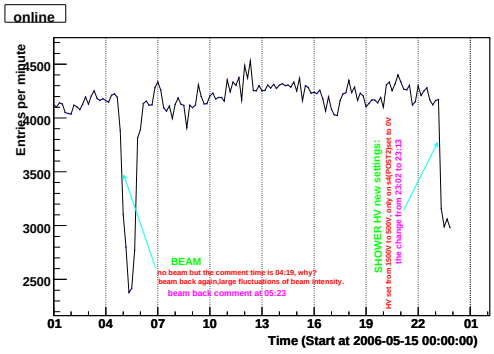

Fig. 1 *An example of the slow control system HV monitor rate of one day.*

2. MDC HV Summary for one HV Channel per Chamber: To find out a good value for the decision of a HV trip in a chamber, the potential of the Field channel 0 was checked for each chamber (see Fig. 2). The important values are the mean, minimum and maximum values of the potential. For this beam time a new safety mechanism was set up in EPICS (Experimental Physics and Industrial Control System, a kind of slow control system), i. e. an automatic ramp up of a tripped channel after some seconds, to limit the amount of downtime. Thus, the mean value is no longer a good value to decide on. Instead, the minimum value was chosen, as it provides a clear signal. If the value goes below 1000 V during the recording time of a file, it is assumed that the chamber tripped.

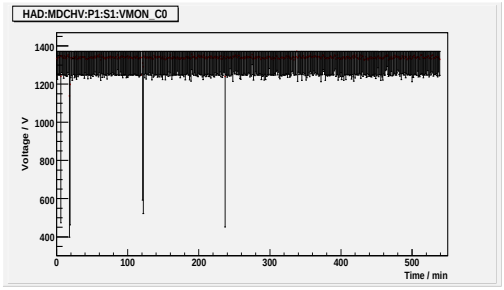

Fig. 2 *An instance of MDC HV summary for one HV channel per chamber.*

3. MDC Files Selection : One has to loop over all files taken from the beam time, checking for each of the HV values for the criteria discussed above. In each file the minimum voltage of all channels is checked and compared against the reference voltage defined in the previous step. If there are two or more trips in one file, it is declared to be unusable (see Fig. 3). Finally, separate lists containing different type of files can be retrieved.

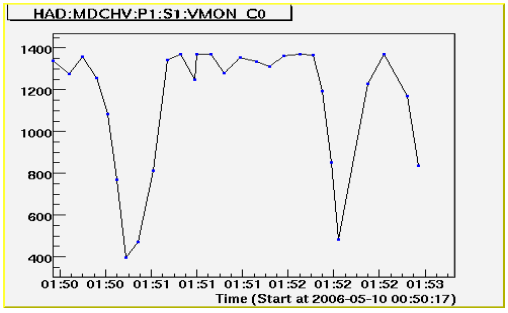

Fig. 3 *A case of HV trips in one file, which is unusable.*

4. MDC Final Validation: The files are validated with these quality factors, according to the following rules. If one of the chambers of plane II to IV had a trip, the file is set unusable. If the trip occurred in plane I, the file is of restricted usability. All other files are fully usable. Three different lists containing the name of the three kind of files separately are formed and put into the HADES database, in order to be used during subsequent step of data analysis.

The introduction of MDC file selection for the Apr06 beam-time of HADES in GSI is complete. For details of this work, please see www-hades.gsi.de.

[1] G. Agakichiev et al., Phys. Rev. Lett. 98 (2007) 052302

Propagation of Broad Meson Resonances in a BUU Type Transport Model: Application to Di-Electron Production [B,E]

H.W. Barz, B. Kämpfer, Gy. Wolf [1], M. Zetenyi[1]

Di-electrons serve as direct probes of dense nuclear matter stages during the course of heavy-ion collisions. The superposition of various sources, however, requires a deconvolution of the spectra by means of models. Of essential interest are the contributions of the light vector mesons ρ and ω. The spectral functions of both mesons are expected to be modified in a strongly interacting environment in accordance with chiral dynamics, QCD sum rules etc. After the first pioneering experiments with the DLS spectrometer now improved measurements with HADES [1] start to explore systematically the baryon-dense region accessible in fixed-target heavy-ion experiments at beam energies in the few AGeV region.

To implement properly the propagation of broad resonances we utilize the kinetic approach of [2] and the spectral function of mesons as a function of the self-energy Σ^{ret}

$$\mathcal{A}(p) = \frac{\hat{\Gamma}(x,p)}{(E^2 - \vec{p}^2 - m_0^2 - Re\Sigma^{ret}(x,p))^2 + \frac{1}{4}\hat{\Gamma}(x,p)^2}\,, \tag{1}$$

where the resonance widths Γ and $\hat{\Gamma}$ are connected via $\hat{\Gamma}(x,p) = -2Im\Sigma^{ret} \approx 2m_0\Gamma$, and m_0 is the vacuum pole mass of the respective particle. The dynamical evolution of spectral function is accomplished within the test particle method. There, the change of the particle mass m is evidenced in the combined transport equation emerging from the separate time evolution of the particle's three-position, three-momentum and energy [2]

$$\frac{dm^2}{dt} = \frac{1}{1-C}\left(\frac{d}{dt}Re\Sigma^{ret} + \frac{m^2 - m_0^2 - Re\Sigma^{ret}}{\hat{\Gamma}}\frac{d}{dt}\hat{\Gamma}\right) \tag{2}$$

with the comoving derivative $d/dt \equiv \partial_t + \vec{p}/E\vec{\partial}_x$ and renormalization factor C. This equation means that the square of the particle mass tends to reach a value shifted by the real part of the self-energy within a range of the value of $\hat{\Gamma}$. Thus, the vacuum spectral function is recovered when the particle leaves the medium. This ensures the smooth transition from the in-medium behavior to the vacuum properties. In Fig. 1 we exhibit the temporal change of the test particle's mass for ρ and ω mesons together with the local density. The spread of the ρ, ω masses is clearly seen as well as the evolution towards the vacuum spectral function in case of long-living ω mesons. The ρ mesons are short-living, thus often rapidly decaying. Fig. 2 exhibits the resulting di-electron spectra from direct ρ and ω decays.

A first comparison with HADES data is published in [3].

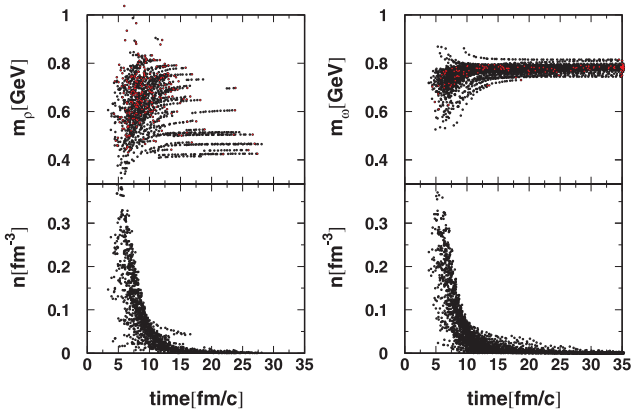

Fig. 1 *Temporal change of selected test particle masses for ρ (left top panel) and ω (right top panel) mesons. The bottom row exhibits the local density of baryon matter surrounding the respective test particle. For the reaction C(2 AGeV) + C. Open circles indicate instances of pion decay.*

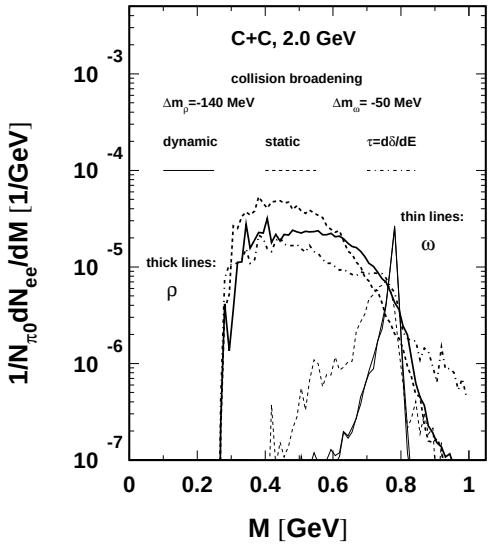

Fig. 2 *Contributions to di-electron spectra from ρ and ω decays calculated with the effect of the mass evolution (solid lines ("dynamic"): using the above evolution equations, dot-dashed lines ("$\tau = d\delta/dE$"): employing $\tau^{-1} = b_c\Gamma^{tot} = b_c(d\delta/dE)^{-1}$ as prescription for the life time). For comparison, the dashed curves ("static") neglect the time evolution of the spectral functions.*

[1] H. Agakishev et al. (HADES collaboration), Phys. Rev. Lett. 98 (2007) 052302

[2] W. Cassing and S. Juchem, Nucl. Phys. A 672 (2000) 417

[3] H.W. Barz, B. Kämpfer, Gy. Wolf, M. Zetenyi, nucl-th/0605036 (2006)

[1] *KFKI Budapest, Hungary*

Di-Electron Bremsstrahlung in Intermediate-Energy *Dp* Collisions [B,E]

L.P. Kaptari [1], **B. Kämpfer**

Published in Nucl. Phys. A 764 (2006) 338-370

Invariant mass spectra of di-electrons stemming from bremsstrahlung processes are calculated in a covariant diagrammatical approach for the exclusive reaction $Dp \to p_{\rm sp}\, np\, e^+e^-$ with detection of a forward spectator proton, $p_{\rm sp}$. We employ an effective nucleon-meson theory for parameterizing the sub-reaction $np \to npe^+e^-$ and, within the Bethe-Salpeter formalism, derive a factorization of the cross section in the form $d\sigma_{Dp\to p_{\rm sp}\, np\, e^+e^-}/dM = d\sigma_{np\to np\, e^+e^-}/dM\times$ kinematical factor related solely to the deuteron (M is the e^+e^- invariant mass). The effective nucleon-meson interactions, including the exchange mesons π, σ, ω and ρ as well as excitation and radiative decay of $\Delta(1232)$, have been adjusted to the process $pp \to pp\, e^+e^-$ at energies below the vector meson production threshold. At higher energies, contributions from ω and ρ meson excitations are analyzed in both, NN and Dp collisions. A relation to two-step models is discussed. Subthreshold di-electron production in Dp collisions at low spectator momenta is investigated as well. Calculations have been performed for kinematical conditions envisaged for forthcoming experiments at HADES.

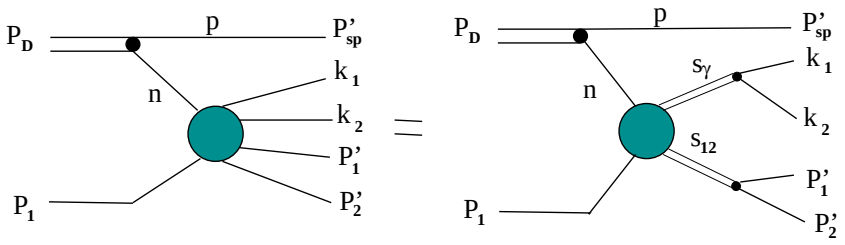

Fig. 1 *Kinematics of the process* $D(P_D) + p(P_1) \to p(P_{\rm sp} + p(P_1') + n(P_2') + e^+(k_1) + e^-(k_2)$ *within the spectator mechanism.*

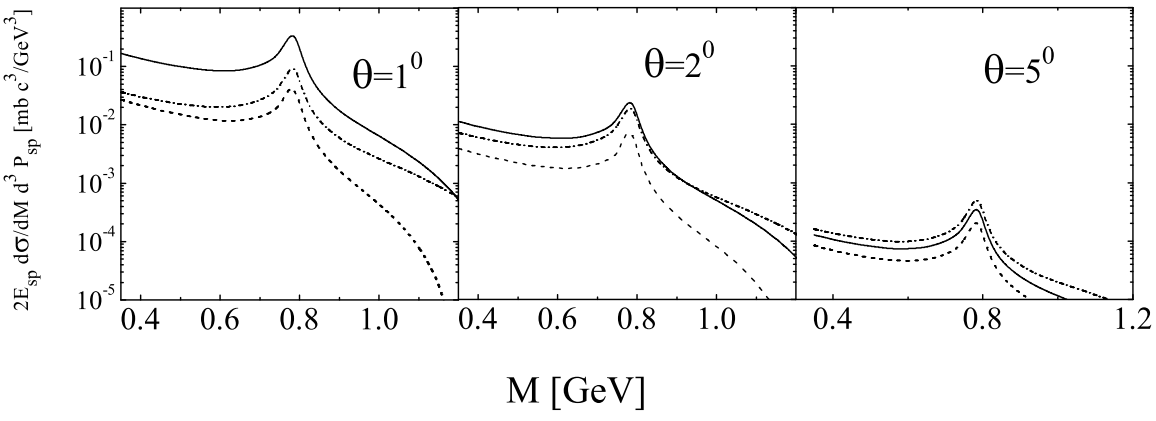

Fig. 2 *Invariant mass distribution* $2E_{\rm sp}\dfrac{d\sigma}{dMd^3p_{\rm sp}}$ *for the reaction* $Dp \to p_{\rm sp}\ np\ e^+e^-$, *at deuteron beam energy* $T_{kin} = 3.5$ *AGeV and three values of the spectator angle in the laboratory system,* $\theta = 1^\circ, 2^\circ$ *and* 5°. *Dot-dashed, solid and dashed curves correspond to values of the spectator momenta as indicated in the legends. Effects of VMD have been taken into account.*

[1] *JINR Dubna, 141980, Russia*

Di-Electrons from η Meson Dalitz Decay in Proton-Proton Collisions [B,E]

L.P. Kaptari [1], **B. Kämpfer**

Published in nucl-th/0702033, submitted to Eur. Phys. J. A

The reaction $pp \to pp\eta \to pp\gamma e^+e^-$ is discussed within a covariant effective meson-nucleon theory. Our focus is on di-electrons from Dalitz decays of η mesons, $\eta \to \gamma\gamma^* \to \gamma e^+e^-$. Numerical results are presented for the intermediate energy kinematics of envisaged HADES experiments.

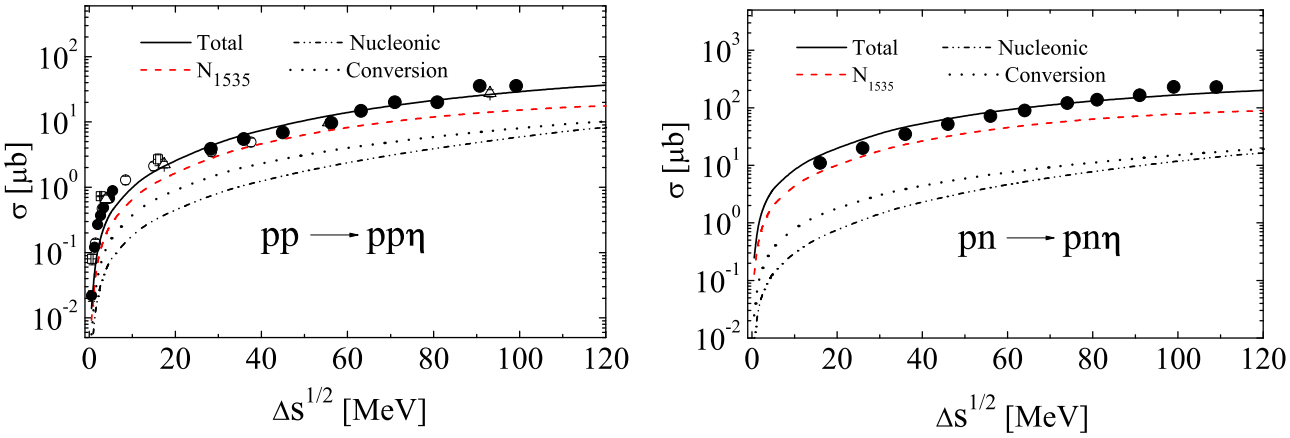

Fig. 1 *Total cross section for the reactions $pp \to pp\eta$ (left panel) and $np \to np\eta$ (right panel) as a function of the excess energy $\Delta s^{1/2} = \sqrt{s} - 2m - m_\eta$. The dot-dashed line corresponds to the nucleon current contribution (without resonances), while the dotted line is for the internal meson conversion diagram. The dashed curve exhibits the contribution of the $S_{11}(1535)$ resonance (nucleon resonance current). Contributions from $P_{11}(1440)$ and $D_{13}(1520)$ are smaller and not displayed. The solid curve is the total contribution with all interferences. References for data are quoted in the full article of this contribution; error bars are suppressed.*

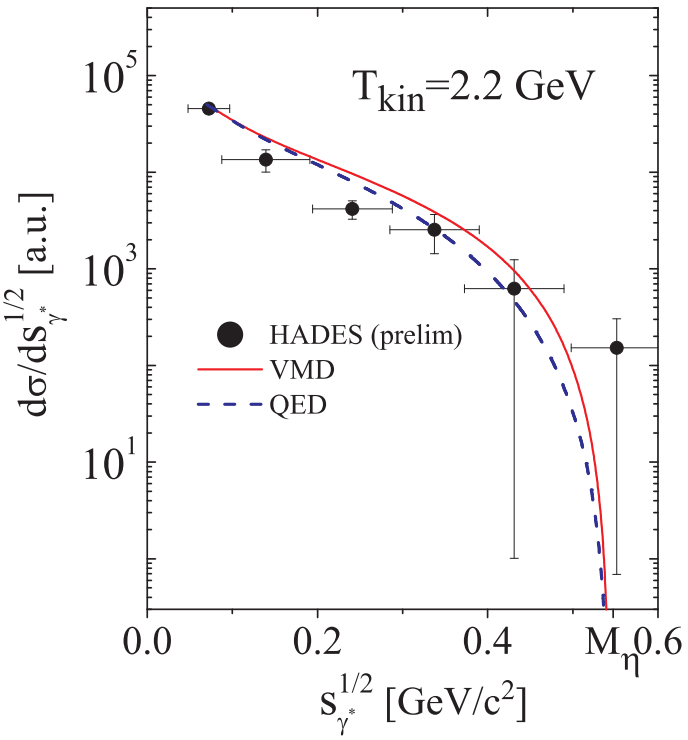

Fig. 2 *Invariant mass distribution of di-electrons produced by Dalitz decay of η mesons in the reaction $pp \to pp\gamma e^+e^-$ at initial kinetic energy $T_{kin} = 2.2\,GeV$. The solid line is for results with the $\eta\gamma\gamma^*$ transition form factor computed within the VMD model, while the dashed line corresponds to a purely QED calculation of the $\eta\gamma\gamma^*$ vertex, i.e., for $|F_{\eta\gamma\gamma^*}|^2 = 1$. The η pole mass position is exposed. Preliminary experimental data are from [1].*

[1] I. Fröhlich et al. (HADES), nucl-ex/0610048

[1] *JINR Dubna, 141980, Russia*

$\omega - \pi\gamma^*$ Transition Form Factor in Proton-Proton Collisions [B,E]

L.P. Kaptari [1], **B. Kämpfer**

Published in Eur. Phys. J. A 31 (2007) 233-243

Dalitz decays of ω and ρ mesons, $\omega \to \pi^0\gamma^* \to \pi^0 e^+e^-$ and $\rho^0 \to \pi^0\gamma^* \to \pi^0 e^+e^-$, produced in pp collisions are calculated within a covariant effective meson-nucleon theory. We argue that the ω transition form factor $F_{\omega\to\pi^0\gamma^*}$ is experimentally accessible in a fairly model independent way in the reaction $pp \to pp\pi^0 e^+e^-$ for invariant masses of the $\pi^0 e^+e^-$ subsystem near the ω pole. Numerical results are presented for the intermediate energy kinematics of envisaged HADES experiments.

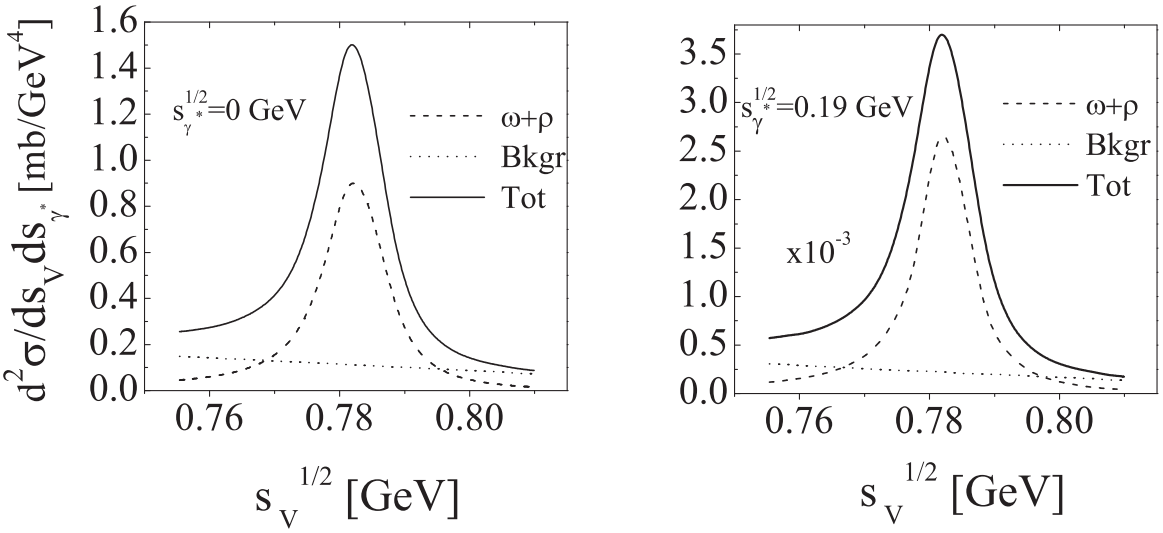

Fig. 1 *The double differential cross section $d\sigma/ds_V ds_{\gamma^*}$ as a function of $s_V^{1/2}$ in the vicinity of the ω pole for $T_{beam} = 2.2\,GeV$ with background contribution taken into account. The relative sign between the resonant and background amplitudes is chosen positively resulting in a constructive interference. The dashed line corresponds to the resonant contributions of diagrams with ω and ρ Dalitz decays, the dotted line corresponds to the background contribution alone, and the solid line is the resulting total cross section. The employed transition form factor is for the VMD model. Left (right) panel is for $\sqrt{s_{\gamma*}} = 2m_e \to 0$ (0.19) GeV.*

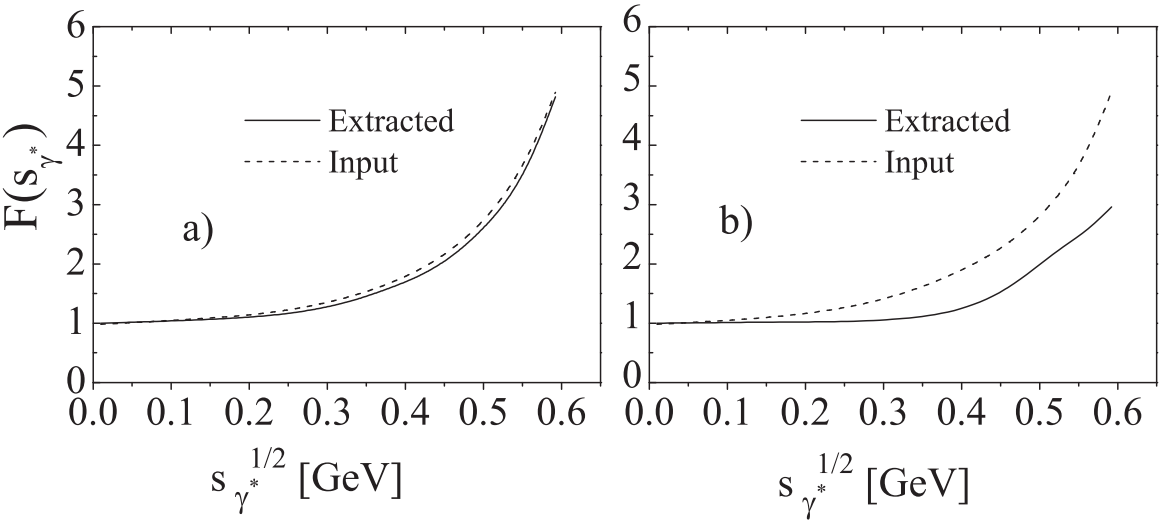

Fig. 2 *The extracted form factor (solid curves) calculated at $T_{beam} = 2.2\,GeV$ with inclusion of the background contribution. Dashed lines correspond to the input FF taken from the VMD model. The averaging has been performed in the ±3.5 % vicinity of the ω pole mass. Panels a) and b) correspond to destructive and constructive interference effects, respectively.*

[1] *JINR Dubna, 141980, Russia*

K^+ and Λ Production in C + C Collisions at 2 AGeV with HADES [B,G]

K. Kanaki, A. Sadovsky, F. Dohrmann, E. Grosse[1], B. Kämpfer, R. Kotte, L. Naumann, J. Wüstenfeld
and the HADES collaboration

Part of the PhD theses K. Kanaki and A. Sadovsky

An analysis of associated strangeness production in Carbon Carbon collisions at 2 AGeV has been performed. The data were taken with the HADES detector. In particular, multiplicities of Λ hyperons [1] and K^+ mesons [2] were determined and new valuable information on strangeness balance, complementary to existing data was gained. Here we present double-differential yields $d^2\sigma/dm_t dy_0$ normalized by $1/m_t^2$, where $m_t = \sqrt{m_0^2 + p_t^2}$ is the transverse mass, p_t is the transverse momentum and m_0 is the kaon rest mass. The statistics collected allowed for evaluating the data in six bins of normalized rapidity $y_0 = (y/y_{\rm cm} - 1)$, where $y = \tanh^{-1}(\beta_z)$ is the Lorentz-invariant longitudinal velocity. This differential information was not available before. Comparisons with results obtained previously by the KaoS collaboration [3] showed consistency within errors for both, inverse slope parameter as well as total cross section (see [2] for details).

Λ hyperons were identified via their charged decay $\Lambda \to p\pi^-$. The multiplicity per event for Λ production in C + C collisions at 2 AGeV was determined to be $\mathcal{M}_{\Lambda+\Sigma^0} = 0.0092 \pm 0.0012(\text{stat.})^{+0.0034}_{-0.0017}(\text{syst.})$. This number includes Λ from Σ^0 decay ($\Sigma^0 \to \Lambda\gamma$, BR $\simeq 100\%$), which experimentally cannot be distinguished from the primary ones with HADES.

[1] K. Kanaki, Ph.D. thesis, TU Dresden (2006)
[2] A. Sadovsky, Ph.D. thesis, TU Dresden (2006)
[3] F. Laue, C. Sturm et al. Phys. Rev. Lett. 82 (1999) 1640; F. Laue, I. Boettcher et al., Eur. Phys. J. A 9 (2000) 397

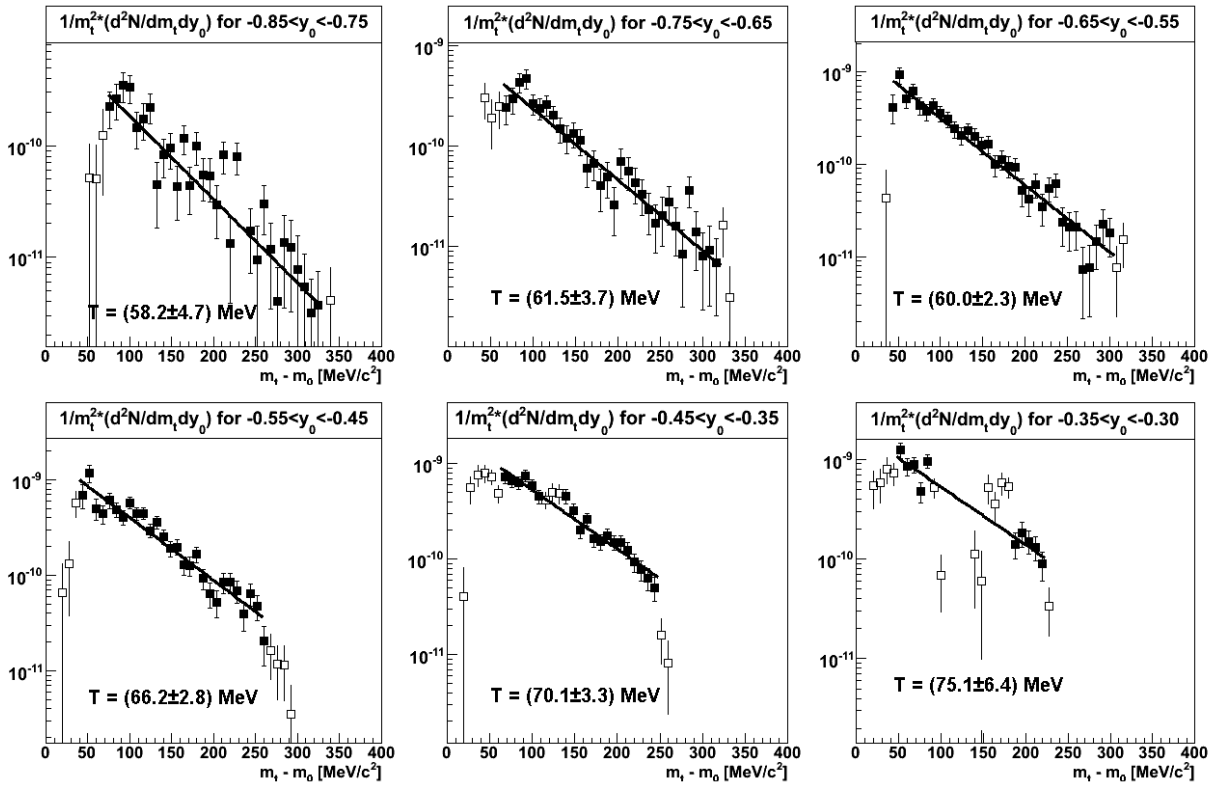

Fig. 1 $\frac{1}{m_t^2} \cdot \frac{d^2\sigma}{dm_t dy_0}$ *distributions of* K^+ *mesons for different rapidity regions. The units for vertical axis are* $b\,[MeV/c^2]^{-3}$. *The data (symbols) are fitted assuming a thermally equilibrated source given by a Maxwell-Boltzmann like distribution with a normalization factor* $A(y_0)$ *and an apparent temperature* T_B

$$\frac{1}{m_t^2} \cdot \frac{d^2\sigma}{dm_t dy_0} = A(y_0) \cdot \exp\Big(-\frac{m_t - m_0}{T_B}\Big).$$

Both parameters, $A(y_0)$ *and* T_B, *are determined by the fits for each of the six intervals in* y_0. *The selected* m_t *regions (filled symbols) used for the fits (solid lines) correspond to the limits given by the phase space accessible with HADES during this experiment. Empty symbols denote data excluded from the fits (see ref. [2] for details).*

[1] *also TU Dresden*

In-Medium Effects on Phase Space Distributions of Antikaons Measured in Proton-Nucleus Collisions [B]

W. Scheinast, F. Dohrmann, E. Grosse[1], L. Naumann, H.W. Barz, B. Kämpfer and the KaoS Collaboration

Published in Phys. Rev. Lett. 96 (2006) 072301, 1-4

Differential production cross sections of $K^{\pm}$ mesons have been measured in p + C and p + Au collisions at 1.6, 2.5 and 3.5 GeV proton beam energy. At beam energies close to the production threshold, the K^- multiplicity is strongly enhanced with respect to proton-proton collisions. According to microscopic transport calculations, this enhancement is caused by two effects: the strangeness exchange reaction $NY \rightarrow K^-NNN$ and an attractive in-medium K^-N potential at saturation density.

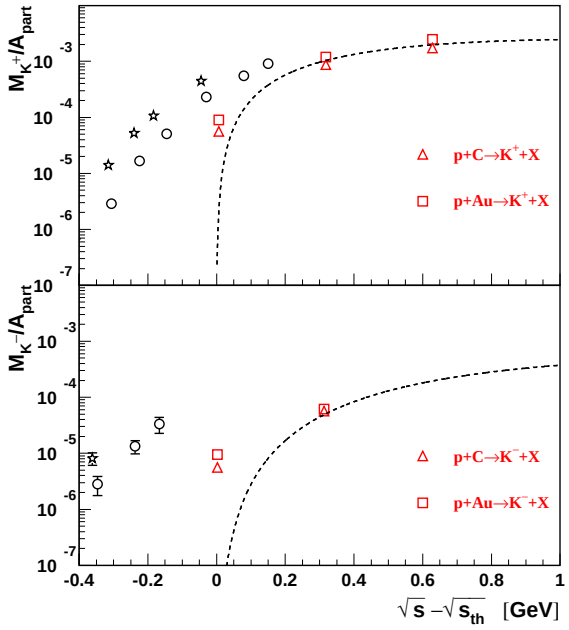

Fig. 1 *Multiplicity normalized by the number of participants as a function of the number of participants for K^+ (upper panel) and K^- (lower panel) for inclusive pAu (open squares) and pC (open triangles) collision as function of the excess energy.*

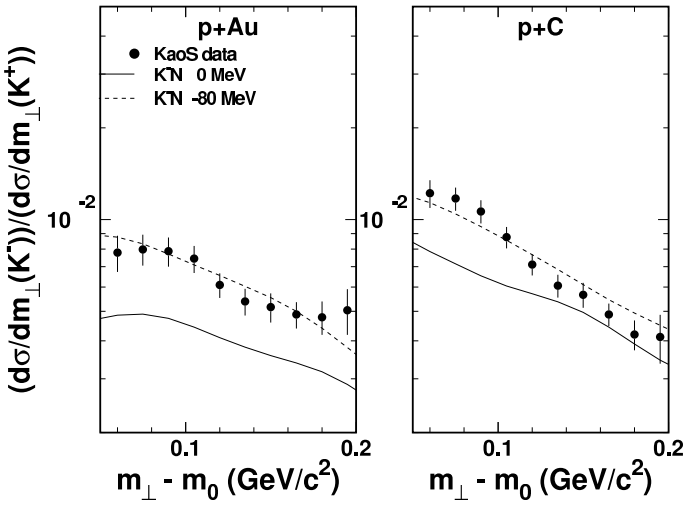

Fig. 2 *Average normalized densities at which $K^{\pm}$ are observed, inferred from BUU calculations for pAu and $AuAu$ collisions.*

[1] *also TU Dresden*

Production of K^+ and of K^- Mesons in Heavy-Ion Collisions from 0.6 to 2.0 A GeV Incident Energy [B]

A. Förster, F. Uhlig, I. Böttcher, D. Brill, M. Dębowski, **F. Dohrmann**, **E. Grosse**[1], P. Koczoń, B. Kohlmeyer, S. Lang, F. Laue, M. Mang, M. Menzel, C. Müntz, **L. Naumann**, H. Oeschler, M. Płoskoń, **W. Scheinast**, A. Schmah, T. J. Schuck, E. Schwab, P. Senger, Y. Shin, J. Speer[†], H. Ströbele, C. Sturm, G. Surówka, A. Wagner, W. Waluś (KaoS Collaboration)

Published in Phys. Rev. C 75 (2007) 024906, 1-19

This paper summarizes the yields and the emission patterns of K^+ and of K^- mesons measured in inclusive C+C, Ni+Ni and Au+Au collisions at incident energies from 0.6 A GeV to 2.0 A GeV using the Kaon Spectrometer KaoS at GSI. For Ni+Ni collisions at 1.5 and at 1.93 A GeV as well as for Au+Au at 1.5 A GeV detailed results of the multiplicities, of the inverse slope parameters of the energy distributions and of the anisotropies in the angular emission patterns as a function of the collision centrality are presented. When comparing transport-model calculations to the measured K^+ production yields an agreement is only obtained for a soft nuclear equation of state (compression modulus $K_N \approx 200$ MeV). The production of K^- mesons at energies around 1 to 2 A GeV is dominated by the strangeness-exchange reaction $K^-N \rightleftharpoons \pi Y$ ($Y = \Lambda, \Sigma$) which leads to a coupling between the K^- and the K^+ yields. However, both particle species show distinct differences in their emission patterns suggesting different freeze-out conditions for K^+ and for K^- mesons.

[1] C. Hartnack, H. Oeschler, J. Aichelin, Phys. Rev. Lett. 96 (2006) 012302

[2] C. Fuchs, A. Faessler, E. Zabrodin, Y. M. Zheng, Phys. Rev. Lett. 86 (2001) 1974

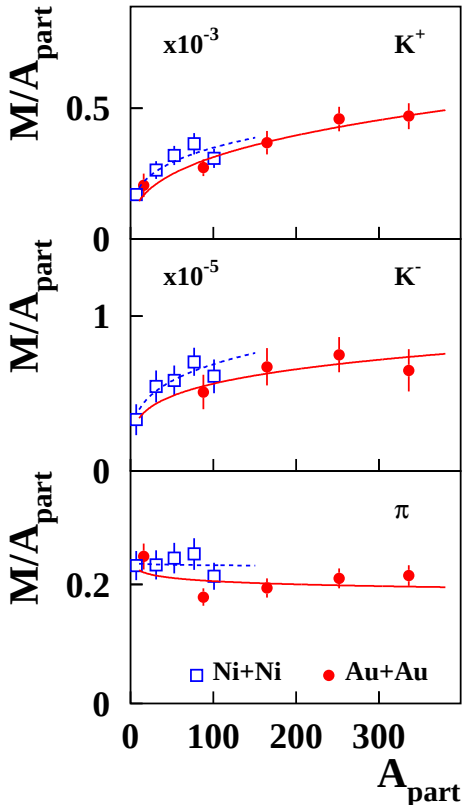

Fig. 1 *Dependence of the multiplicities of K^+ (upper panel) and of K^- mesons (middle panel) as well as of pions (lower panel) on $A_{\rm part}$. Full symbols denote Au+Au, open symbols Ni+Ni, both at 1.5 A GeV. The lines are functions $M \sim A_{\rm part}^{\alpha}$ fitted to the data separately for Au+Au (solid lines) and Ni+Ni (dashed lines). The data have been measured at $\theta_{\rm lab} = 40°$.*

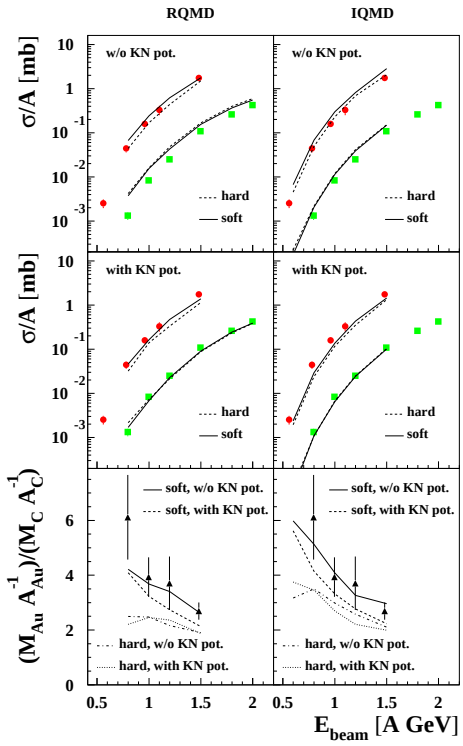

Fig. 2 *Upper and middle panels: Comparison of the K^+ excitation functions ($\sigma(K^+)/A$) for Au+Au (red circles) and for C+C collisions (green squares) with RQMD [2] (left hand side) and with IQMD calculations [1] (right hand side). Solid lines depict a hard EoS, dashed lines depict a soft EoS. The upper panels show calculations without KN potentials, the middle panels calculations with KN potentials. Lower panels: Double ratio of the K^+ multiplicities per mass number M/A in Au+Au divided by the one in C+C and the comparison to the various transport-model calculations.*

[1] *also TU Dresden* [†] *deceased*

Isospin Dependence of Relative Yields of K^+ and K^0 Mesons at 1.528 AGeV [G]

X. Lopez, Y.J. Kim, N. Herrmann, A. Andronic, V. Barret, Z. Basrak, N. Bastid, M.L. Benabderrahmane, R. Caplar, E. Cordier, P. Crochet, P. Dupieux, M. Dzelalija, Z. Fodor, I. Gasparic, Y. Grishkin, O.N. Hartmann, K.D. Hildenbrand, B. Hong, T.I. Kang, J. Kecskemeti, M. Kirejczyk, M. Kis, P. Koczon, M. Korolija, **R. Kotte**, A. Lebedev, Y. Leifels, M. Merschmeyer, **W. Neubert**, D. Pelte, M. Petrovici, F. Rami, W. Reisdorf, M.S. Ryu, A. Schüttauf, Z. Seres, B. Sikora, K.S. Sim, V. Simion, K. Siwek-Wilczynska, V. Smolyankin, G. Stoicea, Z. Tyminski, P. Wagner, K. Wisniewski, **D. Wohlfarth**, Z.G. Xiao, I. Yushmanov, X.Y. Zhang, A. Zhilin (FOPI Collaboration), G. Ferrini, T. Gaintanos

Published in Phys. Rev. C 75 (2007) 011901, 1-5

Results on K^+ and K^0 meson production in $^{96}_{44}$Ru + $^{96}_{44}$Ru and $^{96}_{40}$Zr + $^{96}_{40}$Zr collisions at a beam kinetic energy of 1.528A GeV, measured with the FOPI detector at GSI-Darmstadt, are investigated as a possible probe of isospin effects in high density nuclear matter. The measured double ratio $(K^+/K^0)_{Ru}/(K^+/K^0)_{Zr}$ is compared to the predictions of a thermal model and a Relativistic Mean Field transport model using two different collision scenarios and under different assumptions on the stiffness of the symmetry energy. We find a good agreement with the thermal model prediction and the assumption of a soft symmetry energy for infinite nuclear matter while more realistic transport simulations of the collisions show a similar agreement with the data but also exhibit a reduced sensitivity to the symmetry term.

[1] A. Andronic, P. Braun-Munzinger, J. Stachel, Nucl. Phys. A 772 (2006) 167
[2] T. Gaitanos, Phys. Lett. B 595 (2004) 209
[3] T. Gaitanos, Nucl. Phys. A 732 (2004) 24
[4] G. Ferini, M. Colonna, T. Gaitanos, M. Di Toro, Nucl. Phys. A 762 (2005) 147

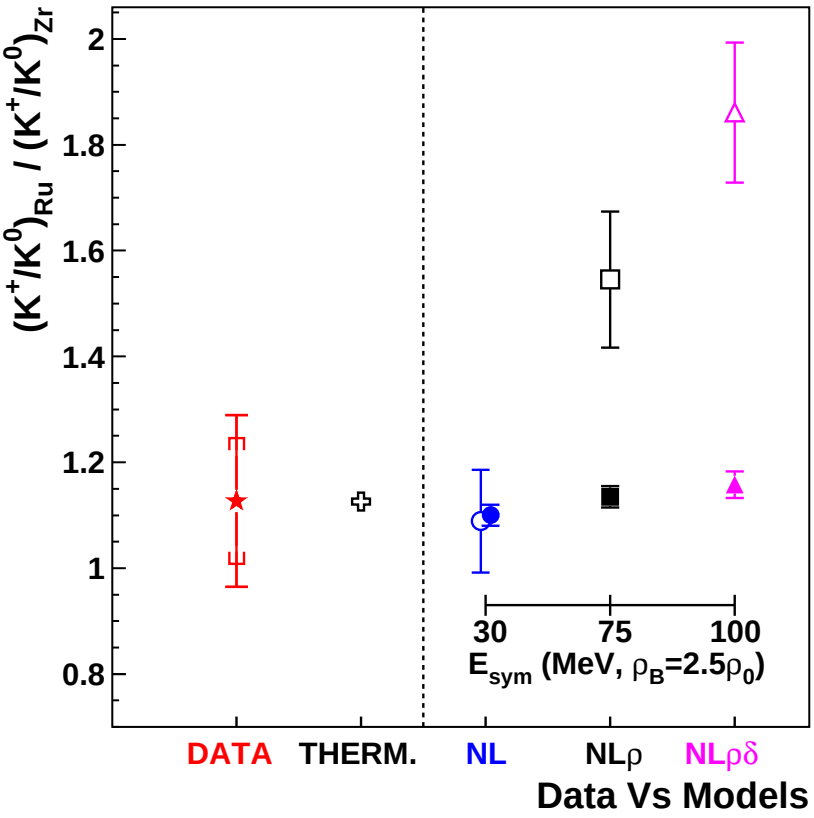

Experimental ratio $(K^+/K^0)_{Ru}/(K^+/K^0)_{Zr}$ (star) and theoretical predictions of the thermal model [1] (cross) and the transport model [2, 3, 4] with 3 different assumptions on the symmetry energy: NL (circles), NLρ (squares) and NL$\rho\delta$ (triangles). The INM and HIC calculations are represented by open and full symbols, respectively. The statistic and systematic errors are represented by vertical bars and brackets, respectively.

Hyperon Production in the Channel $pp \to K^+\Lambda p$ Near the Reaction Threshold [B, J]

S. Abd El-Samad, R. Bilger, A. Böhm, K.-Th. Brinkmann, H. Clement, S. Dshemuchadse, A. Erhardt, W. Eyrich, C. Fanara, A. Filippi, H. Freiesleben, M. Fritsch, R. Geyer, J. Hauffe, A. Hassan, P. Herrmann, D. Hesselbarth, B. Jakob, K. Kilian, H. Koch, J. Kress, E. Kuhlmann, S. Marcello, S. Marwinski, A. Metzger, **P. Michel**, **K. Möller**, H.P. Morsch, **L. Naumann**, E. Roderburg, **A. Schamlott**, P. Schönmeier, M. Schulte-Wissermann, W. Schroeder, M. Steinke, F. Stinzing, G.Y. Sun, J. Wächter, G.J. Wagner, M. Wagner, A. Wilms, S. Wirth, U. Zielinski
(COSY-TOF Collaboration)

Published in Phys. Lett. B 632 (2006) 27-34

Hyperon production in the threshold region was studied in the reaction $pp \to K^+\Lambda p$ using the time-of-flight spectrometer COSY-TOF. Exclusive data, covering the full phase-space, were taken at three different beam momenta p_{beam}= 2.59, 2.68 and 2.85 GeV/c (corresponding to excess energies of ε = 85, 115 and 171 MeV). Total cross-sections were deduced to be $7.4\pm0.5\mu b, 8.6 \pm 0.6\mu b$ and $16.5\pm0.4\mu b$, respectively. Differential observables including Dalitz plots were obtained. From the investigation of the Dalitz plot at p_{beam}=2.85 GeV/c a dominant contribution of the $N^\star(1650)$-resonance to the reaction mechanism was found. In addition the $p\Lambda$-final-state interaction turned out to have a significant influence on the Dalitz plot distribution even 171 MeV above threshold.

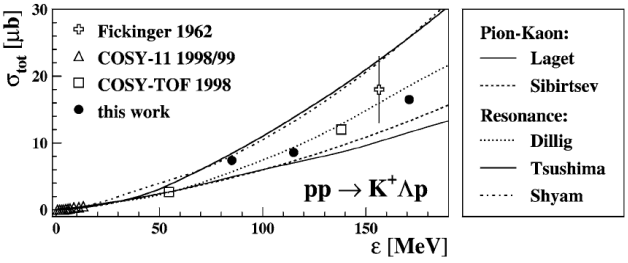

Fig. 1 *Total cross-sections of the channel $pp \to K^+\Lambda p$. All recent data up to $\varepsilon \leq 200MeV$ are shown in comparison with model calculations: pion-kaon exchange model of Laget [1] and Sibirtsev [2], resonance model of Dillig [3], Tsushima as given in [2] and Shyam [4]. The statistical errors are smaller than the size of the symbols. The systematic errors (not shown) are about 10%.*

[1] J.M. Laget, Phys. Lett. B 259 (1991) 24
[2] A. Sibirtsev et al., nucl-th/0004022
[3] F. Kleefeld, M. Dilling, F. Pilotto, Acta Phys. Pol. B 27 (1996) 2867
[4] R. Shyam, Phys. Rev. C 60 (1999) 055213

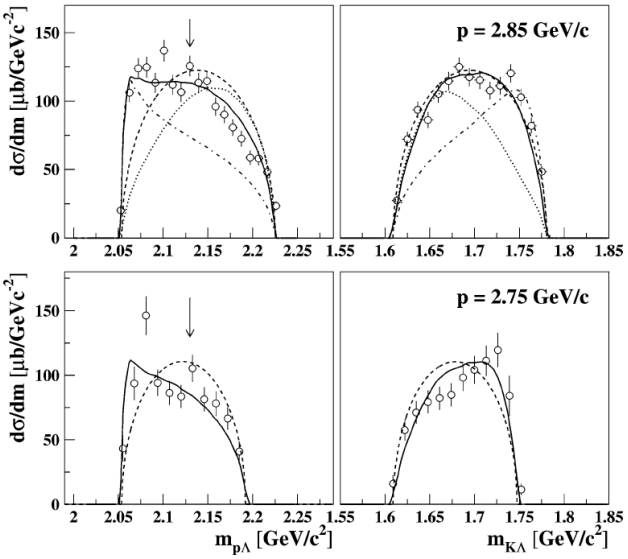

Fig. 2 *Distributions of the invariant mass of the $p\Lambda$- (left) and $K\Lambda$-subsystem (right) at p_{beam} = 2.85GeV/c (top) and 2.75 GeV/c (bottom) in comparison with the model of Sibirtsev (solid line) and pure phase space (dashed line). For the data at $p_{beam} = 2.85GeV/c$ in addition the contributions from the individual components are shown: only resonances (dotted line) and only $p\Lambda$-final-state interaction (dashed-dotted line). Arrows indicate the $p\Sigma^0$-threshold.*

Hunting ϕ Mesons in C + C Collisions at 2 AGeV

R. Kotte and the HADES Collaboration

The HADES spectrometer at SIS/GSI, initially designed for investigating the production of vector mesons via their leptonic decay into e^+e^- pairs, is able to detect hadronic probes, too. Here, we study the channel $\phi \to \mathrm{K^+K^-}$ in collisions of C + C at a beam energy of $E_{beam} = 2$ AGeV [1].

First, we have to find out whether the number of expected ϕ mesons in the data sample of about $N = 10^8$ events is large enough to justify such an experimental analysis. The number of ϕ mesons decaying into charged kaons can be calculated as $N_{\phi\to K^+K^-} = N_{ev}\cdot\epsilon_{trig}\cdot(P_{\phi\to K^+K^-}/P_{K^-})\cdot(\sigma_{K^-}/\sigma_{tot})\cdot\epsilon_{acc}(\Delta p_K, \Delta\theta_K, n_{sec}, E_{beam}, T_\phi)$. $\epsilon_{trig} \simeq 2.8$ is the 1st level trigger vs. minimum bias enhancement as estimated in ref. [2] aimed at $\mathrm{K^+}$ production. The number of anti kaons arising from ϕ decay, $P_{\phi\to K^+K^-}/P_{K^-} \geq 0.22$, is taken from the system Ni + Ni at 1.9 AGeV investigated by the FOPI collaboration [3]. The $\mathrm{K^-}$ production probability, i.e. the ratio of $\mathrm{K^-}$ and total geometrical cross sections, $\sigma_{K^-}/\sigma_{tot} = 2\cdot10^{-4}$, was measured by the KaoS collaboration [4]. Finally, the detector acceptance (including kaon decay) of the decay channel $\phi \to \mathrm{K^+K^-}$ is estimated applying Monte Carlo (MC) simulations. For the daughter kaons a momentum range of $\Delta p_K = (100 - 800)$ MeV/c is assumed. Only the outer part of the time-of-flight detector (TOF system) which exhibits much better time resolution than the inner part (TOFino) will be used in the analysis, hence $\Delta\theta_K = 45^o - 85^o$ was set in MC. Since only three out of six sectors could be used for the present analysis, sectors $n_{sec} = 0, 2, 3$ are activated in MC. The essential parameter of the midrapidity fireball modelled in MC is the inverse slope parameter T_ϕ of the Boltzmann-like c.m. kinetic energy distribution. So far, there is no published data on the momentum-space distribution of ϕ mesons in heavy-ion collisions at SIS energies. Thus, this parameter was chosen to be equal to the corresponding proton one, $T_\phi = T_p = 120$ MeV [5], which yields an acceptance factor of $\epsilon_{acc} = 2.5\cdot10^{-3}$. Having all these numbers at hand, in the above event sample we expect to see $N_{\phi\to K^+K^-} \geq 30$ ϕ mesons via their charged-kaon decay.

For the analysis of the experimental data, "kaon-pair-candidate" N-tuples are filled with the only condition of a ±150 MeV mass window around the nominal kaon mass, roughly corresponding to a 3σ cut at 10% mass resolution. (For masses we set $c = 1$.) Scanning these N-tuples, the same phase-space-relevant cuts as used in MC, i.e. i) TOF system only, ii) sectors 0, 2, 3, and iii) $100 < p_K/(\mathrm{MeV/c}) < 800$, are applied. To enhance the ratio of a possible signal over background, also quality cuts are investigated and optimized, i.e. iv) upper χ^2 limits on the inner ($\chi^2 < 15$) and outer ($\chi^2 < 30\,(17)$ for sectors 0, 3 (2)) track segments fitted to the hit positions measured with multiwire drift chambers (MDCs) in front and behind the HADES magnet, and v) MDC-TOF matching, $\Delta x < 40$ mm and $\Delta y < 10$ mm. About 400 kaon-pair candidates passed these conditions. Finally, kinematically suppressed opening angles ($> 120^o$) are rejected. Figure 1 displays the corresponding invariant mass distribution. Indeed, a peak is visible at the position of the nominal ϕ mass. Integrating the peak over ±8 MeV, an excess yield of about 22 entries with a significance of 2.8 is observed. Note, however, that the deduced width is a factor of $2 \div 3$ smaller than expected from MC simulations.

An order of magnitude more ϕ's is expected for the system Ar + KCl at 1.8 AGeV, due to a larger data sample and full azimuthal coverage of the spectrometer with at least three MDCs. This system is presently prepared for data-summary-tape production.

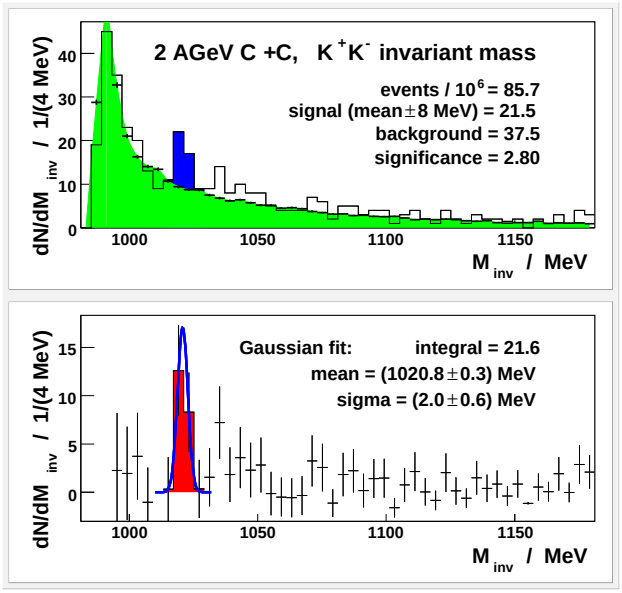

Fig. 1 *Upper panel: The invariant mass distribution of K^+K^- pair candidates (histogram). The light hatched (green) distribution gives the (renormalized at large invariant masses) corresponding uncorrelated background. The dark (blue) histogram is the potential signal within a 8 MeV wide mass window around the peak center. Lower panel: The difference of both distributions. The full line is a Gaussian fit to the yield excess at masses of 1010 MeV - 1030 MeV.*

[1] R. Kotte, HADES collab. meeting, GSI, Oct 2006
[2] A. Sadovsky, Ph.D. thesis, TU Dresden (2007)
[3] A. Mangiarotti et al., Nucl. Phys. A 714 (2003) 89
[4] F. Laue et al., Phys. Ref. Lett. 82 (1999) 1640
[5] P. Tlusty, Proc. XLII Wintermeeting on Nuclear Physics, Bormio 2004, Vol. 120 (2005) 171

Coherent Photo-Excitation of Θ^+ [B,E]

A.I. Titov [1], **B. Kämpfer**, S. Date [2], Y. Ohashi [2]

Published in Phys. Rev. C 74 (2006) 055206, 1-17

We analyze the possibility to produce an intermediate Θ^+ via a $KN \to \Theta^+$ formation process in $\gamma D \to pK^-X$ ($X = nK^+, pK^0$) reactions at some specific kinematical conditions, in which a pK^- pair is knocked out in the forward direction and its invariant mass is close to the mass of Λ^* ($\Lambda^* \equiv \Lambda(1520)$). The Θ^+ signal may appear in the $[\gamma D, pK^-]$ missing mass distribution. The ratio of the signal (cross section at the Θ^+ peak position) to the smooth background processes varies from 0.7 to 2.5 depending on the spin and parity of Θ^+, and it decreases correspondingly if the pK^- invariant mass is outside of the Λ^*-resonance region. We analyze the recent CLAS search for the Θ^+ in the $\gamma D \to pK^-nK^+$ reaction and show that the conditions of this experiment greatly reduce the Θ^+ formation process making it difficult to extract a Θ^+ peak from the data.

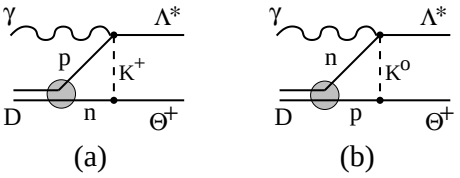

Fig. 1 *Tree level diagrams for the reaction $\gamma D \to \Lambda^*\Theta^+$. The exchange of charged and neutral kaons is shown in (a) and (b), respectively.*

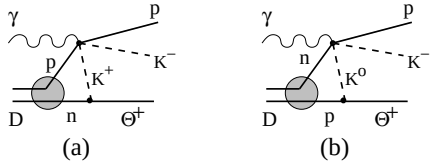

Fig. 2 *Diagrammatic representation of the associated non-resonant $pK^-\Theta^+$ photoproduction.*

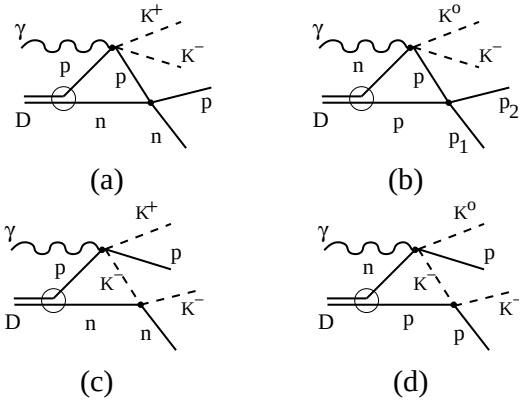

bf Fig. 3 Rescattering of the proton (a,b) and K^- meson (c,d) in pK^-NK photoproduction from the deuteron.

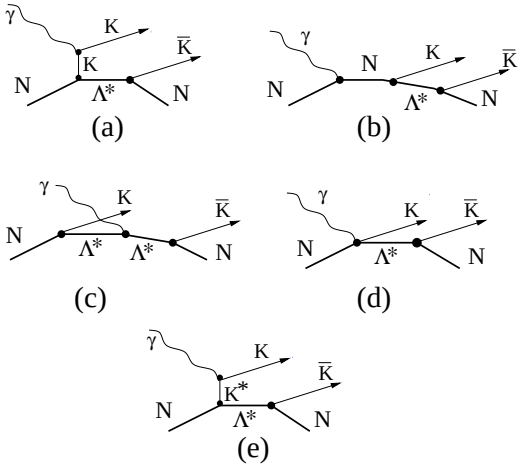

Fig. 4 *Tree level diagrams for the non-resonant subreaction $\gamma N \to \Lambda^* K \to NK\bar{K}$.*

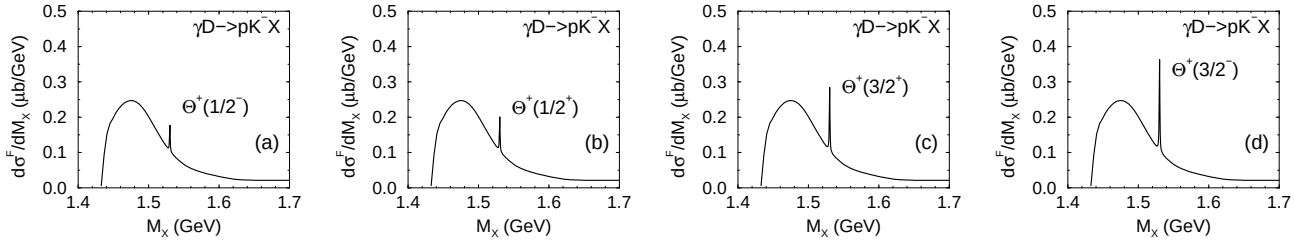

Fig. 5 *Missing mass distribution in the $\gamma D \to pK^-X$ reaction at $E_\gamma = 1.7 - 2.3$ GeV and $M_0 = 1.52$ GeV for different Θ^+ spin and parity: $J^P = \frac{1}{2}^-$ (a), $\frac{1}{2}^+$ (b), $\frac{3}{2}^+$ (c), and $\frac{3}{2}^-$ (d).*

The full article to this contribution is based on preceding ones [1,2].

[1] A.I. Titov, B. Kämpfer, S. Date, Y. Ohashi, Phys. Rev. C 72 (2005) 014005
[2] A.I. Titov, B. Kämpfer, Phys. Rev. C 71 (2005) 062201(R)

[1] *JINR Dubna, 141980, Russia*
[2] *Synchrotron Radiation Research Inst., Sayogun Hyogo 679-5198, Japan*

Production of Strangeness in Hot and Cold Nuclear Matter induced by both Leptonic and Hadronic Projectiles [B]

F. Dohrmann

Published in Int. J. Mod. Phys. E 15 (2006) 761-851

Strangeness production by both hadronic and leptonic projectiles with beam energies of up to a few GeV is reviewed. The focus is on the production of strangeness using proton and ion beams, as well as the photo- and electroproduction of strangeness, as observed at modern facilities. The elementary production of $K^{\pm}$ and ϕ mesons as well as Λ, Σ hyperons on the nucleon is described. Based on these results, the production of strange mesons and strange baryons on nuclear targets, as well as the creation of light hypernuclei is discussed, emphasizing the influence of the nuclear medium.

reaction	observable	experiment
$\gamma p \to K^+\Lambda$	$\frac{d\sigma}{d\cos\theta_K^{\rm CM}}$, P_Λ	CLAS (Jlab Hall B)
$\gamma p \to K^+\Lambda/\Sigma^0$	$\frac{d\sigma}{d\Omega}$, $\sigma_{\rm tot}$, P_{Λ/Σ^0}	SAPHIR (ELSA)
$\gamma p \to K^0\Sigma^+$	$\frac{d\sigma}{d\Omega}$, $\sigma_{\rm tot}$, P_{Σ^+}	SAPHIR (ELSA)
$\gamma p \to K^0\Sigma^+$	$\frac{d\sigma}{d\Omega}$, $\sigma_{\rm tot}$	CLAS (Jlab Hall B)
$\gamma p \to K^+\Sigma^0$	Σ	LEPS (SPring-8)
$\gamma p \to K^+\Lambda$	P, Σ	GRAAL
$\gamma n \to K^+\Sigma^-$	$\frac{d\sigma}{d\Omega}$	CLAS (Jlab Hall B)
$\gamma p \to p\phi$	$\frac{d\sigma}{dt}$, ρ^0_{00} (tensor polarization)	CLAS (Jlab Hall B)
$\gamma p \to p\phi$	K^+ azimuthal decay angle	LEPS (SPring-8)
$\gamma p \to \Xi K^+ K^-$	missing mass	CLAS (Jlab Hall B)
$\gamma p \to K^+\Lambda(1405)$	missing mass	LEPS (SPring-8)
$\gamma n \to K^0\Lambda$	missing mass	LNS (Tohoku)
$\gamma A \to \phi X$	$\sigma_{\phi N}$, A-dependence	LEPS (SPring-8)
$\gamma^* p \to K^+\Lambda/\Sigma^0$	$\frac{d\sigma}{d\Omega}$, σ_L/σ_T	E93018 (Jlab Hall C)
$\gamma^* A \to K^+ X$	$\frac{d\sigma}{d\Omega}$ (quasifree for Λ, Σ hyperons)	E91016 (Jlab Hall C)
$\gamma^{*\,3,4}{\rm He} \to K^{+\,3,4}_{\Lambda}{\rm H}$	$\frac{d\sigma}{d\Omega}$	E91016 (Jlab Hall C)
$\gamma^* p \to K^+\Lambda$	σ_L/σ_T	CLAS (Jlab Hall B)
$\gamma^* p \to K^+\Lambda$	transfer polarization	CLAS (Jlab Hall B)
$\gamma^* p \to K^+\Lambda(1520)$	$\frac{d\sigma}{d\Omega}$, decay angular distr.	CLAS (Jlab Hall B)
$\gamma^* p \to p\phi$	$\frac{d\sigma}{dt}$, σ	CLAS (Jlab Hall B)

Table 1 *Elementary electro- and photoproduction reactions and the observables studied at modern accelerators over the last year. For the references see the full article.*

Systematics of Pion Emission in Heavy Ion Collisions in the 1 AGeV Regime [G]

W. Reisdorf, M. Stockmeier, A. Andronic, M.L. Benabderrahmane, O.N. Hartmann, N. Herrmann, K.D. Hildenbrand, Y.J. Kim, M. Kis, P. Koczon, T. Kress, Y. Leifels, X. Lopez, M. Merschmeyer, A. Schüttauf, V. Barret, Z. Basrak, N. Bastid, R. Caplar, P. Crochet, P. Dupieux, M. Dzelalija, Z. Fodor, Y. Grishkin, B. Hong, T.I. Kang, J. Kecskemeti, M. Kirejczyk, M. Korolija, **R. Kotte**, A. Lebedev, T. Matulewicz, **W. Neubert**, M. Petrovici, F. Rami, M.S. Ryu, Z. Seres, B. Sikora, K.S. Sim, V. Simion, K. Siwek-Wilczynska, V. Smolyankin, G. Stoicea, Z. Tyminski, K. Wisniewski, **D. Wohlfarth**, Z.G. Xiao, H.S. Xu, I. Yushmanov and A. Zhilin (FOPI Collaboration)

Published in Nucl. Phys. A 781 (2007) 459-508

Using the large acceptance apparatus FOPI, we study pion emission in the reactions (energies in A GeV are given in parentheses): $^{40}Ca + ^{40}Ca$ (0.4, 0.6, 0.8, 1.0, 1.5, 1.93), $^{96}Ru + ^{96}Ru$ (0.4, 1.0, 1.5), $^{96}Zr + ^{96}Zr$ (0.4, 1.0, 1.5), $^{197}Au + ^{197}Au$ (0.4, 0.6, 0.8, 1.0, 1.2, 1.5). The observables include longitudinal and transverse rapidity distributions and stopping, polar anisotropies, pion multiplicities, transverse momentum spectra, ratios $(\pi^+/\pi-)$ of average transverse momenta and of yields, directed flow, elliptic flow. The data are compared to earlier data where possible and to transport model simulations.

[1] J. W. Harris et al., Phys. Lett. B 153 (1985) 377
[2] J. W. Harris et al., Phys. Rev. Lett. 58 (1987) 463

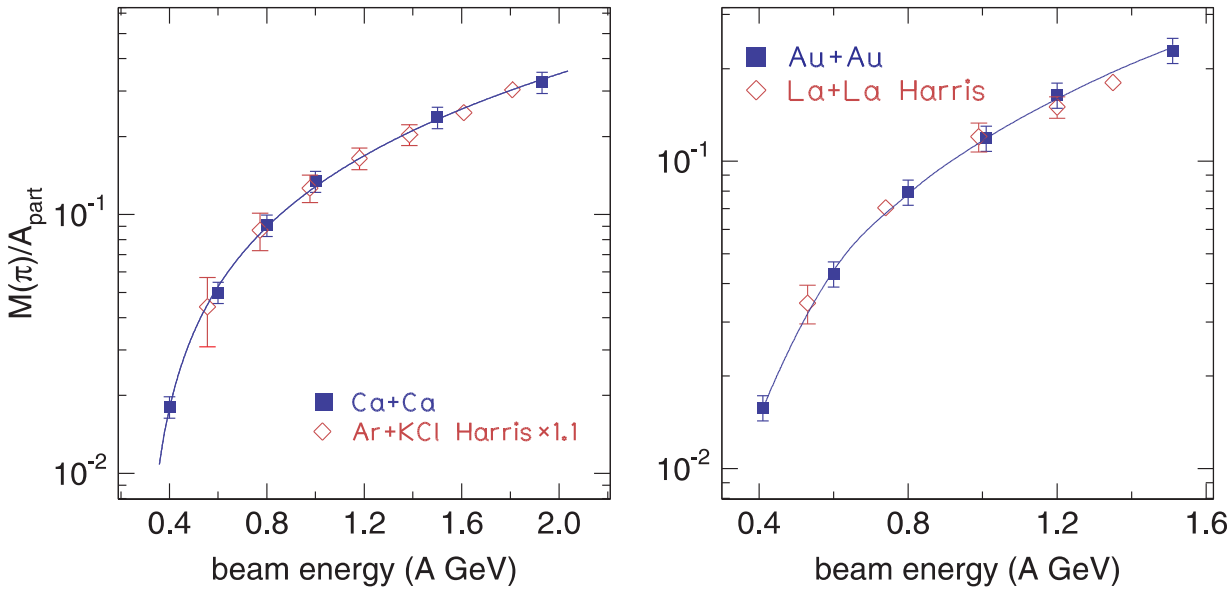

Excitation functions of the reduced pion multiplicity (per participant). The left panel compares the FOPI data for Ca + Ca with the data of Harris et al. [1] for Ar + KCl. The right panel compares the FOPI data for Au + Au with the La + La data [2].

Single-Pion Production in *pp* Collisions at 0.95 GeV/c (I) [B,D,J]

S. Abd El-Samad, R. Bilger, K.-Th. Brinkmann, H. Clement, M. Dietrich, E. Doroshkevich, S. Dshemuchadse, A. Erhardt, W. Eyrich, A. Filippi, H. Freiesleben, M. Fritsch, R. Geyer, A. Gillitzer, J. Hauffe, D. Hesselbarth, R. Jaekel, B. Jakob, L. Karsch, K. Kilian, H. Koch, J. Kress, E. Kuhlmann, S. Marcello, S. Marwinski, R. Meier, **K. Möller**, H.P. Morsch, **L. Naumann**, E. Roderburg, P. Schönmeier, M. Schulte-Wissermann, W. Schroeder, M. Steinke, F. Stinzing, G.Y. Sun, J. Wächter, G.J. Wagner, M. Wagner, U. Weidlich, A. Wilms, S. Wirth, G. Zhang, P. Zupranski
(COSY-TOF Collaboration)

Published in Eur. Phys. J. A 30 (2006) 443-453

The single-pion production reactions $pp \to d\pi^+$, $pp \to np\pi^+$ and $pp \to pp\pi^0$ were measured at a beam momentum of 0.95 GeV/c ($T_p \approx 400$ MeV) using the short version of the COSY-TOF spectrometer. The implementation of a central calorimeter provided particle identification, energy determination and neutron detection in addition to time-of-flight and angle measurements. Thus all pion production channels were recorded with 1-4 overconstraints. The total and differential cross sections obtained are compared to previous data and theoretical calculations. Main emphasis is put on the discussion of the $pp\pi^0$ channel, where we obtain angular distributions different from previous experimental results, however, partly in good agreement with recent phenomenological and theoretical predictions. In particular we observe very large anisotropies for the π^0 angular distributions in the kinematical region of small relative proton momenta revealing there a dominance of proton spinflip transitions associated with π^0 *s*- and *d*-partial waves and emphasizing the important role of π^0 d-waves.

[1] R. Bilger et al., Nucl. Phys. A 693 (2001) 633

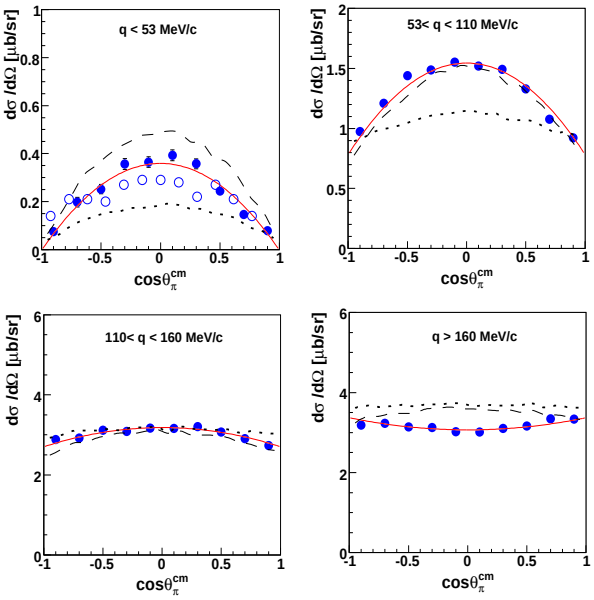

Fig. 1 *Pion angular distribution for four different q-ranges as indicated for $pp \to pp\pi^0$ reaction. Data from this work are shown by full circles, the fit to the data by solid lines. The open circles show data of Bilger et al. [1]. A strong anisotropy with a_2= -1.01 is indicated for $q < 53 MeV/c$.*

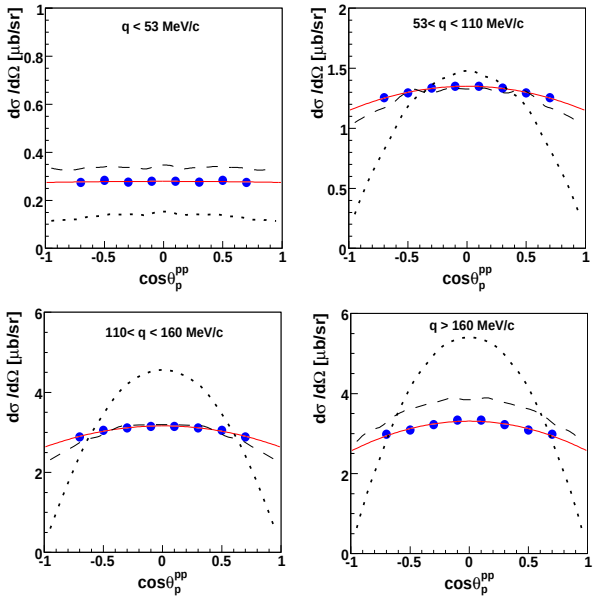

Fig. 2 *Proton angular distribution for four different q-ranges as indicated for $pp \to pp\pi^0$ reaction. Data from this work are shown by full circles, the fit to the data by solid lines.*

Study of Spectator Tagging in the Reaction $np \to pp\pi^-$ with a Deuteron Beam [B,J]

M. Abdel-Bary, K.-Th. Brinkmann, H. Clement, E. Doroshkevich, S. Dshemuchadse, A. Erhardt, W. Eyrich, H. Freiesleben, A. Gillitzer, R. Jaekel, L. Karsch, K. Kilian, E. Kuhlmann, **K. Möller**, H.P. Morsch, **L. Naumann**, N. Paul, C. Pizzolotto, J. Ritman, E. Roderburg, P. Schönmeier, W. Schroeder, M. Schulte-Wissermann, G.Y. Sun, A. Teufel, A. Ucar, G.J. Wagner, M. Wagner, P. Wintz, P. Wüstner and P. Zupranski
(COSY-TOF Collaboration)

Published in Eur. Phys. J. A 29 (2006) 353-361

The reaction $dp \to ppp\pi^-$ has been studied in a kinematically complete experiment at a single beam momentum p_d = 1.85 GeV/c (T = 759MeV). All four ejectiles have been detected in the large-acceptance time-of-flight spectrometer COSY-TOF. We analyzed the data along the lines of the spectator model as a means to isolate the quasi-free $np \to pp\pi^-$ reaction. The spectator proton was identified by its momentum and flight direction thus yielding access to the associated Fermi motion of the bound neutron. A comparison is carried out with Monte Carlo simulations based on two different parameterizations of the deuteron wave function. Up to a Fermi momentum of roughly 150MeV/c no significant deviations between experimental and simulated data of various observables were found from which we conclude that the deuteron can indeed be taken as a valid substitute for the neutron.

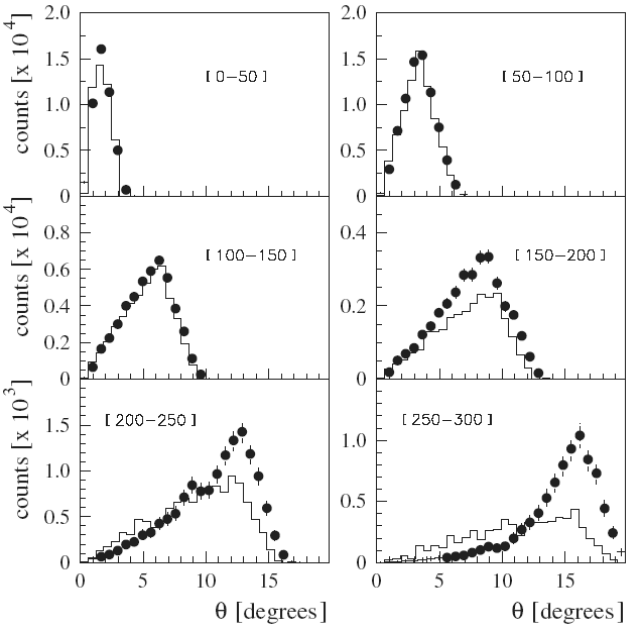

Fig. 1 *Experimentally deduced angular distributions of the spectator proton in the laboratory system (dots with error bars) for indicated bins in Fermi momentum (given in MeV/c) in comparison with Monte Carlo data (solid histograms).*

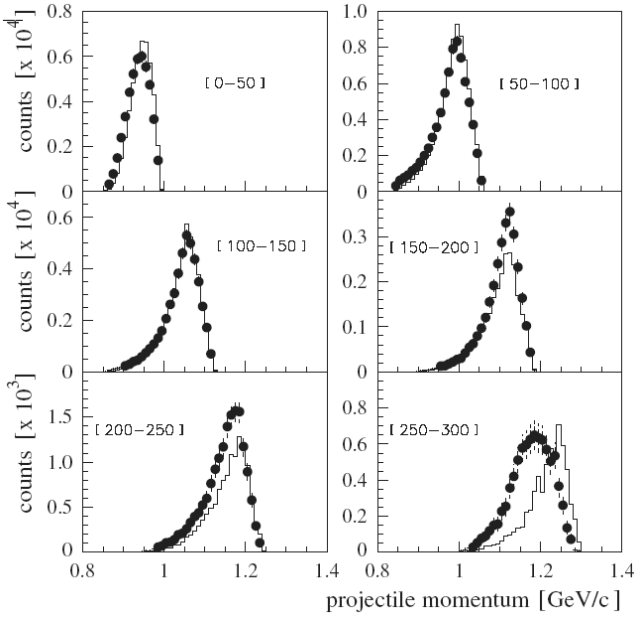

Fig. 2 *Experimentally deduced effective neutron projectile momenta (dots with error bars) for indicated bins in Fermi momentum (given in MeV/c) in comparison with Monte Carlo data (solid histograms).*

Upper Limits on Resonance Contributions to Proton-Proton Elastic Scattering in the c.m. Mass Range 2.05-2.85 GeV/c² [B]

H. Rohdjess, D. Albers, J. Bisplinghoff, R. Bollmann, K. Büsser, O. Diehl, **F. Dohrmann**, H.-P. Engelhardt, P. D. Eversheim, J. Greiff, A. Gross, R. Gross-Hardt, F. Hinterberger, M. Igelbrink, R. Langkau, R. Maier, F. Mosel, M. Müller, M. Münstermann, D. Prasuhn, P. von Rossen, H. Scheid, N. Schirm, F. Schwandt, W. Scobel, H. J. Trelle, A. Wellinghausen, W. Wiedmann, K. Woller, R. Ziegler (EDDA Collaboration)

Published in Eur. Phys. J. A 28 (2006) 115-124

Recently published excitation functions [1,2] in proton-proton (pp) elastic scattering observables in the laboratory energy range 0.5-2.5 GeV provide an excellent data base to establish firm upper limits on the elasticities $\eta_{\rm el} = \Gamma_{\rm el}/\Gamma_{\rm tot}$ of possible isovector resonant contributions to the nucleon-nucleon (NN) system. Such contributions have been predicted to arise from dibaryonic states, with c.m. masses between 2.1-2.9 GeV/c^2, but have not been confirmed experimentally. A method to determine quantitatively the maximum value of $\eta_{\rm el}$ compatible with experimental data is presented. We use energy-dependent phase shift fits to the pp data base to model the non-resonant interaction. Based upon the differential cross-section data measured by the EDDA Collaboration an unbiased statistical test is constructed to obtain upper limits on $\eta_{\rm el}$, that exclude larger values with a 99% confidence level. Results in the c.m. mass range 2.05-2.85 GeV/c^2 and total widths of 10-100 MeV/c^2 in the partial waves 1S0, 1D2, 3P0, 3P1, and 3F3 are presented and discussed.

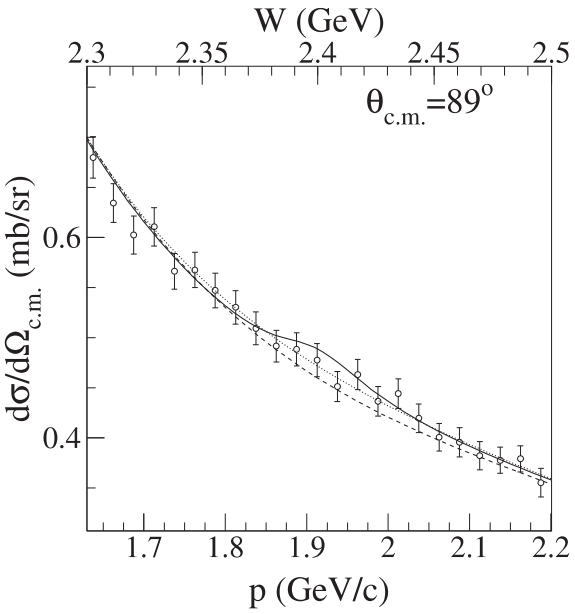

Fig. 1 *Example of an excitation function from [1,2] in comparison to a best-fit PSA without (dotted line) and with (solid line) a resonance in the $^1S_0$ partial wave at $W_R = 2.4$ GeV, with a total width of 50 MeV and a partial elastic width of 2.8 MeV. The non-resonant part of the latter is shown as the dashed line. The presence of this resonance is exclude with 99% CL, based on 28 excitation functions at different scattering angles.*

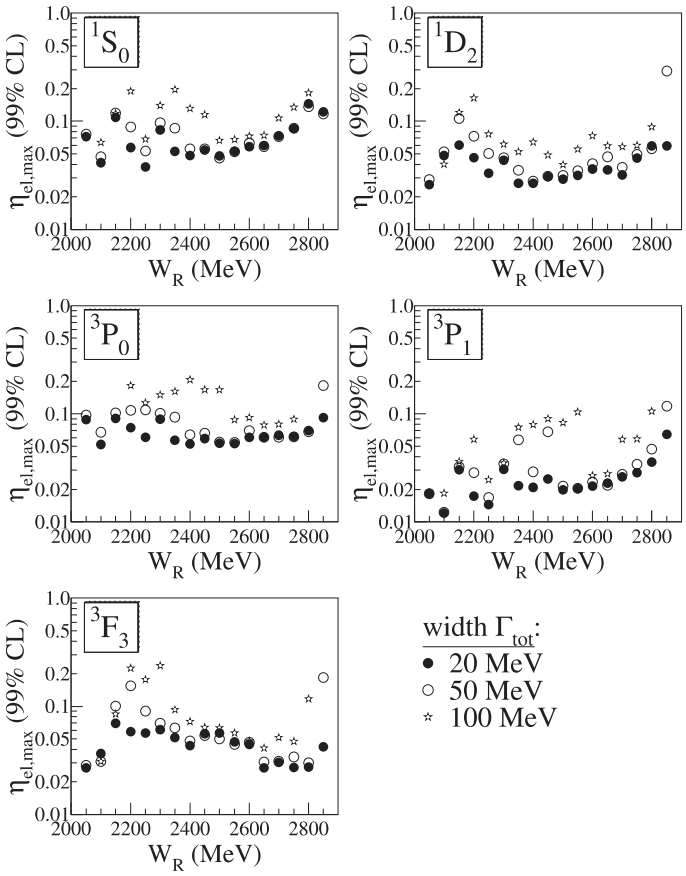

Fig. 2 *Upper limits (99% CL) on $\eta_{\rm el} = \Gamma_{\rm l} = \Gamma_{\rm tot}$ for the lowest uncoupled partial waves as a function the resonance energy W_R for three different total widths $\Gamma_{\rm tot}$ based on the cross-section data of [1,2].*

[1] D. Albers et al., Phys. Rev. Lett. 78 (1997) 1652
[2] D. Albers et al., Eur. Phys. J. A 22 (2004) 125

Four-Quark Condensates at Finite Density in Nucleon QCD Sum Rules [B,G]

R. Thomas, T. Hilger, B. Kämpfer

Part of PhD thesis R. Thomas

The complex hadronic spectrum is governed by the strong interaction which is described by Quantum Chromodynamics (QCD) resting on quarks and gluons as fundamental degrees of freedom. Understanding properties of hadrons is thus impeded by the unsettled confinement mechanism which forms for instance nucleons (protons and neutrons) as building blocks for normal nuclear matter on a microscopic level. A way to gain insight into properties of the ground state of QCD is by probing the impact of this medium at different baryon densities on hadrons, test particles, which are then expected to modify their known vacuum properties (e. g. their spectral density), as pursued by the HADES collaboration where the ρ meson is utilized as probe. The behavior of nucleon effective masses or potentials, respectively, at finite density is strongly related to the stable formation of saturated nuclear matter and can be quantified in scalar and vector nucleon self-energies. For these self-energies chiral effective field theory predicts comparable magnitudes but opposite signs (e. g. [1]).

QCD sum rules relate the nucleon self-energies at non-vanishing baryon densities to properties of the QCD ground state encoded in QCD condensates, which can similarly enter properties of a large set of other hadrons. A specific type, namely four-quark condensates, significantly determine the behavior of nucleon self-energies [2]. We extend such investigations to a more detailed treatment of four-quark condensates and therefore spell out the linear combinations of four-quark condensates

$$\sum c_{i,M} \langle \bar{q} \hat{M}_1 q \bar{q} \hat{M}_2 q \rangle = A \kappa_{\rm i}^{\rm vac} + B \kappa_{\rm i}^{\rm med} n \,,$$

entering the set of three ($i = 1,2,3$) coupled sum rule equations as done for the vacuum case in [3]. The matrices $\hat{M}$ denote the flavor, color and Dirac structures building the full catalog of in-medium four-quark condensates. In this given parametrization the value of $\kappa^{\rm med}$ measures the in-medium modification of the combined four-quark condensates and especially signals deviations from the factorization hypothesis where four-quark condensates are simplified to the square of the chiral condensate $\langle \bar{q} q \rangle$.

A rough analytical estimate reveals (for decoupled sum rules with condensates as in [2], Borel mass $\mathcal{M}^2 = 1$ GeV^2 and threshold $s_0 = 2.5$ GeV^2)

$$\Sigma_v \sim (0.16 + 1.22 \tilde{\kappa}_{\rm v}^{\rm med})\ {\rm GeV} \frac{n}{n_0} \,, \qquad (1)$$

$$\Sigma_s \sim -(0.32 + 0.11 \kappa_{\rm s}^{\rm med} - 0.31 \kappa_{\rm q}^{\rm med})\ {\rm GeV} \frac{n}{n_0} \,, \qquad (2)$$

which elucidates the impact of the density dependence of the three respective four-quark condensate combinations. This dependencies are qualitatively reproduced in full QCD sum rule evaluations: The vector self-energy is solely determined by $\tilde{\kappa}_{\rm v}^{\rm med}$ whereas the scalar self-energy depends on the directly opposed impacts of $\kappa_{\rm s}^{\rm med}$ and $\kappa_{\rm q}^{\rm med}$. This prohibits to find a unique configuration of density dependencies ($\kappa_{\rm s}^{\rm med}$, $\kappa_{\rm q}^{\rm med}$) tuned to the self-energies deduced from chiral effective field theory calculations [1] compared to in Fig. 1. Clearly, the figure shows that constant four-quark condensates would not be sufficient on a quantitative level and neither would be the density dependencies derived from nucleon expectation values of four-quark operators from a perturbative chiral quark model (PCQM) [4].

Consideration of the color structures entering the linear combinations of four-quark condensates in baryon sum rules moreover reveals relations between non-flavor-mixing condensates. Already this makes a translation of the nucleon four-quark condensates to those entering QCD sum rules of light vector mesons impossible. For the ω meson e. g. a strong density dependence compared to the factorization limit of the specific four-quark condensate combination was deduced from a comparison with CB-TAPS data [5]. This and the independent conclusions from the nucleon sum rules are examples questioning the reliability of the factorization ansatz and represent constraints on the exhaustive catalog of four-quark condensates.

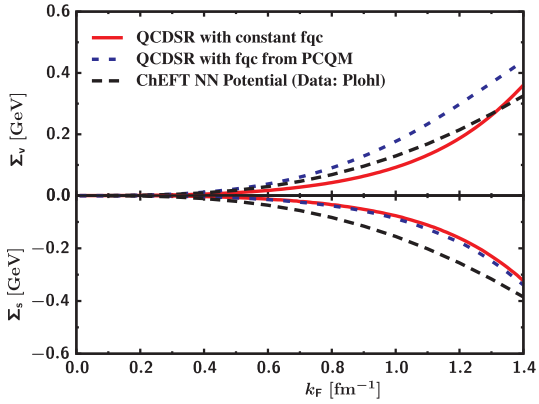

Fig. 1 *Scalar and vector self-energies $\Sigma_{\rm s}$ and $\Sigma_{\rm v}$ of the nucleon as function of the nucleon Fermi momentum $k_{\rm F}$ evaluated from QCD sum rules (SR) for four-quark condensates (fqc) kept constant as well as varied according to [4] compared to advanced nuclear matter calculations [1].*

[1] O. Plohl, C. Fuchs, Phys. Rev. C 74 (2006) 034325
[2] R.J. Furnstahl, D.K. Griegel, T. Cohen, Phys. Rev. C 46 (1992) 1507
[3] R. Thomas, K. Gallmeister et al., Acta. Phys. Hung. A 26 (2006) 35
[4] E.G. Drukarev, M.G. Ryskin et al., Phys. Rev. D 68 (2003) 054021
[5] R. Thomas, S. Zschocke, B. Kämpfer, Phys. Rev. Lett. 95 (2005) 232301

Foundation of the Quasi-Particle Model of Strongly Interacting Matter [B,D,E,G]

M. Bluhm, B. Kämpfer, R. Schulze, D. Seipt

Part of PhD thesis M. Bluhm

The Φ-functional approach [1] allows to derive a formulation of QCD thermodynamics in terms of quasi-particle excitations [2] from the fundamental Lagrangian. In Coulomb gauge, the thermodynamic potential Ω is expressed as a functional of dressed gluon (D) and quark (S) propagators by

$$\frac{\Omega[D,S]}{T} = \frac{1}{2}\mathrm{Tr}[\ln\frac{1}{D} - \Pi D] - \mathrm{Tr}[\ln\frac{1}{S} - \Sigma S] + \Phi[D,S]\,. \tag{1}$$

Here, D consists only of the physical transverse and longitudinal modes and $\Phi[D,S]$ is given by the sum of all 2-particle irreducible skeleton diagrams constructed from D and S. The self-energies are related to the dressed propagators by Dyson's equations. Demanding the stationarity of Ω under functional variation with respect to the dressed propagators, the self-energies follow self-consistently by the gap equations

$$\Pi = 2\frac{\delta\Phi[D,S]}{\delta D}\ ,\ \Sigma = -\frac{\delta\Phi[D,S]}{\delta S}\,. \tag{2}$$

The trace Tr in (1) involves a sum over Matsubara frequencies which can be evaluated by using standard contour integration techniques. With retarded propagators D and S depending on ω and $k = |\vec{k}|$ we find

$$\begin{aligned}\frac{\Omega[D,S]}{V} = &\ \mathrm{tr}\int\tfrac{d^3k}{(2\pi)^3}\int\tfrac{d\omega}{2\pi}n(\omega)\,\mathrm{Im}[\ln D^{-1} - \Pi\, D] \\ &+2\mathrm{tr}\int\tfrac{d^4k}{(2\pi)^4}f(\omega)\,\mathrm{Im}[\ln S^{-1} - \Sigma\, S] + \tfrac{T}{V}\Phi[D,S]\,,\end{aligned} \tag{3}$$

where $n(\omega)$ and $f(\omega)$ denote statistical distribution functions for gluons and quarks. Due to the stationarity property, entropy density $s = -\partial(\Omega/V)/\partial T$ contains only explicit temperature (T) derivatives of $n(\omega)$ and $f(\omega)$. We consider Φ at 2 - loop order given by

$\Phi =$ 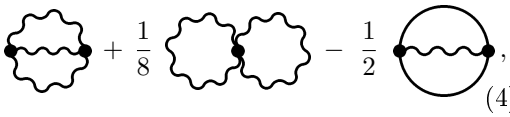 , (4)

and the self-energies read

$\Pi =$ 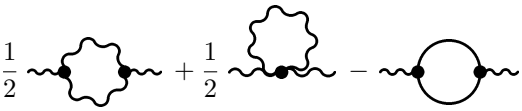 , (5)

$\Sigma =$  . (6)

Here, wiggly (solid) lines denote gluons (quarks).
Truncating Φ, gauge invariance is lost but can be restored by using gauge invariant hard thermal loop (HTL) expressions for Π and Σ [2]. These expressions show the correct behavior near the light cone for momenta $k \sim T, \mu$ as relevant for thermodynamics [3] (Fig. 1). Neglecting imaginary parts in the self-energies, performing the trace tr over color and Dirac indices and approximating the dispersion relations ω_g (ω_q) of gluons (quarks) according to [3], compact expressions for thermodynamic quantities can be derived. Fig. 2 exhibits an example for the entropy density.

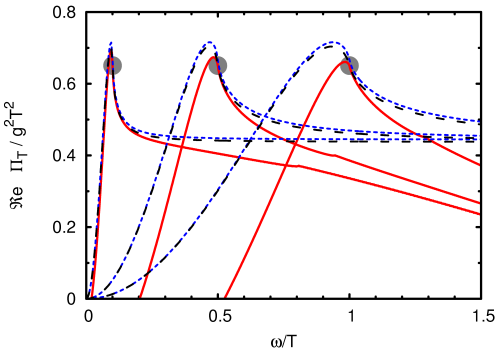

Fig. 1 *Comparison of HTL (dashed; short-dashed with quark mass effects) and 1-loop results (solid) for the transverse gluon self-energy at $k/T = 0.1$, 0.5 and 1 (left to right). Near the light cone (regions marked by circles), both results agree.*

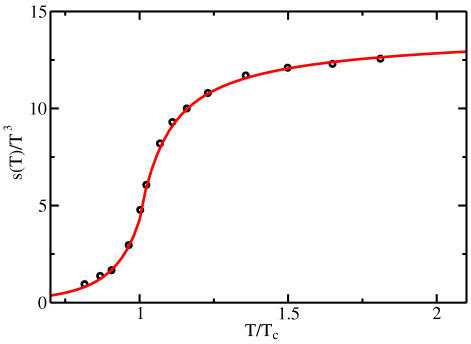

Fig. 2 *Comparison of entropy density s/T^3 as a function of the scaled temperature T/T_c for a two-flavor quark-gluon plasma (solid curve) with lattice QCD data [4] (symbols).*

[1] J.M. Luttinger, J.C. Ward, Phys. Rev. 118 (1960) 1417

[2] J.P. Blaizot, E. Iancu et al., Phys. Rev. D 63 (2001) 065003

[3] M. Bluhm, B. Kämpfer et al., Eur. Phys. J. C 49 (2007) 205

[4] F. Karsch, Nucl. Phys. A 698 (2002) 199

Family of QCD Equations of State within a Quasi-Particle Model [B,D,E,G]

M. Bluhm, B. Kämpfer, R. Schulze, D. Seipt, U. Heinz[1]

Part of PhD thesis M. Bluhm

With growing evidence, ideal hydrodynamics successfully describes the expansion stage of strongly interacting matter created in relativistic heavy-ion collisions. The essential input for solving the equations of motion is the equation of state (EoS) relating pressure p, energy density e and baryon density n_B. Ab initio calculations of QCD on a discretized space-time grid (dubbed lattice) deliver the EoS in form of a Taylor series expansion at small μ/T [1], e.g. the pressure

$$p = T^4 \left(c_0(T) + c_2(T) \left(\frac{\mu}{T}\right)^2 + c_4(T) \left(\frac{\mu}{T}\right)^4 + ... \right) \quad (1)$$

as a function of temperature T and chemical potential μ.

As a flexible parametrization for the EoS, we developed a quasi-particle model (QPM) using dynamically generated self-energies and a non-perturbative coupling as essential input which was shown [2] to successfully reproduce the lattice QCD results. The latter employ too large quark masses at small energy densities e [3]. Thus, we employ the resonance gas model at small energy densities and use our QPM EoS at larger densities. By generating a family of equations of state, cf. Fig. 1, keeping the matching point e_1 to the resonance gas EoS fixed and interpolating linearly to a given matching point e_2 (serving as label) of the QPM EoS, we can study the influence of details in the transition region on observables.

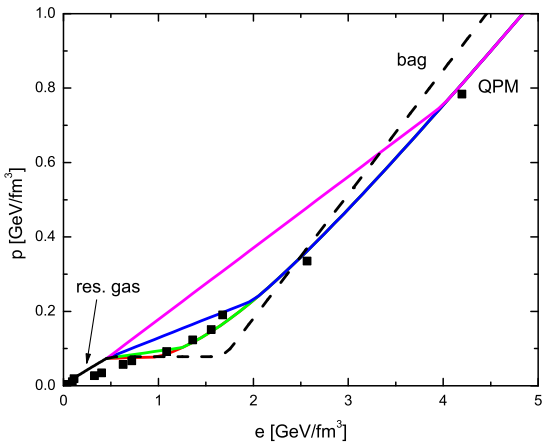

Fig. 1 *Family of equations of state $p(e)$ at small n_B relevant for top RHIC energies: Combination of QPM and resonance gas model as described in the text, $e_1 = 0.45$ GeV/fm^3. Dashed curve represents bag model EoS, squares lattice QCD data [3].*

For instance, in Fig. 2 we compare hydrodynamic calculations obtained with different equations of state with experimental data for the differential elliptic flow at midrapidity $v_2(p_T)$ of strange baryons as a function of transverse momentum p_T. We observe a small but non-negligible impact of EoS details in the transition region on the results.

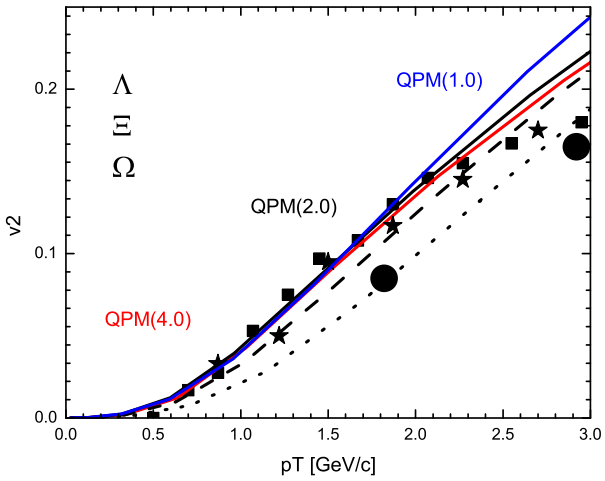

Fig. 2 *$v_2(p_T)$ for strange baryons: Λ (squares), Ξ (stars), Ω (circles); data from [4]. Corresponding results when using the EoS of Fig. 1 with $e_2 = 1$, 2 and 4 GeV/fm^3 (solid curves from top to bottom for Λ) and $e_2 = 2$ GeV/fm^3 (dashed and dotted curves for Ξ and Ω).*

[1] C. R. Allton, M. Doring et al., Phys. Rev. D 71 (2005) 054508

[2] B. Kämpfer, M. Bluhm et al., Nucl. Phys. A 774 (2006) 757

[3] F. Karsch, E. Laermann et al., Phys. Lett. B 478 (2000) 447

[4] J. Adams, M. M. Aggarwal et al. (STAR), Phys. Rev. Lett. 95 (2005) 122301

[1] *Ohio State Univ„ Department of Physics, Columbus, OH 43210, USA*

QCD Critical End-Point Effects in a Quasi-Particle Model [B,D,E,G]

M. Bluhm, B. Kämpfer

Part of PhD thesis M. Bluhm

The phase diagram of strongly interacting matter exhibits an astonishing richness. The first-order transition line separating hadronic and quark-gluon fluid phases at large baryo-chemical potentials μ_B terminates in a critical end point (CP) of second order. While its exact location and the extension of the critical region are matter of current investigations, CP belongs to the universality class of the 3D Ising model for QCD with massive quarks. For smaller μ_B the transition turns into a cross over. Across the phase transition line large variations in energy or various susceptibilities are expected as observable consequences. Within our quasi-particle model (QPM) for the QCD equation of state (EoS) we include phenomenologically CP features. In line with [1] we locate CP at $\mu_B^{CP} = 360$ MeV and estimate the transition line by

$$T_c(\mu_B) = T_c^0 \left(1 + \frac{1}{2} d \left(\frac{\mu_B}{3T_c^0}\right)^2\right) \qquad (1)$$

with $d = -0.122$ and $T_c^0 = 175$ MeV for two-flavor QCD. Accordingly, we find for the temperature T of CP, $T^{CP} = 170$ MeV. Following [2], CP features are included through non-analytic contributions in the bulk thermodynamic quantities with adjustable parameters characterizing the extension of the critical region. To be specific, we model the superposition of the smooth regular and the singular contributions to the entropy density as $s = s_{reg} + s_{sing}$ where the regular part is given by our QPM expression for the entropy density [3] and

$$s_{sing}(T,\mu_B) = \frac{2}{9} A\, c_2(T)\, \mu_B^2 T\, tanh\, S_c(T,\mu_B)\,. \qquad (2)$$

Here, A denotes the relative strength between regular and singular part, c_2 is the leading order Taylor expansion coefficient of the μ_B-dependence of the pressure p and the singular function S_c reads with Gibbs' free energy density G for the 3D Ising model

$$S_c(T,\mu_B) = -\sqrt{\Delta T_c^2 + \Delta\mu_{B,c}^2} \left(\frac{\partial G}{\partial T}\right)_{\mu_B}\,. \qquad (3)$$

Assuming the extension of the critical region to be small (defined by the parameters ΔT_c and $\Delta\mu_{B,c}$) implies that the EoS is given to a large extent by its regular contributions [3], in particular for small μ_B.
In contrast, baryon number susceptibility χ_B being a measure of fluctuations in the baryon density n_B is strongly influenced by CP. In Fig. 1, we show n_B as function of μ_B. For $\mu_B > \mu_B^{CP}$, n_B exhibits a discontinuity across the transition line which is significant for a first-order phase transition. The corresponding result for χ_B is depicted in Fig. 2.

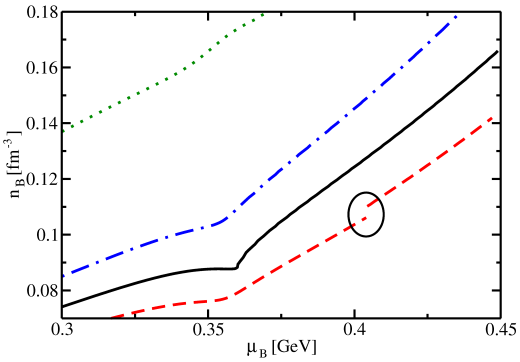

Fig. 1 *n_B as a function of μ_B for different temperatures $T = T^{CP} - 1.25$ MeV, T^{CP}, $T^{CP} + 1.25$ MeV and $T = 176$ MeV (dashed, solid, dash-dotted and dotted curves, respectively). At $T = T^{CP} = T_c(\mu_B^{CP})$, the slope becomes infinite at μ_B^{CP+}, and for $T < T^{CP}$, $n_B(\mu_B)$ exhibits the discontinuous behavior (encircled) of a first-order phase transition.*

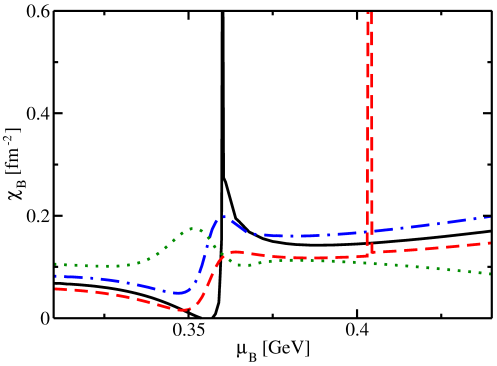

Fig. 2 *Baryon susceptibility $\chi_B = \frac{\partial n_B}{\partial \mu_B}$ as function of μ_B (same line code as Fig. 1). χ_B diverges at μ_B^{CP}, while the spike in the dashed curve at $\mu_B = 0.41$ GeV is an artifact of the numerical differentiation at the discontinuity in n_B.*

[1] Z. Fodor, S. D. Katz, JHEP 0404 (2004) 050
[2] C. Nonaka, M. Asakawa, Phys. Rev. C 71 (2005) 044904
[3] M. Bluhm, B. Kämpfer, PoS (CPOD2006) 004

Relativistic Approaches to Investigations of Few-Nucleon Systems [B,E]

S.M. Dorkin [1], L.P. Kaptari [1], **B. Kämpfer**, S.S. Semikh [1]

Published in Phys. Part. Nucl. 37 (2006) 867-898

Theoretical approaches used in investigations of relativistic effects in high energy lepton and hadron collisions with few nucleon systems are analyzed. The Bethe-Salpeter formalism for describing interacting systems of two spinor particles both in the continuum and bound state is described in detail. Special attention is paid to partial expansions taking into account the analytic properties of Bethe-Salpeter amplitudes and unitary transformations correlating different representations of partial amplitudes. Mathematical methods of numerical solution of equations are considered. Results of calculation of relativistic corrections and effects of interactions in the final state in particular reactions with the deuteron, namely, inelastic pD backward scattering and in reactions of deuteron break-up with production of correlated pairs, are presented.

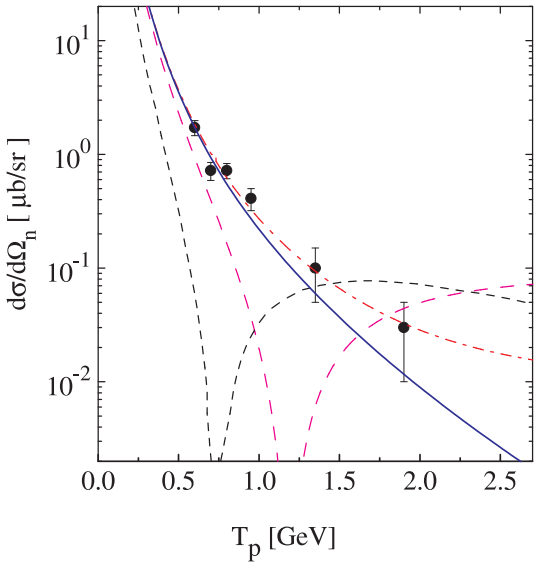

Fig. 1 *Cross section of the reaction* $p + D = (p_1 p_2)(0^0) + n_1(180^0)$ *integrated over the excitation energy* E_x *of the outgoing proton pair as a function of the initial energy* T_p. *Dashed line: non-relativistic calculation (only ++ components of* $^1S_0$ *state without Lorentz boosts), dotted line: Lorentz boost in the main component, dot-dashed line: relativistic calculation (including P waves) without cut-off form factors, solid line: relativistic calculations with form factors.*

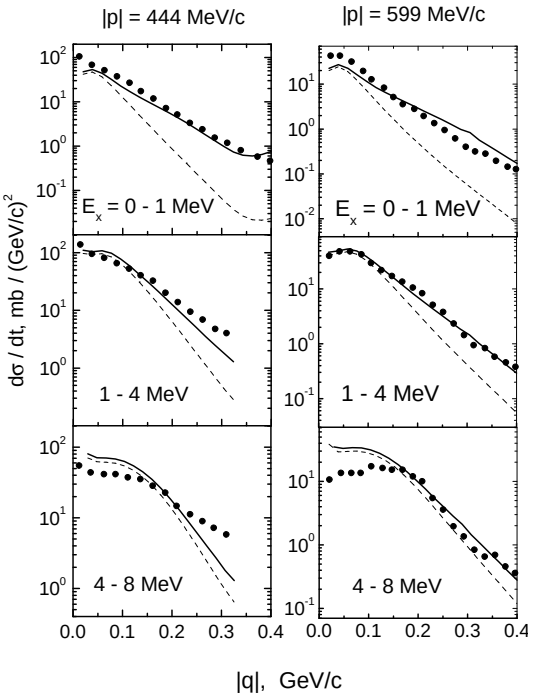

Fig. 2 *Differential cross section of the reaction* $p + \vec{D} = n + (p_1 + p_2)$ *at initial momentum* $|\mathbf{p}| = 0.444\,GeV/c$ *(left column) and* $|\mathbf{p}| = 0.599\,GeV/c$ *(right column). Dashed lines: results of impulse approximation, solid lines: with final state interaction.*

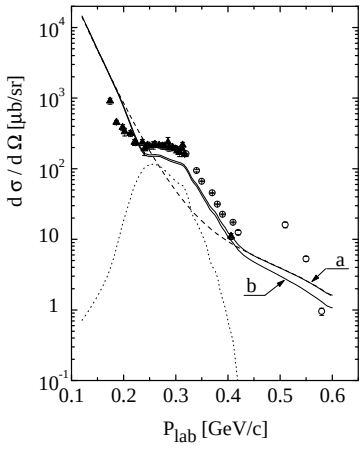

Fig. 3 *Differential cross section for the elastic backward* $pD \to Dp$ *reaction with triangle diagrams and meson exchange corrections. Dashed line: contribution solely from the one-nucleon exchange mechanism, dotted line: meson exchange corrections, solid lines: total contribution with (a) and without (b) P components in the Bethe-Salpeter amplitude.*

[1] *JINR Dubna, 141980, Russia*

Development of Straw Tubes for High Rate Capability Application [G,E]

K. Davkov, V. Davkov, J. Marzec, V. Myalkovskiy, **L. Naumann**, V. Peshekhonov, A. Savenkov, D. Seliverstov, V. Tikhomirov, K. Viryasov, P. Wintz, K. Zaremba, I. Zhukov

The construction of a large size straw tube particle tracking detector for the Compressed Baryonic Matter Experiment at FAIR is under consideration [1]. Drift chambers on the basis of thin-walled drift tubes (straws) have been widely used as tracking detectors in high rate environments [2,3,4]. In the inner part of the first CBM tracker station the expected hit density of charged particles for central Au+Au collisions at 25 AGeV amounts to 0.05 /cm^2. To guarantee a sufficient efficiency of the tracking system, the occupancy of a single drift tube element should be below five percent and the active detector cross-section yields 1 cm^2 for the expected hit density. To realise small area drift detectors long straw tubes with subdivided anodes of different length have been developed. The readout of a section should be independent of each other. Consequently it is possible to reduce the active cross-section of a straw tube to few cm^2. The low-mass inner straw elements and the technology of the multi-anode straw assembly have been devised and checked. A prototype of 19 straws with 57 readout channels has been manufactured. The straws are 500 mm long and 4 mm in diameter. The anodes are subdivided in two, three or four parts of different length. Fig. 1 shows a straw tube layout with four anode segments.

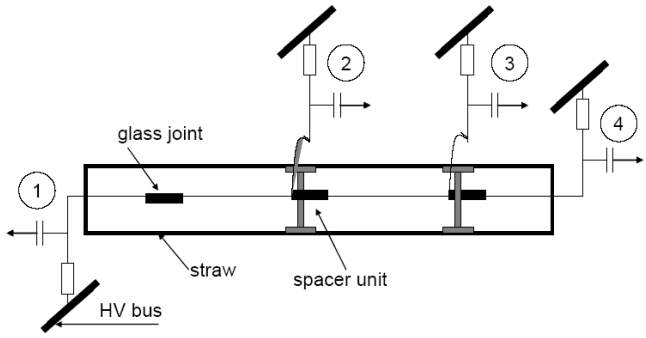

Fig. 1 *Schematical drawing of the straw tube design with four anodes.*

Different readouts have been tested. The front-end readout of the outer anodes has been provided close to the end-plugs. For the inner sectors cables of 15 cm length connect the anode wires with the front-end electronics. In the threefold segmented anode the single glas joint has been removed to investigate the double-sided readout. The current sensitive preamplifiers with an input impedance of 300 Ω are connected to the anodes by a capacitive coupling of 200 pF. Each anode has been supplied with high voltage through a resistor of 1 MΩ. A gas mixture of Ar/CO_2 (70/30) at atmospheric pressure has been supplied through the two end-plugs of each straw. Collimated Gammas (^{55}Fe) irradiated the straws along the anodes with a width of 1 mm perpendicular to the wires. Fig. 2 shows the anode signal amplitude distribution in a threefold subdivided wire. The collimator was moved along the straw. The information from the inner sector is read out over the contact wire fed through the spacer supporting the capillary tube and the hole in the straw wall. To compare the signals going through the straw wall and the end plug, the readout of the right anode has a double-sided layout.

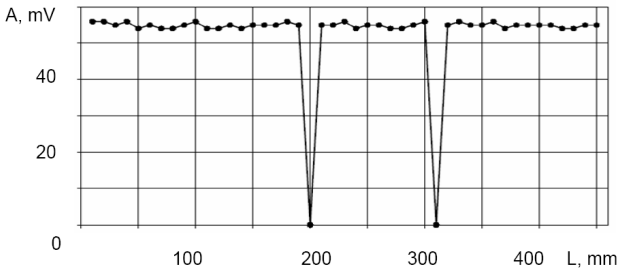

Fig. 2 *Amplitude distribution of the anode signals (A) along the threefold subdivided straw of 500 mm length (L).*

The result shows that detector inefficiencies are only evident in small regions of 7.2 mm length around the spacer units. The straws work stably, no discharges were observed between any construction elements placed inside the straws. The radiation length of the spacer amounts to 0.4 %. For minimum ionizing particles the rate capability amounts up to 4.5 MHz/cm^2 in single straws of 4 mm in diameter with a gain of 5×10^4 [5].

[1] CBM Experiment, Techn. Status Report, GSI Darmstadt (2005)
[2] Y. Arai et al., NIM A381 (1996) 355
[3] ATLAS Inner Tracker Design Report, CERN/LHCC/97-16
[4] V. Bytchkov et al., Particles and Nuclei, Letters N.2 (2002) 75
[5] I. Zhukov et al., JINR Preprint P13-2005-126

Radiation Damage of Polypropylene Fiber Targets in Storage Rings [B]

H. Rohdjess, D. Albers, J. Bisplinghoff, R. Bollmann, K. Büsser, O. Diehl, **F. Dohrmann**, H.-P. Engelhardt, P. D. Eversheim, J. Greiff, A. Gross, R. Gross-Hardt, F. Hinterberger, M. Igelbrink, R. Langkau, R. Maier, F. Mosel, M. Müller, M. Münstermann, D. Prasuhn, P. von Rossen, H. Scheid, N. Schirm, F. Schwandt, W. Scobel, H. J. Trelle, A. Wellinghausen, W. Wiedmann, K. Woller, R. Ziegler (EDDA Collaboration)

Published in Nucl. Instr. Meth. B 243 (2006) 127-133

Thin polypropylene fibers have been used for internal experiments in storage rings as an option for hydrogen targets. The change of the hydrogen content due to the radiation dose applied by the circulating proton beam has been investigated in the range $1{\cdot}10^6$ to $2{\cdot}10^8$ Gy at beam momenta of 1.5 to 3 GeV/c by comparing the elastic pp-scattering yield to that from inelastic p-carbon reactions. It is found that the loss of hydrogen as a function of applied dose receives contributions from a fast and a slow component.

[1] R. Bradley, Radiation Technology Handbook, Marcel Dekker Inc., New York, 1984.

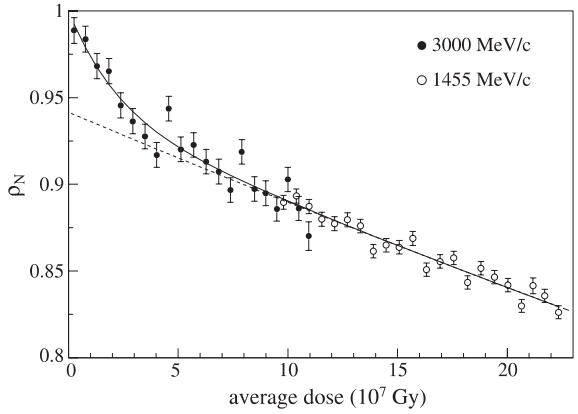

Fig. 1 *Normalized average hydrogen density as a function of the average dose. The result of the fit is shown as the solid line. The dashed line shows the contribution of the slow component only. Note, that the first data point at 1.455 GeV/c corresponds to a lower dose than the last point at 3.0 GeV/c, since the beam is slightly displaced, such that a region of lower accumulated dose is probed.*

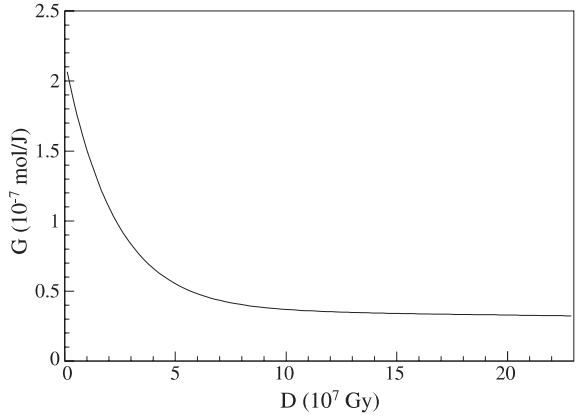

Fig. 2 *G-value for radiolytic loss of H2 as a function of the accumulated dose. The $G(H_2)$-value [1] describes the number of hydrogen molecules δn_X per $\delta E = 100$ eV energy deposited in the polymer. The modern definition of G is the amount of substance n_x (unit mol) per $\delta E = 1$ J, $G = \delta n_x/\delta E$. The old unit 1/(100 eV) corresponds to $1.04{\cdot}10^7$ mol/J. The observed dependence of $G(H_2)$ is very similar to the results shown in this figure.*

Determining Beam Parameters in a Storage Ring with a Cylindrical Hodoscope Using Elastic Proton–Proton Scattering [B]

H. Rohdjess, D. Albers, J. Bisplinghoff, R. Bollmann, K. Büsser, O. Diehl, **F. Dohrmann**, H.-P. Engelhardt, P. D. Eversheim, J. Greiff, A. Gross, R. Gross-Hardt, F. Hinterberger, M. Igelbrink, R. Langkau, R. Maier, F. Mosel, M. Müller, M. Münstermann, D. Prasuhn, P. von Rossen, H. Scheid, N. Schirm, F. Schwandt, W. Scobel, H. J. Trelle, A. Wellinghausen, W. Wiedmann, K. Woller, R. Ziegler (EDDA Collaboration)

Published in Nucl. Instr. Meth. A 556 (2006) 57-65

The EDDA-detector at the cooler-synchrotron COSY/Jülich has been operated with an internal CH_2 fiber target to measure proton"=proton elastic scattering differential cross-sections. For data analysis knowledge of beam parameters, like position, width and angle, are indispensable. We have developed a method to obtain these values with high precision from the azimuthal and polar angles of the ejectiles only, by exploiting the coplanarity of the two final-state protons with the beam and the kinematic correlation. The formalism is described and results for beam parameters obtained during beam acceleration are given.

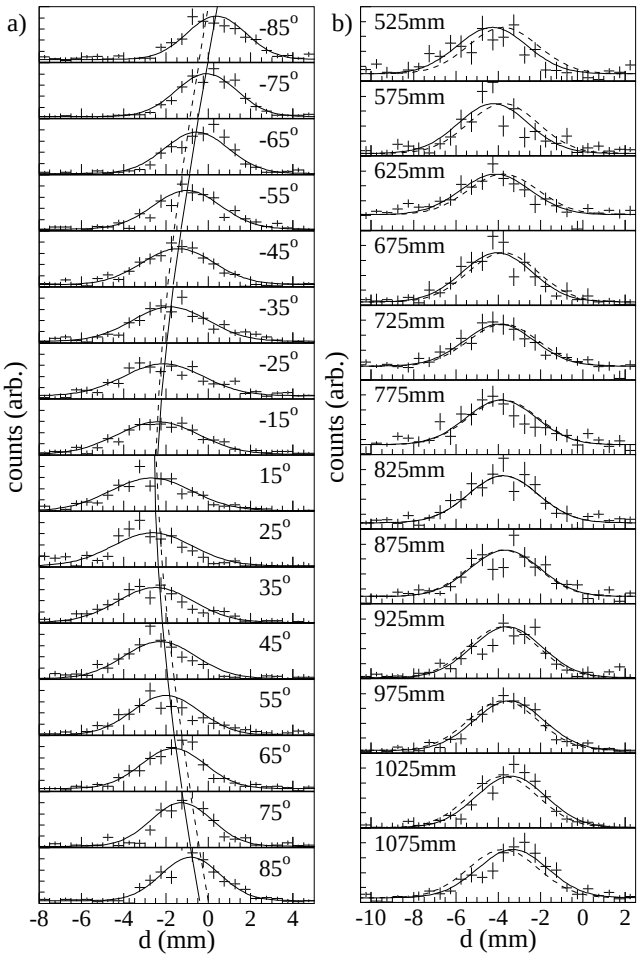

Fig. 1 *(a) Variation of the d-distribution for different bins in ϕ_d. The fit (solid Gaussian) to the data (crosses) yields a beam displacement of $x_b = -2.51$ mm, $y_b = -0.41$ mm. The mean value is shown as the solid vertical curve, for the dashed curve y_b was fixed to zero. (b) Variation of the d-distribution at $\phi_d = 15 \pm 5°$ with $z_1 + z_2$ and the result of the fit (solid line) yielding $x'_b \approx 5$ mrad. The dashed line shows the fit at 825 mm for comparison. The measured value of d for a displaced (x_b, y_b) and tilted (x'_b, y'_b) beam is given by:*

$$d = (x_b + \frac{z_1 + z_2}{2} x'_b) \cos\phi_d + (y_b + \frac{z_1 + z_2}{2} y'_b) \sin\phi_d$$

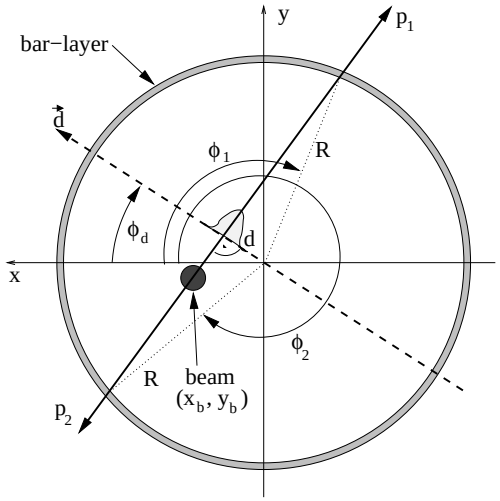

Fig. 2 *Geometry for a beam parallel to the detector symmetry axis. EDDA measures the points of interception of two prongs with a bar layer (R=164 mm).*

Studies of a Separator Dipole Magnet for Tagging Experiments for Photon-Induced Transmutation at ELBE [E]

F. Dohrmann, A. Sytcheva, E. Grosse [1]

The ELBE electron linac provides, in addition to primary electrons, high intensity and highly collimated secondary beams. Irradiating a probe with electrons or photons from bremsstrahlung may be desirable for applications in nuclear physics, cross sections for transmutation as well as studying structural defects and ageing due to high radioactive doses within material.

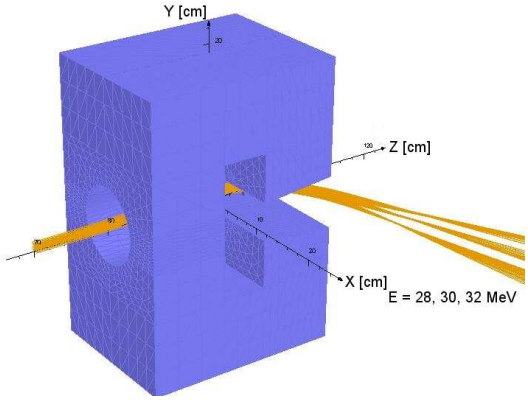

Fig. 1 *Simulation of a clam magnet with rectangular pole shoes. The average magnetic flux density was ∼ 0.8 T, average gap 5 cm (note the clam design). Electron beams of 28–32 MeV are shown.*

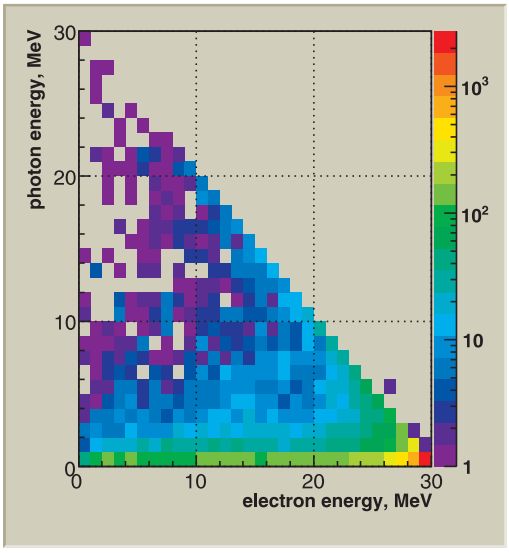

Fig. 2 *Simulation of bremsstrahlung produced on a 0.2 mm Be foil by 30 MeV electrons after a dipole magnet similar as in Fig. 1. The correlation between the electron and bremsstrahlung photon energies is shown.*

In order to separate bremsstrahlung photons from electrons, a conceptual design of a dedicated separator magnet was started and continued. This dipole magnet should be part of a spectrometer setup with which photons may be energetically marked by measuring the residual energy of the electrons, which have undergone bremsstrahlung.

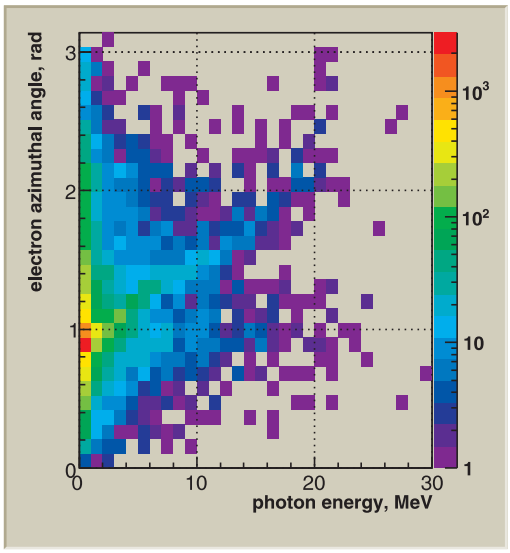

Fig. 3 *Same setup as in Fig. 2. Shown is the correlation between azimuthal angle in radians and energy of bremsstrahlung photons.*

Using the Opera-3D/TOSCA [1] program package several configurations were simulated. A possible use of non-flat pole shoes (clam design) may provide additional focussing. Since space is limited, the yoke of the magnet may be designed with a hole through which the electron beam is directed. Such a configuration is displayed in Fig. 1. The solution (field map) of the simulation result is then extracted and used for further simulations. Using the program package Geant4 a realistic setup of experimental conditions at the ELBE beam may be studied, including beam divergences, material properties etc. In a first step, a dipole magnet has been simulated and correlations of electron and photon energy as well as electron angle and photon energy are displayed in Figs. 2 and 3. The bremsstrahlung takes place in a Be foil of thickness 0.2 mm.

[1] Opera-3D user guide, Vector Fields Ltd., Oxford, England
http://www.vectorfields.co.uk
[2] S. Agostinelli et al. (Geant4 collaboration), Nucl. Instr. Meth. A 506 (2003) 250
http://geant4.web.cern.ch/geant4/

[1] *also TU Dresden*

Testing the Performance of Timing MRPC Detectors at ELBE [E]

R. Kotte, F. Dohrmann, J. Hutsch, L. Naumann, D. Stach

Published in Nucl. Instr. Meth. A 564 (2006) 155-163

The timing performance of multigap resistive plate chambers (MRPCs) [1-7] has been tested at the Rossendorf electron linac ELBE. Electrons with energies of 20 - 40 MeV have been used to mimic minimum ionizing hadrons to be detected in large-scale time-of-flight (TOF) detectors for future heavy-ion collision experiments. Referencing the TOF measurement to the accelerator radio frequency, no fast start detector was necessary. A typical time resolution (including contributions from front-end electronics) of about 70 ps has been achieved for individual strips of the multistrip-anode MRPCs. Rate dependencies and detection efficiencies have been investigated.

[1] P. Fonte et al., Nucl. Instr. Meth. A 443 (2000) 201
[2] P. Fonte et al., Nucl. Instr. Meth. A 449 (2000) 295
[3] A. Blanco et al., Nucl. Instr. Meth. A 485 (2002) 328
[4] M. Petrovici et al., Nucl. Instr. Meth. A 487 (2002) 337
[5] M. Petrovici et al., Nucl. Instr. Meth. A 508 (2003) 75
[6] A. Schüttauf, Nucl. Instr. Meth. A 533 (2004) 65
[7] A. Schüttauf, Nucl. Phys. B (Proc. S.) 158 (2006) 52

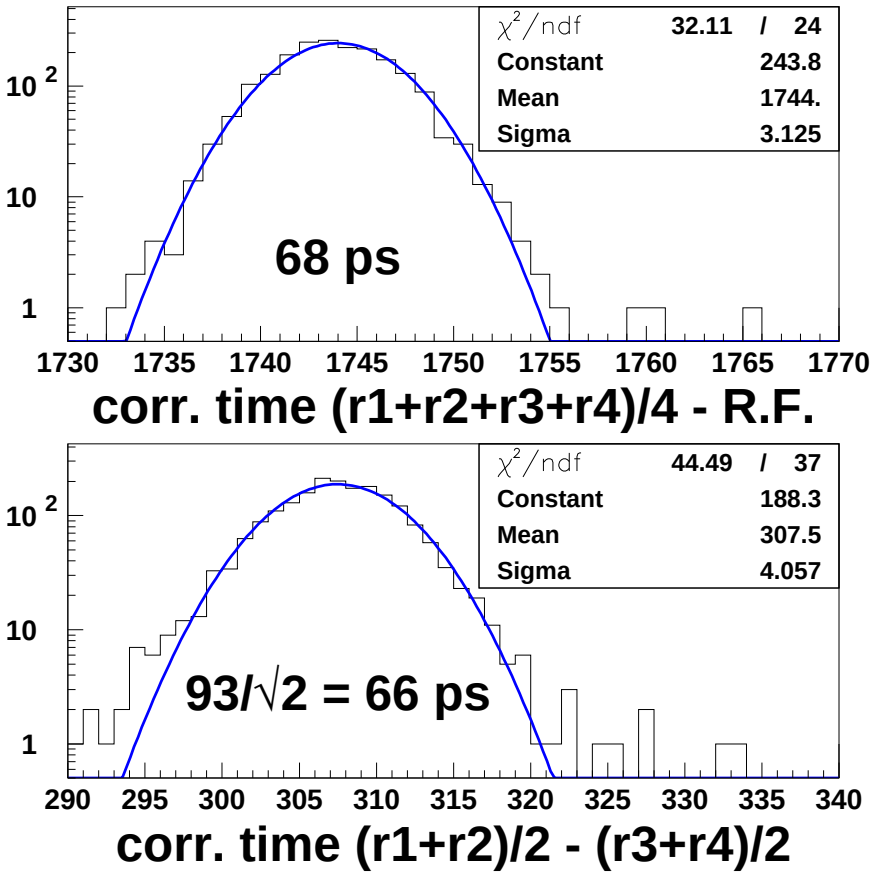

Upper panel: The mean timing w.r.t. the accelerator RF of four (time slewing corrected) signals from two strips of two identical MRPCs built in the detector laboratory of the Institute of Radiation Physics. For the given resolution a 34 ps contribution of the TDC resolution is quadratically subtracted. Lower panel: The time resolution of the difference between the mean timing of two strips from different MRPCs (full lines: Gaussian fits, TDC time slope 24.5 ps/ch).

Dipole Response of ^{88}Sr up to the Neutron-Separation Energy [D]

R. Schwengner, G. Rusev, N. Benouaret, R. Beyer, M. Erhard, E. Grosse, A.R. Junghans, J. Klug, K. Kosev, L.K. Kostov, C. Nair, N. Nankov, K.D. Schilling, A. Wagner

Submitted to Phys. Rev. C

The detailed understanding of the response of atomic nuclei to photons has received increasing attention in recent years. Information on the low-energy tail of the Giant Dipole Resonance is important for an estimate of the effect of high temperatures during the formation of heavy elements in the cosmos. In particular, reaction rates in the so-called p-process are influenced by the behaviour of dipole-strength distributions close to the neutron-separation energy S_n [1]. This behaviour may be affected by excitations like the Pygmy Dipole Resonance (see, e.g., Refs. [2, 3]).

The bremsstrahlung facility [3] at the superconducting electron accelerator ELBE of the research center Dresden-Rossendorf opens up the possibility to study the dipole response of the stable nuclei with even the highest neutron-separation energies in photon-scattering experiments. In the course of a systematic study of dipole-strength distributions for varying neutron and proton numbers in nuclei around $A = 90$ we started with the magic $N = 50$ nuclide ^{88}Sr. Bremsstrahlung was produced with electron beams of 9.0 and 13.2 MeV kinetic energy and with average currents of 520 μA and 400 μA hitting radiators consisting of niobium foils of 4 μm and 7 μm thickness, respectively. Gamma rays were measured with two HPGe detectors placed at 90° and two at 127° relative to the photon beam. Ground-state transitions have been identified by comparing the transitions observed at different electron energies. 160 levels were identified with a total dipole strength of 201 meV/MeV^3. Spin $J = 1$ could be deduced from the angular correlations of the ground-state transitions for about 90 levels including 84% of the total dipole strength. A measurement of linear polarizations of the γ rays by using polarized bremsstrahlung reveals that almost all transitions with energies greater than 6 MeV are $E1$ transitions. These $E1$ transitions comprise about 63% of the total dipole strength of all ground-state transitions.

The intensity distribution obtained from the measured spectra after a correction for detector response and a subtraction of atomic background in the target contains a continuum part in addition to the resolved peaks. It turns out that the dipole strength in the resolved peaks amounts to about 77% of the dipole strength in the continuum. In order to estimate the intensities of inelastic transitions to low-lying levels we have applied statistical methods [3]. By means of simulations of γ-ray cascades intensities of branching transitions could be removed from this intensity distribution and the intensities of ground-state transitions could be corrected for their branching ratios.
A comparison of the photoabsorption cross section obtained in this way from the present (γ, γ') experiments with (γ, n) data shows a smooth connection of the data of the two different types of experiments and gives new information about the extension of the dipole-strength distribution towards energies around and below the threshold of the (γ, n) reaction. In comparison with a simple approximation of the Giant Dipole Resonance by a Lorentz curve one observes extra dipole strength in the energy range from 6 to 11 MeV which may be considered of a Pygmy Dipole Resonance.

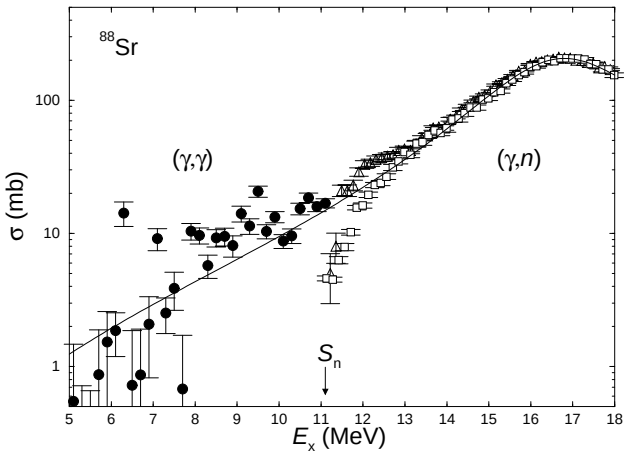

Fig. 1 *Photoabsorption cross section deduced from the present (γ, γ') data for ^{88}Sr after correction for branching transitions (filled circles) in comparison with (γ, n) data taken from Ref. [6] (open triangles) and Ref. [7] (open squares). The solid line is a Lorentz curve with the parameters $E_0 = 16.8$ MeV, $\Gamma = 4.0$ MeV and $\sigma_0 = 206$ mb which are consistent with the Thomas-Reiche-Kuhn sum rule [8] resulting in $\sigma_0 = 2/(\pi\Gamma) \cdot 60NZ/A$ mb.*

[1] M. Arnould and S. Goriely, Phys. Rep. 384 (2003) 1
[2] S. Goriely, Phys. Lett. B 436 (1998) 10
[3] A. Zilges, M. Babilon et al., Progr. Part. Nucl. Phys. 55 (2005) 408
[4] R. Schwengner, R. Beyer et al., Nucl. Instr. Meth. A 555 (2005) 211
[5] G. Rusev, Thesis, TU Dresden 2007, unpublished
[6] A. Lepretre, H. Beil et al., Nucl. Phys. A 175 (1971) 609
[7] A. M. Goryachev and G. N. Zalesnyy, Vopr. Teor. Yad. Fiz. 8 (1982) 121
[8] P. Ring and P. Schuck, in *The Nuclear Many Body Problem*, (Springer, New York, 1980)

Dipole-Strength Distributions in the Stable Even-Mass Mo Isotopes [D]

G. Rusev, R. Schwengner, M. Erhard, E. Grosse[1], A. R. Junghans, K. Kosev, K. D. Schilling, A. Wagner

Part of PhD thesis G. Rusev

Dipole-strength distributions in the stable even-mass Mo isotopes up to the neutron-separation energies have been studied in photon-scattering experiments at the superconducting electron accelerator ELBE. The measurements were performed at identical experimental conditions for an electron-beam energy of 13.2 MeV. Since only about 30 % of the strength is located in the identified peaks a novel method for analysis of the measured spectra was developed [1] in order to determine the total dipole strength below the neutron-separation energy. The measured spectra of scattered photons were corrected for detector response and atomic background obtained from simulations using the code GEANT3 [2]. Simulations of γ-ray cascades [1] were performed in order to correct the transition intensities for feeding from higher-lying levels and to deduce the branching ratios for transitions to the ground state. The cross sections resulting from this correction method for stable even-mass Mo isotopes are directly compared to nuclear photo effect data from literature [3] in Fig. 1 resulting in a photoabsorption cross section covering the full range from 4 to above 15 MeV, which is of interest for nuclear astrophysics network calculations. The dipole strength from the photon-scattering experiments on the even-mass Mo isotopes is compared with results for the dipole strength in the neighbouring odd-mass Mo isotopes obtained from (n,γ) experiments [4] (cf. Fig. 1). Novel information about the low-energy tail of the Giant Dipole Resonance (GDR) and the energy spreading of its strength can be derived. We represent the photoabsorption cross section σ_γ of the GDR as a superposition of three Lorentzian functions:

$$\sigma_\gamma = \frac{2S_{\mathrm{TRK}}}{3\pi} \sum_{i=1}^{3} \frac{E_x^2 \Gamma_0}{(E_x^2 - E_i^2)^2 + E_x^2 \Gamma_0^2}, \qquad (1)$$

where the cross section integral is given by the Thomas-Reiche-Kuhn sum rule: $S_{\mathrm{TRK}} = \int \sigma_\gamma dE = 60ZN/A$ mb MeV. The width Γ_0 is selected to be 4 MeV from the parametrisation of the GDR in the spherical nuclei ^{92}Mo and ^{88}Sr [5]. The maxima E_i of the three Lorentzian curves are calculated according to the Nilsson model [6]:

$$E_i = E_0 \left(1 - \frac{2}{3} \varepsilon \cos\left(\gamma - \frac{2\pi i}{3} \right) \right), \qquad (2)$$

where the deformation parameters ε and γ are taken from our previous investigation on the $M1$ strength in the stable even-mass Mo isotopes [7] and E_0 is a parameter describing the energy of the maximum of the GDR.

[1] *also TU Dresden*

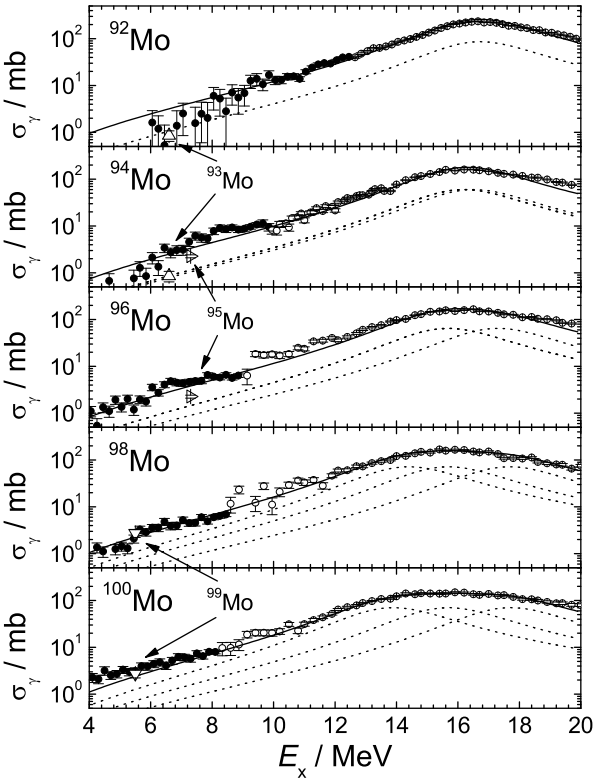

Fig. 1 *Photoabsorption cross sections in the stable even-mass Mo isotopes. The results from our photon-scattering experiments (filled circles) are combined with (γ,n) cross sections [3] (open circles) and compared with the dipole strength in the neighbouring odd-mass Mo isotopes (open triangles) obtained from (n,γ) experiments [4]. A parametrisation of the GDR (solid lines) resulting from a superposition of three Lorentzian curves (dashed lines) is compared with the experimental data.*

The presented results for the photoabsorption cross section and parametrisation of the low-energy tail of the GDR allow an extension of the knowledge for the shape of the GDR to exotic nuclei, which is of importance for a more precise modelling of astrophysical processes.

[1] R. Schwengner, N. Benouaret, at al., Nucl. Phys. A (2007), in print

[2] CERN Program Library Long Writeup W5013, Geneva 1993, unpublished

[3] H. Beil, R. Bergère et al., Nucl. Phys. A 277 (1974) 427

[4] J. Kopecky and M. Uhl, IAEA, Bologna, 1994

[5] R. Schwengner, G. Rusev, et al., Phys. Rev. C, submitted

[6] S. G. Nilsson and I. Ragnarsson, "Shapes and Shells in Nuclear Structure", Cambridge University Press, 1995

[7] G. Rusev, R. Schwengner et al., Phys. Rev. C 73 (2006) 044308

Origin of the Magnetic Dipole Strength in the Stable Even-Mass Mo Isotopes [D]

G. Rusev, R. Schwengner, F. Dönau, M. Erhard, S. Frauendorf, E. Grosse, A.R. Junghans, L. Käubler, K. Kosev, L.K. Kostov, S. Mallion, **K.D. Schilling, A. Wagner**, H. von Garrel, U. Kneissl, C. Kohstall, M. Kreutz, H.H. Pitz, M. Scheck, F. Stedile, P. von Brentano, J. Jolie, A. Linnemann, N. Pietralla, V. Werner

Published in Phys. Rev. C 73 (2006) 044308, 1-12

The nuclides ^{92}Mo, ^{98}Mo and ^{100}Mo were investigated in photon-scattering experiments with bremsstrahlung. Various electron-beam energies were used in order to resolve branching transitions in ^{98}Mo and ^{100}Mo. Five $J = 1$ states up to $E_x = 4$ MeV in ^{98}Mo and 14 in ^{100}Mo were observed for the first time. The transition strengths deduced from the present experiments for ^{92}Mo, ^{98}Mo, and ^{100}Mo together with known values for ^{94}Mo [1, 2] and ^{96}Mo [3] allowed us to study the systematics of the low-lying magnetic dipole excitations in the chain of stable even-even Mo isotopes. The results of the present study have been published in Ref. [4].

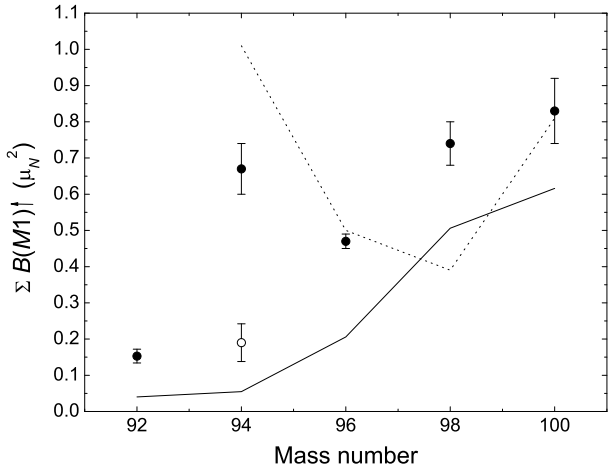

Fig. 1 *Comparison of the experimental summed $M1$ strengths up to 4 MeV (filled circles) with predictions of the QRPA calculations (solid line) and the shell-model calculations (dotted line). The open circle represents the $M1$ strength in ^{94}Mo without the contribution of the four-particle state.*

The experimental results are compared with predictions of QRPA calculations in a deformed basis, and with predictions of the shell model in Fig. 1. The QRPA calculations reproduce the growing and the spread of the $M1$ strength with increasing neutron number. As a result of the QRPA calculations we found the $M1$ strengths in the nearly spherical nuclei to be generated by isovector-spin vibrations only while the $M1$ strengths in the deformed nuclei are a combination of isovector-orbital vibrations and isovector-spin vibrations. The shell-model calculations especially reproduce the large $M1$ strength in ^{94}Mo as caused by a special four-particle configuration that is outside the scope of the QRPA.

In addition to the energy range covered by the present experiments we have performed QRPA calculations up to an excitation energy of 10 MeV. The predicted $M1$-strength distributions are shown in Fig. 2. The contributions of isovector-orbital vibrations to the total $M1$ strengths in the spherical ^{92}Mo and the deformed ^{100}Mo are depicted in Fig. 2.

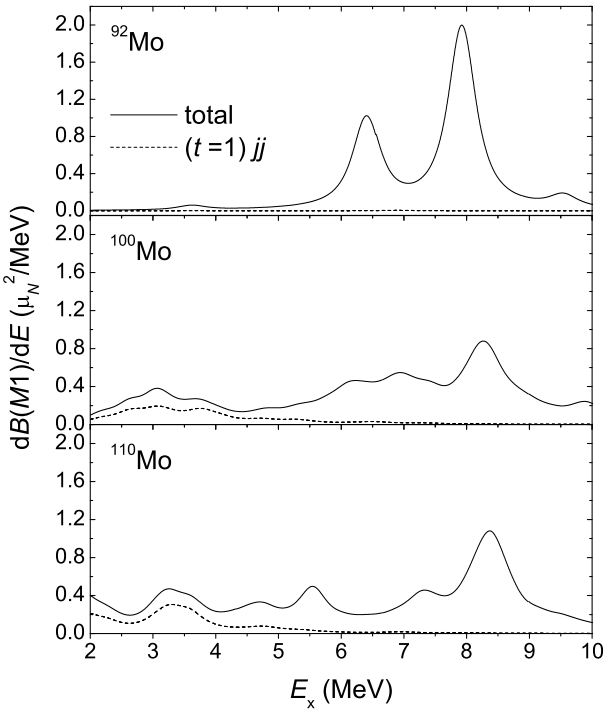

Fig. 2 *Contributions of different types of vibrations to the $M1$-strength distributions in ^{92}Mo (top), ^{100}Mo (middle), and ^{110}Mo (bottom) as predicted from QRPA. The solid lines represent the total strengths while the dashed lines show the isovector-orbital contributions.*

[1] N. Pietralla, C. Fransen et al., Phys. Rev. Lett. 83 (1999) 1303

[2] C. Fransen, N. Pietralla et al., Phys. Rev. C 67 (2003) 024307

[3] C. Fransen, N. Pietralla et al., Phys. Rev. C 70 (2004) 044317

[4] G. Rusev, R. Schwengner et al., Phys. Rev. C 73 (2006) 044308

Effect of Nuclear Deformation on the Electric Dipole Strength in the Particle-Emission-Threshold Region [D]

F. Dönau, G. Rusev, R. Schwengner, A.R. Junghans, K.D. Schilling, A. Wagner

Submitted to Phys. Rev. C

The role of nuclear deformation for the photoabsorption cross section in the tail region of the electric Giant Dipole Resonance (GDR) is studied in terms of a deformed oscillator model and a Nilsson-plus-random-phase-approximation model. It is found within the framework of these approaches that extra electric dipole strength is generated at energies below the GDR maximum if the nuclear system is spatially deformed. This is important for the prediction of the stellar photodisintegration rates knowing that an extra strength can affect these rates even below the particle separation energies through the so-called γ process. Because the nuclear deformation is governed by shell effects this extra strength does not directly correlate with neutron excess.

The effect of the deformation on the photoabsorption cross section is shown in Fig. 1 for the isotopic chain of stable even-even mass samarium isotopes starting at the spherical ^{144}Sm ($N = 82$) and ending at the deformed ^{154}Sm. Fig. 2 compares calculations with and without deformation for the isotopic chain of stable even-even molybdenum isotopes. This comparison clearly demonstrates that the increase of $E1$ strength in the energy range from 8 to 14 MeV while going from the shell closure at ^{92}Mo ($N = 50$) to the heavier isotopes is caused by increasing deformation. This predicted increase of $E1$ strength is consistent with experimental results of recent systematic photon-scattering experiments performed for the Mo isotopes at the ELBE accelerator [3].

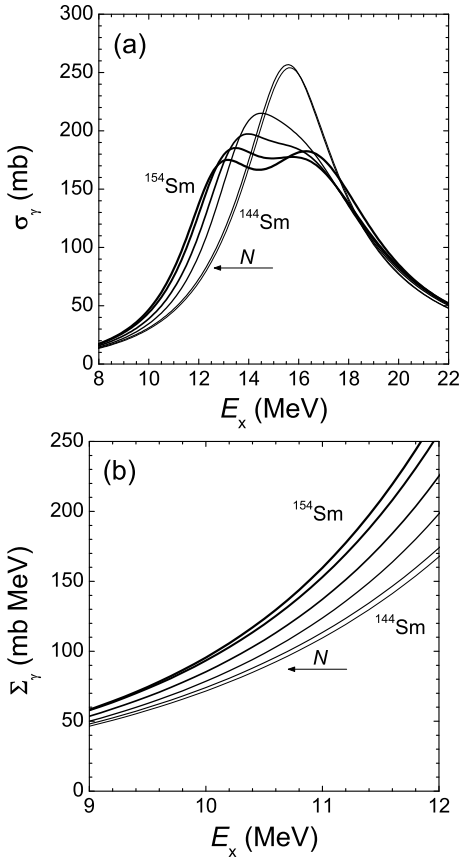

(a) The photoabsorption cross sections of $^{144-154}$Sm calculated in the oscillator approximation adopting the deformation parameters from Ref. [1] and using a Lorentzian-like level broadening (see text). (b) The integrated cross sections of even-even Sm isotopes $\Sigma_\gamma(E_x) = \int_0^{E_x} \sigma_\gamma(E')dE'$ in the interval $E_x = 9 - 12$ MeV.

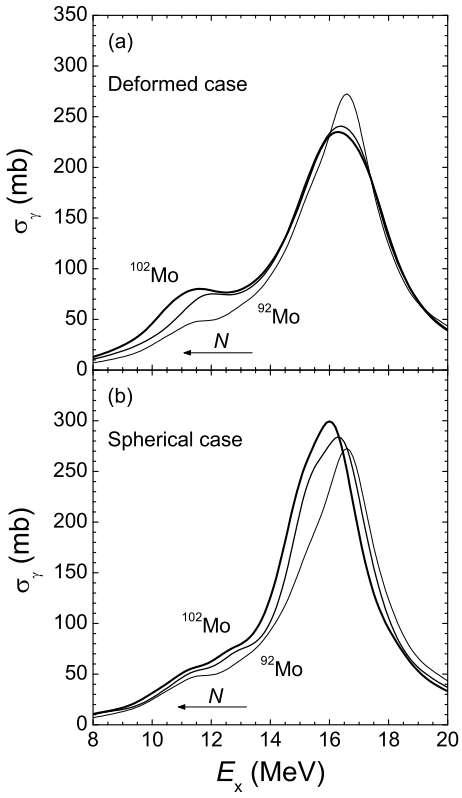

Calculated photoabsorption cross sections σ_γ for ^{92,98,102}Mo (a) including deformation parameters as used in Ref. [2] and (b) assuming spherical shapes.

[1] P. Möller, J. R. Nix, W. D. Myers, and W. J. Swiatecki, At. Data Nucl. Data Tables 59 (1995) 185

[2] G. Rusev, R. Schwengner et al., Phys. Rev. C 73 (2006) 044308

[3] G. Rusev, R. Schwengner et al., contribution to this report, p. 40

Low-Lying $E1$, $M1$, and $E2$ Strengths in ^{124,126,128,129,130,131,132,134,136}Xe: Systematic Photon Scattering Experiments in the Mass Region of a Nuclear Shape or Phase Transition[D]

H. v. Garrel, P. v. Brentano, C. Fransen, G. Friessner, N. Hollmann, J. Jolie, F. Käppeler, **L. Käubler**, U. Kneissl, C. Kohstall, L. Kostov, A. Linnemann, D. Mücher, N. Pietralla, H.H. Pitz, **G. Rusev**, M. Scheck, **K.D. Schilling**, C. Scholl, **R. Schwengner**, F. Stedile, S. Walter, V. Werner, K. Wisshak

Published in Phys. Rev. C 73 (2006) 054315, 1-20

Nuclear shape or phase transitions are a current topic in nuclear structure physics. The properties of spherical, axially deformed, and γ-soft even-even nuclei can well be described in the framework of algebraic models in the dynamical symmetry limits of U(5), SU(3), and O(6), as is well known [1]. Moreover, three newly introduced so-called critical-point symmetries [2] allow the description of nuclei in mass regions of nuclear phase or shape transitions. Nuclei at critical points should exhibit dramatic changes in their structure and hence of the experimental observables, such as level orderings, γ-transition probabilities, and branchings of the deexcitation paths. The Xe isotopic chain crosses the U(5), E(5) values and reaches the O(6) limit. Therefore, this chain provides a unique case to investigate systematically the changes of spectroscopic observables expected for shape or phase transitions near critical points.

The Xe isotopes were studied in photon-scattering experiments using the bremsstrahlung facility at the Dynamitron accelerator of the Stuttgart University [15] at an electron energy of 4.1 MeV. For the first time in photon-scattering experiments thin-walled high-pressure target cells were used containing isotopically enriched Xe gas of about 70 bar. The cells were delivered by Forschungszentrum Karlsruhe [4].

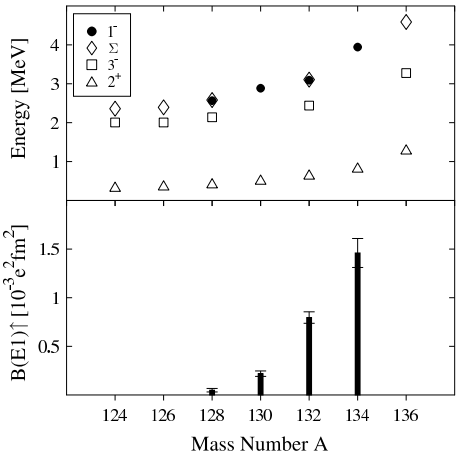

Fig. 1 *Systematics of $2^+ \otimes 3^-$ two-phonon excitations in the even-even Xe isotopes. Upper part: Experimental energies of the 2^+ (open triangles), 3^- (open squares) states and of the observed 1^- two-phonon states (filled circles) in $^{124-136}$Xe compared to the energy sums $\Sigma = E_{2^+} + E_{3^-}$ (open rhombs). Lower part: Experimental $B(E1)\uparrow$ values for the two-phonon excitations.*

Systematics of the 1^- members of $2^+ \otimes 3^-$ two-phonon excitations as resulting from the present work are shown in Fig. 1. The steep decrease of $B(E1)\uparrow$ strengths observed when moving away from the closed shell at $N = 82$ (^{136}Xe) is reproduced by Quasiparticle-Phonon-Model calculations [5, 6].

Systematics of candidates of 1^+ mixed-symmetry states are shown in Fig. 2. The total $B(M1)\uparrow$ strengths exhaust the IBA predictions in the O(6) limit [7] for the light isotopes up to ^{128}Xe but deviate from these predictions for the heavier isotopes which may be a hint for a phase transition near $A = 130$.

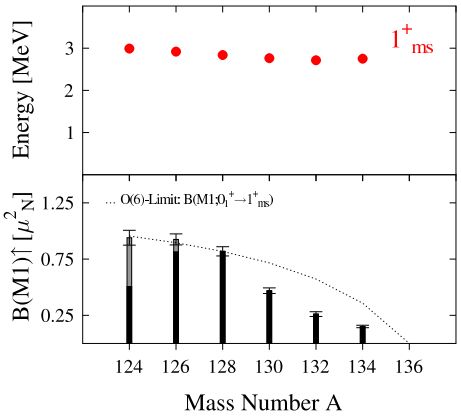

Fig. 2 *Systematics of the candidates for mixed-symmetry $1^+_{\rm ms}$ states in the even-even Xe isotopes versus mass number A. Upper part: Excitation energies. Lower part: $B(M1)\uparrow$ excitation strengths. The dotted line gives the strengths predicted by the IBM-2 model in the O(6) limit. The grey areas in the bars for ^{124,126}Xe represent the summed strengths of the fragments of the M1 excitations.*

[1] R. F Casten, *Nuclear structure from a simple perspective*, Oxford University Press, New York, Oxford (1990)
[2] F. Iachello, Phys. Rev. Lett. 85 (2000) 3580; 87 (2001) 052502; 91 (2003) 132502
[3] U. Kneissl, H.H. Pitz and A. Zilges, Prog. Part. Nucl. Phys. 37 (1996) 349
[4] R. Reifarth, M. Heil et al., Phys. Rev. C 66 (2002) 064603
[5] M. Grinberg and Ch. Stoyanov, Nucl. Phys. A 573 (1994) 231
[6] V. Yu. Ponomarev, Ch. Stoyanov et al., Nucl.Phys. A 635 (1998) 470
[7] P. van Isacker, K. Heyde et al., Ann. Phys. (N.Y.) 171 (1986) 253

Quadrupole Moment of the 8^+ Yrast State in ^{84}Kr[E]

R. Schwengner, D.L. Balabanski, G. Neyens, N. Benouaret, D. Borremans, N. Coulier, M. De Rydt, G. Georgiev, S. Mallion, G. Rainovski, **G. Rusev**, S. Teughels, K. Vyvey

Published in Phys. Rev. C 74 (2006) 034309, 1-6

Nuclear moments are very sensitive to the structure of nuclear states and their measurement is therefore a stringent test of nuclear models. States with a structure dominated by a few nucleons outside a closed shell are good candidates for tests of predictions of the shell model. In particular, effective g factors and effective charges accounting for the influence of orbits not included in the model space may be examined.

The quadrupole moment of the 8^+ yrast isomer (τ = 2.65(6) μs) in ^{84}Kr was measured at the CYCLONE facility in Louvain-la-Neuve using level-mixing spectroscopy (LEMS) [1, 2]. In a LEMS experiment recoiling nuclei are implanted into a suitable host with a non-cubic lattice, where they experience a combined electric quadrupole and magnetic dipole interaction. A split-coil superconducting magnet provides an external magnetic field of up to $B = 4.4$ T which is oriented parallel to the beam axis and thus coincides with the normal vector of the plane in which the spins are oriented after a fusion-evaporation reaction. At low strength of the magnetic field, the electric quadrupole interaction between the electric field gradient, V_{zz}, and the quadrupole moment of the isomer of interest, Q, dominate, and destroy the initial spin orientation. At a high magnetic field this interaction is negligible in comparison to the magnetic dipole interaction, and the spins perform a Larmor precession around the magnetic field $\vec{B}$. As the magnetic field is along the normal vector of the spin-orientation plane, a high field leads to an anisotropy of the intensities of isomeric transitions at 0° and 90° relative to the beam as induced by the spin alignment produced in a fusion-evaporation reaction. The anisotropy is measured as a function of the magnetic field, giving rise to the LEMS curve, which yields the ratio of the electric quadrupole frequency, $\nu_Q = eQV_{zz}/h$, to the magnetic interaction frequency, $\nu_\mu = \mu B/hJ$. From the LEMS curve measured in the present experiment we have deduced a quadrupole moment of $Q = 36(4)e\mathrm{fm}^2$ for the 8^+ yrast state in ^{84}Kr. Experimental quadrupole moments of ^{84}Kr and neighboring nuclei [5] are compared with predictions of the shell model in Fig. 1. Shell-model calculations were performed with a model space including the active proton orbits $\pi(0f_{5/2}, 1p_{3/2}, 1p_{1/2}, 0g_{9/2})$ and neutron orbits $\nu(1p_{1/2}, 0g_{9/2}, 1d_{5/2})$ relative to a hypothetic ^{66}Ni core using a combination of various empirical interactions and surface delta interactions. For details see, e.g., Refs. [3, 4]. Various sets of effective charges used in the literature have been applied: $e_\pi = 1.35e$, $e_\nu = 0.35e$ (SM1); $e_\pi = 1.72e$, $e_\nu = 1.44e$ (SM2). While the quadrupole moment in ^{84}Kr deduced in the present work is well reproduced with set SM1, the general behaviour of the quadrupole moments shows that e_π is too large in SM2 and e_ν is too small in SM1. Therefore, we applied a modified set of $e_\pi = 1.35e$, $e_\nu = 1.0e$ (SM1N) which improves the overall agreement between calculated and experimental quadrupole moments of the neutron-dominated states (see Fig. 1).

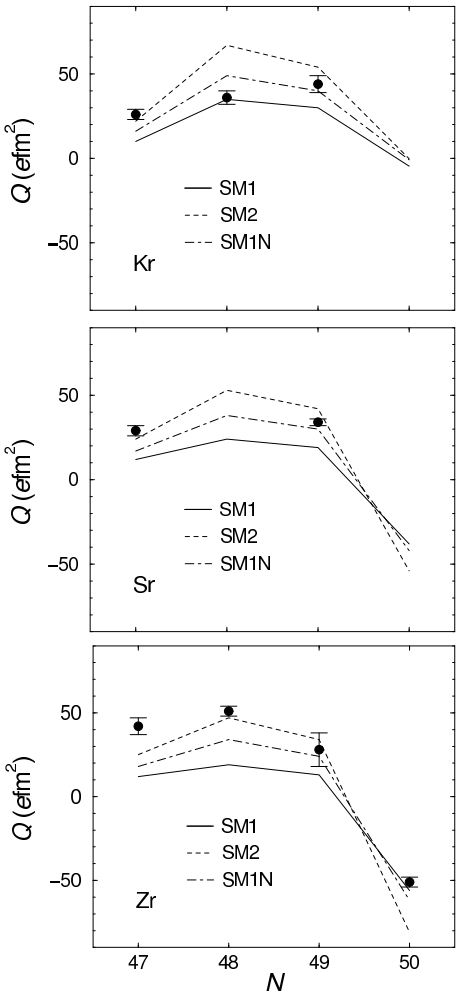

Fig. 1 *Comparison of experimental and calculated quadrupole moments for $9/2^+$ and 8^+ states in the Kr, Sr and Zr isotopes with $N = 47 - 50$. The calculations were performed with different sets of effective charges (see text).*

[1] F. Hardeman, G. Schevenfeels et al., Phys. Rev. C 43 (1991) 130
[2] G. Neyens, Rep. Prog. Phys. 66 (2003) 633
[3] G. Winter, R. Schwengner et al., Phys. Rev. C 49 (1994) 2427
[4] R. Schwengner, J. Reif et al., Phys. Rev. C 57 (1998) 2892
[5] N.J. Stone, At. Data Nucl. Data Tables 90 (2005) 75

Beta Decay of ^{101}Sn [G]

O. Kavatsyuk, C. Mazzocchi, Z. Janas, A. Banu, L. Batist, F. Becker, A. Blazhev, W. Brüchle, J. Döring, T. Faestermann, M. Górska, H. Grawe, A. Jungclaus, M. Karny, M. Kavatsyuk, O. Klepper, R. Kirchner, M. La Commara, K. Miernik, I. Mukha, C. Plettner, A. Pł'ochocki, E. Roeckl, M. Romoli, K. Rykaczewski, M. Schädel, K. Schmidt, **R. Schwengner**, J. Żylicz

Published in Eur. Phys. J. A 31 (2007) 319-325

The measurement of properties of doubly-magic nuclei and their closest neighbours is of great interest as it provides information on the underlying shell structure. Concerning the closest neighbours of the heaviest particle-stable self-conjugated nucleus $^{100}_{50}$Sn, namely $^{99}_{49}$In, $^{99}_{50}$Sn, $^{101}_{50}$Sn and $^{101}_{51}$Sb, only one of them is known so far: ^{101}Sn. The scarce experimental information available on this nucleus stems from studies of its β^+/EC decay [1, 2] or from investigating the α-decay chains ^{105}Te→^{101}Sn [3] and ^{109}Xe→^{105}Te→^{101}Sn [4]. In order to approach experimentally these nuclei, heavy-ion induced fusion-evaporation reactions have been found to be a suitable production mechanism.

The nuclide ^{101}Sn was produced at the GSI on-line mass separator [5] by using the ^{50}Cr(^{58}Ni,α3n)^{101}Sn fusion-evaporation reaction. A ^{58}Ni beam provided by the linear accelerator UNILAC impinged on a ^{50}Cr target (3 mg/cm^2, enriched to 97%).

In a βp experiment the mass-separated beam was periodically switched between two carbon foils in consecutive grow-in (12 s) and decay (12 s) intervals, the collected βp activity being recorded by two identical ΔE-E Si-detector telescopes. The ΔE singles and ΔE-E coincidence events were tagged by the time elapsed since the start of each 24 s cycle. The resulting time profiles were used to determine the half-life of ^{101}Sn.

In the $\beta\gamma$ experiment, three Si detectors were placed in a cube-like geometry inside of a small vacuum chamber. The other three sides of the cube, which remained open, were used to let the beam pass onto a tape in the centre of the cube and to guide the tape to the implantation position and away from it. Around the Si-detector setup two GSI VEGA-Super Clover detectors and a small Clover detector were mounted. The measurement was performed in grow-in mode, *i.e.* during the time when the mass-separated ion beam was continuously implanted into the tape at rest. After a pre-selected time of 8 s the implanted activity was removed from the implantation position.

Based on the measurement of β-delayed protons the half-life of ^{101}Sn was determined to be $T_{1/2} = 1.9(3)$ s. This result is in good agreement with but considerably more accurate than the previously obtained values of 3(1) s [1] and 1.5(6) s [2].

As a result of the measurement of $\beta - \gamma$ and $\gamma - \gamma$ coincidences, β-delayed γ rays following the decay of ^{102}Sn were tentatively assigned for the first time, yielding weak evidence for a cascade of 352 and 1065 keV transitions in ^{101}In.

The decay scheme of ^{102}Sn including the two tentative transitions is shown in Fig. 1 and compared with the results of shell-model calculations. In these calculations, the model space $\pi(p_{1/2}, g_{9/2})$ $\nu(d_{5/2}, g_{7/2}, d_{3/2}, s_{1/2}, h_{11/2},)$ was used with respect to ^{88}Sr as an inert core and a newly developed interaction [6] was applied.

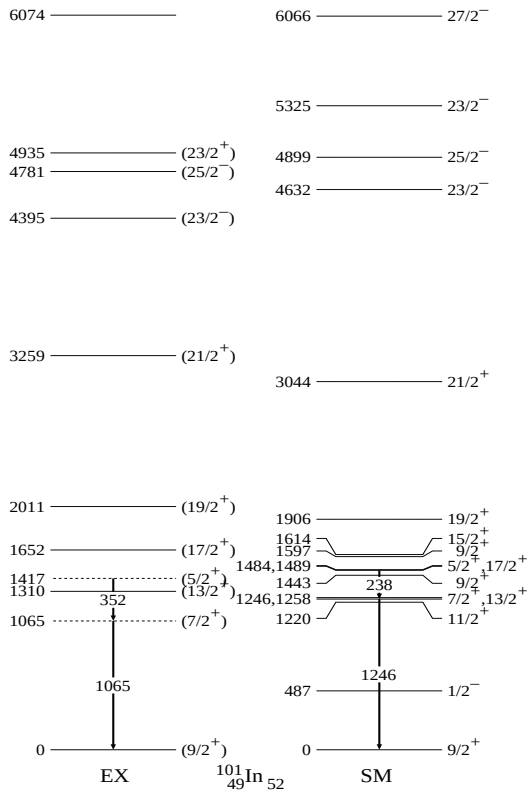

Fig. 1 *Experimental and shell-model high-spin yrast and low-energy low-spin states in ^{101}In. The newly assigned tentative γ-ray cascade observed in the present work and possible shell model predictions are shown, too.*

[1] Z. Janas et al., Phys. Scr. T 56 (1995) 262
[2] A. Stolz, Ph.D. Thesis, TU München (2001)
[3] D. Seweryniak et al., Phys. Rev. C 73 (2006) 061301(R)
[4] S.N. Liddick et al., Phys. Rev. Lett. 97 (2006) 082501
[5] E. Roeckl et al., Nucl. Instr. Meth. B 204 (2003) 53
[6] H. Grawe, to be published

Beta Decay of the Proton-Rich Nuclei ^{102}Sn and ^{104}Sn[G]

M. Karny, L. Batist, A. Banu, F. Becker, A. Blazhev, W. Brüchle, J. Döring, T. Faestermann, M. Górska, H. Grawe, Z. Janas, A. Jungclaus, M. Kavatsyuk, O. Kavatsyuk, R. Kirchner, M. La Commara, S. Mandal, C. Mazzocchi, K. Miernik, I. Mukha, S. Muralithar, C. Plettner, A. Pł'ochocki, E. Roeckl, M. Romoli, K. Rykaczewski, M. Schädel, K. Schmidt, **R. Schwengner**, J. Żylicz

Published in Eur. Phys. J. A 27 (2006) 129-136

Beta decays of nuclei close to ^{100}Sn with $Z \leq 50$ and $N \geq 50$ are characterised by large decay energies and pure Gamow-Teller (GT) transitions between $\pi g_{9/2}$ and $\nu g_{7/2}$ orbits. These features make studies of these decays especially useful to test the nuclear shell model in general and its predictions of (the quenching of) the GT strength in particular. As the half-life of these nuclei are between fraction of a second and few minutes experiments using on-line mass separation are feasible.

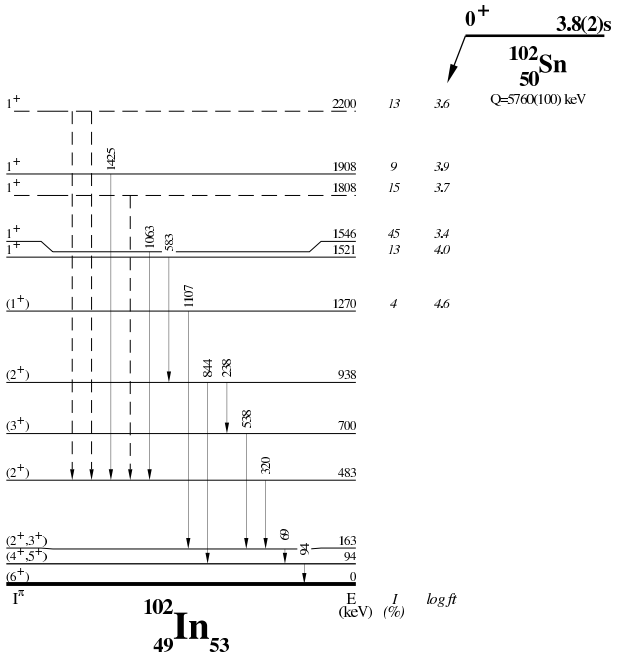

Fig. 1 *Decay scheme of ^{102}Sn established in this work. The γ-ray energies and ^{102}In level energies marked by solid lines represent results from the high-resolution measurement, while dashed lines indicate levels and γ transitions added to the level scheme in order to reproduce the TAS spectrum. The β feeding (I_β) and the comparative half-lives ($log ft$) stem from TAS data.*

In the present experiments, the two isotopes were produced by means of fusion-evaporation reactions between a ^{58}Ni beam delivered by the UNILAC accelerator and a ^{50}Cr target at beam energies between 284 and 302 MeV. After passing the GSI on-line mass separator the ions were directed to either a Total Absorption Spectrometer (TAS) for a β-feeding measurement or to a high-resolution array consisting of one CLUSTER, two CLOVER and two conventional HPGe detectors for measuring γ rays, and of three Si detectors for measuring electrons.

The decay schemes of ^{102}Sn and ^{104}Sn resulting from the present work are shown in Figs. 1 and 2, respectively. The present results have been compared with shell-model calculations using the model space $\pi(p_{1/2}, g_{9/2})^{11}$, $\nu(g_{7/2}, d_{5/2}d_{3/2}, s_{1/2}, h_{11/2})^3$ and the SNC interaction [1, 2].

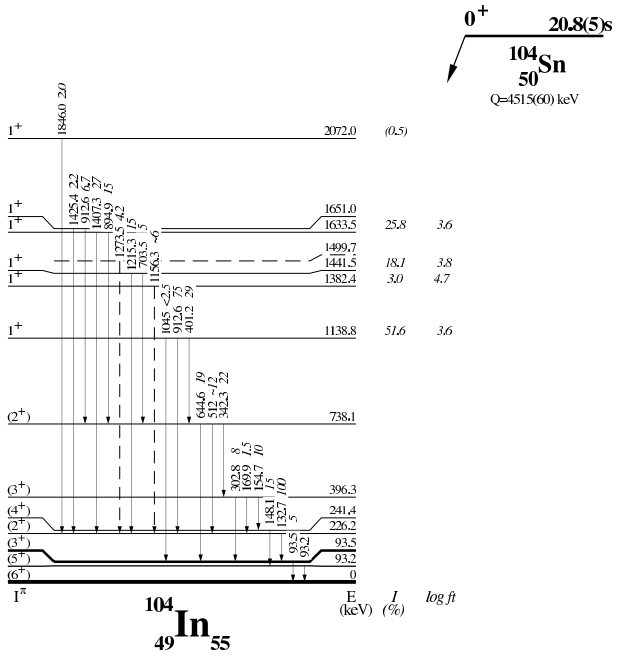

Fig. 2 *Decay scheme of ^{104}Sn. The γ-ray intensities, normalised to that of the 133 keV transition, represent results of the present high-resolution measurement combined with results of Ref. [3]. The β intensities (I_β) and the comparative half-lives ($log ft$) stem from TAS data. Dashed lines indicate tentative assignments.*

[1] B.A. Brown, K. Rykaczewski, Phys. Rev. C 50 (1994) R2270
[2] Z. Hu et al., Phys. Rev. C 62 (2000) 064315
[3] J. Szerypo et al., Nucl. Phys. A 507 (1990) 357

Photon Scattering Experiments on the Quasistable, Odd-Odd Mass Nucleus ^{176}Lu [D]

S. Walter, F. Stedile, J.J. Carroll, C. Fransen, G. Friessner, N. Hollmann, H. von Garrel, J. Jolie, O. Karg, F. Käppeler, U. Kneissl, C. Kohstall, P. von Neumann-Cosel, A. Linnemann, D. Mücher, N. Pietralla, H.H. Pitz, **G. Rusev**, M. Scheck, C. Scholl, **R. Schwengner**, V. Werner, K. Wisshak

Published in Phys. Rev. C 75 (2007) 034301, 1-6

The quasistable odd-odd-mass nucleus ^{176}Lu is of special interest in nuclear structure physics and, moreover, in nuclear astrophysics. This isotope is one of the only nine known stable or quasistable naturally occurring odd-odd mass nuclei. It has a ground-state spin of $J_0^\pi = 7^-$ ($K = 7$) and decays by β^- decay with a halflife of about $4 \cdot 10^{10}$ a [1, 2] to ^{176}Hf. In addition, a low-lying $J^\pi = 1^-, K = 0$ isomer occurs in ^{176}Lu at an excitation energy of 122.9 keV with a halflife of only 3.635 h, which decays also by β^--transitions to ^{176}Hf. Such large spin differences of low-lying levels are common features in heavy odd-odd nuclei and originate from aligned and antialigned couplings of the unpaired protons and neutrons in high-spin Nilsson orbits. In the case of ^{176}Lu these orbits are the $\pi 7/2^+[404]$ and $\nu 7/2^-[514]$ orbits [3]. Because of the long halflife of 40 Ga and the fact that the isotope is shielded against an r-process synthesis, ^{176}Lu was suggested to be an appropriate s-process chronometer [4, 5, 6]. However, answering the question to what extent ^{176}Lu may serve as a cosmic clock or represents rather a stellar thermometer is complicated because of its nuclear structure and depends critically on a possible photoexcitation of the 1^- isomer and its subsequent short-lived 3.635 h β-decay within the photon bath of a stellar s-process scenario [6, 7, 8, 9, 10, 11]. Therefore, the electromagnetic coupling between the ground state and the low-lying isomeric state via low-lying intermediate states (IS) is of fundamental importance for the nucleosynthesis of ^{176}Lu and for tests of stellar models [6, 12, 13]. The possible coupling of these states is illustrated in Fig. 1. IS can be determined from the kinks in the yield curves observed in photoactivation experiments using bremsstrahlung photon beams (see, e.g., Ref. [14]). However, in such experiments the energy determination is limited to an accuracy of about 30 keV. On the other hand, in photon-scattering experiments the excitation energies of such IS can be measured with accuracies of better than 1 keV.

Photon-scattering experiments on ^{176}Lu were performed at the bremsstrahlung facility of the Stuttgart University [15]. Measurements using electron beams of 2.3 and 3.1 MeV delivered by the Dynamitron accelerator were carried out to achieve an optimum sensitivity, in particular in the low-energy range of astrophysical interest.

As a result of the present experiments a total of 29 transitions in ^{176}Lu have been found in the energy range from 1.3 MeV to 2.9 MeV and their transition strengths have been determined. For the lowest proposed IS at 838.6 keV an upper limit for the scattering-cross section integral of $I_s < 1.5$ eVb, corresponding to a minimum lifetime of $\tau \approx 1.5$ ps can be given. This limit is consistent with the result of a GRID measurement [9].

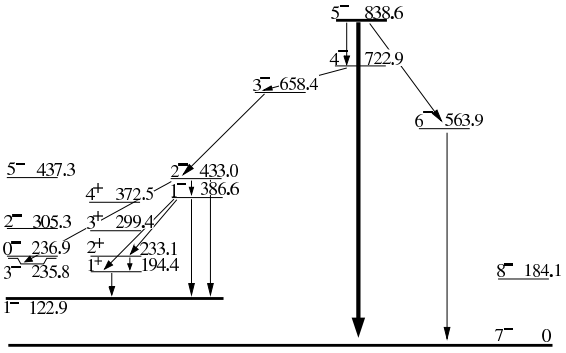

Fig. 1 *Level scheme showing a possible coupling between the ground state of ^{176}Lu and the isomer at 122.9 keV via the IS at 838.6 keV with a spin of 5^- and quantum number $K = 4^-$ (taken from Ref. [8]).*

[1] G.F. Grinyer, J.C. Waddington et al., Phys. Rev. C 67 (2003) 014302
[2] Y. Nir-El and G. Haquin, Phys. Rev. C 68 (2003) 067301
[3] M. S. Basunia, Nucl. Data Sheets 107 (2006) 791
[4] J. Audouze, W.A. Fowler and D. N. Schramm, Nature 238 (1972) 8
[5] M. Arnould, Astron. & Astrophys. 22 (1973) 311
[6] F. Käppeler, H. Beer and K. Wisshak, Rep. Prog. Phys. 52 (1989) 945
[7] N. Klay, F. Käppeler et al., Phys. Rev. C 44 (1991) 2801
[8] N. Klay, F. Käppeler et al., Phys. Rev. C 44 (1991) 2839
[9] C. Doll, H.G. Börner et al., Phys. Rev. C 59 (1999) 492
[10] K.T. Lesko, E.B. Norman et al., Phys. Rev. C 44 (1991) 2850
[11] J. Vanhorenbeeck, J.M. Lagrange et al., Phys. Rev. C 62 (2000) 015801
[12] F. Käppeler, Prog. Part. Nucl. Phys. 43 (1999) 419
[13] D. Belic, C. Arlandini et al., Phys. Rev. Lett. 83 (1999) 5242; Phys. Rev. C 65 (2002) 035801
[14] D. Belic, J. Besserer et al., Nucl. Instr. Meth. A 463 (2001) 26
[15] U. Kneissl, H.H. Pitz and A. Zilges, Prog. Part. Nucl. Phys. 37 (1996) 349

The Two-Step Gamma Cascade Method as a Tool for Studying Photon Strength Functions of Intermediate-Weight and Heavy Nuclei

F. Bečvář, J. Honzátko, M. Krtička, S. Pašić, **G. Rusev**, I. Tomandl

In press in Nucl. Instr. Meth. B

The method of two-step γ cascades (TSC) following the thermal-neutron capture is described. An example of two-step cascade data from measurements with ^{162}Dy target is given (cf. Fig. 1) together with interpretation of this data in terms of scissors-mode resonances built on excited levels in ^{163}Dy (cf. Fig. 2). With the aim of verifying the correctness of the method results of benchmark testing measurements with ^{56}Fe (cf. Fig. 3) are compared with the outcome of the GEANT3 simulations (cf. Fig. 4).

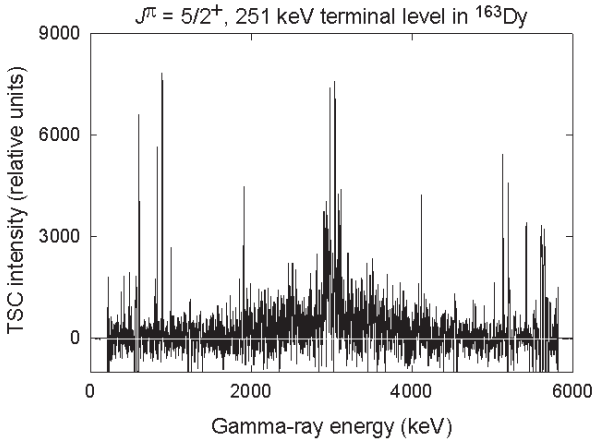

Fig. 1 *An example of a TSC spectrum measured in the thermal ^{162}Dy(n,γ)^{163}Dy reaction.*

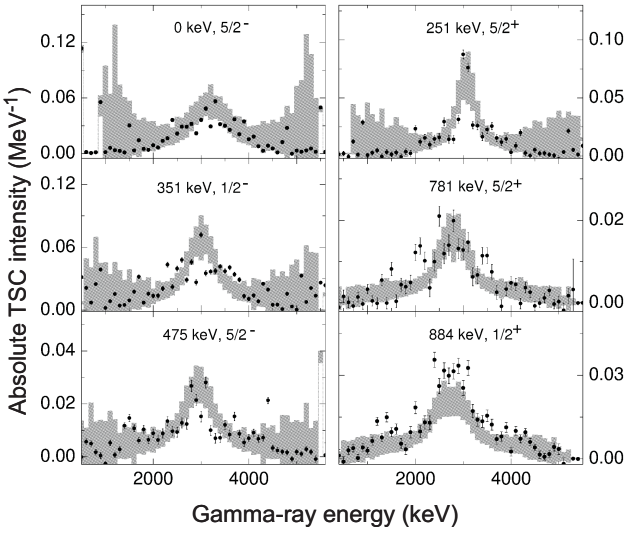

Fig. 2 *TSC spectra for 6 terminal levels in ^{163}Dy (data points) and their comparison with predictions of the statistical model (shaded areas). Energies and J^π values of the levels are indicated.*

The simulations clearly demonstrate that the TSC spectra represent clean data for studying decay properties of the levels in the quasi continuum with excitation energies $E_f + 1.5\text{MeV} < E_x < B_n - 1.5\text{MeV}$.

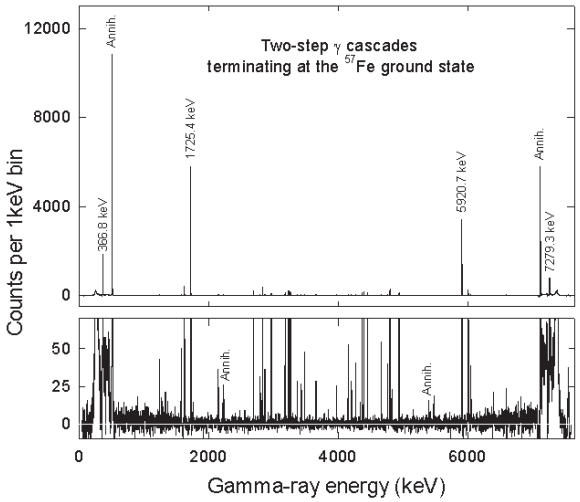

Fig. 3 *The spectrum of TSCs terminating at the ^{57}Fe ground state. Gamma-lines associated with positron annihilation are labeled, as well as lines belonging to the pair of the strong γ cascades. The inherent symmetry of the spectrum is apparent.*

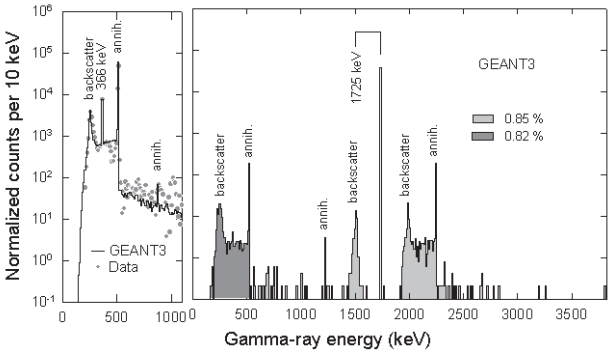

Fig. 4 *Left panel: a comparison between the data and the results of the simulation. In the simulation only two most prominent TSCs and the primary transition to the ^{57}Fe ground state were taken into account. Right panel: the results of simulations of the response of the detector system to the strongest TSC proceeding via the 1725.4 keV level; only the low-energy part of the spectrum is shown.*

Electromagnetic Excitations in Nuclei: from Photon Scattering to Photodisintegration

M. Erhard, C. Nair, R. Beyer, E. Grosse[1], A.R. Junghans, J. Klug, K. Kosev, N. Nankov, G. Rusev, K.D. Schilling, R. Schwengner, A. Wagner

Part of PhD thesis M. Erhard

Accepted by Proc. of Science (2007), PoS(NIC-IX)056

In explosive nucleosynthesis temperatures are high enough for photodisintegration reactions to occur, e.g. leading to the production of p-process nuclei. In order to understand the reaction rates of element production and element disruption we started an experimental program at the new bremsstrahlung facility of the superconducting electron accelerator ELBE of FZ Dresden-Rossendorf. The bremsstrahlung facility and the detector setup are designed such that the scattering of photons from nuclei and the photodisintegration of nuclei around the particle separation energies can be studied under optimized background conditions. In activation measurements with bremsstrahlung at end-point energy from 10.0 to 16.5 MeV (γ,p), (γ,n) and (γ,α) reactions of ^{92,100}Mo have been studied. Our activation yields can be described within a factor 2-3 or better with calculations using the cross sections from recent Hauser-Feshbach models.

[1] A.J. Koning, S. Hillaire et al., *Proc. Int. Conf. Nucl. Data for Science and Technology, ND2004,* Santa Fe, USA, 2004, AIP Conference proceedings 769 (2005) 177

[2] T. Rauscher and F.-K. Thielemann, At. Data and Nucl. Data Tables 88 (2004) 1

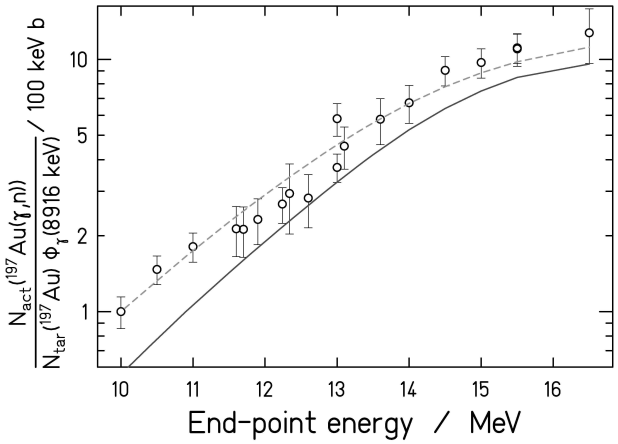

Fig. 1 *Preliminary activation yield of $^{197}Au(\gamma,n)$ measured at the target position. The experimental yield is normalized to the number of ^{197}Au atoms and to the absolute photon flux at the energy E_γ = 8916 keV. The data are compared to yield integrals computed with the cross sections from TALYS [1] and NON-SMOKER [2] using the absolute photon flux determined from known transitions in a sample containing ^{11}B.*

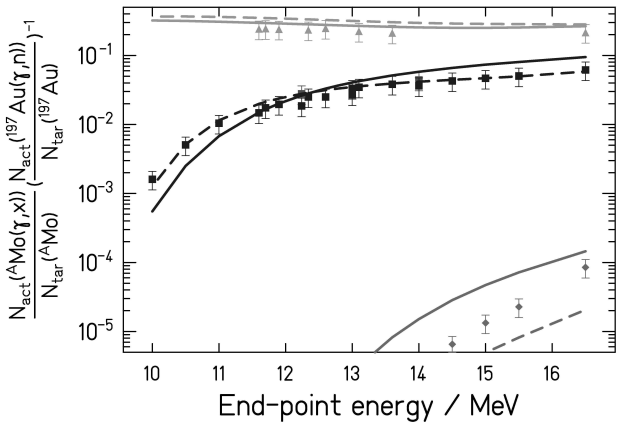

Fig. 2 *Measured activation yields at the photoactivation site for different Mo-Isotopes normalized to the activation yield from $^{197}Au(\gamma,n)$ irradiated simultaneously and to the number of the respective target atoms as a function of the bremsstrahlung end-point energy. The full symbols denote experimental yields from $^{100}Mo(\gamma,n)$ (triangles), $^{92}Mo(\gamma,p)$ + (γ,n) (squares), and $^{92}Mo(\gamma,\alpha)$ (diamond). The lines are calculated with photodisintegration cross sections from NON-SMOKER (full) and TALYS (dashed).*

[1] *also TU Dresden*

Photodisintegration Studies on p-Nuclei: The Case of Sm Isotopes

C. Nair, A.R. Junghans, M. Erhard, E. Grosse[1], K.D. Schilling, R. Schwengner, A. Wagner

Part of PhD thesis C. Nair

In explosive stellar environments like supernovae, the temperatures are high enough for the production of heavy neutron deficient nuclei, the so-called p-nuclei. These are thought to be produced in such scenarios either through chains of photodisintegration reactions like (γ,n), (γ,p) and (γ,α) on heavy seed nuclei or by a recently suggested mechanism interpreted as the νp process[1]. The precise knowledge of the cross sections of these reactions are of crucial importance for the prediction of the p-nuclei abundances in nucleosynthesis network calculations.

At the ELBE bremsstrahlung facility, photodisintegration studies on the astrophysically relevant p-nuclei ^{92}Mo and ^{144}Sm have been performed via the photoactivation technique. All the three types of photodisintegration reactions were observed for the two nuclei and in particular the (γ,α) reactions of the mentioned nuclei were studied for the first time. Bremsstrahlung endpoint energies chosen ranged from 10.0 to 16.5 MeV. Details and main results of the photoactivation studies on ^{92}Mo are comprised in [2].

Samples of fine Sm_2O_3 powder (mass $\approx$ 3 g, diameter 18 mm) were irradiated in the photoactivation site located behind the electron beam dump together with an Au sample. During the same experiment, another Au sample was irradiated at the target position in the bremsstrahlung cave together with a ^{11}B sample. By using the known ^{197}Au(γ,n) cross section and the known scattering cross section of transitions in ^{11}B we could estimate the photon flux in the electron beam dump. For more details of the experimental setup and method see, [2, 3].

The number of radioactive nuclei $N_{act}(E_0)$ produced in a photoactivation measurement is proportional to the integral of the absolute photon flux $\phi_\gamma(E,E_0)$ multiplied by the photodisintegration cross section $\sigma_{\gamma,x}(E)$ from the reaction threshold energy E_{thr} up to the bremsstrahlung spectrum end-point energy E_0:

$$N_{act}(E_0) = N_{tar} \cdot \int_{E_{thr}}^{E_0} \sigma_{\gamma,x}(E)\phi_\gamma(E,E_0)dE.$$

The symbol x stands for the emitted particle (i.e, n,p or α). N_{tar} is the number of target atoms in the sample. $N_{act}(E_0)$ can be experimentally determined with a low-level counting setup using the HPGe detector as

$$N_{act}(E_0) = N_\gamma(E_0,E_\gamma) \cdot \kappa_{corr}/(\epsilon(E_\gamma) \cdot p(E_\gamma)).$$

Here $N_\gamma(E_0,E_\gamma)$ denotes the full-energy peak counts of the observed transition corrected for dead-time and pile-up , $\epsilon(E_\gamma)$ and $p(E_\gamma)$ stand for the absolute full-energy peak efficiency of the detector and the emission probability of the photon for the energy E_γ, respectively. The factor κ_{corr} accounts for the decay losses during irradiation and measurement and this corrects the measured number of decays to the number of radioactive nuclei in the sample.

Measured reaction yields relative to the ^{197}Au reaction yield are as shown in fig. 1. The experimental data are compared with the yield integrals calculated with a simulated thick-target bremsstrahlung spectrum and photodisintegration cross sections predicted by Hauser-Feshbach models [4, 5]. The ^{144}Sm(γ,n) reaction cross section is dominant for energies above 10.5 MeV. Since ^{144}Sm(γ,p) has the reaction threshold at 6.3 MeV, it is necessary to do the experiment with endpoint energies between 6.3 MeV and 10.5 MeV in order to measure pure (γ,p) yields. Experiments in this regard are in progress.

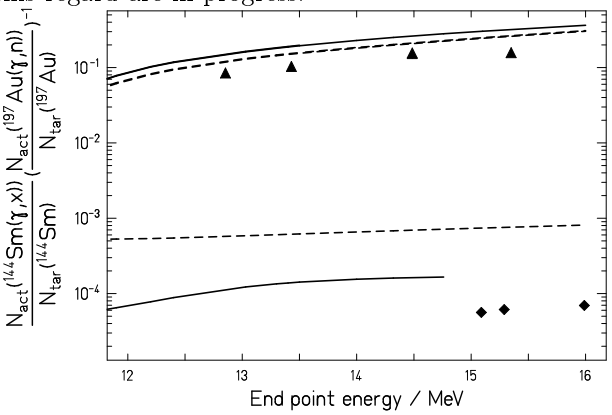

Fig. 1 *Experimental activation yields for photodisntegration reactions on ^{144}Sm isotopes normalized to the activation yield from ^{197}Au(γ,n) irradiated simultaneously. Symbols stand for ^{144}Sm(γ,n) (triangles) and ^{144}Sm(γ,α) (diamonds). The solid line shows calculations using cross sections from [4] and the dotted one stands for the predictions from [5]*

[1] C. Fröhlich et al., Phys. Rev. Lett. 96 (2006) 142502
[2] M. Erhard et al., PoS-(NIC-IX) 056 (2006)
[3] R. Schwengner et al., NIM A 555 (2005) 211
[4] T. Rauscher, F. -K. Thielemann, Atomic Data and Nuclear Data Tables 88 1(2004)
[5] A. J. Koning et al., AIP-(ND-2004) 769 (2005) 1154

[1] *also TU Dresden*

Commissioning of a Pneumatic Delivery System for Photoactivation Experiments at the Electron Accelerator ELBE

A. Wagner, J. Claussner[1], P. Crespo, M. Erhard, M. Fauth[2], E. Grosse[2], A. Hartmann, C. Nair, A.R. Junghans, K.D. Schilling, R. Schwengner, M. Sobiella, J. Steiner

The new facility for experiments on photodisintegration of nuclei using bremsstrahlung has been set into operation at the electron accelerator ELBE of the Forschungszentrum Dresden-Rossendorf [1]. In order to access short-lived nuclides with half-lives below 10 min, the irradiated samples are transported within about 5 s from the electron beam dump into a well-shielded low-level counting setup by means of a pneumatic delivery system. The whole system is hermetically closed in order to prevent leakage of activated air. The radioactive decay is measured by a coaxial high-purity Germanium (HPGe) detector with a relative efficiency of 90%. The data acquisition is based on an ORTEC[3] 919 multichannel analyzer system for long-term measurements of long-lived activities and a dedicated CAMAC-based list-mode data acquisition system for measurements with strongly varying count rates stemming from short-lived decays. The list-mode systems named CAP (CAMAC Acquisition by PCI) allows us to determine the precise dead time during data taking and the correction for signal pile-up in time slices down to 1 ms depending on the detector count rates. The list-mode system consists of NIM and CAMAC modular electronics which are read out by a LINUX-based personal computer. The data taking, analyzing, and visualizing software has been developed based on the Qt open source package[4].

As a first commissioning experiment we studied several (γ, n) reactions close to the neutron separation energies. Table 1 shows the parameters of the reactions leading to β-unstable nuclei. The photon emission following β-decay is used unambiguously to identify the amount of nuclei being activated. Several samples of Mo ($\approx$0.8 g) and Sm_2O_3 ($\approx$3 g) were irradiated for 15 min inside the electron beam dump and the decay was measured for 15 min after 13 s transport to the low-level counting setup. The fractional lifetime of the data taking system was always higher than 0.75.

From the energy dependent activation yields shown in Fig. 1 we conclude that the explicit identification of nuclei from photoactivation allows for a precise determination of activation yields of nuclei with short half lives.

The energy scale of the experimental data was adjusted by a factor of 0.96 to the value deduced from the measurement of the magnetic rigidity of the electron beam.

Reaction	S_n^{eff}	E_γ	$T_{\frac{1}{2}}$
$^{197}Au(\gamma,n)^{196}Au$	8.07 MeV	356 keV	6.2 d
$^{144}Sm(\gamma,n)^{143}Sm$	10.52 MeV	1057 keV	525 s
$^{144}Sm(\gamma,n)^{143m}Sm$	11.27 MeV	754 keV	66 s
$^{92}Mo(\gamma,n)^{91m}Mo$	13.33 MeV	653 keV	15 s

Table 1 *Reactions, effective neutron separation energies S_n^{eff}, photon energies E_γ, and decay half lives $T_{\frac{1}{2}}$ used in photoactivation experiments.*

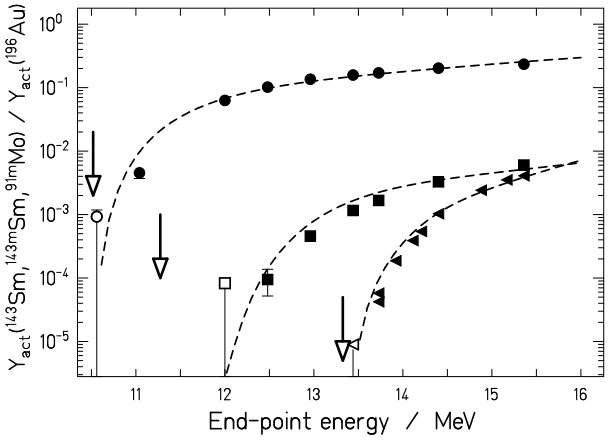

Fig. 1 *Photo-activation yields relative to the reaction $^{197}Au(\gamma,n)^{196}Au$ for $^{92}Mo(\gamma,n)^{91m}Mo$ (triangles), $^{144}Sm(\gamma,n)^{143}Sm$ (circles), and $^{144}Sm(\gamma,n)^{143m}Sm$ (squares). The effective neutron separation energies are marked by arrows. Open symbols denote the detection threshold for the lowest measured energies. Dashed lines show predictions from theoretical models [3].*

[1] K.D. Schilling et al., IKH Annual Report 2005, FZR-442 (2006) 42

[2] M. Fauth et al., this report, p. 52

[3] A. Koning et al., Proc. Int. Conf. Nuclear Data Science and Technology, ND2004, Santa Fe, NM, USA, AIP Conf. Proc. 769, 177 (2005)

[1] *Department of Research Technology, FZD*
[2] *also TU Dresden*
[3] *ORTEC Inc., Oak Ridge, TN 37830 U.S.A.*
[4] *Qt development framework, http://www.trolltech.com*

A CAMAC-Based Data Acquisition System for Photoactivation Experiments at the Electron Accelerator ELBE

M. Fauth[1], P. Crespo, M. Erhard, A.R. Junghans, C. Nair, K.D. Schilling, A. Wagner

A CAMAC-based data acquisition system named CAP (for CAMAC Acquisition through PCI) has been developed for photo-activation experiments at ELBE using high-purity germanium-detectors. The system enables to handle rapidly changing detector count rates from decaying radioactivities with strongly varying data-acquisition dead-times and detector pile-up by using list-mode data taking.

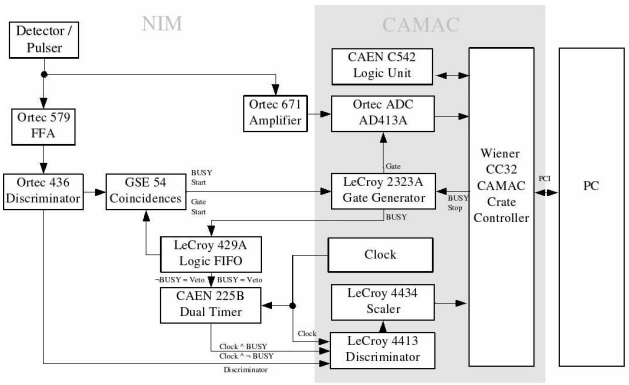

Fig. 1 *Electronics scheme of the CAP system.*

Fig. 1 shows the electronics chain implemented with CAP. The detector's preamplifier signal arrives at an ORTEC[2] 671 main amplifier and an ORTEC 479 fast filter amplifier.

The main amplifier provides a Gaussian-shaped signal for an ORTEC AD413 13-bit analog-to-digital converter read out by CAMAC through a WIENER[3] CAMAC to PCI computer interface. The fast filter amplifier produces a fast rise-time signal with 200 ns differentiation time which is fed into a discriminator. The discriminator signals are counted directly and gated by the data-acquisition dead-time logic using a fast LeCroy[4] 4434 scaler. The gated discriminator signal provides the ADC gate, as well. In parallel, a 1 MHz clock signal is processed in the same way which allows for a precise determination of the data taking time and an independent determination of the dead-time (and detector pile-up) correction. Fig. 2 shows the electronic timing diagram of the CAP system.

The software routines developed for CAP and the list-mode data-format are based on the routines developed for the data acquisition CAGE [1] (CAMAC Acquisition through GPIB and Ethernet). The system performance was analyzed using the decay of activated Sm_2O_3 samples where the various isotopes decay with significantly different half-lives. The plot in Fig. 3 shows three different decay curves for the full energy spectrum, the 103 keV transition from $^{154}\mathrm{Sm}(\gamma,n)^{153}\mathrm{Sm}(\beta^-)^{153}\mathrm{Eu}$ with a half-live of 46.3 h, and the 1057 keV transition from $^{144}\mathrm{Sm}(\gamma,n)^{143}\mathrm{Sm}(\beta^+)^{143}\mathrm{Pm}$ with a half-live of 8.83 min. We conclude that radioactivity from short-lived nuclei can be quantified even for strongly varying detector count rates.

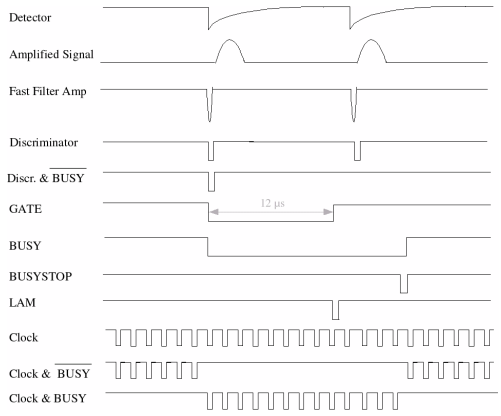

Fig. 2 *Electronic timing diagram of the CAP system.*

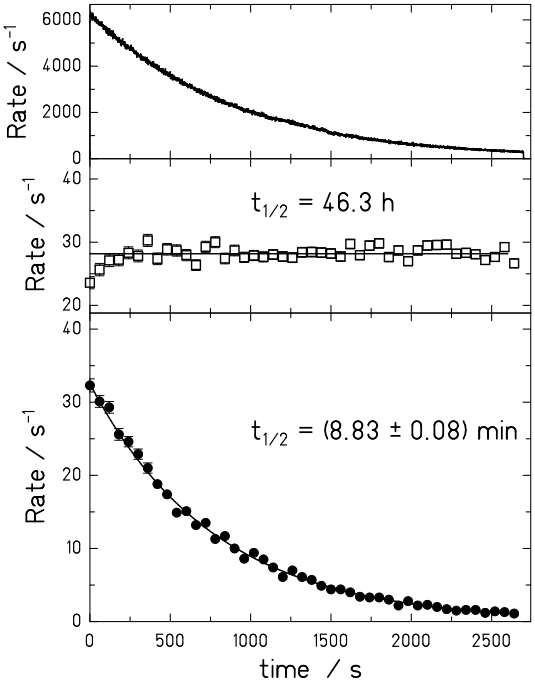

Fig. 3 *Data acquisition rate, rate of detected decays from* ^{153}Sm, *and rate of detected decays from* ^{143}Sm.

[1] http://www.fzd.de/FWK/MITARB/crespo/cage.html

[1] *also TU Dresden*
[2] *ORTEC Inc., Oak Ridge, TN 37830 U.S.A.*
[3] *WIENER, Plein & Baus GmbH, 51399 Burscheid, Germany*
[4] *LeCroy Corp., Chestnut Ridge, NY 10977 U.S.A.*

Improving the Timing Properties of the Photo-Fission Setup

K. Kosev, N. Nankov[1], M. Friedrich[2], **E. Grosse[3], A. Hartmann, K. Heidel, A.R. Junghans, K.D. Schilling, R. Schwengner, M. Sobiella, A. Wagner**

Part of PhD thesis K. Kosev

A double time-of-flight spectrometer is under construction which would eventually enable the detection of fission fragments produced by the high-intensity photon beam from bremsstrahlung at ELBE. In this spectrometer Micro-Channel Plate detectors play an important role. The quality of the timing information derived from them is crucial for the experiment.

In a standard setups, the electronic MCP signals are processed by capacitively coupled devices with low impedance (50 Ω) input. The low impedance input is necessary to preserve the signal shape using shielded 50 Ω coaxial cable transmission and hence the signal timing information. Since the MCP back and front signals in our setup are derived from thin rings with ill defined impedance, impedance matching problems arise, causing ringing and signal distortion. Although it is not impossible to build 50 Ω impedance signal collectors [1], an electronic matching is the easier and cheaper solution[2]. Consequently, a simple and fast capacitively coupled transimpedance amplifier has been developed (see Fig. 1).

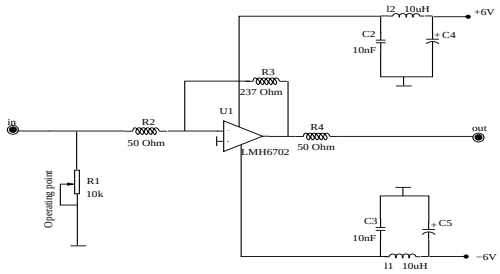

Fig. 1 *The circuit diagram.*

The amplifier is designed to be used with a high input and a low (50 Ω) output impedance without a coupling capacitor. The resistors R1 and R2 determine the operating point of the amplifier U1, the input impedance of the circuit and therefore the quality of the impedance matching. The amplifier U1 is an ultra-wideband monolithic OP-Amp (LMH6702, National Semiconductor) using inverting gain circuit. It has been optimised for exceptionally low harmonic distortion. The amplification formed by the input resistor R2 and the feedback resistor R3 does not exceed factor 4, yet improving the signal-to-noise ratio. R5 serves for impedance line matching. By mounting this circuit as close to the MCP detectors surface as possible, we succeed in preserving the signal rise time and improving the CFD sensitivity, because of the additional amplification.
Finally the setup is tested under beam conditions at the 5 MeV FZD TANDEM accelerator (see Fig. 2).

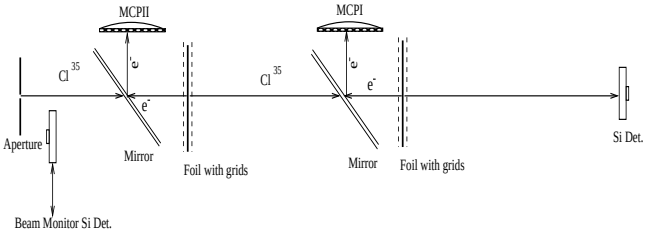

Fig. 2 *Experimental setup. The heavy ion beam enters the setup from the left. After interacting with the foils for secondary electron production, the accelerated electrons are deflected and detected by the MCPs.*

Our first test measurements with the transimpedance amplifiers show satisfactory results (see Fig. 3). It is also worth mentioning that the beam quality can also affect the observed timing resolutions [3].

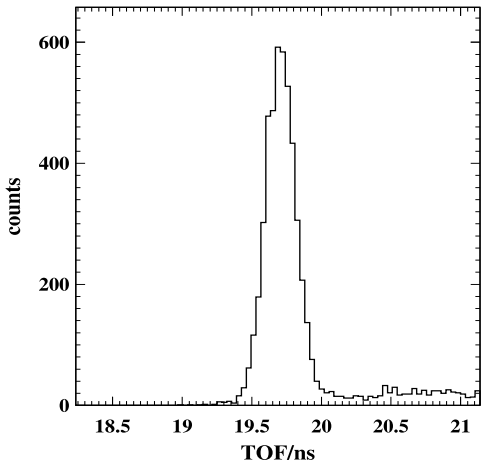

Fig. 3 *TOF spectrum between the two MCPs using transimpedance amplifiers for a ^{35}Cl beam of 40 MeV and foil-to-foil distance of 27 cm. The FWHM results in 240 ps. Assuming identical detectors, the apparent time resolution of one detector corresponds to 170 ps.*

[1] P. Wurz and L. Gubler, Rev. Sci. Instrum. 65 (1994) 871
[2] P. Schwartze et al., Rev. Sci. Instrum. 72 (2001) 3125
[3] K.Kosev et al., IKH Annual Report 2005, FZR-442 (2005) 12

[1] *INRNE, Sofia, Bulgaria*
[2] *Inst. of Ion Beam Physics and Materials Research, FZD*
[3] *also TU Dresden*

Low-Threshold Proton-Recoil Detectors for nELBE

R. Beyer, E. Grosse,[1] **K. Heidel, J. Hutsch, A.R. Junghans, J. Klug,** D. Légrády,[2] R. Nolte,[3] S. Röttger,[3] **M. Sobiella, A. Wagner**

Part of Diploma thesis R. Beyer

For experiments with neutrons at the new neutron time-of-flight source (nELBE) [1] at FZD, and at the existing bremsstrahlung facility [2] fast plastic-scintillation detectors with relatively high efficiency also for neutrons with kinetic energies below 100 keV have been developed [3].

The detectors are made from strips of EJ-200 and have a detection area of 1000 x 42 mm^2 and thicknesses of 11 or 22 mm. In order to determine the position of the detection reaction and to improve the signal to noise ratio, the scintillators are read out in coincidence by two Hamamatsu R2059-01 PMTs, one at each end. A dedicated VMEbus-based data acquisition (DAQ) setup was assembled. Two 32-channel QDCs (CAEN V792) integrate the analog signals of both PMTs to obtain the light output signal. One TDC (CAEN V1190A) is used to determine the timing information. The timing signals are delivered by CFDs (CFT5386), which are an inhouse development being optimized for the signals of the scintillator material used. The start for the time-of-flight (ToF) measurement is given by a reference signal (e.g. the timing signal of the ELBE accelerator). To obtain a low neutron detection threshold, the PMTs are operated at highest gain ($\sim 2{\cdot}10^7$) while the CFD threshold is set to about 50 mV, resulting in a trigger level just below the single-photo-electron peak (SEP) of the PMTs. By adjusting the trigger threshold relative to the SEP, one can set a quite stable and well reproduceable detection threshold [3].

From measurements with a collimated ^{90}Sr electron source one obtains a position resolution of about 5.3 cm (FWHM) and a time resolution of of about 670 ps (FWHM). For neutrons with a kinetic energy of 1 MeV and a flight path of 4 m this time resolution causes an energy resolution of less than $\Delta E/E =$ 0.5 %. The efficiency of the detectors has been determined at Physikalisch-Technische Bundesanstalt (PTB), Braunschweig, with quasi-monoenergetic neutron fields from (p,n) reactions on ^{3}H or ^{7}Li [4]. The neutron yield is monitored by well-calibrated neutron counters [5]. In Fig. 1 the measured ToF spectra taken with one detector and a neutron energy of 73 keV are shown. In the upper panel the comparison of the time-of-flight spectra measured with and without a polyethylene shadow bar is shown. Both measurements have been normalised to the same neutron fluence. The width of the ToF peak is dominated by the energy loss of the proton beam inside the target which was simulated with the Monte-Carlo program TARGET [6]. The background subtracted spectrum is shown in the lower panel of Fig. 1 for comparison with the simulated spectrum. Even the background of scattered neutrons can be reproduced reasonably well. Six plastic scintillation detectors were calibrated at five different neutron energies E_n: 24, 73, 150, 560 and 1200 keV. The results of the efficiency determination are plotted in Fig. 2. The main result is, that for neutrons with a kinetic energy of only 24 keV, efficiencies of about ten percent were obtained for all detectors.

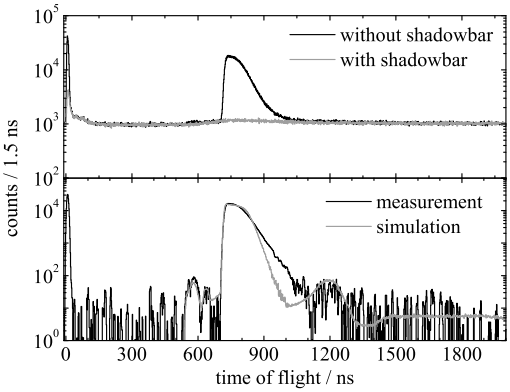

Fig. 1 *Measured ToF spectra for one detector at E_n = 73 keV (see text).*

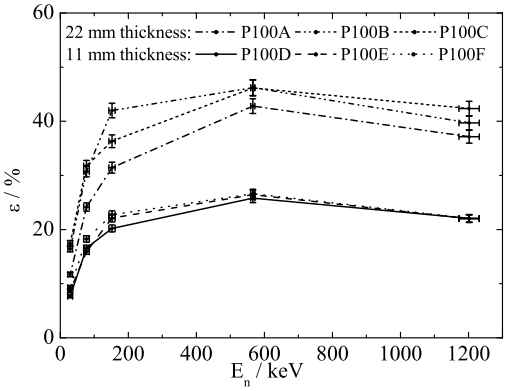

Fig. 2 *Measured intrinsic neutron-detection efficiency for 6 different detectors. The efficiency may vary due to different light collection efficiencies.*

[1] E. Altstadt, C. Beckert et al., Ann. Nucl. Ener. (2007) in press

[2] R. Schwengner, R. Beyer et al., Nucl. Instr. Meth. A 555 (2005) 211

[3] R. Beyer, E. Grosse et al., Nucl. Instr. Meth. A (2007) submitted

[4] H.J. Brede, M. Cosack et al., Nucl. Instr. Meth. 169 (1980) 349

[5] D. Schlegel, S. Guldbakke, PTB-6.41-02-03 (2002)

[6] D. Schlegel, PTB-6.42-05-2 (2005)

[1] *also TU Dresden* [2] *Inst. of Safety Research, FZD*
[3] *PTB Braunschweig*

A BaF_2 Detector Array for Neutron-Capture γ-Rays

J. Klug, E. Altstadt[1], C. Beckert[1], **R. Beyer,** H. Freiesleben[4], V. Galindo[1], M. Greschner[4], **E. Grosse**[also 4], **A.R. Junghans,** D. Légrády[1], B. Naumann[2], K. Noack[1], **G. Rusev, K.D. Schilling,** R. Schlenk[3], S. Schneider[3], K. Seidel[4], **A. Wagner,** F.-P. Weiss[1,also4]

Submitted to Nucl. Instr. Meth. A

The neutron time-of-flight system at ELBE will produce neutrons in the energy interval E_n = 50 keV−10 MeV, where there is a need for neutron cross section measurements for transmutation, fission and fusion reactor applications [1].

For measurements of neutron-capture γ-rays, a scintillation detector array covering up to 96 % of the total solid angle is being built from 42 BaF_2 crystals, each 19 cm long, having a hexagonal cross section with an inner diameter of 53 mm. Two adjacent inner rings of 12 crystals each are surrounded by an outer ring of 18 crystals. They are read out by fast, UV sensitive Hamamatsu R2059 photomultiplier tubes [2], able to measure both the slow and the fast component of the scintillation light, enabling pulse-shape discrimination to separate photon signals from intrinsic α-particle background. A fast digital data acquisition system based on the Acqiris DC282 digitiser [3] is under development.

The efficiency ε of the BaF_2 array due to (n,γ) reactions in a target of 1 cm^3 (7.87 g) of ^{56}Fe has been simulated. It depends on two mechanisms:

(1) The detailed behavior of the γ-cascades following neutron capture. A Monte Carlo code developed at FZD [4] was used to simulate cascades from capture of S-neutrons in ^{56}Fe by exciting levels with spin $\frac{1}{2}$ in ^{57}Fe. The excitation in ^{57}Fe was selected from the range $E_X = 7.6-15$ MeV, corresponding to capture of neutrons with energies $E_n = 0.0-7.4$ MeV. The γ-ray multiplicity and the individual γ-ray energies E_γ were determined in each cascade.

(2) The interactions in the crystals of the emitted γ-rays. Energy deposition tables for γ-ray transport in the array were created using MCNP5, where monoenergetic photons of energy E_{tab} were emitted isotropically from the ^{56}Fe target in steps of 0.5 MeV, up to $E_{tab} = 15$ MeV. The photons were traced through the setup, providing a step-by-step account of all interactions until final absorption or escape. This was done for 90000 γ-rays for each energy and resulted in a table containing the energy deposited in the 42 BaF_2 crystals in a (90000 × 42) array. The sum energy of all 42 entries for a γ-ray starting with energy E_γ may be anywhere between zero and E_γ, depending on how much energy was lost along the track (which may span over one or more crystals).

The calculation of ε proceeded by selecting a γ-ray with energy E_γ from a cascade and identifying the energy deposition table with E_{tab} closest to E_γ. One of the 90000 events was chosen by random, and the energy deposited in each of the 42 detectors was obtained by multiplying the entries with the scale factor E_γ/E_{tab}. This was done for all γ-rays in the cascade, giving the total energy. By repeating the process for all cascades, the instrumental multiplicity m, the energy distribution of the detected cascades, and ε were obtained. The calculation can be performed with several threshold requirements: a minimum energy E_{thr} deposited in each hit BaF_2 crystal, a minimum total energy E_{THR} in the array, and a minimum multiplicity m_{thr}. Thereby a comparison can be made with a real situation where, e. g., background reduction may call for coincident signals in at least two detectors.

Fig. 1 shows the response for neutrons in the range $E_n = 0.0 - 7.4$ MeV with (i) no condition, (ii) $E_{thr} \geq$ 300 keV combined with $E_{THR} \geq$ 7.6 MeV, and (iii) $E_{thr} \geq$ 300 keV plus $m_{thr} \geq 2$. In case (ii), only events above the neutron separation energy are studied, where the high threshold may allow also for $m = 1$ events. In (iii), coincident signals in at least two detectors are utilised instead of a high threshold on the total energy. The efficiencies are (i) $\varepsilon = 0.91$, (ii) $\varepsilon = 0.53$, and (iii) $\varepsilon = 0.67$.

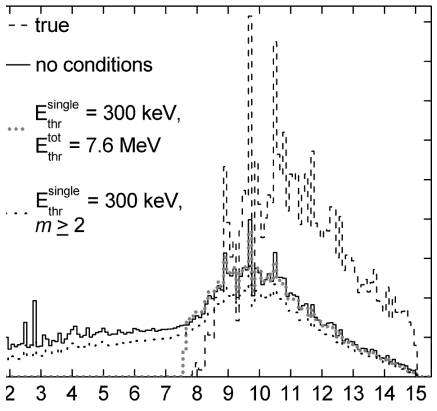

Fig. 1 *Total cascade energy (dashed line), and energy detected by the BaF_2 array under conditions indicated.*

[1] M. Herman (comp) INDC(NDS)-428 and INDC(NDS)-423, IAEA, Vienna, Austria (2001)

[2] http://www.hamamatsu.com

[3] http://www.acqiris.com

[4] G. Rusev, Ph.D. thesis, TU Dresden (2007)

[1] *Inst. for Safety Research, FZD*
[2] *Department for Techn. Infrastructure, FZD*
[3] *Department of Research Technology, FZD*
[4] *TU Dresden*

A Photo-Neutron Source for Time-of-Flight Measurements at the Radiation Source ELBE

J. Klug, E. Altstadt[1], C. Beckert[1], **R. Beyer,** H. Freiesleben[2], V. Galindo[1], M. Greschner[2], **E. Grosse** [also 2], **A. R. Junghans,** D. Légrády[1], B. Naumann[3], K. Noack[1], **G. Rusev, K.D. Schilling,** R. Schlenk[4], S. Schneider[4], K. Seidel[2], **A. Wagner,** F.-P. Weiss [1,also 2]

Submitted to Nucl. Instr. Meth. A

The radiation source ELBE at FZD uses the electron beam to produce various secondary beams. Electron beam intensities of up to $I_e = 1$ mA at energies up to $E_e = 10$ MeV can be delivered with a pulse width of 5 ps at FWHM.

With these parameters, the electron beam allows to generate sub-ns neutron pulses by stopping the electrons in a heavy (high atomic number) radiator and producing neutrons by bremsstrahlung photons through (γ,n) reactions. In order to enable measurements of energy-resolved neutron cross sections like (n,γ), (n,n$'\gamma$), (n,p), (n,α), and (n,f) at a time-of-flight arrangement with a short flight path of only a few meters, it is necessary to keep the volume of the radiator for neutron production as small as possible to avoid multiple scattering of the emerging neutrons, which would broaden the neutron pulses. It is the primary physics objective of this neutron source to measure neutron cross sections firstly for construction materials of fusion and fission reactors, for which it is important to select materials with low activation cross sections, and secondly for the handling of waste from such reactors, especially in order to find processes which transmute long-lived radioactive nuclides into short-lived and finally stable ones. Furthermore, experiments can be performed which address problems of nuclear astrophysics.

The power deposition of the electron beam in the small neutron radiator volume of 1 cm^3 reaches up to 25 kW. This is such a high power density that any solid high Z number material would melt. Therefore, the neutron radiator consists of liquid lead circulated by an electromagnetic pump. The heating power introduced by the electrons is removed through a heat exchanger in the liquid-lead circuit. Typical flow velocities of the lead are between 1 m/s and 5 m/s in the radiator section. From the thermal and mechanical point of view, molybdenum turned out to be the most suited target wall material in the region where the electrons impinge on the neutron radiator.

To reduce the radiation background at the measurement position, the neutrons are decoupled from the radiator at an angle of about 90° with respect to the impinging electrons. Particle transport calculations using the Monte Carlo codes MCNP and FLUKA predict a neutron source strength in the range of $7.9 \cdot 10^{12}$ n/s to $2.7 \cdot 10^{13}$ n/s for electron energies between $E_e = 20$ and 40 MeV. At the measuring place 3.9 m away from the radiator, a neutron flux of about $1.5 \cdot 10^7$ will be obtained. The short beam pulses allow for a neutron energy resolution better than 1 % for neutron energies between $E_n = 50$ keV and 5 MeV. The usable energies range up to about 10 MeV.

The complete setup has been installed in its final position in hall 123 of the ELBE building. The lead loop and the beamdump sit on a lifter that brings the device into position for the experiments, and that lowers it into a lead shield for radiation protection in the periods inbetween. The lifter was tested by raising and lowering it 40 times, giving deviations in vertical position of only 0.2-0.3 mm, and in horizontal position of 0.2 mm orthogonally to the electron beam and 0.7 mm in the direction of the electron beam.

Supplies of cooling water, argon, pressurized air and heating have been installed. The stainless-steel neutron beam collimator tube has been cast into the concrete wall between the halls 123 and 111c. Tungsten shutters to be used for sealing off the neutron beamline when using other experiment setups in hall 123 are under construction.

Several tests of filling and emptying the lead loop confirm the function of the valves, and a one-week uninterrupted run with heated lead demonstrates a stable mode of operation. An emergency shutdown was also successfully tested.

The hut containing the data-acquisition electronics is being installed on top of the experiment caves.

A comprehensive report on the technical aspects of the liquid-lead radiator is given in Ref.[1], while Ref. [2] accounts for simulations done to determine neutron beam characteristics and detector responses. The latter is also reported upon in another contribution to this annual report.

[1] A. Altstadt et al, A photo-neutron source for time-of-flight measurements at the radiation source ELBE, Ann. Nucl. Energy 34 (2007) 36

[2] J. Klug et al, Development of a neutron time-of-flight source at the ELBE accelerator, Nucl. Instr. Meth. A (to be submitted)

[1] *Inst. of Safety Research, FZD*
[2] *TU Dresden*
[3] *Department for Techn. Infrastructure, FZD*
[4] *Department of Research Technology, FZD*

Low-Energy Cross Section of the ^{7}Be(p,γ)^{8}B Solar Fusion Reaction from the Coulomb Dissociation of ^{8}B

F. Schümann, S. Typel, F. Hammache, K. Sümmerer, F. Uhlig, I. Böttcher, D. Cortina, A. Förster, M. Gai, H. Geissel, U. Greife, **E. Grosse**, N. Iwasa, P. Koczon, B. Kohlmeyer, R. Kulessa, H. Kumagai, N. Kurz, M. Menzel, T. Motobayashi, H. Oeschler, A. Ozawa, M. Ploskon, W. Prokopowicz, E. Schwab, P. Senger, F. Strieder, C. Sturm, S. Zhi-Yu, G. Surowka, **A. Wagner**, W. Walus

Published in Phys. Rev. C 73 (2006) 15806, 1-13

An exclusive measurement of the Coulomb breakup of ^{8}B into ^{7}Be + p at 254 A MeV was used to infer the low-energy ^{7}Be(p,γ)^{8}B cross section. The radioactive ^{8}B beam was produced by projectile fragmentation of 350 A MeV ^{12}C and separated with the FRagment Separator (FRS) at Gesellschaft für Schwerionenforschung in Darmstadt, Germany. The Coulomb-breakup products were momentum-analyzed in the KaoS magnetic spectrometer; particular emphasis was placed on the angular correlations of the breakup particles. These correlations demonstrate clearly that E1 multipolarity dominates within the angular cuts selected for the analysis. The deduced astrophysical S_{17} factors exhibit good agreement with the most recent direct ^{7}Be(p,γ)^{8}B measurements. By using the energy dependence of S_{17} according to the recently refined cluster model for ^{8}B of P. Descouvemont [1], we extract a zero-energy S factor of $S_{17}(0)=20.6 \pm 0.8(\mathrm{stat}) \pm 1.2(\mathrm{syst})$ eV b. These errors do not include the uncertainty of the theoretical model to extrapolate to zero relative energy, estimated by Descouvemont to be about 5%.

[1] P. Descouvement, Phys. Rev. C 70 (2004) 065802

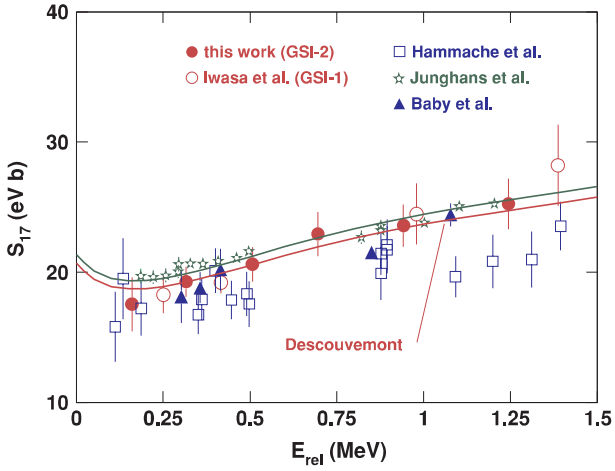

S_{17} from this work (filled circles) in comparison with direct measurements. The latter data were corrected for the contribution of the M1 resonance by the authors. The theoretical curves from [1] have been fitted to the most recent Seattle data (asterisks, upper curve) and the present data (lower curve).

Study of Radiative Proton Capture to the Ground State in ^{15}O

Gy. Gyürky[1], **M. Marta**, A. Formicola[2], **D. Bemmerer**, R. Bonetti[3], C. Broggini[4], F. Confortola[5], P. Corvisiero[5], H. Costantini[5], Z. Elekes[1], Zs. Fülöp[1], G. Gervino[6], A. Guglielmetti[3], C. Gustavino[2], G. Imbriani[7], M. Junker[2], A. Lemut[5], B. Limata[8], R. Menegazzo[4], P. Prati[5], V. Roca[8], C. Rolfs[10], C. Rossi Alvarez[4], E. Somorjai[1], O. Straniero[8], F. Strieder[10], F. Terrasi[9], H.P. Trautvetter[10]

Part of PhD thesis M. Marta

The previous LUNA studies of the ^{14}N(p,γ)^{15}O reaction have shown [1, 2, 3, 4] that the cross section at energies of astrophysical interest is a factor 2 lower with respect to the value adopted in the NACRE compilation, with significant astrophysical implications [5].
The main conclusion from the LUNA data has been confirmed by an independent study at higher energy [6]. However, a discrepancy amounting to 15 % of the total extrapolated S factor at energies corresponding to solar hydrogen burning remains between the R-matrix extrapolations of the different experiments [1, 6]. This discrepancy is due to the extrapolation of the capture to the ground state in ^{15}O, a transition that is strongly affected by interference effects between several resonances and the direct capture mechanism. Removing this discrepancy by precision cross section data would make it possible to study the solar center [7] by comparing the calculated flux of CNO neutrinos with the low energy neutrino data to be provided by the BOREXINO experiment at Gran Sasso.
A new experiment on ^{14}N(p,γ)^{15}O is currently underway, taking advantage of the uniquely low gamma-ray background for $E_\gamma \sim 7$ MeV [8] evident in the LUNA underground facility and of the segmentation of a Clover HPGe detector (see figure). The aim of this new study is to provide precision cross section data for the ground state capture at energies where the R-matrix fit can be effectively constrained.

[1] A. Formicola et al., Phys. Lett. B 591 (2004) 61
[2] G. Imbriani et al., Eur. Phys. J. A 25 (2005) 455
[3] A. Lemut et al., Phys. Lett. B 634 (2006) 483
[4] D. Bemmerer et al., Nucl. Phys. A 779 (2006) 297
[5] G. Imbriani et al., Astron. Astrophys. 420 (2004) 625
[6] R.C. Runkle et al., Phys. Rev. Lett. 94 (2005) 082503
[7] G. Fiorentini and B. Ricci, astro-ph/0310753 (2003)
[8] D. Bemmerer et al., Eur. Phys. J. A 24 (2005) 313
[9] Z. Elekes et al., Nucl. Inst. Meth. A 503 (2003) 580

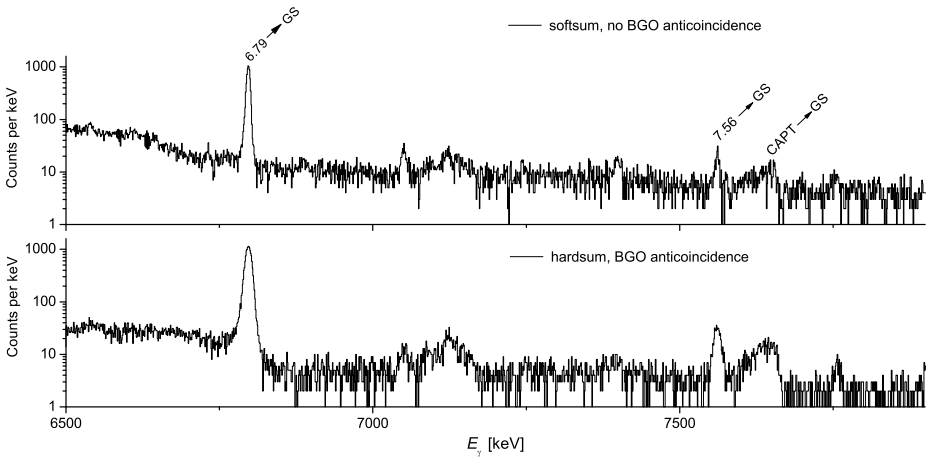

Gamma-ray spectra observed at LUNA with the ATOMKI Clover detector [9] above the $E = 259$ keV resonance. The software sum of the four segments (free running, softsum) is compared with the sum of the analog signals of the same segments (veto from the Clover BGO anticompton shield, hardsum).

[1] *Inst. of Nuclear Research (ATOMKI), Debrecen, Hungary*
[2] *INFN, Lab. Nazionali Gran Sasso (LNGS), Assergi (AQ), Italy*
[3] *Istituto di Fisica Generale Applicata, Univ. Milano, INFN Sezione Milano, Italy*
[4] *Istituto Nazionale di Fisica Nucleare (INFN), Sezione Padova, Italy*
[5] *Univ. Genova, INFN Sezione Genova, Italy*
[6] *Dipartimento di Fisica Sperimentale, Univ. Torino, and INFN Sezione di Torino, Italy*
[7] *Dipartimento di Scienze Fisiche, Univ. Napoli "Federico II", and INFN Sezione di Napoli, Italy*
[8] *Osservatorio Astronomico di Collurania, Teramo, and INFN Sezione Napoli, Italy*
[9] *Seconda Univ. di Napoli, Caserta, and INFN Sezione di Napoli, Italy*
[10] *Inst. für Experimentalphysik III, Ruhr-Univ. Bochum, Germany*

^{3}He(α,γ)^{7}Be cross section at low energies

Gy. Gyürky, F. Confortola, H. Costantini], A. Formicola, **D. Bemmerer**, R. Bonetti, C. Broggini, P. Corvisiero, Z. Elekes, Zs. Fülöp, G. Gervino, A. Guglielmetti, C. Gustavino, G. Imbriani, M. Junker, M. Laubenstein, A. Lemut, B. Limata, V. Lozza, **M. Marta**, R. Menegazzo, P. Prati, V. Roca, C. Rolfs, C. Rossi Alvarez, E. Somorjai, O. Straniero, F. Strieder, F. Terrasi, H.P. Trautvetter

Accepted in Phys. Rev. C (2007), nucl-ex/0702003

The flux of ^{7}Be and ^{8}B neutrinos from the Sun and the production of ^{7}Li via primordial nucleosynthesis depend on the rate of the ^{3}He(α,γ)^{7}Be reaction. In extension of a previous study [1] showing cross section data at 127 - 167 keV center of mass energy, the present work reports on a measurement of the ^{3}He(α,γ)^{7}Be cross section at 106 keV performed at Italy's Gran Sasso underground laboratory by the activation method. This energy is closer to the solar Gamow energy than ever reached before. The result is $\sigma = 0.567 \pm 0.029_{\rm stat} \pm 0.016_{\rm syst}$ nbarn. The data are compared with previous activation studies at high energy, and a recommended $S(0)$ value for all ^{3}He(α,γ)^{7}Be activation studies, including the present work, is given.

[1] D. Bemmerer *et al.*, Phys. Rev. Lett. 97 (2006) 122502

[2] J. Osborne *et al.*, Phys. Rev. Lett. 48 (1982) 1664 Nucl. Phys. A 419 (1984) 115

[3] R. Robertson *et al.*, Phys. Rev. C 27 (1983) 11

[4] B. N. Singh *et al.*, Phys. Rev. Lett. 93 (2004) 262503

[5] P. Parker and R. Kavanagh, Phys. Rev. 131 (1963) 2578

[6] K. Nagatani *et al.*, Nucl. Phys. A 128 (1969) 325

[7] H. Kräwinkel *et al.*, Z. Phys. A 304 (1982) 307

[8] T. Alexander *et al.*, Nucl. Phys. A 427 (1984) 526

[9] M. Hilgemeier *et al.*, Z. Phys. A 329 (1988) 243

[10] P. Descouvemont *et al.*, At. Data Nucl. Data Tables 88 (204) 203

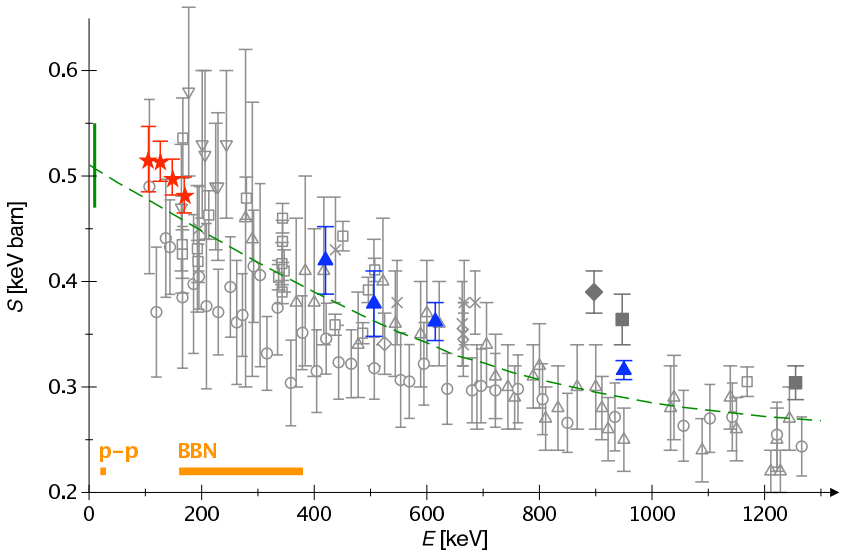

Astrophysical S factor for ^{3}He(α,γ)^{7}Be. Activation data: filled squares [2], filled diamonds [3], filled triangles [4], stars (present work and [1]). Prompt-γ data: triangles [5], inverted triangles [6], circles [7] (renormalized by a factor 1.4 [9]), squares [2], diamonds [8], crosses [9]. Dashed line: previously adopted R-matrix fit [10]. Horizontal bars: energies relevant for solar p–p hydrogen burning and for big bang nucleosynthesis.

Cooling Dynamics in Multi-Fragmentation Processes

T.X. Liu, W.G. Lynch, M.J. van Goethem, X.D. Liu, R. Shomin, W.P. Tan, M.B. Tsang, G. Verde, **A. Wagner**, H.F. Xi, H.S. Xu, W.A. Friedman, S.R. Souza, R. Donangelo, L. Beaulieu, B. Davin, Y. Larochelle, T. Lefort, R.T. de Souza, R. Yanez, V. Viola, R.J. Charity, L.G. Sobotka

Published in Europhys. Lett. 74 (2006) 806-812

Fragment energy spectra of neutron-deficient isotopes are significantly more energetic than those of neutron-rich isotopes of the same element. This trend is well beyond what can be expected for the bulk multi-fragmentation of an equilibrated system. It can be explained, however, if some of these fragments are emitted earlier through the surface of the system while it is expanding and cooling.

[1] W.A. Friedman, Phys. Rev. C, 42 (1990) 667
[2] W.P. Tan, et al., Phys. Rev. C, 68 (2003) 034609

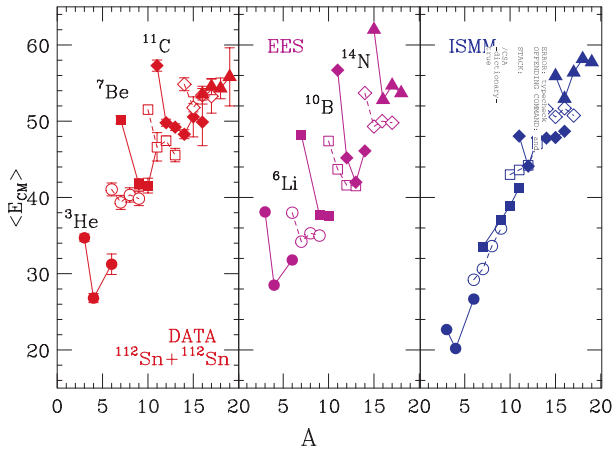

Left panel: experimental fragment mean kinetic energies. Middle panel: mean kinetic energies calculated with the EES[1] model. Right panel: mean kinetic energies calculated with the ISMM[2] model.

▷ Biostructures and Radiation

Secondary Structure and $Pd^{(II)}$ Coordination in S-Layer Proteins from *Bacillus Sphaericus* Studied by Infrared and X-Ray Absorption Spectroscopy

K. Fahmy, M. Merroun[1], K. Pollmann[1], J. Raff[1], **O. Savchuk**, C. Hennig[1], S. Selenska-Pobell[1]

Published in Biophys. J. 91 (2006) 996-1007 and Biotechnol. Adv. 24 (2006) 58-68

Abstract

The S-layer of *Bacillus sphaericus* strain JG-A12, isolated from a uranium-mining site, exhibits a high metal-binding capacity. This property has allowed the use of this and other S-layers as self-assembling organic templates for the synthesis of nano-sized heavy metal cluster arrays. However, little is known about the molecular basis of the metal protein interactions and their impact on secondary structure. We have studied the secondary structure, protein stability, and $Pd^{(II)}$ coordination in S-layers from the *B. sphaericus* strains JG-A12 and NCTC 9602 to elucidate the molecular basis of the metal nanocluster growth. Fourier transform infrared (FTIR) spectroscopy reveals similar secondary structures, containing $\approx 35\,\%$ β-sheets and little helical structure. pH-induced IR absorption changes of the side chain carboxylates evidence a remarkably low pK < 3 in both strains and a structural stabilisation when $Pd^{(II)}$ is bound. The COO– stretching absorptions reveal a predominant $Pd^{(II)}$-coordination by chelation / bridging by Asp and Glu residues. This agrees with XANES and EXAFS data revealing oxygens as coordinating atoms to $Pd^{(II)}$. The additional participation of nitrogen is assigned to side chains rather than to the peptide backbone. These side chains are thus prime targets for the design of engineered S-layer-based nanoclusters.

Results and Discussion

In the present study [1], extended X-ray absorption fine structure (EXAFS), X-ray absorption near edge structure (XANES), and FTIR spectroscopy were used to analyse the general features of the complexation of $Pd^{(II)}$ within the large number of binding sites of the native S-layer proteins of the strains *Bacillus sphaericus* JG-A12 and NCTC 9602. Specifically, the predominant chemical elements involved in the complexation are identified and their location within side chain or backbone groups is addressed. In addition, the secondary structure and pH-dependent structural transitions of these proteins were studied, because the organisms are specifically adapted to a low pH environment. Experiments were designed to investigate the function of carboxylates in metal protein interactions in these S-layers which are rich in Asp and Glu residues found to be specifically involved in metal protein interactions. Additional coordination by nitrogen is likely to also originate in side chain interactions rather than coordination to the peptide backbone.

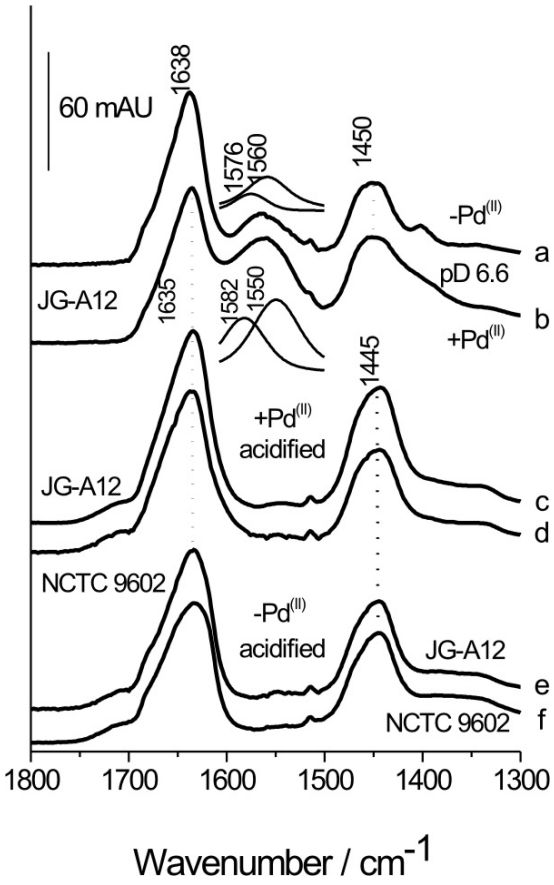

Fig. 1 *FTIR spectra of S-layers of B. sphaericus strain JG-A12 and NCTC 9602 measured in D_2O. a) Spectrum of JG-A12 at pH 7, metal-free. b) Spectrum of JG-A12 at pH 7, $Pd^{(II)}$-bound. Note the broadening of the 1400 cm^{-1} absorption (sym. COO– stretching) and the increase of the $\approx$1560 cm^{-1} absorption (antisym. COO– stretching) as compared to a). The antisymmetric COO- stretching modes where fitted by two components absorbing at 1576 and 1560 cm^{-1} (inset). Besides the strong absorption enhancement, the salient effect of $Pd^{(II)}$ binding is the 10ß,cm^{-1} downshift of the 1560 cm^{-1} absorption, whereas the upshift of the high frequency part is less pronounced. c) Absorption of JG-A12 in the $Pd^{(II)}$-bound state acidified with DCl. d) Absorption of NCTC 9602 in the $Pd^{(II)}$-bound state acidified with DCl. Note the absence of residual absorption in the 1560-1570 cm^{-1} range and the lack of pH sensitivity in the amide II' mode (1450 cm^{-1}) in c) and d) as compared to a) and b). e) Absorption of JG-A12 in the metal-free state acidified with DCl. f) Absorption of NCTC 9602 in the metal-free state acidified with DCl. Note the correspondence of the amide II' modes in c) and e) and in d) and f.*

[1] *Institute of Radiochemistry, FZD*

Fig. 1 shows the pH and Pd sensitivity of the antisymmetric carboxylate vibrations around 1560 cm^{-1} in D_2O, i.e. free of overlap from amide modes. The absorption intensity increases drastically upon $Pd^{(II)}$ binding and the centre of the antisymmetric stretching frequency shifts from 1567 to 1558 cm^{-1} in the S-layer of *B. sphaericus* JG-A12 (Fig. 2 (a) and (b)), characteristic of carboxylates that chelate a metal ion [2, 3, 4]. Thus, bidentate coordination appears to be the predominant $Pd^{(II)}$ binding mode in the S-layer of strain JG-A12. The lack of a significant shift of the antisymmetric COO^- stretching mode in NCTC 9602 suggests that a bridging coordination is more prevalent in this strain.

Fig. 2 shows the XANES regions of the XAS spectrum obtained with the $Pd^{(II)}$-bound S-layer from strain JG-A12 and for reference compounds containing two oxidation states of palladium: $Pd^{(II)}$ (PdO, $[Pd(NH_3)_4]Cl_2$, $PdCl_2$, Na_2PdCl_4) and metallic Pd (0.025 mm thick palladium foil). Comparison of the experimental spectrum to the reference spectra clearly shows that Pd is present as $Pd^{(II)}$ in the Pd-loaded S-layer protein sample because the two absorption maxima (ca. 24360 and ca. 24380 eV) characteristics of metallic Pd (feature marked (a) in Fig. 5) are absent. The fine structure of XANES of the Pd-loaded S-layer resembles that of $[Pd(NH_3)_4]Cl_2$ and PdO, indicating that Pd-O and Pd-N are the predominant bonds that contribute to the metal protein binding. The XANES data indicate that oxygen and nitrogen are the predominant groups that coordinate $Pd^{(II)}$ in the S-layer of JG-A12. Their relative contributions were calculated to correspond to a mixture containing 55 % of Pd-O and 45 % of Pd-N bonding.

In summary, we have shown that carboxylates of Asp and Glu residues exhibit an unusually low pK and are coordination sites for $Pd^{(II)}$ in the two related *B. sphaericus* strains JG-A12 and NCTC 9602 which become structurally stabilised by the heavy metal. Acidic amino acids and probably nitrogen-bearing side chains are thus prime targets for the site-directed modification of S-layer properties such as metal-binding capacity and secondary structure stability which are relevant to metallisation-based biotechnological applications.

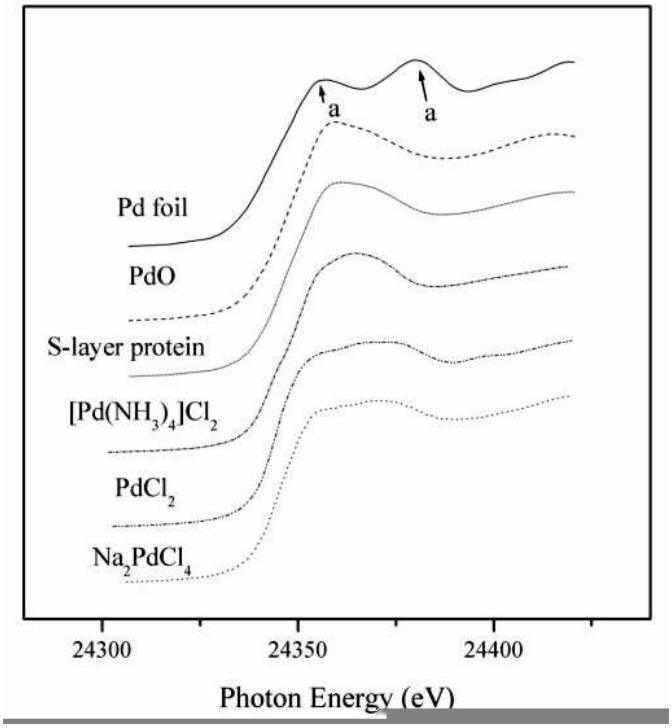

Fig. 2 *Pd K-edge XANES region of EXAFS spectra of Pd-loaded S-layer protein of B. sphaericus JG-A12 and reference compounds (Pd foil, PdO, Na_2PdCl_4, $[Pd(NH_3)_4]Cl_2$, and $PdCl_2$).*

[1] K. Fahmy, M. Merroun, K. Pollmann, J. Raff, O. Savchuk, C. Hennig, S. Selenska-Pobell, Biophys. J. 91 (2006) 996

[2] G.B. Deacon, R.J. Phillips, Coord. Chem. Rev. 33 (1989) 227

[3] M. Nara, M. Tasumi, M. Tanokura, T. Hiraoki, M. Yazawa, A. Tsutsumi, FEBS Lett. 349 (1994) 84

[4] M. Nara, M. Tanokura, T. Yamamoto, M. Tasumi, Biospectroscopy 1 (1995) 47

Linkage between the Intramembrane H-bond Network around Aspartic Acid 83 and the Cytosolic Environment of Helix 8 in Photoactivated Rhodopsin

N. Lehmann, U. Alexiev[1], **K. Fahmy**

Accepted for publication in J. Mol. Biol. (2007)

Abstract

Understanding the coupling between conformational changes in the intramembrane domain and at the membrane-exposed surface of the bovine photoreceptor rhodopsin, a prototypical G protein-coupled receptor (GPCR), is crucial for the elucidation of molecular mechanisms in GPCR activation. Here, we have combined FTIR- and fluorescence spectroscopy to address the coupling between conformational changes in the intramembrane region around the retinal and the environment of helix 8, a putative cytosolic surface switch region in class-I GPCRs. Using FTIR / fluorescence cross-correlation we show specifically that surface alterations monitored by emission changes of fluorescein bound to Cys^{316} in helix 8 of rhodopsin are highly correlated with (i) H-bonding to Asp^{83} proximal of the retinal Schiff base but not to Glu^{122} close to the β-ionone and (ii) with a MII-specific 1643 cm−1 IR absorption change, indicative of a partial loss of secondary structure in helix 8 upon MII formation. These correlations are disrupted by limited C-terminal proteolysis but are maintained upon binding of a transducin α-subunit ($G_{t\alpha}$)-derived peptide, which stabilizes the MII state. Our results suggest that additional C-terminal cytosolic loop contacts monitored by an amide II absorption at 1557 cm^{-1} play a functionally crucial role in keeping helix 8 in the position in which its environment is strongly coupled to the retinal-binding site near the Schiff base. In the intramembrane region, this coupling is mediated by the H-bonding network that connects Asp^{83} to the NPxxY(x)F motif preceding helix 8.

Results and Discussion

We have investigated the coupling of receptor domains in the hydrophobic core of rhodopsin to surface-exposed regions, particularly to the environment of helix 8 and its C-terminal extension [1]. Changes in the helix 8 environment where specifically monitored by emission from fluorescein linked to Cys^{316} in helix 8. The time evolution of the C=O stretching modes of protonated Asp^{83} and Glu^{122} after MII formation served as sensors of the relaxation of the internal H-bond networks in FTIR difference spectra recorded at defined time intervals after photoactivation. The fluorescence time trace recorded over 15 min was transformed in frequency domain and correlated pairwise with the transform of the absorption changes at each wavenumber using OPUS 2-D-correlation software.

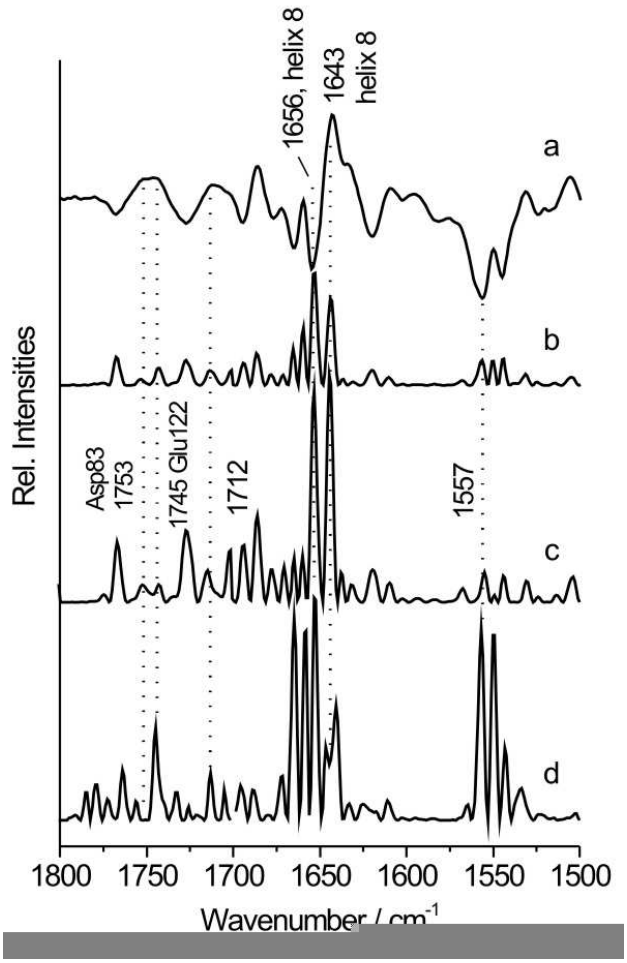

Fig. 1 *Cross-correlational analysis of IR-absorption changes with fluorescence emission from fluorescein at Cys^{316}. a) MII difference spectrum of fluoresceine-labeled WMs. b) Squared 2nd derivative of the spectrum in (a). Data evaluation is based on 2nd derivatives, which resolve overlapping bands. The 2nd derivatives were further squared to generate purely positive bands. c) Squared amplitudes of the synchronous correlation of fluorescence changes from the label in helix 8 with the temporal changes in the 2nd derivative IR spectra measured over 15 min. d) Squared amplitudes of the corresponding asynchronous correlation. The amplitudes, of the absorption changes above 1700 cm^{-1} have been enlarged by a factor of 10. Spectra are scaled such that $2 * R^{1/2}$ equals Δk in percent of k, with Δk the rate difference between fluorescence and IR-absorption change, k the average rate of both changes, and R the ratio of a peak in d) versus c). The tentative assignment of helix 8 bands correlated with the fluorescence of the label in helix 8 is indicated.*

[1] *FU Berlin*

Fig. 1 (c) and (d) display the squared synchronous and asynchronous spectrum, respectively, obtained. IR-bands that are strongly correlated with the emission of fluorescein at helix 8 exhibit a small or no amplitude in the asynchronous spectrum, but are present in the synchronous spectrum. Among the amide I modes, this is particularly the case for the MII-characteristic absorption at 1643 cm^{-1} (Fig. 4 (c) and (d)), which has the lowest ratio R of squared amide I amplitudes in the asynchronous versus the synchronous spectrum. It is thus caused by a secondary-structural change, which evolves in almost perfect concert with alterations in the molecular environment of Cys^{316}. This strong correlation is surpassed only by the absorption of the C=O stretching mode of Asp^{83} in MII (1750-1760 cm^{-1}), which is almost completely restricted to the synchronous spectrum. In contrast, the intensity in the absorption range of the C=O stretching mode of Glu^{122} (1740-1750 cm^{-1}) exhibits a 20-fold larger R than the 1643 cm^{-1} band. The temporal difference in the H-bond changes around the two carboxylates shows that they are (i) coupled to disjunct H-bond networks and (ii) they sample unsynchronized conformational relaxations in the respective protein domains. The kinetic distinction between both domains relative to the helix 8 environment suggests the existence of "modular reaction domains" with network-1 (connecting helices 1 (Asn^{55}), 2 (Asp^{83}), and 7 (Ala^{299}, Asn^{302})) being important for the long-range coupling of the retinal-binding site to a specific G-protein-activating interface. The cross-correlation data fully agree with peptide-derived models that employ partial unwinding of helix 8 during GPCR activation [2, 3], thus giving rise to the fluorescence change of the label and to the 1643 cm^{-1} absorption increase in MII and the corresponding loss of helical structure of the dark state accounting for part of the negative band at 1656 cm^{-1}.

The different correlations of the H-bonds to Asp^{83} and Glu^{122} with the fluorescence from the label in helix 8 is remarkable. We propose that the intramembrane H-bond network connected to Asp^{83} represents chromophore-protein interactions that are essential predominantly for transmitting intramembrane conformational changes to the cytosolic face via helix 8 movements and that Glu^{122} senses chromophore-protein interactions that are essential for specific retinal binding. The proposed distinction between mainly activity-promoting ligand protein interactions in the Asp^{83} / Schiff base environment and mainly specificity-defining interactions around the Glu^{122} / β-ionone ring agrees with the almost normal initial rate of MII formation in rhodopsin containing acyclic retinal[45] and is paralleled by the conservation pattern of the two carboxylic acids. Asp^{83} is strictly conserved throughout the rhodopsin-like class of GPCRs carrying the $NPxxY(x)_{5,6}F$ motif, whereas homologues of Glu^{122} are restricted to opsins. Thus, the linkage of the helix 8 environment to the H-bond network that contains Asp^{83} may represent a conserved functional connectivity from the ligand-binding site to the Gt-interacting domain in class I GPCRs.

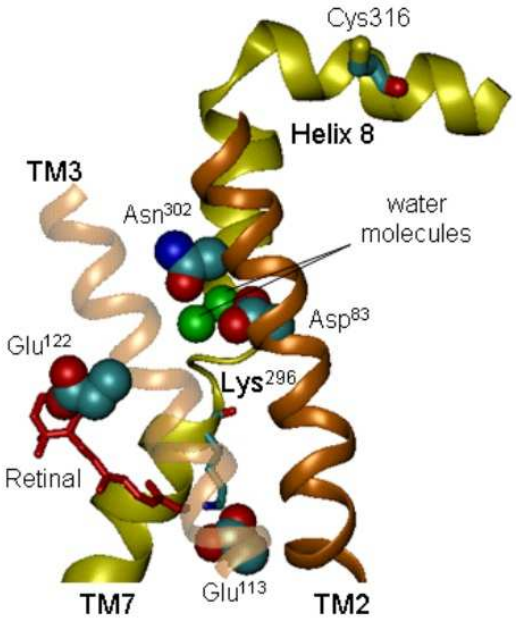

Fig. 2 *Rhodopsin structure showing the different intramembraneous regions sampled by the internal carboxylic acids Asp^{83} and Glu^{122}. The cross-correlation data indicate that the water molecules connecting Asp^{83} with Asn^{302} provide the critical H-bonds that couple the helix 8 environment through the $NPxxY(x)_{5,6}F$ motif to Asp^{83} in H-bond network-1, rather than to the H-bond network-2 around Glu^{122} in the vicinity of the β-ionone ring. TM designates the intramembraneous helices.*

[1] N. Lehmann, U. Alexiev, K. Fahmy, J. Mol. Biol. 2006 Dec 15; [Epub ahead of print]

[2] S. Mukhopadhyay, S.M. Cowsik, A.M. Lynn, W.J. Welsh, A.C. Howlett, Biochemistry 38 (1999) 3447

[3] S. Mukhopadhyay, H.H. McIntosh, D.B. Houston, A.C. Howlett, Mol. Pharmacol. 57 (2000) 162

Physical Properties of the Transmembrane Segment 3 of Rhodopsin

S. Madathil, G. Furlinski, K. Fahmy

Published in Biopolymers 82 (2006) 329-333

Abstract

Activation of G protein-coupled receptors (GPCRs) originates in ligand-induced protein conformational changes that are transmitted to the cytosolic receptor surface. In the photoreceptor rhodopsin, and possibly other rhodopsin-like GPCRs, protonation of a carboxylic acid in the conserved E(D)RY motif at the cytosolic end of transmembrane helix 3 (TM3) is coupled to receptor activation [1]. Here, we have investigated the structure of synthetic peptides derived from rhodopsin TM3. Polarized FTIR-spectroscopy reveals a helical structure of a 31-mer TM3 peptide reconstituted into PC vesicles and helical structure is also observed for the TM3 peptide in detergent micelles and depends on pH especially in the C-terminal sequence. In addition, the fluorescence emission of the single tyrosine of the D(E)RY motif in the TM3 peptide exhibits a pronounced pH sensitivity that is abolished when Glu is replaced by Gln demonstrating that protonation of the conserved Glu side chain affects the structure in the environment of the D(E)RY motif of TM3. The pH-regulation of the C-terminal TM3 structure may be an intrinsic feature of the E(D)RY motif in other class I receptors allowing the coupling of protonation and conformation of membrane-exposed residues in full length GPCRs.

Results and Discussion

In this study [2] the synthetic peptide TM3 (108-138), derived from helix 3 of rhodopsin was reconstituted in to large unilamellar PC vesicles and detergent micelles in which they exhibit typical alpha helical structure. The IR data gathered from the pH change of the TM3 peptide reveals that the amide 1 bond is found at $1655\,cm^{-1}$ with a slight shoulder at $1624\,cm^{-1}$ which is more pronounced at pH 8.8 than at pH 2. Acidic pH favors the helical content and the IR data imply the solvent accessibility of Glu^{134}, the only titratable group in the accessed range. The pH induced structural transition was further addressed by the fluorescence of Tyr^{136} in detergent solubilised TM3. The pH dependent spectral changes of Tyr^{136} were recorded and a pKa of 6 of the acid-induced decrease of tyrosine emission is found, whereas emission increases again below pH 4. The pH dependence is almost completely abolished when Glu^{134} is replaced by Gln. In combination with FTIR data, the results show that the conserved carboxylate is solvent-accessible in micelles and confers pH sensitivity to the TM3 peptide secondary structure specifically in the environment of the D(E)RY motif. In conclusion we have proved here that TM3 sequence forms an α-helix in the absence of helix packing interactions and the measured tilt of the helical axis argues that the C- and the N- termini localize at the lipid bilayer. The demonstrated protonation of Glu^{134} thus occurs at the hydrophobic / hydrophilic phase boundary in lipids or detergent micelles and in the latter the protonation state of Glu^{134} affects the neighboring tyrosine and stabilizes the helical TM3 structure. We hypothesize that the conserved hydrophobicity profile around the D(E)RY motif renders the carboxylate to be a critical side chain for the pH- dependent positioning of TM3 by generating a more contigious hydrophobic region at the TM3 C-terminus in the protonated site.

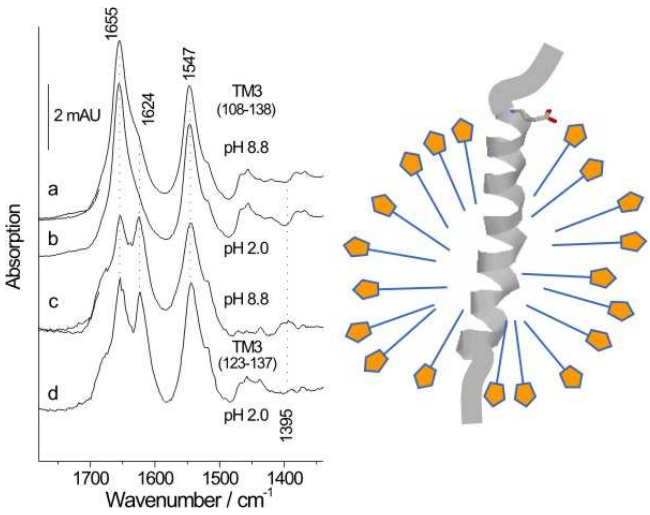

Fig. 1 *ATR-FTIR-spectra of detergent- solubilised TM3 peptides. TM3 of rhodopsin (108-138) in 5% dodecylmaltoside at pH 8.8 (a) and pH 2 (b). Absorption of a TM3 fragment (123-137) at pH 8.8 (c) and at pH 2 (d). The sketch to the right shows the proposed peptide structure in the micelle with the titratable carboxylate which induces local helicity upon protonation.*

[1] K. Fahmy, T.P. Sakmar, F. Siebert, Biochemistry 39 (2000) 10607-10612.

[2] S. Madathil, G. Furlinski, K. Fahmy, Biopolymers. 82 (4) (2006) 329-333

Structure-Function Relationship of Actin-Flavonoid Interactions

S. Madathil, K. Fahmy , M. Böhl[1], F. Pfennig[1], H.O. Gutzeit[1], S. Tietze[2], A. Sokoll[2], J. Apostolakis[3]

Submitted to Biophys. J.

Abstract

Flavonoids are secondary plant metabolites that have been widely studied because of their potential health benefits and their ubiquitous appearance in the human diet [1]. Based on the identification of actin as a target protein [2] for the flavonol quercetin, the biochemical parameters of this interaction were studied using fluorescence and infrared spectroscopy and the binding parameters of related flavonoids were compared. Furthermore, the potential biological relevance of the flavonoid/actin interaction in the cytoplasm and the nucleus was addressed using an actin polymerisation and a transcription assay, respectively. While flavonols inhibit actin functions, the structurally related epigallocatechin tends to promote actin activity in the two test systems. Infrared spectroscopy evidence suggests that flavonoid-specific conformational changes of actin mediate the different effects on its activity. Docking studies provide models of flavonoid binding and biological activity for the different known binding sites in actin.

Results and Discussion

In this study, the intrinsic quenching of tryptophan fluorescence of actin when treated with a set of flavonoids was used as a marker of actin-flavonoid complex formation. The data suggest that the actin forms stable complexes with flavonoids and the flavonoids from different subgroups show similar quenching efficiencies and exhibit K_d values that differ only by 10-30 % within and between subclasses depending on the specific hydroxyl group substitution pattern. A pyrenyl-actin-based fluorescence assay has been developed to study the influence of flavonoids on actin polymerisation. The magnitude of the effect of flavonoids on polymerisation and transcription follows the same order. The impact of two flavonols, quercetin and epigallocatechin exhibiting opposite effects in the actin polymerisation assays, on the conformational equilibrium and structural stability of actin under most native-like conditions was assessed by FTIR spectroscopy. The data show that both flavonols bind to actin in the ATP- and Ca^{2+}b-bound state and induce distinct and flavonol-specific structural changes. A detailed docking analysis using four different structures of actin [3] pointed out tetramethylrhodamine as a realistic candidate for flavonol binding in actin. Based on our results we show that structurally related flavonoids bind to actin and affect its biological function in a dose and structure dependent manner.

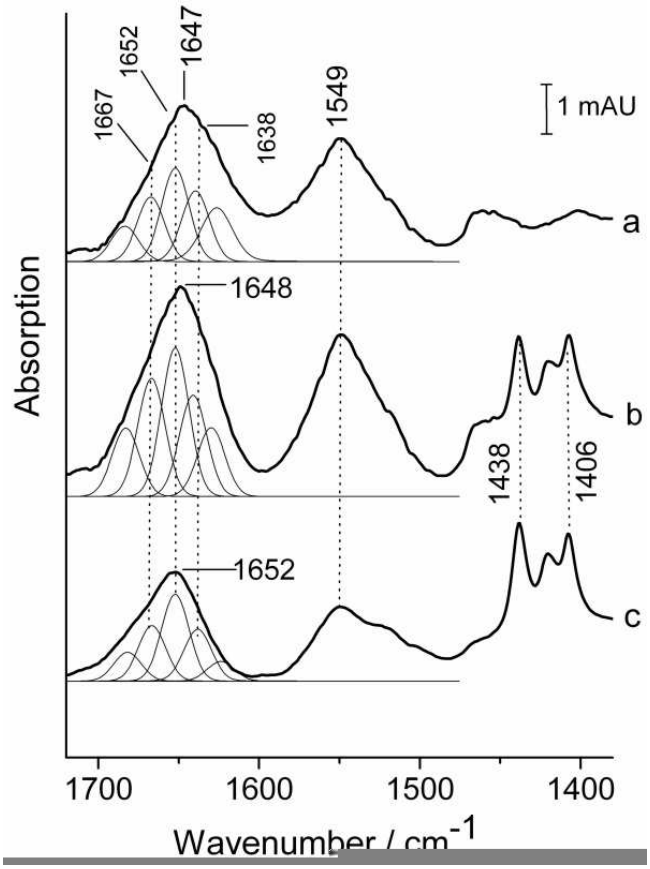

Fig. 1 *ATR-FTIR spectra in the amide I and II spectral range of free and flavanol-bound actin. (a) Actin in the absence of flavanols (b) Actin in the presence of 50 µM epigallocatechin. (c) Actin in the presence of 50 µM quercetin. The amide I contour was fitted by gaussian / lorentzian bands.*

[1] E. Middleton, C. Kandaswami, T.C. Theoharides, Pharmacol. Rev. 52 (2000) 673-751.
[2] M. Böhl, C. Czupalla, S.V. Tokalov, B. Hoflack, H.O. Gutzeit, Anal. Biochem. 346 (2005) 295-299
[3] D.S. Kudryashow, M.R. Sawaya, T.O. Yeates et al., PNAS 102 (2005) 13105-13110.

[1] *TU Dresden*
[2] *Ruhr Univ. Bochum*
[3] *Ludwig-Maximilians Univ. München*

Structural Properties of the Kinesin "Coiled-Coil Break 1" Region

S. Madathil, K. Fahmy , A.H. Crevenna[1], D.N. Cohen[1], J. Howard[1]

Submitted to Biophys. J.

Abstract

Kinesin-1 transports cargo along microtubules. In vivo, several kinesins move a single organelle and it is important that they operate in a coordinated fashion so that they do not interfere with each other. Coordination is thought to be facilitated by flexible domains. The tail of kinesin-1 is predicted to be a coiled-coil with two main interruptions, the swivel (380-442aa) and the hinge (560-624aa). In a gliding assay, [1] deletion of the swivel impaired motor cooperation at large kinesin densities. The torsion elasticity constant (k) was measured by analyzing the rotational random motion of microtubules tethered to a glass surface by single kinesin molecules. Removal of the swivel has no effect on the stiffness of the motor ($k = 7 \pm 1\, k_bT/rad$) nor has the removal of the hinge and subsequent tail domains ($k = 8 \pm 1\, k_bT/rad$) when compared to the full length ($9 \pm 3\, k_bT/rad$). The structure and thermal stability of the swivel region was studied by CD, FTIR, and fluorescence spectroscopy of model peptides. The data indicate the existence of secondary structure within the ≈50 central residues in the Swivel flanked by random stretches. Dimer formation between these more stable helical domains of the Swivel in the two kinesin heavy chains may account for the unexpected large torsional rigidity of the Swivel observed here at the single molecule level. We propose that the localized helical propensity in the swivel provides a mechanism for a reversible structural transition that generates the required flexibility at high motor densities by strain-dependent helix unwinding.

Results and Discussion

The functional studies carried out in this project convincingly show that the Coiled-Coil Break-1 behaves differently from what is expected for a disordered structure: (1) its torsion elasticity is higher than predicted by the WLC model, (2) its deletion doesn't cause an increase of stiffness. These results suggest that a certain degree of secondary and / or tertiary structure may be present in this region which was experimentally demonstrated by the structural studies on the five 30 aa long overlapping pieces of synthetic model peptides derived from this region. CD spectroscopy at 20°C revealed that the peptides 3 and 4 (corresponding to the central part of Coiled-Coil Break-1) show characteristic α-helical far UV-CD spectra and display the greatest molar ellipticity corresponding to around 70% total helical content. Peptide 1 and 5 have a low percentage of helicity and peptide 2 is the most unstructured one, supporting previous findings. The FTIR data of the most helical peptides 3 and 4 suggest that these helices form coiled-coils [2]. The energetics of the structural transitions of the model peptides, addressed by fluorescence-based thermal unfolding experiments, is in full agreement with the presence of defined secondary structure demonstrated by CD and FTIR spectroscopy. Based on the ensemble of our functional and structural studies we suggest that only at high motor densities the strain exerted on the swivel induces the transition of the structured regions from helical to disordered stretches, thereby providing the required flexibility in a function-dependent manner.

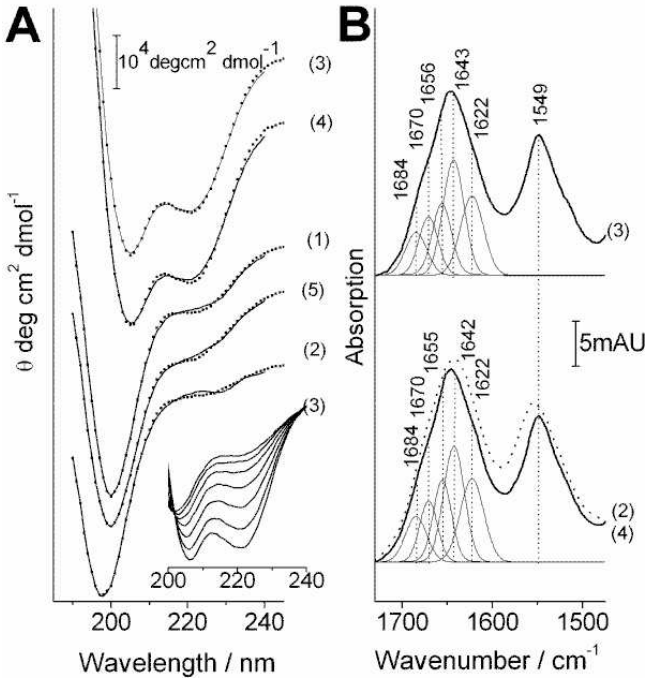

Fig. 1 *(A) CD spectra of the 5 model peptides at 20°C and the inset shows the CD spectra of peptide 3 from 2-60°C. (B) FTIR spectra of peptide 3 and 4 which form coiled coils and of peptide 2 which is unstructured.*

[1] J. Howard, A.J. Hudspeth, R.D. Vale, Nature. 342 (1989) 154-158

[2] S. Krimm, J. Bandekar. Adv. Prot. Chem. 38 (1986) 181-236

[1] *MPI-CBG Dresden*

Dynamics of FEL-Light-Induced Changes in Thin DNA Films Observed by Brewster Angle Microscopy

M. Sczepan, G. Furlinski, D. Wohlfarth, W. Seidel, K. Fahmy

Abstract

The function of biopolymers is determined by their structural dynamics. Investigation of the structural dynamics is thus important for understanding the processes and superstructures involved in the function of biomolecules. A large number of superstructures is particularly important for DNA function. Our experiments aim at the induction and kinetic analysis of the IR-induced transitions between such states.

In order to observe changes induced in thin DNA films by FEL irradiation, Brewster angle microscopy, which is a proven technique for the evaluation of thin organic films [1] has been employed. If a sample is observed under Brewster angle conditions, small changes in the refractive index of the surface can be detected and thus thin layers on the surface of a substrate or liquid can be made visible. Small changes in the refractive index and thickness of a thin film as a result of structural transitions will induce changes in the reflectivity of the film.

Results and Discussion

Experiments have been performed using thin layers of DNA (pUC21 plasmid DNA, PlasmidFactory) on ZnSe and CaF_2 substrates. The thickness of the layers has been estimated to be 50-800 nm by interference fringe counting in combination with absorbance measurements. These samples were irradiated with FEL light at different wavelengths. Fast changes of reflectivity - following the temporal structure of the FEL light intensity which are followed by slow relaxation processes ($\approx$ 30 ms) were observed (see Fig. 1). Experiments to determine the influence of the micropulse energy (20-100 nJ), film thickness, macro bunch length (200-1200 μs) and humidity have been performed and revealed a strong influence of these parameters on amplitudes and time constants of the reflectivity variations.

Analysis of the data for films of different thicknesses - especially for films with thicknesses between 50 nm and 150 nm - reveal that changes in the reflectivity on the longer time scale are the result of a decrease in the refractive index of the sample while the fast ($< 30\,\mu$s) changes can be attributed to variations (increase followed by decrease) of film thickness due to heating. A model for the heat transport in the sample has been established, allowing the estimation of the temperature reached in the sample as a function of film thickness and pump power. Estimated temperature jumps were found to be in the 50-500 K range with the equilibrium temperature established within less than 50 μs. For high film thicknesses and pump intensities resulting in high film temperatures, a more complex behaviour of the reflectivity was observed. In this case, thickness changes - probably as a result of variations in sample hydration - seem to contribute to the slow changes in reflectivity. The changes in the refractive index of the sample can be the result of structural changes (base pair stacking, strand opening [2]) as well as of variations in the hydration state of the DNA [3]. In summary, we have shown that FEL-pulses can induce rapid DNA melting, allowing to observe base pair separation and annealing with a time resulution not accessible by conventional experiments on DNA-structural transitions.

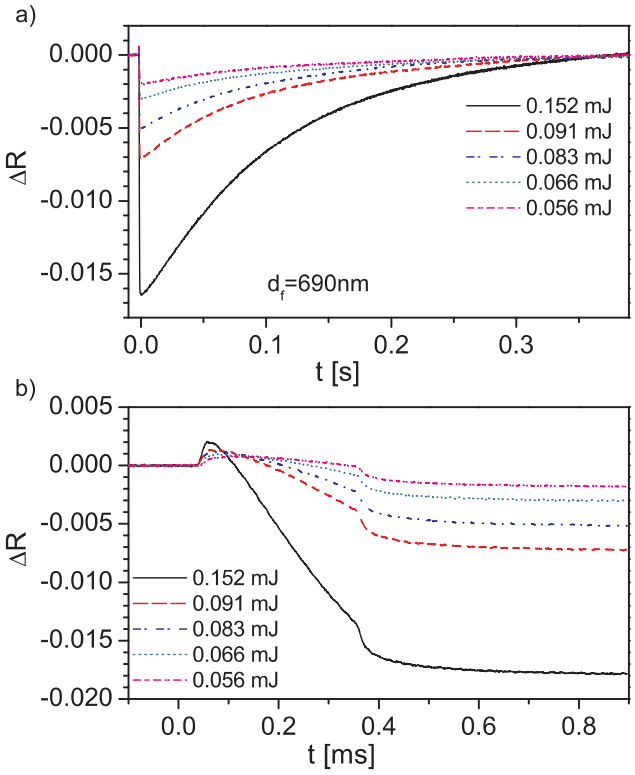

Fig. 1: *Change of reflectivity of a DNA film (thickness 690 nm) during and past FEL irradiation in long (a) and short (b) time scale as a function of light intensity/macro bunch energy.*

[1] S. Hénon, J. Meunier, Rev. Sci. Instr. 62 (1991) 936

[2] S. Elhadj, G. Singh, R. Saraf, Langmuir 20 (2004) 5539

[3] S. Weidlich, S.M. Lindsay, A. Rupprecht, Biopolymers 26 (1987) 439

Identification of Actinide Molecule Complexes by Vibrational Photothermal Beam Deflection Spectroscopy

H. Foerstendorf[1], K. Heim[1], **W. Seidel**, G. Bernhard[1]

Accepted for publication in J. Nucl. Mat. (2007)

Abstract Photothermal Beam Deflection (PTBD) spectroscopy in the infrared region combines the low detection limits, the surface selectivity of photothermal methods [1, 2] and vibrational spectroscopic information of the sample under investigation [3]. We present first results of model samples containing actinide molecule complexes obtained by PTBD using an FEL as a coherent pump source. The spectra are compared with those obtained by Fourier-transform infrared (FT-IR) spectroscopy.
The setup of the PTBD-FEL experiment is described elsewhere [4]. All samples were prepared as KBr pellets as typically used for FT-IR spectroscopy. PTBD absorption spectra and FT-IR transmission spectra represent the average of 128 scans for each data point and spectrum, respectively. Spectral resolution was 2 - 3 cm^{-1} for PTBD (depending on wavelength) and 4 cm^{-1} for FT-IR spectroscopy.

Results and Discussion The infrared spectra of a Np(V)nitrate test sample in the spectral region (880 - 680 cm^{-1}) where the ν_3 mode of the NpO_2^+ cation can be expected are shown in Fig. 1. A comparison of the spectra demonstrates the high accuracy which can be achieved by the PTBD technique in the infrared region. In this spectral range the ν_2 and ν_4 modes of the nitrate group generally show up as well. In fact, the spectra show three partially overlapping bands at 839, 820 and 755 cm^{-1}. Today only a tentative assignment of the bands can be given. From Raman spectroscopic investigation [5] we assign the band at 820 cm^{-1} to the ν_3 mode of the NpO_2^+ cation. Consequently, the bands at 839 and 755 cm^{-1} have to be assigned to the ν_2 and ν_4 mode of the nitrate group, respectively.
Fig. 2 presents the spectra of the KBr pellets containing the lowest concentrations of $UO_2(NO_3)_2{\cdot}6H_2O$ which provide a clear vibrational UO_2^{2+} band obtained by PTBD and FT-IR spectroscopy. Again the high accuracy of the spectra demonstrates the applicability of the PTBD technique to identify actinide molecule complexes in solid samples. Although it has been shown that photothermal spectroscopy is capable of measuring absorptions below 10^{-6} [1] the dynamic reserve of the PTBD technique in our FEL experiment is in the same order of magnitude as for FT-IR spectroscopy since no well-defined absorption bands of the ν_3 uranyl mode were observed at lower concentrations (data not shown). The limitations are obviously set by the KBr matrix which shows a background absorption over the whole spectral range most probably due to residual water and other possible impurities. However, the quantity of the actinide and the dimension of the sample which is necessary for generating a significant deflection signal is considerably reduced in the PTBD experiment due to its geometrical setup. The generation of the thermal wave and of the deflection signal occurs next to the surface of the sample. This potentially provides access to investigations of natural mineral surfaces in future times.

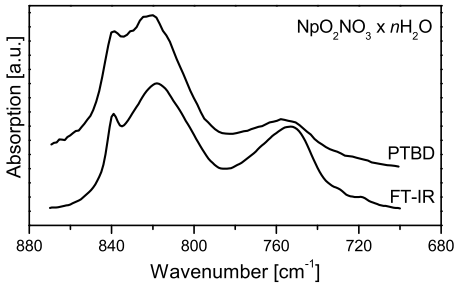

Fig. 1 *Infrared spectra of the ν_3 mode region of the neptunyl(V) cation measured by PTBD (upper trace) and FT-IR (lower trace).*

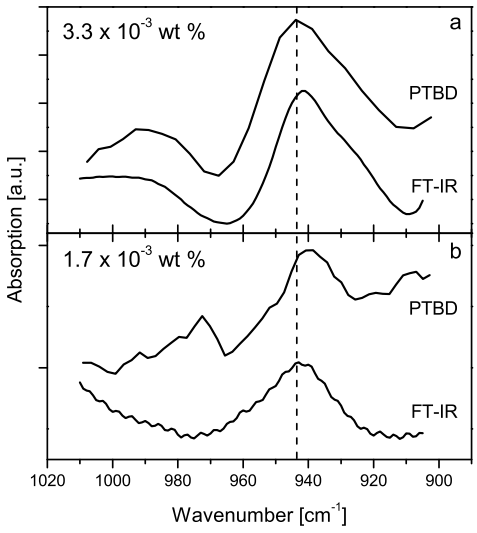

Fig. 2 *PTBD (upper traces) and FT-IR (lower traces) spectra of the ν_3 mode region of the uranyl(VI) cation at different concentrations of $UO_2(NO_3)_2{\cdot}6H_2O$. (a): 3.3 $\cdot 10^{-3}$ wt % ($\approx$ 150 μM); (b): 1.7 $\cdot$ 10^{-3} wt % ($\approx$ 75 μM).*

[1] T.D. Harris et al., Appl. Spectrosc. 39 (1985) 28
[2] M. Commandre et al., Appl. Optics 35 (1996) 5021
[3] W. Seidel et al., Eur. Phys. J-Appl. Phys. 25 (2004) 39
[4] H. Foerstendorf et al., J. Nucl. Mat. (2007) in press
[5] A.C. Gregoire-Kappenstein et al., Radiochim. Acta 91 (2003) 665

[1] *Institute of Radiochemistry, FZD*

Remote Controlled IR-Diagnostic Station for the Rossendorf FELs

W. Seidel, R. Jainsch[1], M. Justus, K.-W. Leege[1], D. Proehl[1], H. Weigelt, **D. Wohlfarth**

Part of Diploma thesis H. Weigelt

Starting in the summer 2005, FEL beam time has been offered to external users in the frame of the EC funded "Integrating Activity on Synchrotron and Free Electron Laser Science" (FELBE project [1]). It is of great importance for routine user operation at ELBE that, after changing the beam path or after beam interruptions stable operation in all wavelength ranges can be provided within a short time (some minutes). Extensive diagnostics for the optical components of the FEL are very important to achieve fast availability.

We have developed an optical beam diagnostic system (see Fig. 1) to properly characterize and adapt the output of the two FELs (U27 and U100). The present system is compatible with a tuning range from 3 μm to 150 μm, and can be extended beyond 150 μm, if necessary.

The FEL beam from each undulator will be transported separately from the resonator to the diagnostic area through beam pipes using reflective optics. Both lines will be merged on the diagnostic table, which may be purged with dry nitrogen to avoid absorption in air, if necessary. From here both beams follow the same path.

Two flipper mirrors may deflect the beam in a bypass to a plasma switch which reduces the repetition rate from 13 MHz down to 1 kHz (first results see [6]). The switch is based on the principle of photo-induced reflectivity of an optically excited electron-hole plasma [2, 3]. In this way, subsequent FEL micropulses are selected out of the 13 MHz pulse train. An additional focusing mirror ensures the same beam parameters as the direct beam has.

From the main beam, approximately 1-5 percent of the total power is separated by a scraper mirror on a translation stage for wavelength measurement and power monitoring.

The transmitted beam passes an attenuator and can be delivered to 6 optical laboratories. In this attenuator precisely fabricated metal grids diffract a calibrated percentage of power (3, 5, and 3 $\times$ 10 dB) out of the beam. The rejected light is absorbed in the walls of the housing. The mode structure and other properties of the transmitted beam including the divergence and the M^2 parameters are fully preserved, the polarisation as well [7]. Finally, a non-collinear background-free autocorrelator system is used to determine the length of the ultrashort FEL pulses. We use a CdTe crystal as SHG medium [2, 5] since it is transparent for a wide wavelength range in the infrared.

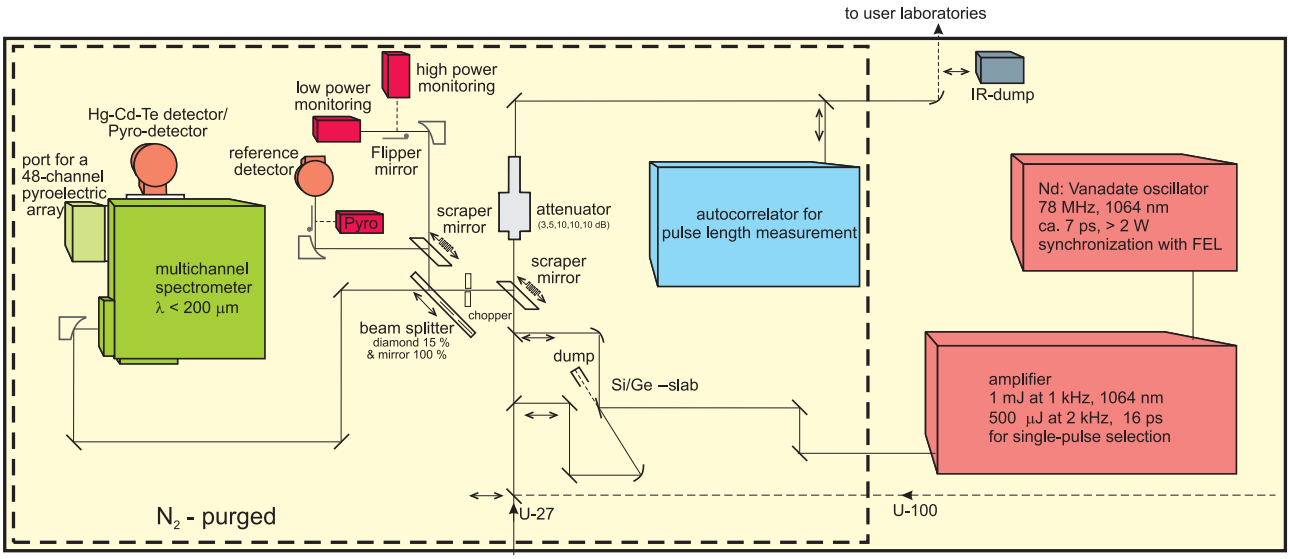

Fig. 1 *Arrangement of the different optical components and devices on the table.*

[1] *Department of Research Technology, FZD*

The part of the beam deflected by the scraper mirror goes through a synchronized chopper for measurement in CW-mode. Next to this, the outcoupled beam is deflected by a mirror or a diamond beam splitter (350 μm thick, under 45 degrees, deflection 15 %) at a pneumatic translation stage (this part of the diagnostic is described in detail in [8]). The beam transmitted through the diamond beam splitter (85 %) is transported to the spectrometer. The spectrum is measured with a Czerny-Turner type spectrometer which contains a turret with three different gratings to cover the whole wavelength range from 3 μm to about 200 μm. In the near future the monochromator will be equipped with a 48-channel pyroelectric linear array detector. We use the second side-exit slit equipped with a single Hg-Cd-Te or Ge-Ga detector for measurements with higher sensitivity.

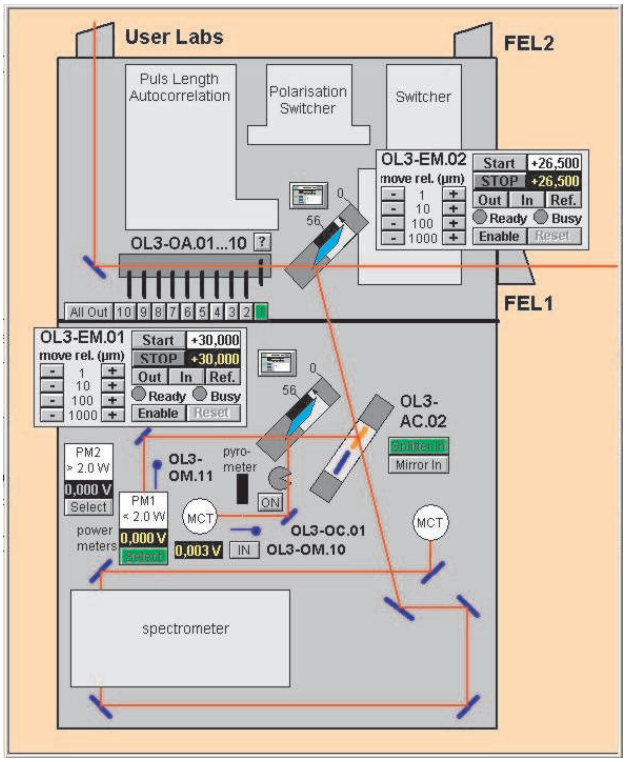

Fig. 2 *Interface of the remote controlled part of the IR-diagnostic station. One attenuator, two scraper mirrors on stepper controlled stages, one mirror and one beam splitter on a common pneumatic stage, spectrometer and different power meters are indicated. The lines show different paths for the radiation when both scraper mirrors are not entirely within the beam.*

The part reflected from the pneumatic device is distributed with another scraper mirror and two flipper mirrors to different power meters (<2 W and >2 W) and reference detectors (Hg-Cd-Te and pyro-detectors) for monitoring the lasing process (see Fig. 2).
The FEL diagnostic instrumentation has been integrated into the existing Programmable Logic Control (PLC) and Human-Machine-Interface (HMI) environment of ELBE (see Fig. 3). It ensures the access both for operators and users of the FEL. The basic technologies are the WinCC server/client system, the SIMATIK PLC system and distributed I/O by Beckhoff Automation for controlling the pneumatic components (i.e. attenuators), analogue data logging (FEL power, MCT) and other instrumentation. The stepper control drivers for the scraper mirrors are integrated system components, whereby expensive separate controllers could be avoided.

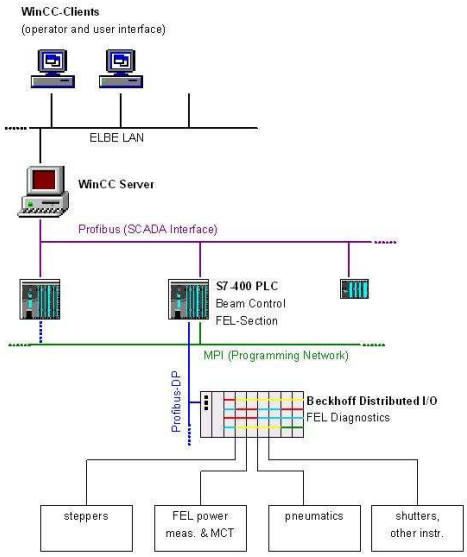

Fig. 3 *The programmable Logic Control (PLC) and Human-Machine-Interface (HMI) environment of ELBE with the integrated FEL diagnostics instrumentation*

[1] http://www.fzd.de/felbe
[2] J. Xu et al., Opt. Comm. 197 (2001) 379
[3] P. Haar, Ph.D. thesis, Stanford University (1996)
[4] E.H. Haselhoff et al., Nucl. Instr. and Meth. A 358 (1995) ABS28
[5] W. Seidel and D. Stehr, this Report, p. 78
[6] W. Seidel and S. Winnerl, this Report, p. 74
[7] F. Keilmann, SPIE Vol. 666 (1986) 213
[8] H. Weigelt, Diplomarbeit, Hochschule Mittweida, 2006

Extraction of Single FEL Radiation Pulses Using a Laser-Activated Plasma Switch

W. Seidel, S. Winnerl[1]

In order to decrease the average radiation power of the Rossendorf free-electron laser FELBE (FELBE project [1]), as required for certain experiments (high pulse energies but moderate or low average power), the FEL repetition rate can be reduced from 13 MHz to 1 kHz. To this end, plasma switching of FEL radiation pulses was demonstrated for cw operation.

The plasma switch is based on the principle of photo-induced reflectivity by an optically excited electron-hole plasma [2, 3]. Germanium serves as semiconductor material for the switch. The semiconductor was illuminated by a Nd:YAG laser amplifier system (1 kHz, λ = 1064 nm, $\tau \sim$ 16 ps, <1 Watt), generating an electron-hole plasma at the front surface of the semiconductor. The generation of a sufficient plasma density leads to a variation of the optical semiconductor properties for the infrared FEL-radiation (strongly focused and under Brewster's angle of 76°). For realizing the pulse selection the frequencies of both laser sources (FEL and Nd:YAG) were synchronised with RF electronics. For the exact timing of both laser pulses, when they hit the semiconductor, they were detected with a photon-drag detector or a fast pyroelectric detector (FEL) and a photo diode (Nd:YAG) and were adjusted on each other with cables, phase-shifter (trombone) and through moving a precision linear stage. Fig. 1 shows the experimental set-up. A gold mirror served as a reference for determining the reflectivity of the Germanium. The selected FEL pulses were detected by a fast MCT detector with a bandwidth of 20 MHz. Fig. 2 shows the switched pulse in two amplitude scales. The signal from the switch laser (photo diode) is shown in red. From the comparison of the black and blue curves we obtained an amount of dark pulses in the switched beam of about 0.5 % due to the angle of beam spread from the focussing. The time-resolved measurement of the reflectivity yields an exponential decay with a time constant of 590 ps. For the highest value of the Nd:YAG laser amplifier peak fluence of 25 mJ/cm^2, a reflectivity of Ge for FEL radiation ($\lambda = 11\mu m$) of 100 % was achieved (see Fig. 3). We thus succeeded to extract single FEL radiation pulses out of the 13 MHz pulse train, indicating that this plasma switch is most suitable for the Rossendorf FEL. Further examinations will concentrate on achieving similar results for shorter wavelength. To integrate this plasma-switch into the existing diagnostic station we have to build an additional by-pass to the Germanium or Silicon slab which is under Brewster's angle (see [4]). The selected micro pulse will be refocused to the waist parameters outside of the by-pass line and transported to the user stations.

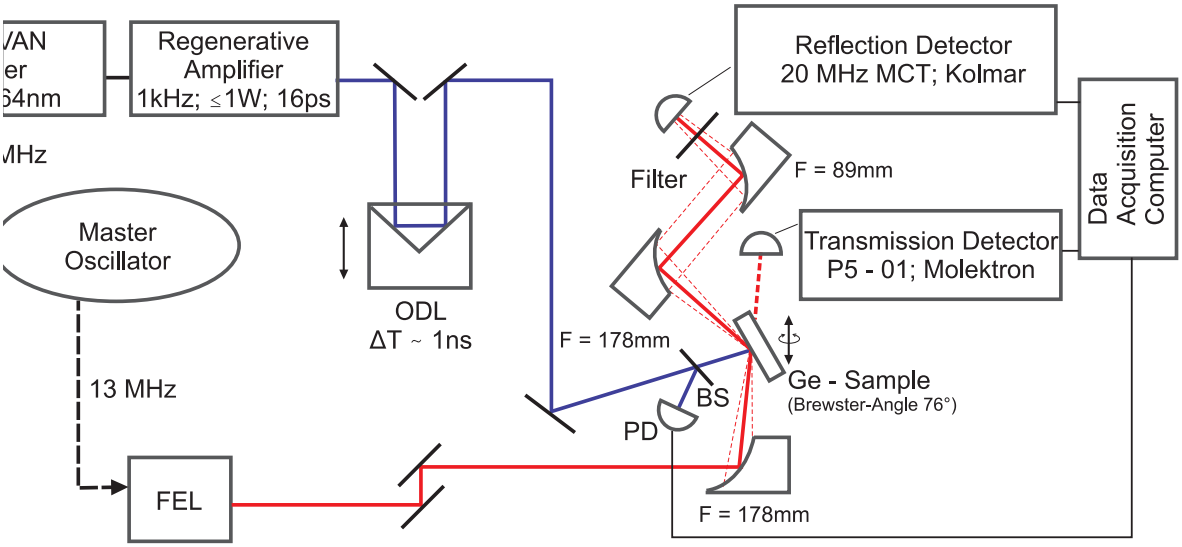

Fig. 1 *Setup for the plasma switch (for details see above)*

[1] *Inst. of Ion Beam Physics and Materials Research, FZD*

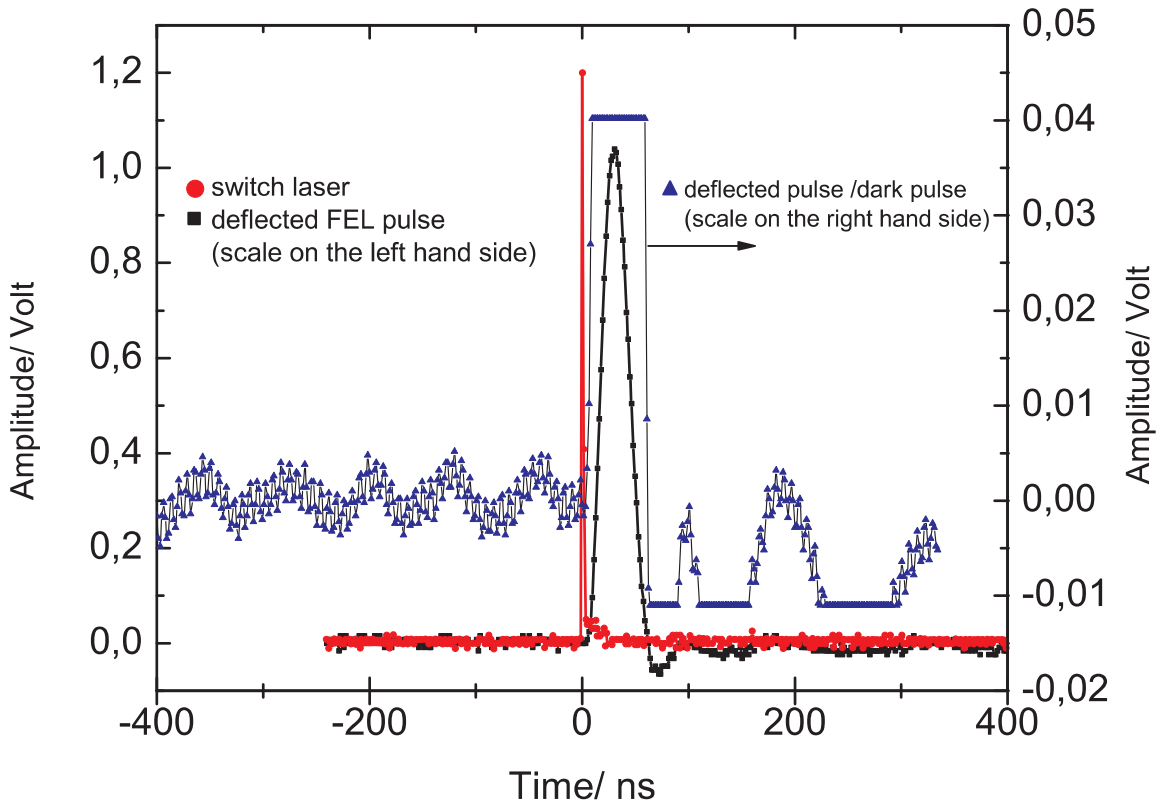

Fig. 2 *The switched FEL pulse at 11 μm in two different amplitude scales is measured by a fast MCT detector with a bandwidth of 20 MHz. The signal from the switch laser (photo diode) is shown in the curve with circles. From the comparison of the curve with squares and curve with triangles we obtain an amount of dark pulse in the switched beam of about 0.5%.*

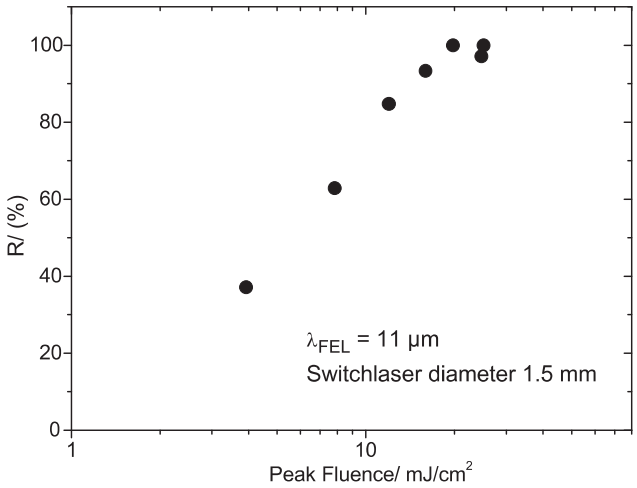

Fig. 3 *Dependence of reflectivity on the pump-laser peak fluence.*

[1] http://www.fzd.de/elbe

[2] P. Haar, Ph.D. thesis, Stanford University (1996)

[3] E.H. Haselhoff et al., Nucl. Instr. and Meth. A358 (1995) ABS28

[4] W. Seidel et al., this Report, p. 72

The IR Beam Line from the FELs to the High Magnetic Field Laboratory

W. Seidel, A. Winter[1], **R. Wünsch**, S. Zvyagin[2]

An infrared (IR) beam line has been designed which connects the two free-electron lasers (FEL) in the ELBE building [1] with the experimental high magnetic field setup located in the building of the Dresden High Magnetic Field Laboratory (HLD) of the Forschungszentrum Dresden - Rossendorf.

The ELBE FELs produce short, a few picosecond long pulses with a repetition rate of 13 MHz in the medium- and far-infrared region (between 3 and 200 μm). The repetition rate can be reduced down to 1 kHz. The average radiation power does not exceed a few tens of Watts. The light is linearly polarized. Owing to the large wavelength range we use reflective optics with metal mirrors (gold coated copper or stainless steel). Their reflectivity is larger than 97.5% in the operated wavelength range.

The ELBE-HLD beam line is one of the branches of the general line which delivers the laser light from the IR FELs in the ELBE building to several user laboratories [2]. The beam is guided in pipes which are either evacuated or purged with nitrogen gas. It starts at the outcoupling holes of the resonator mirrors of the U100- and U27-FEL, respectively. The size of the outcoupling holes can be varied. Hole diameters of 2, 4.5 and 7 mm are available for the U100-FEL, while 1.5, 2, 3 and 4 mm holes can be used at the U27-FEL. The beam line has to be adapted to the different outcoupling holes and to the resulting beam divergence which, in addition, depends strongly on the wavelength of the beam. Positions and focal lengths of the used mirrors have been determined to achieve better propagation conditions of the light inside the pipe (including passing through several bottlenecks, e. g. at the window between the preparation room and the magnet lab, waists in the HLD building, etc.). We use the Method of the Equivalent Gaussian Beam [3] to calculate the propagation of radiation along the beam line. Beam radii w are calculated according to the Gaussian beam propagation laws.

First, the beams are transported from the outcoupling holes using separate lines to a diagnostic table in the neighboring room (see Fig. 1). The beam profile has a waist on the diagnostic table. Waist size and position are the same for beams coming from both FELs. The waist position is independent of the wavelength, but the size is proportional to the diameter of the outcoupling hole. The narrow beam size in the vicinity of the waist is used for various beam measurements and modifications. Behind the diagnostic table the beam is distributed between user laboratories using one line. By inserting the plane mirror MH1 into the beam line the beam is becoming bent down to a specific line, guiding the beam via mirrors MH2 - MH4 into a tunnel (27 m long) on the basement level and connecting the ELBE building with the HLD. At the tunnel entrance, the beam is refocused (MH4), becoming a nearly parallel beam. However, diffraction effects increase the IR-beam size much stronger than for visible light. Thus, towards the end of the tunnel the pipe diameter has to be increased to 20 cm. The beam size calculated along the beam line is illustrated in Figs. 2 and 3.

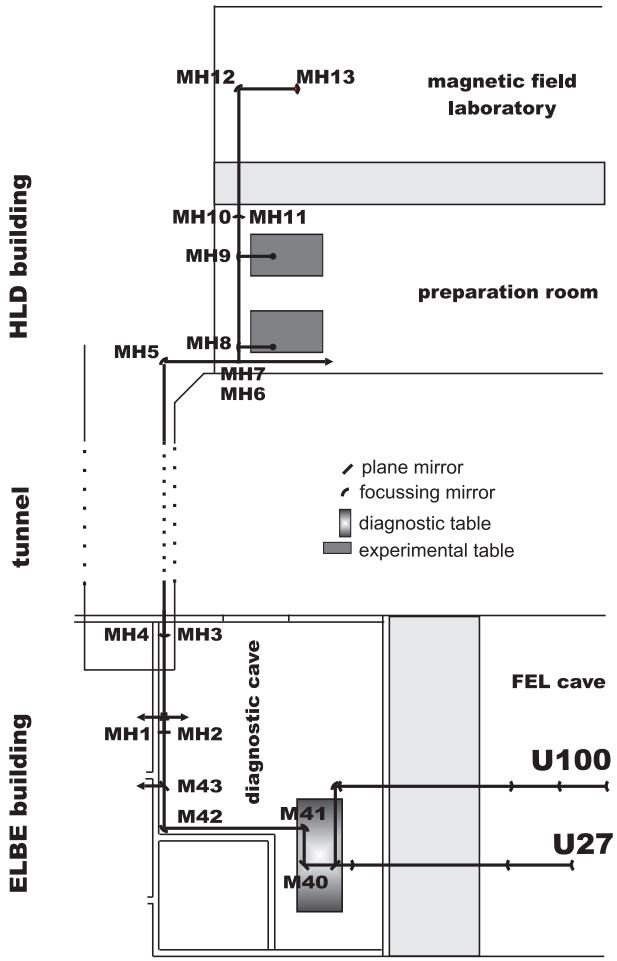

Fig. 1 *Top view of the beam line from the U100 and U27 FEL in the ELBE building to user stations in the HLD building via diagnostic table and tunnel.*

In the HLD building, the beam has to be deflected within shorter distances. The deflecting mirrors can be used to refocus the beam and to keep the necessary pipe diameter at 10 cm. We assume that a diameter of 3*w is sufficient in this branch of the beam line. Behind the mirror MH5 at the end of the tunnel the beam size decreases clearly. Mirror MH6

[1] *Department of Research Technology, FZD*
[2] *Dresden High Magnetic Field Laboratory (HLD), FZD*

focuses the beam additionally, and deflects it upwards to the experimental preparation room in the ground floor. This mirror can be removed to guide the beam to other laboratories in future. Mirror MH7 brings the beam into horizontal direction 108 cm above floor level. Two removable focusing mirrors (MH8, MH9) allow to deflect the beam to an experimental table, where a beam waist is produced approximately 90 cm behind the mirror. Here, the beam is only a few millimeters wide. The beam going straight on enters the high magnetic field laboratory through a safety window. This window is 46 cm higher than the beam and the beam line is shifted to that level by means of mirrors MH10 and MH11. In the magnet laboratory, a first beam waist is just behind the wall. Here, the beam is between 5 and 15 mm wide ($2*w$), depending on wavelength and size of the outcoupling hole. The small beam size allows us to insert a diamond window at this place. After the window, the beam is first deflected by the mirror MH12 and then deflected downwards by MH13 and focused onto the entrance of a circular waveguide which finally guides the beam into the cryostat of the high-field magnet. Another diamond window is located 10 cm in front of the entrance into the waveguide at the end of the beam line.

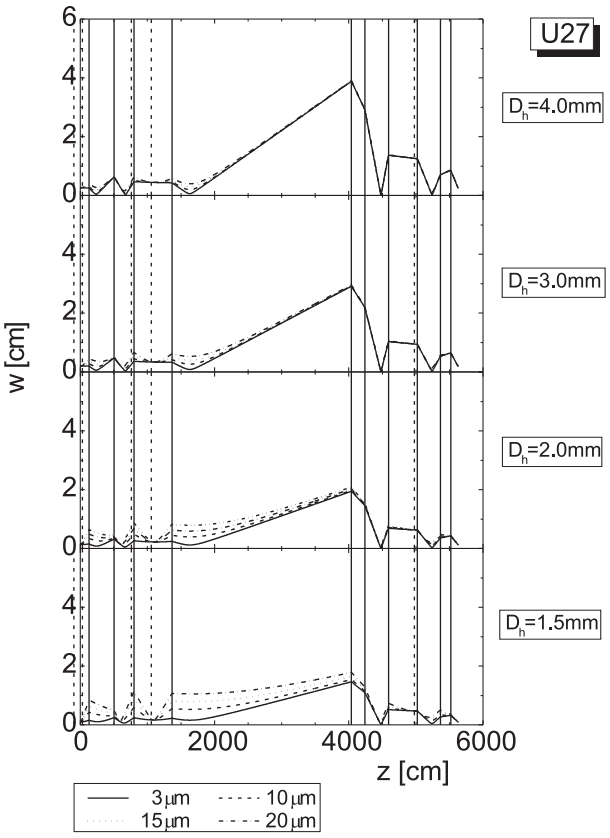

Fig. 2 *Radius w of the U27 FEL beam calculated from the waist on the diagnostic table to the HLD for different hole sizes D_h and wavelengths. The vertical solid and broken lines indicate the positions of focusing and plane mirrors, respectively.*

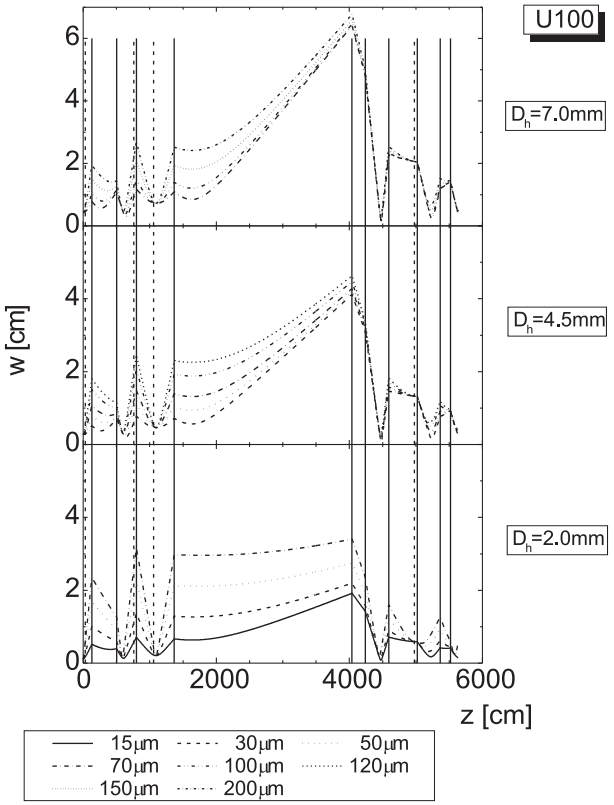

Fig. 3. *The same as in Fig. 2 for the beam from the U100 FEL.*

The mirrors are adjusted by means of He-Ne laser beams introduced into the beam line and aligned with the IR-beam. A first alignment beam starts from the FEL resonator. It is used in the laboratories of the ELBE building. Towards the end of the tunnel this beam gets rather wide and fades away. That is why we introduce another He-Ne laser beam into the beam line between mirrors MH2 and MH3. This beam is aligned with the first one and can be used for adjusting the mirrors in the HLD. Furthermore, the HLD users may use this beam for setting up high-field experiments.

A broad range of high-field experiments using the FEL facility at the Forschungszentrum Dresden - Rossendorf can be performed. It includes Electron Cyclotron Resonance in metals and semiconductors; Electron Paramagnetic, Antiferromagnetic and Ferromagnetic Resonances in various magnetic dielectrics; investigation of non-linear parametric processes in materials of functional optics and spintronics, pump-probe experiments on quantum wells, high-resolution time-domain spectroscopy of highly-correlated electron systems (including high-T_c materials, heavy-Fermion systems, etc.).

[1] http://www.fzd.de/elbe, 12.01.2007

[2] Th. Dekorsy et al., Proc. Free Electron Laser Conf. 2002, pp. 35,36

[3] H. Kogelnik, Appl. Opt. **4** (1965) 1562-1569

Spectral Width and Duration of the IR-Pulses from FELBE

W. Seidel, D. Stehr[1]

From a user's perspective, the three valuable characteristics of the free electron laser FELBE (among the wavelength range) are its peak power, variable picosecond optical micropulse length, and variable transform limited spectral bandwidth. Precise control of the FEL optical pulse has been essential for many time-resolved measurements performed at FELBE. The optical pulse length can sensitively be tuned by varying the FEL resonator length with respect to the nominal length resulting from the electron bunch repetition rate. At minimum detuning one yields the highest saturated power and the shortest optical pulse length. By detuning the resonator, the spectral width can be decreased simultaneously increasing the pulse length.

To characterize the ultrashort pulses generated by the FEL we built a non-collinear background-free autocorrelator system. We used a CdTe crystal as SHG medium [1], since it is transparent for a wide wavelength range in the infrared. We measured the autocorrelation function at maximum power in the detuning curve at a wavelength of 11.09 μm (see Fig. 1) generated in the FEL-U27 [2].

We deduced a pulse duration of 0.89 ps (FWHM), assuming a Gaussian temporal pulse shape. The measured FWHM of the spectrum is approx. 176 nm (corresponding to a relative spectral width of 1.6 %). The calculated time-bandwidth product is about 0.4 which indicates Fourier-transform limited operation. Long IR pulses with narrow bandwidth can be obtained from a detuned U27 resonator (pulse duration of 3.4 ps with 0.4 % bandwidth).

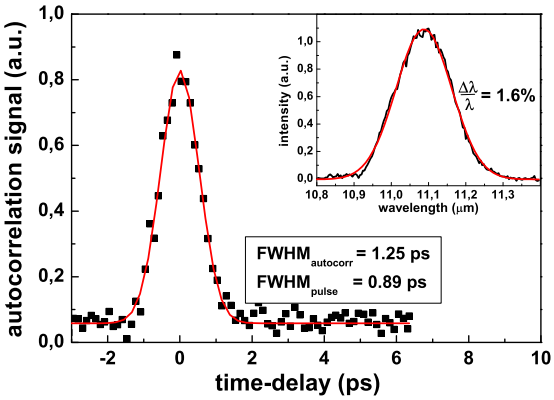

Fig. 1 *Autocorrelation trace and the corresponding FWHM of the wavelength (inset) of 11 μm at maximum of the detuning curve of the FEL-U27.*

First pulse length measurements and corresponding spectra at different detuning points of the FEL-U100 [3] are shown in Fig. 2. Here we deduced the pulse duration by assuming a sech^2 temporal pulse shape, in contrast to a Gaussian pulse shape for the U27.

[1] J. Xu et al., Opt. Comm. 197 (2001) 379
[2] W. Seidel, IKH Annual Report 2004, FZR-423 (2005) 60
[3] Th. Dekorsy et al., IKH Annual Report 2004, FZR-423 (2005) 65

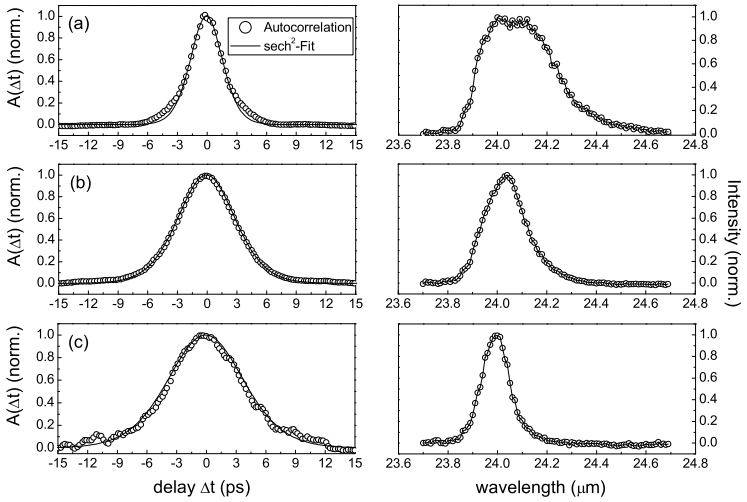

Fig. 2 *Autocorrelation functions (left) and the corresponding spectra (right) for 24 μm radiation at three different detuned resonator lengths of the FEL-U100 (a: ΔL=-2 μm, $FWHM_{pulse}$=2.5 ps; b: ΔL=-14 μm, $FWHM_{pulse}$=4.4 ps; c: ΔL=-24 μm, $FWHM_{pulse}$=5.8 ps).*

[1] *Inst. of Ion Beam Physics and Materials Research, FZD*

Influence of the System Matrix on the Quality of the Reconstruction of In-Beam PET Data [E, G]

G. Shakirin, P. Crespo, W. Enghardt[1]

Part of PhD thesis G. Shakirin, submitted to IEEE TNS

At the experimental heavy ion therapy facility at the GSI Darmstadt an in-beam PET scanner is operated for quality assurance monitoring simultaneously to the therapeutic irradiation. A fully 3D maximum likelihood expectation maximization (MLEM) reconstruction algorithm has been developed and adapted to the special conditions of in-beam PET [1].

The system response function (system matrix) for that algorithm is implemented by separately calculating its components (geometry, scatter, attenuation and detector sensitivity). The geometry component of the system matrix is calculated "on-the-fly" during the reconstruction. In order to determine this component, the volume of each tube of response (TOR) is sampled by a number of lines whose endpoints are randomly distributed over the crystal surfaces. The number of lines used in the method is called a level. The higher the level, the more accurate and slower is the calculation.

We investigated the accuracy for this approach as well as for another method for calculating of the geometry component of the system matrix based on the approximation with splines [2]. An influence of the system matrix on the quality of reconstructed images was evaluated for MLEM and ordered subsets expectation maximization (OSEM) algorithms using real treatment data collected during the therapeutic irradiations at the GSI.

The accuracy of both methods for the system matrix calculation ("on-the-fly" and with splines approximation) was checked by means of analyzing the normalized mean square error (NMSE) (Fig.1 left). The method with splines approximation achieves high accuracy (NMSE = 0.00047) and performs with the same speed as "on-the-fly" method with level equal to 50. For visual comparison of accuracy the system matrix was calculated for one TOR with the two different methods (Fig. 1 right).

The influence of system matrix on the reconstruction quality was evaluated by means of an ensemble mean square error (EMSE) [3]. The true β^+-activity distributions were generated by means of the PosGen Monte Carlo code based on real treatment data of 9 patients. EMSE was calculated for reconstructions with the MLEM algorithm (50 iterations) and with the OSEM algorithm (8 subsets, 10 iterations). EMSE does not depend significantly on the quality of the system matrix when reconstructions are performed by MLEM algorithm, but significant deviations are observed when using the OSEM algorithm (Fig. 2).

As a conclusion, it is profitable to use the splines approximation method for reconstructions with OSEM algorithm where higher quality of the system matrix leads to lower mean square error and slightly better images. However, in the specific conditions of in-beam PET (dual-head geometry and low counting statistics) the best result for reconstructions performed by the MLEM algorithm by means of EMSE is achieved with the system matrix of poor quality (with "on-the-fly" method with level = 3) and visual comparison gives no significant difference.

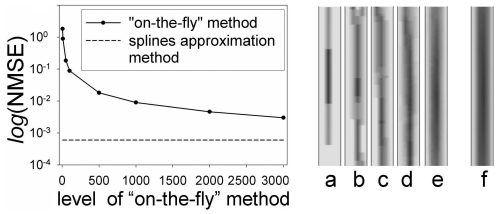

Fig. 1 *Left: NMSE calculated for different levels for "on-the-fly" method comparing with NMSE for splines approximation method. Right: central slice of one TOR filled with system matrix values calculated with the "on-the-fly" method with level equal to 5 (a), 10 (b), 20 (c), 100 (d), 1000 (e) and with the splines approximation method (f).*

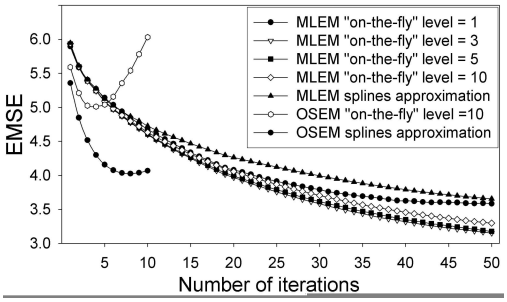

Fig. 2 *EMSE for images reconstructed with MLEM and OSEM (8 subsets) algorithms and different methods for calculation of the system matrix.*

[1] K. Lauckner, Ph.D. Thesis, Technische Universität Dresden (1999)

[2] G. Shakirin, P. Crespo, W. Enghardt, GSI Sci. Rep. (2005) p. 394

[3] H. H. Barrett, K. J. Myers, ISBN: 0-471-15300-1 (2003) pp. 879-883

[1] *also TU Dresden*

Optimum Voxel Size for Direct Time-of-Flight In-Beam PET [E,G]

G. Shakirin, P. Crespo, F. Fiedler, W. Enghardt[1], E. Grosse[1], A. Wagner

Part of PhD thesis G. Shakirin

The direct time-of-flight (TOF) reconstruction algorithm [1] can improve significantly the image quality for in-beam positron emission tomography (PET) [2] when applied to data measured with a tomograph having detectors with a coincidence time resolution of 100 ps (full width at half maximum). Such tomograph does not exist yet but its simulations are already feasible taking into account recent works on TOF detectors [3]. Typically, activity densities reached in fractionated carbon ion therapy are in the order of 200 Bq cm^{-3} Gy^{-1}, resulting in low statistics datasets. We investigate the influence of the voxel size onto image quality by simulating two treatments with different irradiated volumes and statistics. A very large irradiated volume (pelvic chordoma, high image statistics, lower activity density), and a large head-and-neck irradiation (large image statistics, slightly larger activity density). For each case study a low-dose (fractionated radiotherapy ~0.6 Gy) and a high-dose (hypofractionation ~6 Gy) scenario is taken into account. For both cases and doses the generated β^+-activity distributions were simulated by means of the PosGen Monte Carlo code [4, 5].

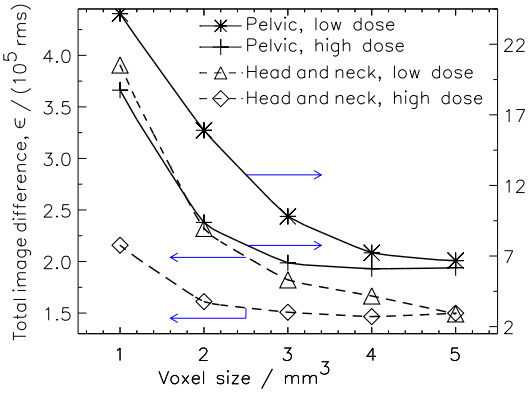

Fig. 1 *Total image difference for the two study-cases considered. The root-mean-square (rms) difference of images obtained in each scenario (voxel size and dose) refers to the (not clinically feasible) image computed with a dose-enhancement factor of 1 000 (cf. Figs. 2 and 3, top rows).*

In order to find the optimum voxel size for each irradiation scenario, Fig. 1 was constructed. It shows the differences obtained between images reconstructed with several voxel sizes and a reference image obtained with ultra-high (~600 Gy) statistics. It can be seen that for a low-dose pelvic irradiation an optimum voxel size yielding the minimum deviation lies at (5 mm)^3. Fig. 2 confirms that, in this situation, the small loss of spatial resolution still suffices to monitor sensitive organs (colon) lying close to the irradiated volume (tumor). For monitoring low-dose head-and-neck treatments a higher spatial resolution is required due to the finer structures present in the skull (Fig. 3). Despite Fig. 1 pointing to smaller deviations with an image voxel of (5 mm)^3, visual inspection of the reconstructed images introduces an optimum voxel size of (3 mm)^3 in order to conserve the spatial resolution required to monitor finer anatomic structures (Fig. 3).

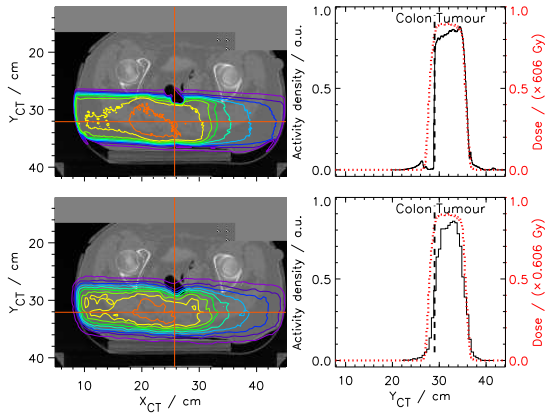

Fig. 2 *Pelvic irradiation. Top: very-high activity density (simulated dose enhanced by 1 000), sampled with 1 mm^3 voxel. Botom: low-dose scenario reconstructed with a simulated, dual-head, direct TOF tomograph with (5 mm)^3 image voxel. All images submitted to a 3D median filter.*

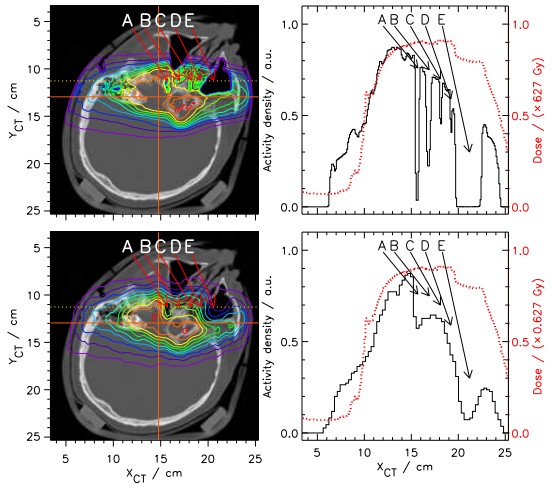

Fig. 3 *Head-and-neck irradiation. Simulated dose and reconstruction details like in Fig. 2, except for the (3 mm)^3 voxel size of the low-dose scenario (bottom). The arrows indicate fine structures of the skull: sphenoidal sinus (A), right (B), left (C and D) posterior meatus, and left maxillary sinus (E).*

[1] P. Crespo et al., Phys. Med. Biol. to be submitted
[2] W. Enghardt, P. Crespo et al., NIM A 525 (2004) 284
[3] J. Glodo, A. Kuhn et al., IEEE Nucl. Sci. Symp., 2006
[4] B.G. Hasch, Thesis, Technische Universität Dresden, 1996
[5] F. Pönisch, K. Parodi et al., Phys. Med. Biol. 49 (2004) 5217

[1] *also TU Dresden*

In-Beam PET Measurements of Biological Half-Lives of ^{12}C Irradiation Induced β^+-Activity [E,G]

F. Fiedler, M. Sellesk [1], P. Crespo, R. Jülich, K. Parodi[2], J. Pawelke, F. Pönisch, W. Enghardt [3]

Part of PhD thesis F. Fiedler

Introduction

The in-beam PET method is a valuable tool to measure the distribution of the delivered dose in the irradiated tissue in carbon ion therapy which has so far been applied to more than 300 patients. In order to evaluate the PET data with respect to the patient anatomy, positioning and range of the beam [1], they need to be compared with a simulation of the expected activity distribution [2]. Although these algorithms are well adapted to the therapeutic situation, there are differences that can be attributed to metabolic processes taking place in living organisms, such as the predominant perfusion-driven washout of the positron emitters. Since comprehensive data of the washout as a function of the tissue and the type of the radionuclides are not available, these processes are not taken into account in the current simulation code. In order to obtain such data, we analysed the results of a set of in-beam PET data scans taken during therapeutic ^{12}C irradiation.

Patient studies

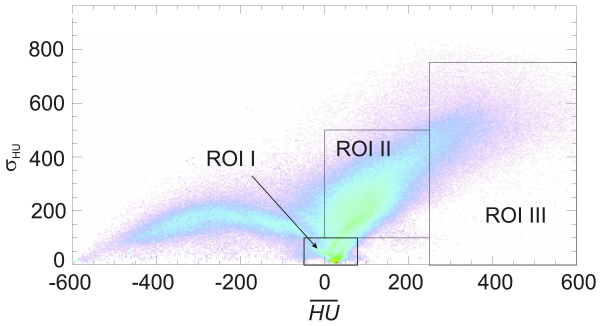

Fig. 1 *Two-dimensional histogram of the fraction of the LOR intersecting the planned target volume as a function of $\overline{HU}$ and σ_{HU}. The corresponding anatomical regions for a particular patient can be seen in Fig. 2.*

We expect a correlation between the tissue type along the lines of response (LOR) of the positron camera and the effective half life. The only available information in this respect is provided by the planning CT, i.e. the Hounsfield unit (HU). However, the mean HU, $\overline{HU}$, along a LOR is not sufficient for classification, the standard deviation of the HU within each LOR (σ_{HU}) was additionally introduced to take into account tissue inhomogeneity (cf. Fig. 1). These two quantities were classified into 3 different regions of interest (ROI) for 14 patients. ROI I was supposed to contain rather homogeneous brain tissue (e.g. brain), ROI II was expected to include soft, but inhomogeneous tissue, and ROI III was for bone. The anatomical mapping is displayed in Fig. 2. No dependence of the effective half life on the $\overline{HU}$ and σ_{HU} was found.

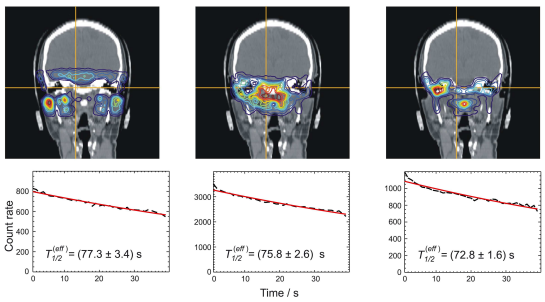

Fig. 2 *Effective half-lives in the patient according to the ROIs defined in Fig. 1. The left figure corresponds to ROI I, the middle to ROI II and the right to ROI III, respectively.*

Therefore, we investigated the effect of the different dose levels on the effective half live by analysing two other groups of LOR. The first contained at least ten voxels with 90 % of the maximum dose. The second set of LOR contained voxel with 0 - 90 % of the maximum dose with no voxel higher than 90 %. Combining data of 55 patients, a lower effective half live for the 0 - 90 % region was found ($T_{1/2} = 71.8 \pm 0.6$ s) than for the 90 - 100 % region ($T_{1/2} = 79.5 \pm 1.8$ s) possibly due to less perfusion in the tumour. **Conclusions** The in-beam PET data acquired during 40 s after finishing therapeutic irradiation indicate that on this rather short time scale no differentiation of tissue with respect to the washout rate of the ^{12}C beam induced β^+-radioactivity was observed. Therefore, if in-beam PET measurements can be restricted to scanning times below 100 s, the influence of tissue dependent washout processes to the spatial distribution of beam induced β^+-activity can be expected to be drastically diminished. This is expected to improve the correspondence between the measured in-beam PET images and those predicted from the treatment plan.

[1] W. Enghardt, P. Crespo et al., Nucl. Inst. Meth. A 525 (2004), 284.

[2] F. Pönisch, K. Parodi et al., Phys. Med. Biol. 49 (2004) 5217.

[1] *also TU Bergakademie Freiberg*
[2] *Ionenstrahl-Therapiezentrum Heidelberg*
[3] *also TU Dresden*

The Feasibility of In-Beam PET for Therapeutic Beams of ^{3}He [G,E]

F. Fiedler, P. Crespo, K. Parodi[1], **M. Sellesk**[2], **W. Enghardt**[3]

Published in IEEE Transactions on Nuclear Science 53 (2006) 2252

At the experimental carbon ion treatment facility at the Gesellschaft für Schwerionenforschung (GSI) Darmstadt the clinical benefit of the in-beam PET method has been proven. It led to a significant improvement of the quality of patient treatment. Several heavy ion treatment facilities, which will provide in the near future a large variety of ions, are in planning or even under construction. The deduction of clinically relevant parameters from in-beam PET data requires a precise knowledge of the spatial distribution of beam induced positron emitters in the irradiated volume. Therefore, the β^+-activity induced by ^{3}He has been studied for the first time at the Gesellschaft für Schwerionenforschung with three mono-energetic ^{3}He beams of 130.03 AMeV to 207.92 AMeV and mean intensities varying from $2.0 \cdot 10^8$ to $3.5 \cdot 10^8$ ions / s. The beams were stopped in homogeneous thick targets consisting of PMMA, graphite and water, which were placed in the center of the field of view of the PET-scanner at the experimental carbon ion therapy at GSI. Results on the production rate and the spatial distribution of ^{3}He ion induced positron activity is presented and compared with data from ^{12}C-irradiation (cf. Fig. 1). The accuracy and resolution for determining the range of the ^{3}He primary beams is deduced. Furthermore, energy dependent thick target cross sections for different reaction channels leading to positron emitters are estimated from the experimental data (cf. Fig. 2).

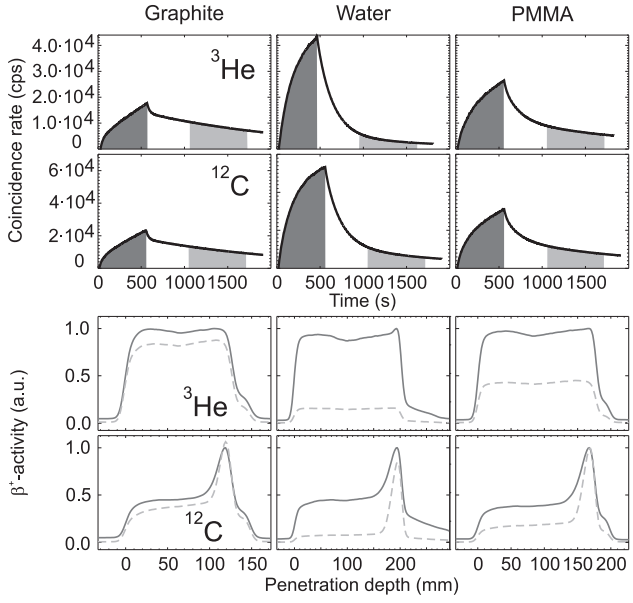

Fig. 1 *Time-event histograms and depth profiles of β^+-activity induced by ^{3}He and ^{12}C-beams at 207.92 AMeV and 337.5 AMeV, respectively, in graphite (left), water (middle) and PMMA (right) targets. 1st row: Measured time-event-histograms for ^{3}He-ions. 2nd row: As 1, but for ^{12}C-projectiles. 3rd row: β^+-activity depth profiles for ^{3}He-ions. The solid lines display the activity measured during the irradiation (left marked area in 1st row), the gray dashed lines (right marked area in 1st row) give the activity from 10 to 20 min after the end of the irradiation normalized to the maximum of the activity measured during the irradiation. The ordinate is in arbitrary units. 4th row: as 3, but for ^{12}C-projectiles. In the case of ^{12}C-projectiles the main contribution coming from the projectile fragments is nearly the same in both periods. In case of a graphite target there is a slightly higher signal for the decay measurement due to the longer measuring time. The mentioned absence of projectile fragments in case of ^{3}He-projectiles leads to a larger difference in the counting statistics between these two time intervals. For the water target the largest difference was observed due to the short half life of the dominating positron emitter, ^{15}O. Since human tissue consists of about 65% of water the importance of measuring during the irradiation by means of in-beam PET increases when going to projectiles which do not form β^+-emitting fragments.*

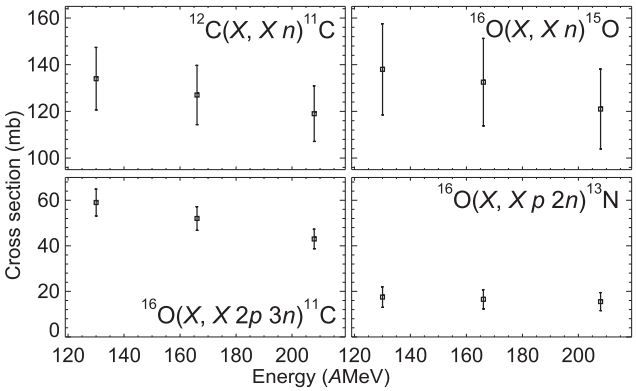

Fig. 2 *Results of thick target cross section calculation from experimental data. Additionally the cross section of the reaction $^{12}C(X, X\ 2n)^{10}C$ was found to be (9.0 ± 1.5) mb. The reactions are mainly induced by ^{3}He, but there are also non-negligible contributions coming from reactions with secondary particles like protons, deuterons and neutrons, thus $X = \{^3He, p, n, d\}$. Furthermore, in the exit channel $X = \{^3He, d\}$ the deuteron may be disintegrated into nucleons.*

[1] *Ionenstrahl-Therapiezentrum Heidelberg*
[2] *also TU Bergakademie Freiberg*
[3] *also TU Dresden*

In-beam PET at High-Energy Photon Beams: A Feasibility Study

H. Müller, W. Enghardt[1]

Published in Phys. Med. Biol. 51 (2006) 1779-1789

For radiation therapy with carbon ion beams, either of the stable isotope ^{12}C or of the radioactive one ^{11}C, it has been demonstrated that the β^+-activity distribution created or deposited, respectively, within the irradiated volume can be visualised by means of positron emission tomography (PET). Those PET images provide valuable information for quality assurance and precision improvement of ion therapy. Dedicated PET scanners have been integrated into treatment sites at HIMAC (Japan) and GSI (Germany) to make PET imaging feasible during therapeutic irradiation (in-beam PET). A similar technique may be worthwhile for radiotherapy with high-energy bremsstrahlung. In addition to monitoring the dose delivery process which in-beam PET has been primarily developed for, it may be expected that radiation response of tissue can be detected by means of in-beam PET. We investigate the applicability of PET for treatment control in case of using bremsstrahlung spectra produced by 15 - 50 MeV electrons. Target volume activation due to (γ, n) reactions at energies above 20 MeV yields moderate β^+-activity levels, which can be employed for imaging. The radiation from positrons produced by pair production is not presently usable because the detectors are overloaded due to the low duty factor of medical electron linear accelerators. However the degradation of images caused by positron motion between creation and annihilation seems to be tolerable.

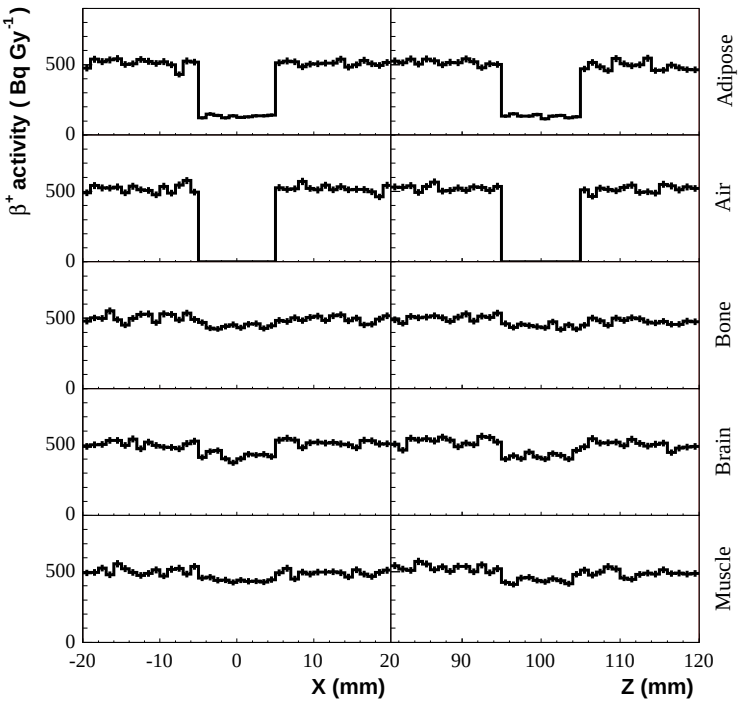

Distribution of β^+ activity deposited transverse (X) (left panel) and longitudinal (Z) right panel) to the beam direction for various types of tissues embedded in water as indicated the figure. The hard variant of the 50 MeV spectrum has been used for the calculations. The vertical bars represent the statistical errors.

[1] *also TU Dresden*

Results of First Experiments on In-Beam PET at 34 MV Bremsstrahlung Beams[E]

D. Möckel, T. Kluge, J. Pawelke, W. Enghardt[1]

Part of PhD thesis D. Möckel and part of Diploma thesis T. Kluge

Since there are good experiences with in-beam PET for quality assurance in carbon ion therapy [1] it is highly desirable to extend this method to other radiation treatment modalities. For example, in-beam PET seems to be feasible for high energy photon irradiation with energies above ∼20 MeV because of the generation of positron emitters in tissue (predominantly ^{11}C and ^{15}O) by (γ, n) reactions as already shown in simulations [2]. First experimental studies concerning the measurement of photon induced activity distribution have already been done by means of off-beam PET experiments [3]. In these investigations only the ^{11}C activity distribution could be measured, since the time interval between irradiation and measurement was about 15 half-lives of ^{15}O. To shorten this time interval by combining irradiation and measurement and thus to increase the measured activity, an in-beam measuring setup, adapted from the PET scanner for education presented in [4], was built up at ELBE.

The irradiation setup is similar to that used in the off-beam PET experiments. Additionally, for coincident registration of the annihilation photons of the generated positron emitters, two commercial BGO block detectors (ECAT EXACT, Siemens) have been mounted face-to-face at a distance of ∼30 cm with the phantom between them. They are coupled and moved linearly in beam direction. So during the irradiation the detectors scan a selected region several times. The list mode data acquisition proceeds continuously during the movement. After each scan the data are reconstructed and a two-dimensional image of the measured activity distribution is obtained. Various homogeneous as well as inhomogeneous phantoms were irradiated by 34 MV bremsstrahlung. The generated activity distribution was measured simultaneously. During irradiation not only positrons from (γ, n) reactions are emitted but also a high number of positrons produced by pair production [2]. Their signals in combination with the high radiation background at the irradiation site lead to an overloading of the detectors. Therefore, the accelerator was operated in macropulse mode and data were only acquired in the macropulse pauses.

By means of the performed in-beam PET experiments the ^{11}C and ^{15}O activity distributions could be measured. Higher activity concentrations are determined in comparison to the off-beam PET experiments depending on the oxygen content. Due to the different half-lives of ^{11}C and ^{15}O ($T_{1/2}(^{11}\mathrm{C}) = 20.38$ min, $T_{1/2}(^{15}\mathrm{O}) = 2.03$ min) a good contrast between materials with various density values and stoichiometry can be achieved. One example is shown in Fig. 1. The two-dimensional activity distribution as well as a schematic representation of an inhomogeneous, tissue equivalent phantom, irradiated by 34 MV bremsstrahlung, is displayed.

Since the coincidence events are acquired in list mode the activity in dependence on the measuring time could be investigated, too. The time course of the activity shows the production during and the decay after the irradiation in dependence on the carbon and oxygen content (cf. Fig. 2).

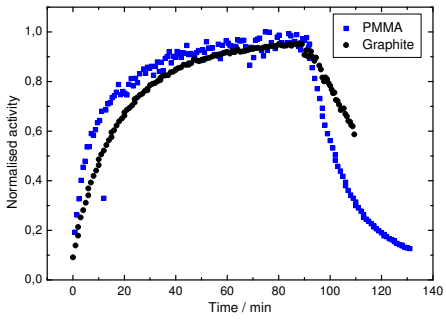

Fig. 2 *Production and decay of activity, generated by 34 MV bremsstrahlung, for PMMA and graphite.*

[1] W. Enghardt, P. Crespo et al., Nucl. Instr. Meth. A 525 (2004) 284

[2] H. Müller and W. Enghardt, Phys. Med. Biol. 51 (2006) 1779

[3] D. Möckel, J. Pawelke et al., IKH Annual Report 2005, FZR-442 (2006) 59

[4] T. Würschig and W. Enghardt, IKH Annual Report 2005, FZR-442 (2006) 60

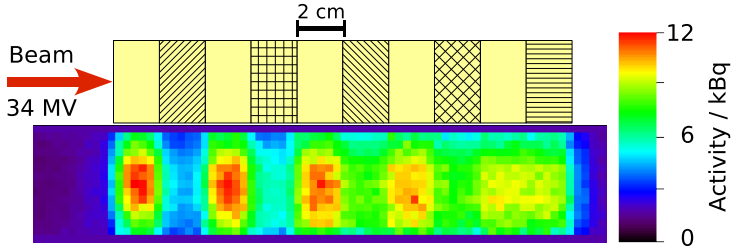

Fig. 1 *Schematical illustration (top) as well as two-dimensional distribution of the generated positron emitters (^{11}C and ^{15}O) in an inhomogeneous phantom for an electron energy of 34 MeV (bottom).*

[1] *also TU Dresden*

Electron Beam Monitoring for Channeling Radiation Measurements

W. Neubert, B. Azadegan, W. Enghardt, K. Heidel, J. Pawelke, W. Wagner

Published in Nucl. Instr. Meth. B 254 (2007) 319-328

A secondary emission monitor (SEM) and an auxiliary Faraday cup necessary for calibration purposes (Fig. 1) have been constructed and installed at the radiation physics beam line of ELBE. These devices are to be applied for the precise beam-current monitoring in measurements of channeling radiation. Miscellaneous simulations of underlying interactions of the beam electrons with the target material as well as with the materials of the monitor equipment have been performed to optimize the design and to evaluate possible correction factors inherent to transmission monitoring (Fig. 2).

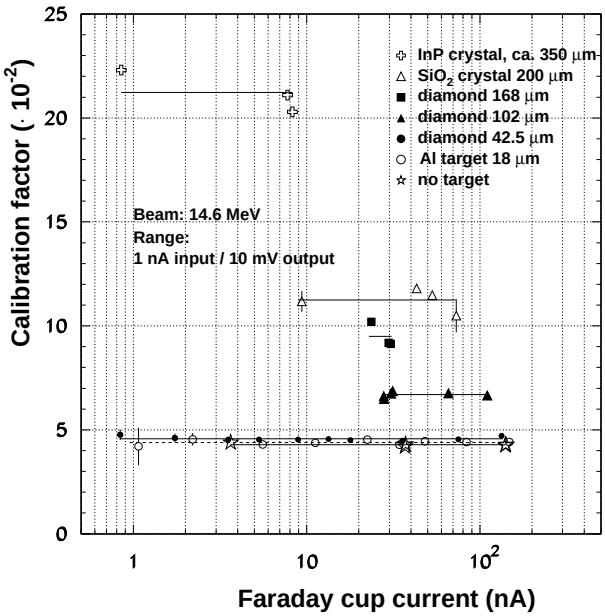

Fig. 1 *Calibration factors of the SEM for different targets in dependence on the beam current determined by means of the Faraday cup. The data are not corrected for beam losses due to multiple scattering.*

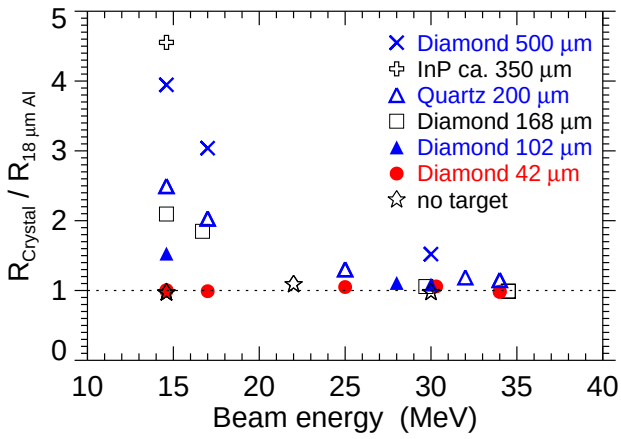

Fig. 2 *Experimentally determined relative calibration factors of the SEM used for beam current monitoring in measurements of channeling radiation.*

Investigation of Planar Channeling Radiation from Different Plane of Quartz

B. Azadegan, W. Wagner, J. Pawelke

Part of PhD thesis B. Azadegan

First results of measurements of planar electron channeling radiation (CR) on quartz are presented in Ref. [1]. The stimulation of CR by ultrasonic vibrations excited in piezoelectric crystals has been considered in Refs. [2, 3]. The observation of predicted phenomena such as CR line splitting or even selective intensity amplification, however, requires the detailed knowledge of the transverse electron states in the crystal planes of quartz. The spectrometry of CR on quartz provides information about the suitability of different crystal planes for the ultrasonic stimulation of CR. Therefore, we performed systematic measurements of CR from different planes of quartz.

The analysis of the measurements bases on the application of the theory of CR. Real planar continuum potentials of quartz, transition energies, line widths and relative intensities have been calculated. Compared with the CR observed on monatomic crystals (e.g. diamond or Si), which have a more simple cubic structure, the registration of CR on quartz is to some degree complicated by the large variety of closely adjacent planes in the hexagonal lattice of this binary crystal. For illustration of this feature, the zone of the x-cut axis $[2\bar{1}\bar{1}0]$ of α-quartz is shown in Fig. 1. The planes, in which CR has been generated, are given by full lines. No CR has been observed from planes given by dashed lines

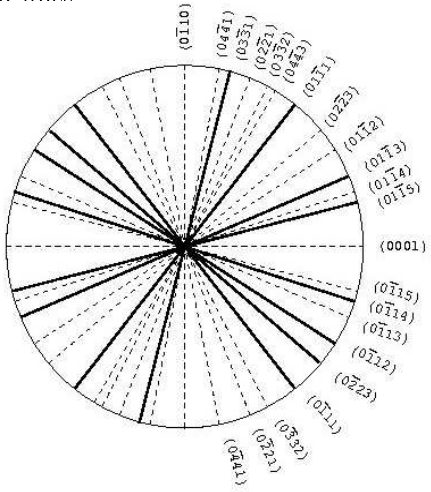

Fig. 1 *Zone of the $[2\bar{1}\bar{1}0]$ axis of quartz.*

The CR spectra from 32 MeV electrons channeled in the $(01\bar{1}1)$ and $(0\bar{1}11)$ planes are shown in Figs. 2 and 3, respectively, together with the calculated planar potentials. The calculated transition energies between bound states are indicated by vertical bars, the heights of which have been chosen proportional to the transition rates assuming equilibrium initial population of states.

According to Refs. [2, 3], these two planes are probably suitable candidates for some observation of CR stimulated by ultrasonic waves with frequencies of $\leq 10\,\mathrm{GHz}$.

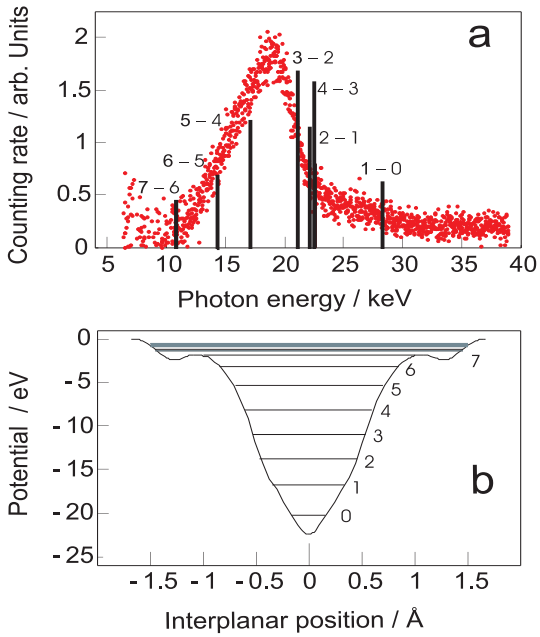

Fig. 2 *Background corrected spectrum of planar CR observed for 32 MeV electrons channeled along the $(01\bar{1}1)$ plane of quartz (a) and the corresponding planar potential (b).*

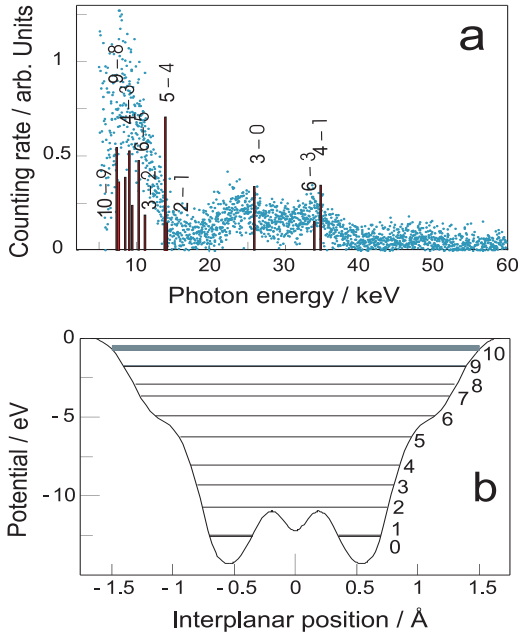

Fig. 3 *Analogous to Fig. 2 but for the $(0\bar{1}11)$ plane.*

[1] B. Azadegan, W. Wagner, J. Pawelke, L.Sh. Grigoryan, IKH Annual Report 2005, FZR-442 (2006) 66

[2] L.Sh. Grigoryan et al., Nucl. Instrum. Meth. B 173 (2001) 184

[3] L.Sh. Grigoryan et al., Nucl. Instrum. Meth. B 212 (2003) 51

Dependence of the Linewidth of Planar Electron Channeling Radiation on the Thickness of the Diamond Crystal

B. Azadegan, W. Wagner, J. Pawelke

Published in Phys. Rev. B 74 (2006) 045209, 1-11

Measurements of (110) planar channeling radiation have been performed at the radiation source ELBE at electron energies of 14.6, 17, 30 and 34 MeV using diamond crystals of thickness 42.5, 102, 168 and 500 μm. The influence of different line-broadening mechanisms on the spectral shape of radiation from the 10 transition has been investigated. The analysis bases on fitting a convolution of the intrinsic Lorentz-like line shape with a Gaussian-like multiple-scattering distribution to the measured spectra (Fig. 1). The asymmetry parameter (α) involved relates to the standard deviation of the effective multiple-scattering angle. Its dependence on the crystal thickness was found to be weaker than for nonchanneled particles (Fig. 2). The deduced coherence lengths show no significant dependence on the electron energy.

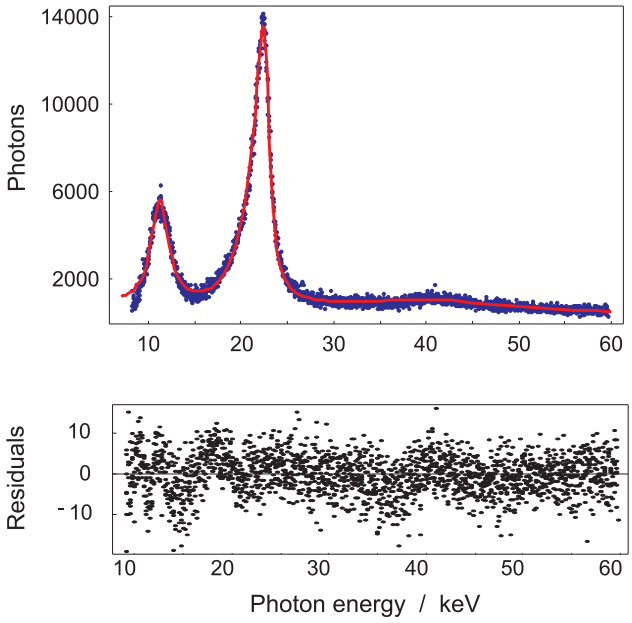

Fig. 1 *Upper panel: Measured spectral distribution of (110) planar channeling radiation for a 168 μm thick diamond crystal at an electron energy of 17 MeV (blue). Two asymmetric line profiles and a polynomial background distribution were fitted to the spectrum (red). Lower panel: Residuals between the measured and the approximated distribution.*

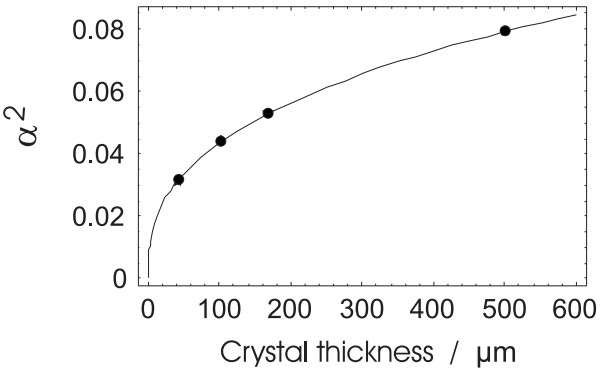

Fig. 2 *Dependence of the squared line-asymmetry parameter on the crystal thickness.*

RBE of 25 kV X-Rays for the Survival and Induction of Micronuclei in the Human Mammary Epithelial Cell Line MCF-12A

A. Lehnert, E. Lessmann, J. Pawelke, W. Dörr[1]

Published in Radiat. Environ. Biophys. 45 (2006) 253-260

The broad application of low energy X-rays below about 50 keV in radiation therapy and diagnostics and especially in mammography substantiates the precise determination of their relative biological effectiveness (RBE). A quality factor of 1 is stated for photons of all energies in the ICRP Recommendations. However, the RBE of low-energy X-rays compared to high-energy photons was found to be dependent on photon energy, cell line and endpoints studied, hence varying from less than 1 up to about 4. In the present study, the human mammary epithelial cell line MCF-12A has been chosen due to the implementation of the results in the estimation of risk from mammography procedures. The RBE of 25 kV X-rays (W anode, 0.3 mm Al filter) relative to 200 kV X-rays (W anode, 0.5 mm Cu filter) was determined for clonogenic survival in the dose range 1–10 Gy and micronuclei induction in the range 0.5–3.5 Gy. The RBE for clonogenic survival was found to be significantly higher than 1 for surviving fractions in the range $0.005 < S < 0.2$. The RBE decreased with increasing survival, with an $RBE_{0.1}$ at 10 % survival of 1.13 ± 0.03. The effectiveness of soft X-rays for micronuclei induction was found to be 1.40 ± 0.07 for the fraction of binuclear cells (BNC) with micronuclei (MN) and 1.44 ± 0.17 for the number of MN per BNC (cf. Fig. 1). In contrast, the RBE determined from the number of MN per MN-bearing BNC was found to be 1.08 ± 0.32. This indicates that the effectiveness of 25 kV X-rays results from an increase in the number of damaged cells, which, however, do not have higher number of micronuclei per cell.

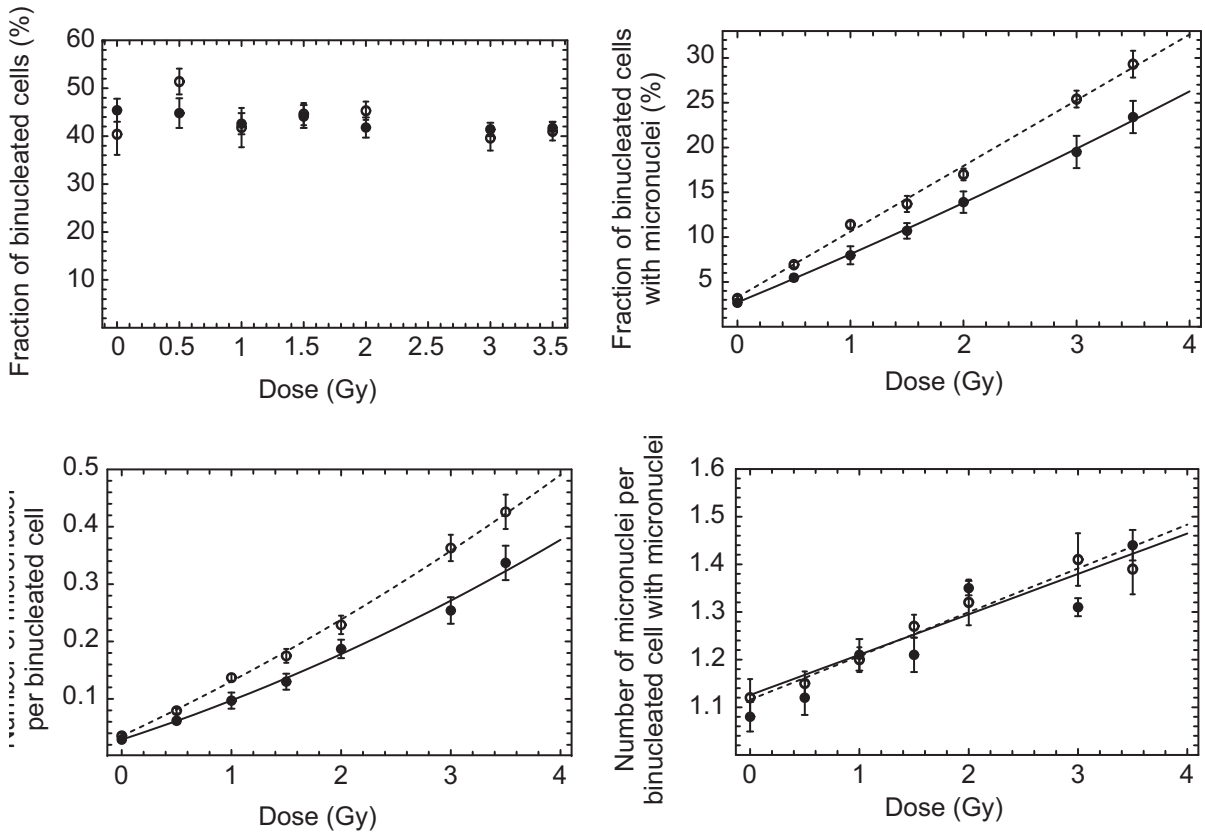

Fig. 1 *Dose response of micronuclei induction after irradiation of MCF-12A cells with 25 kV X-rays (open circles, dashed lines) and 200 kV X-rays (closed circles, solid lines). The fraction of BNC (top, left), fraction of BNC with MN (top, right), number of MN per BNC (bottom, left) as well as the number of MN per MN-bearing BNC (bottom, right) are presented. The mean values and the SEM from 6 experiments are shown.*

[1] *TU Dresden*

Repair Kinetics of DNA Double Strand Breaks Induced in Human Mammary Epithelial Cells

E. Beyreuther, W. Dörr[1], **E. Lessmann, J. Pawelke**

Part of PhD thesis E. Beyreuther

The introduction of mammography screening programs in some countries initiated a continuous discussion about the benefit or possible accompanied risk of the used radiation qualities. Contributing to this discussion we used different methods, such as clonogenic survival and the analysis of chromosomal aberrations by Fluorescence in situ Hybridisation (FISH), to study biological effects with the human mammary epithelial cell line 184A1, which is of interest especially for the induction of breast cancer. Radiation qualities applied were 10 and 25 kV soft X-rays and a 200 kV X-ray tube as reference radiation source. Furthermore, we develop these methods and investigate the repair kinetics of DNA double strand breaks (DSB) with cell line 184A1 to learn more about underlying processes.

The DNA damage response, following irradiation, includes an efficient DSB recognition system as well as different DSB repair mechanisms. Important contributions to these processes are the phosphorylation of histone H2AX (γH2AX) and the localization and phosphorylation of the p53 binding protein 1 (53BP1) at the sides of DNA DSBs. Both molecules are essential for the recognition of DNA DSBs and hence for the induction of repair processes. Using appropriate antibodies, the phosphorylated molecules can be visualized as nuclear foci and their time-dependent formation can be followed after irradiation.

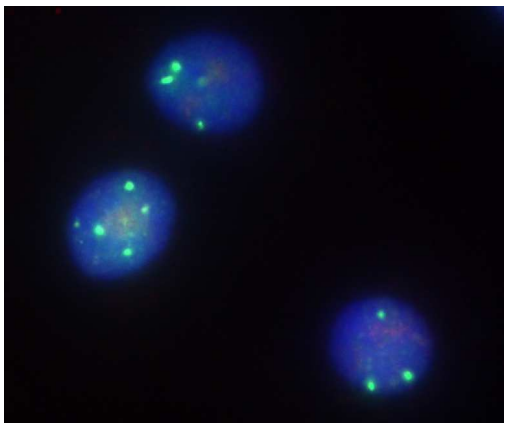

Fig. 1 *Marked foci of cell line 184A1, induced by 25kV X-rays and observed 2 hours after irradiation*

The time-dependent formation of γH2AX- and 53BP1-foci, was used to investigate the induction and rejoining of DNA DSBs up to 48 hours after irradiation. Two different antibodies and their corresponding fluorochromes were used to visualize and quantify the foci induced by two different doses of 0.25 and 2 Gy for 25 and 200 kV X-rays, respectively.

The kinetics obtained after irradiations with 2 Gy show a similar shape and therefore energy independence for both energies, which can be explained by the same underlying repair processes. Shortly after irradiation the number of foci per cell shows a steep increase, resulting in a maximum after 2 hours and a subsequent 2-phase decrease.

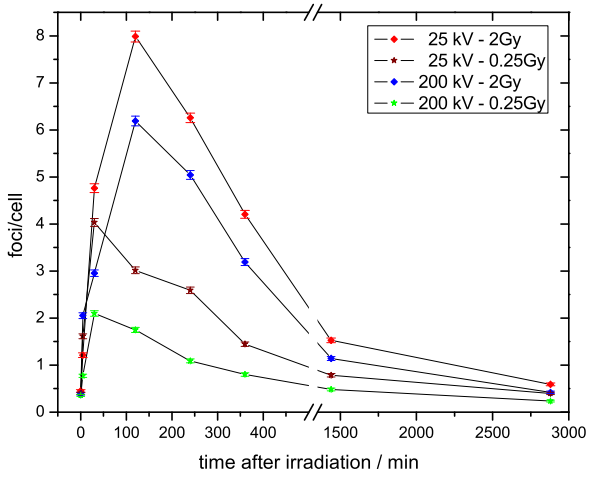

Fig. 2 *Kinetics of the DNA DSB induced by 0.25 and 2 Gy of 25 kV and 200 kV X-rays.*

Although the position of the maximum is the same, the number of foci per cell differs for 25 kV and 200 kV X-rays, being 7.99 $\pm$ 0.12 and 6.19 $\pm$ 0.10, respectively. The rejoining of DSBs, deduced by the decrease of number of foci per cell, can be divided in a first phase, which seems to be faster, and a slower second one. During the first phase, the number of foci per cell is reduced to about 50% of the maximum and in the second phase they are reduced to the control level, whereas for 25 kV a significant number of foci per cell remain. These results implicate that, on the one hand, the number of the induced DNA DSBs is significantly higher for 25 kV X-rays and, that on the other hand, some DSBs remain unrepaired. These DSBs can influence the genomic integrity and can result in chromosomal aberrations.

The experiments for the irradiations with 0.25 Gy for both energies show the same shape as that with higher dose, but the maximum is derived at 30 minutes after irradiation. The maximum number of foci per cell was 4.03 $\pm$ 0.08 for 25 kV and 2.10 $\pm$ 0.06 for 200 kV X-rays, which is about the half or less compared to the results of 2 Gy with the same energies.

[1] *TU Dresden*

AMOS - An Effective Tool for Adjoint Monte Carlo Photon Transport [D]

D. Gabler[1], J. Henniger[1], **U. Reichelt**

Published in Nucl. Instr. Meth. B 251 (2006) 326-332

In order to expand the photon version of the Monte Carlo transport program AMOS to an adjoint photon version, AMOS Pt, the theory of adjoint radiation transport is reviewed and evaluated in this regard. All relevant photon interactions, photoelectric effect, coherent scattering, incoherent scattering and pair production, are taken into account as proposed in the EPDL 97. In order to simulate pair production and to realise physical source terms with discrete energy levels, an energy point detector is used. To demonstrate the qualification of AMOS Pt a simple air-over-ground problem is simulated by both the forward and the adjoint programs. The results are compared and total agreement is shown (Fig. 1 and Fig. 2).

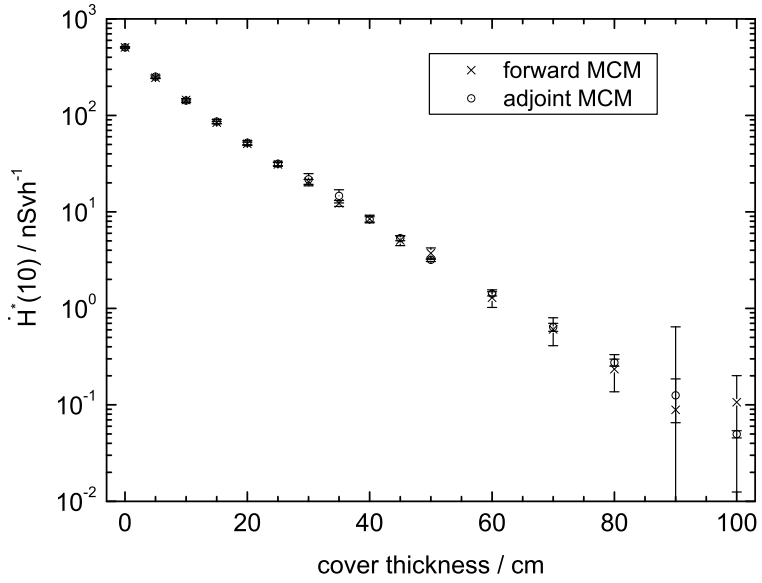

Fig. 1 *Comparison of forward and adjoint results for the ambient dose equivalent rate of the air-over-ground problem. Therein a small detector is positioned over a infinite source distribution covered by a soil layer of variable thickness.*

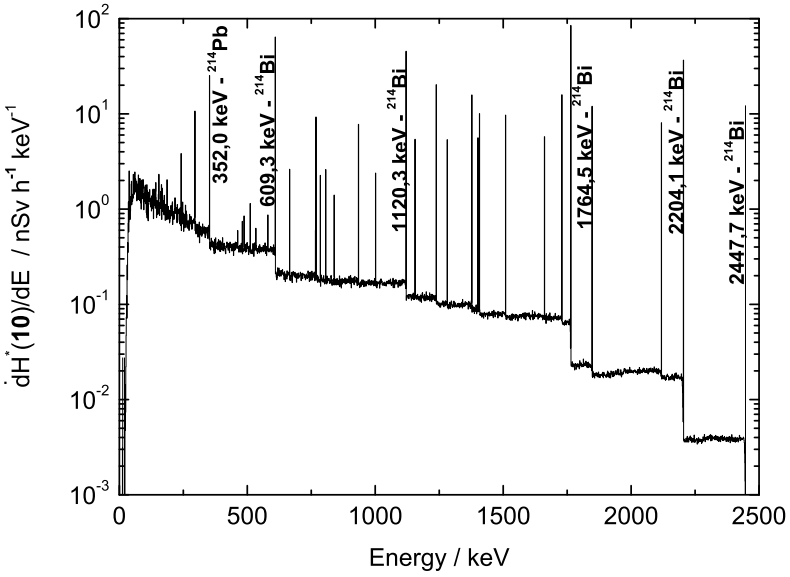

Fig. 2 *Adjoint simulated spectrum of the ambient dose equivalent rate for a cover thickness of 0 cm. The corresponding nuclides for some dose peaks are added.*

[1] *TU Dresden*

Application of Advanced Monte Carlo Methods in Numerical Dosimetry [D]

U. Reichelt, J. Henniger[1], C. Lange[1]

Published in Radiat. Prot. Dosim. 119 (2006) 479-482

Many tasks in different sectors of dosimetry are very complex and highly sensitive to changes in the radiation field. Often, only the simulation of radiation transport is capable of describing the radiation field completely. Down to sub-cellular dimensions the energy deposition by cascades of secondary electrons is the main pathway for damage induction in matter. A large number of interactions take place until such electrons are slowed down to thermal energies. Also for some problems of photon transport a large number of photon histories need to be processed. Thus the efficient non-analogue Monte Carlo program, AMOS, has been developed for photon and electron transport. Various applications and benchmarks are presented showing its ability. For radiotherapy purposes the radiation field of a brachytherapy source is calculated according to the American Association of Physicists in Medicine Task Group Report 43 (AAPM/TG43) (see Fig. 1). As additional examples, results for the detector efficiency of a high-purity germanium (HPGe) detector (Fig. 2) and a dose estimation for an X-ray shielding for radiation protection are shown.

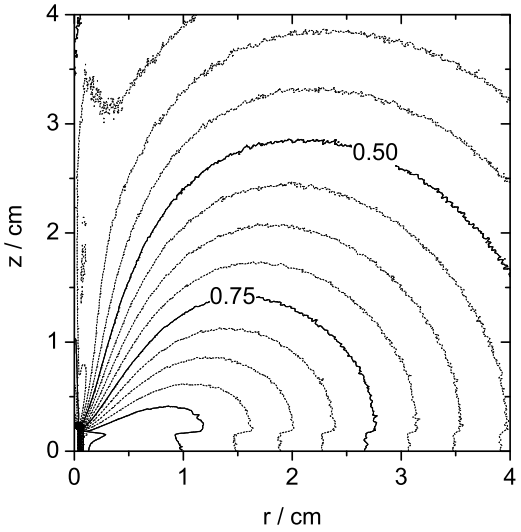

Fig. 1 *Relative dose distribution in surrounding water of a cylindrical ^{125}I Bebig brachy therapy source designed for interstitial cancer therapy of prostate gland.*

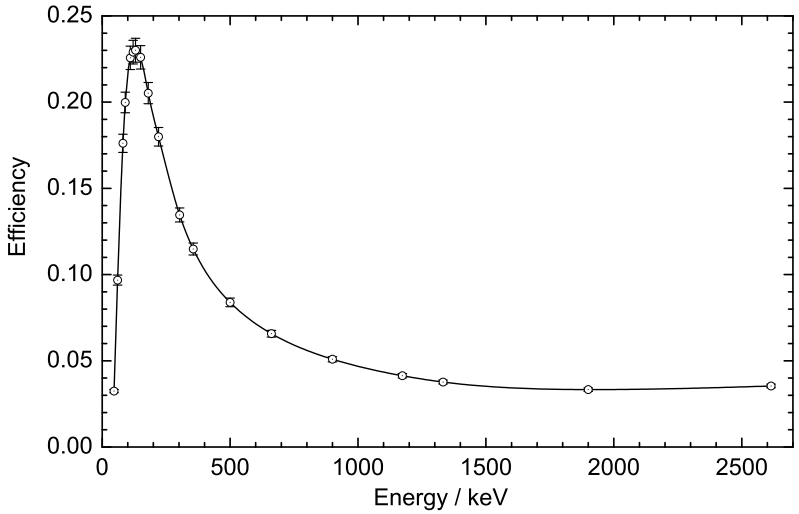

Fig. 2 *Simulated peak efficiency of full energy events for a HPGe detector.*

[1] *TU Dresden*

- ▷ **Publications**
- ▷ **Proceedings and Posters**
- ▷ **Talks and Teaching Activities**
- ▷ **Theses and Workshops**

Publications[1]

Hyperon Production in the Channel $pp \to K^+\lambda p$ Near the Reaction Threshold

Phys. Lett. B 632 (2006) 27

Abd El-Samad, S., R. Bilger, A. Böhm, K-Th. Brinkmann, H. Clement, S. Dshemuchadse, W. Eyrich, A. Erhardt, C. Fanara, A. Filippi, H. Freiesleben, M. Fritsch, R. Geyer, J. Hauffe, A. Hassan, P. Herrmann, D. Hesselbarth, B. Jakob, K. Kilian, H. Koch, J. Kress, E. Kuhlmann, S. Marcello, S. Marwinski, A. Metzger, P. Michel, K. Möller, H.P. Morsch, **L. Naumann**, E. Roderburg, A. Schamlott, P. Schönmeier, M. Schulte-Wissermann, W. Schroeder, M. Steinke, F. Stinzing, G.Y. Sun, J. Wächter, G.J. Wagner, M. Wagner, A. Wilms, S. Wirth, U. Zielinski

Single-Pion Production in pp Collisions at 0.95 GeV/c (I)

Eur. Phys. J. A 30 (2006) 443

Abd El-Samad, S., R. Bilger, K.-Th. Brinkmann, H. Clement, M. Dietrich, E. Doroshkevich, S. Dshemuchadse, A. Erhardt, W. Eyrich, A. Filippi, H. Freiesleben, M. Fritsch, R. Geyer, A. Gillitzer, J. Hauffe, D. Hesselbarth, R. Jaekel, B. Jakob, L. Karsch, K. Kilian, H. Koch, J. Kress, E. Kuhlmann, S. Marcello, S. Marwinski, R. Meier, K. Möller, H.P. Morsch, **L. Naumann**, E. Roderburg, P. Schönmeier, M. Schulte-Wissermann, W. Schroeder, M. Steinke, F. Stinzing, G.Y. Sun, J. Wächter, G.J. Wagner, M. Wagner, U. Weidlich, A. Wilms, S. Wirth, G. Zhang, P. Zupranski

Study of Spectator Tagging in the Reaction $np \to pp\pi^-$ with a Deuteron Beam

Eur. Phys. J. A 29 (2006) 353

Abdel-Bary, M., K.-Th. Brinkmann, H. Clement, E. Doroshkevich, S. Dshemuchadse, A. Erhardt, W. Eyrich, H. Freiesleben, A. Gillitzer, R. Jäkel, L. Karsch, K. Kilian, E. Kuhlmann, K. Möller, H.P. Morsch, **L. Naumann**, N. Paul, C. Pizzolotto, J. Ritman, E. Roderburg, P. Schönmeier, W. Schroeder, M. Schulte-Wissermann, G.Y. Sun, A. Teufel, A. Ucar, G.J. Wagner, M. Wagner, P. Wintz, P. Wüstner, P. Zupranski

Dielectron Production in $^{12}C + ^{12}C$ Collisions at 2 AGeV with HADES

Phys. Rev. Lett. 98 (2007) 052302

Agakichiev, G., C. Agodi, H. Alvarez-Pol, A. Balanda, D. Bertini, J. Bielcik, G. Bellia, M. Böhmer, H. Bokemeyer, J.L. Boyard, P. Braun-Munziger, P. Cabanas, S. Chernenko, T. Christ, R. Coniglione, L. Cosentino, J. Diaz, **F. Dohrmann**, I. Duran, T. Eberl, **W. Enghardt**, L. Fabbietti, O. Fateev, O. Fernandez, P. Finocchiaro, J. Friese, I. Fröhlich, B. Fuentes, C. Garabatos, J.A. Garzon, R. Gernhäuser, M. Golubeva, D. Gonzalez-Diaz, **E. Grosse**, F. Guber, T. Hennino, S. Hlavac, R. Holzmann, J. Homolka, A. Ierusalimov, I. Iori, A. Ivashkin, M. Jaskula, M. Jurkovic, M. Kargalis, M. Kajetanowicz, **B. Kämpfer, K. Kanaki**, T. Karavicheva, A. Kastenmüller, L. Kidon, P. Kienle, I. Koenig, W. Koenig, H.J. Körner, B.W. Kolb, **R. Kotte**, R. Krücken, A. Kugler, W. Kühn, R. Kulessa, A. Kurepin, S. Lang, S. Lange, J. Lehnert, E. Lins, D. Magestro, C. Maiolino, A. Malarz, J. Markert, V. Metag, J. Mousa, M. Münch, C. Müntz, **L. Naumann**, A. Nekhaev, J. Novotny, J. Otwinowski, Y. Pachmayer, V. Pechenov, T. Perez, P. Piattelli, J. Pietraszko, R. Pleskac, M. Ploskon, V. Pospisil, W. Prokopovicz, W. Przygoda, B. Ramstein, A. Reshetin, J. Ritman, M. Roy-Stephan, A. Rustamov, **A. Sadovsky**, B. Sailer, P. Salabura, M. Sanchez, P. Sapienza, A. Schmah, H. Schön, W. Schön, R.S. Simon, V. Smolyankin, L. Smykov, S. Spataro, B. Spruck, H. Ströbele, J. Stroth, C. Strurm, M. Sudol, M. Suk, A. Taranenko, P. Tlusty, A. Toia, M. Traxler, H. Tsertos, D. Vassiliev, A. Vazquez, V. Wagner, W. Walus, M. Wisniovski, T. Wojcik, **J. Wüstenfeld**, Y. Zanevsky, K. Zeitelhack, D. Zoviec, P. Zumbruch

[1] From the authors printed in **bold** further information can be obtained

Vibrational Excitations and Tilted Rotation in Lu-163

Phys. Scr. T125 (2006) 139

Almehed, D., R.G. Nazmitdinov, **F. Dönau**

Performance of RPC with low-resistive silicate glass electrodes exposed to an intense continuous electron beam

Nucl. Instr. Meth. Phys. Res. A (2007) in print

Ammosov, V., M. Ciobanu, **F. Dohrmann**, V. Gapienko, F. Guber, N. Herrmann, K.D. Hildenbrand, A. Ivashkin, **R. Kotte**, W.F.J. Müller, **L. Naumann**, A. Schüttauf, A. Semak, P. Senger, Yu. Sviridov, **A. Sytcheva, D. Stach**, V. Tiflov, **J. Wüstenfeld**, V. Zaets

Dependence of the Linewidth of Planar Electron Channeling Radiation on the Thickness of the Diamond Crystal

Phys. Rev. B 74 (2006) 045209

Azadegan, B., W. Wagner, J. Pawelke

Quasi-Particle Description of Strongly Interacting Matter: Towards a Foundation

Eur. Phys. J. C 49 (2007) 205

Bluhm, M., B. Kämpfer, R. Schulze, D. Seipt

The Two-Step Gamma Cascade Method as a Tool for Studying Photon Strength Functions of Intermediate-Weight and Heavy Nuclei

Nucl. Instr. Meth. Phys. Res. B, (2007) in print

Bečvář F., J. Honzátko, M. Krtička, S. Pašić, **G. Rusev**, I. Tomandl

Proton-Recoil Detectors for Time-of-Flight Measurements of Neutrons with Kinetic Energies from some tens of keV to a few MeV

Nucl. Instr. Meth. A (2007) in print

Beyer, R., E. Grosse, K. Heidel, J. Hutsch, A. R. Junghans, J. Klug, D. Légrády, R. Nolte, S. Röttger, **M. Sobiella, A. Wagner**

On the Detector Arrangement for In-Beam PET for Hadron Therapy Monitoring

Phys. Med. Biol. 51 (2006) 2143

Crespo, P., G. Shakirin, W. Enghardt

Effect of nuclear deformation on the electric-dipole strength in the particle-emission threshold region

Phys. Rev. C (2007) submitted

Dönau, F., G. Rusev, R. Schwengner, A.R. Junghans, K.D. Schilling, A. Wagner

Production of Strangeness in Hot and Cold Nuclear Matter Induced by Both Leptonic and Hadronic Projectiles

Int. J. Mod. Phys. E 15 (2006) 761

Dohrmann, F.

Relativistic Approaches to Investigations of Few-Nucleon Systems

Phys. Part. Nucl. 37 (2006) 867

Dorkin, S.M., L.P. Kaptari, **B. Kämpfer**, S.S. Semikh

Photodissociation of p-Process Nuclei Studied by Bremsstrahlung Induced Activation

Eur. Phys. J. A 27 (2006) s01, 135

Erhard, M., A.R. Junghans, R. Beyer, E. Grosse, J. Klug, K. Kosev, C. Nair, N. Nankov, G. Rusev, K.D. Schilling, R. Schwengner, A. Wagner

Secondary Structure and Pd(II) Coordination in S-Layer Proteins from Bacillus Sphaericus Studied by Infrared and X-Ray Absorption Spectroscopy

Biophys. J. 91 (2006) 996

Fahmy, K., M. Merroun, K. Pollmann, J. Raff, **O. Savchuk**, C. Hennig, S. Selenska-Pobell

In-Beam PET Measurements of Biological Half-Lives of ^{12}C Irradiation Induced β^+-Activity

Phys. Med. Biol. (2006) submitted

Fiedler, F., M. Sellesk, **P. Crespo**, R. Jülich, K. Parodi, **J. Pawelke, F. Pönisch, W. Enghardt**

Identification of Actinide Molecule Complexes: A New Vibrational Spectroscopic Approach at the Free Electron Laser Facility FELBE

J. Nucl. Mat. (2007) in print

Foerstendorf, H.,**W. Seidel**, K. Heim, G. Bernhard

Production of K^+ and of K^- Mesons in Heavy-Ion Collisions from 0.6 to 2.0 A GeV Incident Energy

Phys. Rev. C 75 (2007) 024906

Förster, A., F. Uhlig, I. Böttcher, D. Brill, M. Debowski, **F. Dohrmann, E. Grosse**, P. Koczon, B. Kohlmeyer, S. Lang, F. Laue, M. Mang, M. Menzel, C. Müntz, **L. Naumann**, H. Oeschler, M. Ploskon, W. Scheinast, A. Schmah, T.J. Schuck, E. Schwab, P. Senger, Y. Shin, J. Speer, H. Ströbele, C. Sturm, G. Surowka, **A. Wagner**, W. Walus

Orbits, shapes and currents

Phys. Scr. T125 (2006) 1

Frauendorf, S.

AMOS - An Effective Tool for Adjoint Monte Carlo Photon Transport

Nucl. Instr. Meth., Phys. Res. B 251 (2006) 326

Gabler, D., J. Henniger, **U. Reichelt**

Low-lying E1, M1, and E2 Strength Distributions in ^{124,126,128,129,130,131,132,134,136}Xe: Systematic Photon Scattering Experiments in the Mass Region of a Nuclear Shape or Phase Transition

Phys. Rev. C 73 (2006) 054315

Garrel, von, H., P. von Brentano, C. Fransen, G, Friessner, N. Hollmann, J. Jolie, F. Käppeler, **L. Käubler**, U. Kneissl, C. Kohstall, L. Kostov, A. Linnemann, D. Mücher, N. Pietralla, H.H. Pitz, **G. Rusev**, M. Scheck, **K.D. Schilling**, C. Scholl, **R. Schwengner**, F. Stedile, S. Walter, V. Werner, K. Wisshak

^{3}He$(\alpha,\gamma)^7$Be cross section at low energies

Phys. Rev. C 2007, in print

Gyürky, Gy., F. Confortola, H. Costantini, A. Formicola, **D. Bemmerer**, R. Bonetti, C. Broggini, P. Corvisiero, Z. Elekes, Zs. Fülöp, G. Gervino, A. Guglielmetti, C. Gustavino, G. Imbriani, M. Junker, M. Laubenstein, A. Lemut, B. Limata, V. Lozza, **M. Marta**, R. Menegazzo, P. Prati, V. Roca, C. Rolfs, C. Rossi Alvarez, E. Somorjai, O. Straniero, F. Strieder, F. Terrasi, H.P. Trautvetter

Chiral symmetry breaking in nuclei

Czech.J. Phys. 56 (2006) c85

Hamilton, J.H., S.J. Zhu, Y.X. Luo, P.M. Gore, A.V. Ramayya, J.O. Rasmussen, **S. Frauendorf**, E.F. Jones, J.K. Hwang

QCD Matter within a Quasi-Particle Model and the Critical End Point

Nucl. Phys. A 774 (2006) 757

Kämpfer, B., M. Bluhm, R. Schulze, D. Seipt, U. Heinz

Di-Electron Bremsstrahlung in Intermediate-Energy pn and Dp Collisions

Nucl. Phys. A 764 (2006) 338

Kaptari, L.P., **B. Kämpfer**

$\omega - \pi\gamma^*$ Transition Form Factor in Proton-Proton Collisions

Eur. Phys. J. A 31 (2007) 233

Kaptari, L.P., **B. Kämpfer**

Di-electrons from eta meson Dalitz decay in proton-proton collisions

Eur. Phys. J. A (2007) submitted

Kaptari, L. P., **B. Kämpfer**

Beta Decay of the Proton-Rich Nuclei ^{102}Sn and ^{104}Sn

Eur. Phys. J. A 27 (2006) 129

Karny, M., L. Batist, A. Banu, F. Becker, A. Blazhev, B.A. Brown, W. Brüchle, J. Döring, T. Faestermann, M. Górska, H. Grawe, Z. Janas, A. Jungclaus, M. Kavatsyuk, O. Kavatsyuk, R. Kirchner, M. La Commara, S. Mandal, C. Mazzocchi, K. Miernik, I. Mukha, S. Muralithar, C. Plettner, A. Pochocki, E. Roeckl, M. Romoli, K. Rykaczewski, M. Schädel, K. Schmidt, **R. Schwengner**, J. Zylicz

Beta Decay of ^{101}Sn

Eur. Phys. J. A 31 (2007) 319

Kavatsyuk, O., C. Mazzocchi, Z. Janas, A. Banu, L. Batist, F. Becker, A. Blazhev, W. Brüchle, J. Döring, T. Faestermann, M. Górska, H. Grawe, A. Jungclaus, M. Karny, M. Kavatsyuk, O. Klepper, R. Kirchner, M. La Commara, K. Miernik, I. Mukha, C. Plettner, A. Pochocki, E. Roeckl, M. Romoli, K. Rykaczewski, M. Schädel, K. Schmidt, **R. Schwengner**, J. Zylicz

Development of a neutron time-of-flight source at the ELBE accelerator

Nucl. Instr. Meth. Phys. Res. A (2007) submitted

Klug, J., E. Altstadt, C. Beckert, **R. Beyer**, H. Freiesleben, V. Galindo, **E. Grosse, A.R. Junghans**, D. Légrády, B. Naumann, K. Noack, **G. Rusev, K.D. Schilling**, R. Schlenk, S. Schneider, K. Seidel, **A. Wagner**, F.-P. Weiss

A high-resolution time-of-flight spectrometer with tracking capabilities for fission fragments and beams of exotic nuclei

Nucl. Instr. Meth. Phys. Res. A (2007) submitted

Kosev, K., N. Nankov, M. Friedrich, **E. Grosse, A. Hartmann, K. Heidel, A.R. Junghans, K.D. Schilling, R. Schwengner, M. Sobiella, A. Wagner**

Testing Timing RPC Detectors at the Rossendorf Electron Linac ELBE

Nucl. Instr. Meth. Phys. Res. A 564 (2006) 155

Kotte, R., F. Dohrmann, J. Hutsch, L. Naumann, D. Stach

RBE of 25 kV X-rays for the Survival and Induction of Micronuclei in the Human Mammary Epithelial Cell Line MCF-12A

Rad. Env. Biophys. 45 (2006) 253

Lehnert, A., E. Lessmann, J. Pawelke, W. Dörr

Investigation of a TSEE Dosimetry System for Determination of Dose in a Cell Monolayer

Rad. Measurements (2007) submitted

Lehnert, A., E. Beyreuther, E. Lessmann, J. Pawelke

RBE of 10 kV X-Rays Determined for the Human Mammary Epithelial Cell Line MCF-12A

Rad. Res. (2007) submitted

Lehnert, A., E. Lessmann, J. Pawelke, W. Dörr

Linkage Between the Intramembrane H-bond Network Around Aspartic Acid 83 and the Cytosolic Environment of Helix 8 in Photoactivated Rhodopsin

J. Molecular Biol. 366 (2007) 1129

Lehmann, N., U. Alexiev, **K. Fahmy**

Cooling Dynamics in Multi-Fragmentation Processes

Eur. Lett. 74 (2006) 806

Liu, T. X., W.G. Lynch, M.J. van Goethem, X.D. Liu, R. Shomin, W.T. Tan, M.B. Tsang, G. Verde, **A. Wagner**, H.F Xi, H.S. Xu, W.A. Friedman, S.R. Souza, R. Donangelo, L. Beaulieu, B. Davin, Y. Larochelle, T. Lefort, R.T. de Souza, R. Yanez, V.E. Viola, R.J. Charity, L.G. Sobotka

Isospin Dependence of Relative Yields of K^+ and K^0 Mesons at 1.528 AGeV

Phys. Rev. C 75 (2007) 011901

Lopez, X., Y.J. Kim, N. Herrmann, A. Andronic, V. Barret, Z. Basrak, N. Bastid, M.L. Benabderrahmane, R. Caplar, E. Cordier, P. Crochet, P. Dupieux, M. Dzelalija, Z. Fodor, I. Gasparic, A. Gobbi, Y. Grishkin, O.N. Hartmann, K.D. Hildenbrand, B. Hong, T.I. Kang, J. Kecskemeti, M. Kirejczyk, M. Kis, P. Koczon, M. Korolija, **R. Kotte**, A. Lebedev, Y. Leifels, M. Merschmeyer, **W. Neubert**, D. Pelte, M. Petrovici, F.

Rami, W. Reisdorf, M.S. Ryu, A. Schüttauf, Z. Seres, B. Sikora, K.S. Sim, V. Simion, K. Siwek-Wilczynska, V. Smolyankin, G. Stoicea, Z. Tyminski, P. Wagner, K. Wisniewski, **D. Wohlfarth**, Z. Xiao, I. Yushmanov, A. Zhilin, G. Ferini, T. Gaitanos

First Sub-Threshold Measurement of Sigma(1385) Production in Al+Al Collisions at 1.9 AGeV

Phys. Rev. Lett. (2007) submitted

Lopez, X., N. Herrmann, P. Crochet, A. Andronic, Z. Basrak, N. Bastid, M.L. Benabderrahmane, P. Bühler, M. Cargnelli, R. Caplar, E. Cordier, P. Dupieux, M. Dzelalija, L. Fabietti, Z. Fodor, I. Gasparic, Y. Grishkin, O.N. Hartmann, K.D. Hildenbrand, B. Hong, T.I. Kang, J. Kecskemeti, M. Kirejczyk, Y.J. Kim, M. Kis, P. Koczon, M. Korolija, **R. Kotte**, A. Lebedev, Y. Leifels, J. Marton, M. Merschmeyer, **W. Neubert**, D. Pelte, M. Petrovici, F. Rami, W. Reisdorf, M.S. Ryu, A. Schüttauf, Z. Seres, B. Sikora, K.S. Sim, V. Simion, K. Siwek-Wilczynska, V. Smolyankin, G. Stoicea, K. Suzuki, Z. Tyminski, P. Wagner, K. Wisniewski, **D. Wohlfarth**, Z. Xiao, I. Yushmanov, X.Y. Zhang, A. Zhilin, J. Zmeskal

Structure and pH-Sensitivity of the Transmembrane Segment 3 of Rhodopsin

Biopolymers 82 (2006) 329

Madathil, S., G. Furlinski, K. Fahmy

95 MeV neutron scattering on hydrogen, deuterium, carbon, and oxygen

Phys. Rev. C 74 (2006) 054002

Mermod, P., J. Blomgren, C. Johansson, A. Öhrn, M. Österlund, S. Pomp, B. Bergenwall, **J. Klug**, L. Nilsson, N. Olsson, U. Tippawan, P. Nadel-Turonski, O. Jonsson, A. Prokofiev, P.-U. Renberg, Y. Maeda, H. Sakai, A. Tamii, K. Amos, R. Crespo, A. Moro

Development of an Algorithm for Respiratory Motion Correction in Gated PET Investigations of the Thorax

Phys. Med. Biol. (2007) submitted

Möckel, D., U. Just, J. van den Hoff

Quantification of β^+ activity generated by hard photons by means of PET

Phys. Med. Biol. (2007) submitted

Möckel, D., H. Müller, J. Pawelke, M. Sommer, E. Will, **W. Enghardt**

In-beam PET at High-Energy Photon Beams: A Feasibility Study

Phys. Med. Biol. 51 (2006) 1779

Müller, H., W. Enghardt

Isotope ratios and isoscaling of spallation products in p(1 GeV) + A reactions

Eur. Phys. J. A 31 (2007) 125

Neubert, W., M.N. Andonenko, L.N. Andonenko

Electron beam monitoring for channeling radiation measurements

Nucl. Instr. Meth., Phys. Res. B 245 (2007) 319

Neubert, W., B. Azadegan, W. Enghardt, K. Heidel, J. Pawelke, W. Wagner

Metal Binding by Bacteria from Uranium Mining Waste Piles and its Technological Applications

Biotechnology Adv. 24 (2006) 58

Pollmann, P., J. Raff, M. Merroun, **K. Fahmy**, S. Selenska-Pobell

HADES Experiment: Di-Lepton Spectroscopy in p+p (2.2 GeV) and C+C (1 and 2 AGeV) Collisions

Acta Phys. Pol. B 37 (2006) 139

Przygoda, W., G. Agakishiev, C. Agodi, H. Alvarez-Pol, A. Balanda, R. Bassini, G. Bellia, D. Belver, J. Bielcik, A. Blanco, M. Boehmer, C. Boiano, A. Bortolotti, J. Boyard, S. Brambilla, P. Braun-Munzinger, P. Cabanelas, S. Chernenko, T. Christ, R. Coniglione, M. Dahlinger, J. Diaz, R. Djeridi, **F. Dohrmann**, I. Duran, T. Eberl, **W. Enghardt**, L. Fabbietti, O. Fateev, P. Finocchiaro, P. Fonte, J. Friese, I. Froehlich, J. Garzon, R. Gernhaeuser, M. Golubeva, D. Gonzalez-Diaz, **E. Grosse**, F. Guber, T. Heinz, T. Hennino, S. Hlavac, J. Hoffmann, R. Holzmann, A. Ierusalimov, I. Iori, A. Ivashkin, M. Jaskula, M. Jurkovic, M. Kajetanowicz, **B. Kämpfer, K. Kanaki**, T. Karavicheva, D. Kirschner, I. Koenig, W. Koenig, B. Kolb, U. Kopf, **R. Kotte**, J. Kotulic-Bunta, R. Kruecken, A. Kugler, W. Kuehn, R. Kulessa, S. Lang, J. Lehnert, L. Maier, P. Maier-Komor, C. Maiolino, J. Marin, J. Markert, V. Metag, N. Montes, E. Moriniere, J. Mousa, M. Muench, C. Muentz, **L. Naumann**, R. Novotny, J. Novotny, W. Ott, J. Otwinowski, Y. Pachmayer, T. Perez, V. Pechenov, J. Pietraszko, J. Pinhao, R. Pleskac, V. Pospisil, A. Pullia, N. Rabin, B. Ramstein, S. Riboldi, J. Ritman, P. Rosier, M. Roy-Stephan, A. Rustamov, **A. Sadovsky**, B. Sailer, P. Salabura, P. Sapienza, A. Schmah, W. Schoen, C. Schroeder, E. Schwab, P. Senger, R. Simon, V. Smolyankin, L. Smykov, S. Spataro, B. Spruck, H. Stroebele, J. Stroth, C. Sturm, M. Sudol, V. Tiflov, P. Tlusty, A. Toia, M. Traxler, H. Tsertos, I. Turzo, V. Wagner, W. Walus, C. Willmott, S. Winkler, M. Wisniowski, T. Wojcik, **J. Wüstenfeld**, Y. Zanevsky, P. Zumbruch

Application of Advanced Monte Carlo Methods in Numerical Dosimetry

Rad. Prot. Dos. 119 (2006) 479

Reichelt, U., J. Henniger, C. Lange

Systematics of Pion Emission in Heavy Ion Collisions in the 1 A GeV Regime

Nucl. Phys. A 781 (2007) 459

Reisdorf, W., M. Stockmeier, A. Andronic, M.L. Benabderrahmane, O.N. Hartmann, N. Herrmann, K.D. Hildenbrand, Y.J. Kim, M. Kis, P. Koczon, T. Kress, Y. Leifels, X, Lopez, M. Merschmeyer, A. Schüttauf, J.P. Alard, V. Barret, Z. Basrak, N. Bastid, R. Caplar, P. Crochet, P. Dupieux, M. Dzelalija, Z. Fodor, Y. Grishkin, B. Hong, T.I. Kang, J. Kecskemeti, M. Kirejczyk, M. Korolija, **R. Kotte**, A. Lebedev, T. Matulewicz, **W. Neubert**, M. Petrovici, F. Rami, M.S. Ryu, Z. Seres, B. Sikora, K.S. Sim, V. Simion, K. Siwek-Wilczynska, V. Smolyankin, G. Stoicea, Z. Tyminski, K. Wisniewski, **D. Wohlfarth**, Z. Xiao, H.S. Xu, I. Yushmanov, A. Zhilin

Multiple octupole-type band structures in ^{220}Th: Reflection-asymmetric tidal waves?

Phys. Rev. C 74 (2006) 044305

Reviol, W., C.J. Chiara, M. Montero, D. G. Sarantitis, O.L. Pechenaya, M.P. Carpenter, R.V.F. Janssens, T.L. Khoo, T. Lauritsen, C. J. Lister, D. Seweryniak, S. Zhu, **S. Frauendorf**

Determining Beam Parameters in a Storage Ring with a Cylindrical Hodoscope Using Elastic Proton-Proton Scattering

Nucl. Instr. Meth. Phys. Res. A 556 (2006) 57

Rohdjeß, H., D. Albers, J. Bisplinghoff, R. Bollmann, K. Büßer, O. Diehl, **F. Dohrmann**, H.-P. Engelhardt, P.D. Eversheim, M. Gasthuber, J. Greiff, A. Groß, R. Groß-Hardt, F. Hinterberger, M. Igelbrink, R. Langkau, R. Maier, F. Mosel, M. Müller, M. Münstermann, D. Prasuhn, P. von Rossen, H. Scheid, N. Schirm, F. Schwandt, W. Scobel, H.J. Trelle, A. Wellinghausen, W. Wiedmann, K. Woller, R. Ziegler

Radiation Damage of Polypropylene Fiber Targets in Storage Rings

Nucl. Instr.. Meth. Phys. Res. B 243 (2006) 127

Rohdjeß, H., D. Albers, J. Bisplinghoff, R. Bollmann, K. Büßer, O. Diehl, **F. Dohrmann**, H.-P. Engelhardt, P.D. Eversheim, J. Greiff, A. Groß, R. Groß-Hardt, F. Hinterberger, M. Igelbrink, R. Langkau, R. Maier, F. Mosel, M. Müller, M. Münstermann, D. Prasuhn, P. von Rossen, H. Scheid, N. Schirm, F. Schwandt, W. Scobel, H.J. Trelle, A. Wellinghausen, W. Wiedmann, K. Woller, R. Ziegler

Upper Limits on Resonance Contributions to Proton-Proton Elastic Scattering in the c.m. Mass Range 2.05-2.85 GeV/c^2

Eur. Phys. J. A 28 (2006) 115

Rohdjeß, H., M. Altmeier, F. Bauer, J. Bisplinghoff, R. Bollmann, Büßer, M. Busch, O. Diehl, **F. Dohrmann**, H.-P. Engelhardt, J. Ernst, P.D. Eversheim, K.O. Eyser, O. Felden, R. Gebel, A. Groß, R. Groß-Hardt, F. Hinterberger, R. Langkau, J. Lindlein, R. Maier, F. Mosel, D. Prasuhn, P. von Rossen, H. Scheid, F. Schulz-Rojahn, F. Schwandt, V. Schwarz, W. Scobel, H.-J. Trelle, K. Ulbrich, E. Weise, A. Wellinghausen, K. Woller, R. Ziegler

Pygmy Dipole Strength Close to Particle-Separation Energies - the Case of the Mo Isotopes

Eur. Phys. J. A 27 (2006) s01, 171

Rusev, G., E. Grosse, M. Erhard, A.R. Junghans, K. Kosev, K.D. Schilling, R. Schwengner, A. Wagner

Systematics of Magnetic Dipole Strength in the Stable Even-Mass Mo Isotopes

Phys. Rev. C 73 (2006) 044308

Rusev, G., R. Schwengner, F. Dönau, M. Erhard, S. Frauendorf, E. Grosse, A.R. Junghans, L. Käubler, K. Kosev, L.K. Kostov, S. Mallion,**K.D. Schilling, A. Wagner**, H. von Garrel, U. Kneissl, C. Kohstall, M. Kreutz, H.H. Pitz, M. Scheck, F. Stedile, P. von Brentano, J. Jolie, A. Linnemann, N. Pietralla, V. Werner,

In-Medium Effects on Phase Space Distributions of Antikaons Measured in Proton-Nucleus Collisions

Phys. Rev. Lett. 96 (2006) 072301

Scheinast, W., I. Böttcher, M. Debowski, **F. Dohrmann**, A. Förster, **E. Grosse**, P. Koczoń, B. Kohlmeyer, F. Laue, M. Menzel, **L. Naumann**, E. Schwab, P. Senger, Y. Shin, H. Ströbele, C. Sturm, G. Surówka, F. Uhlig, **A. Wagner**, W. Waluś, **B. Kämpfer, H.W. Barz**

Low-Energy Cross Section of the ^{7}Be(p,γ)^{8}B Solar Fusion Reaction from Coulomb Dissociation of ^{8}B

Phys,. Rev. C 73 (2006) 015806

Schümann, F., S. Typel, F. Hammache, K. Sümmerer, F. Uhlig, I. Böttcher, D. Cortina, A. Förster, M. Gai, H. Geissel, U. Greife, **E. Grosse**, N. Iwasa, P. Koczoń, B. Kohlmeyer, R. Kulessa, H. Kumagai, N. Kurz, M. Menzel, T. Motobayashi, H. Oeschler, A. Ozawa, M. Płoskoń, W. Prokopowicz, E. Schwab, P. Senger, F. Strieder, C. Sturm, Zhi-Yu Sun, G.Surówka, **A. Wagner**, W. Waluś

Quadrupole moment of the 8$^+$ yrast state in ^{84}Kr

Phys. Rev. C 74 (2006) 034309

Schwengner, R., D.L. Balabanski, G. Neyens, N. Benouaret, D. Borremans, N. Coulier, M. de Rydt, G.

Georgiev, S. Mallion, G. Rainovski, **G. Rusev**, S. Teughels, K. Vyvey

Dipole-strength distributions up to the particle-separation energies and photodissociation of Mo isotopes

Nucl. Phys. A (2007) in print

Schwengner, R., N. Benouaret, **R. Beyer, F. Dönau, M. Erhard, S. Frauendorf, E. Grosse, A.R. Junghans, J. Klug, K. Kosev, C. Nair**, N. Nankov, **G. Rusev, K.D. Schilling, A. Wagner**

Dipole response of ^{88}Sr up to the neutron-separation energy

Phys. Rev. C (2007) submitted

Schwengner, R., G. Rusev, N. Benouaret, **R. Beyer, M. Erhard, E. Grosse, A.R. Junghans, J. Klug, K. Kosev**, L. Kostov, **C. Nair**, N. Nankov, **K.D. Schilling, A. Wagner**

A Method for System Matrix Construction and Processing for Reconstruction of In-Beam PET Data

IEEE Transactions on Nucl. Science (2007) submitted

Shakirin, G., P. Crespo, W. Enghardt

Investigating the accuracy of the FLUKA code for transport of therapeutic ion beams in matter

Phys. Med. Biol. 51 (2006) 4385

Sommerer, F., K. Parodi, A. Ferrari, K. Poljanc, **W. Enghardt**, H. Aiginger

Light-Ion Production in the Interaction of 96 MeV Neutrons with Oxygen

Phys. Rev. C 73 (2006) 034611

Tippawan, U., S. Pomp, A. Atac, B. Bergenwall, J. Blomgren, S. Dangtip, A. Hildebrand, C. Johansson, **J. Klug**, P. Mermod, L. Nilsson, M. Österlund, N.Olsson, A. Prokofiev, P. Nadel-Turonski, V. Corcalciuc, A. Koning

Θ^+ formation in Inclusive $\gamma D \to pK^-X$

Phys. Rev. C 74 (2006) 055206

Titov, A. I., **B. Kämpfer**, S. Date, Y. Ohashi

Electromagnetic Probes of Strongly Interacting Matter: Probes of Chiral Symmetry Restoration?

Heavy Ion Phys. 26 (2006) 35

Thomas, R., K. Gallmeister, **S. Zschocke, B. Kämpfer**

Transition Probabilities in ^{134}Pr: A Test for Chirality in Nuclear Systems

Phys. Rev. Lett. 96 (2006) 052501

Tonev, D., G. de Angelis, P. Petkov, A. Dewald, S. Brant, **S. Frauendorf**, D.L. Balabanski, P. Pejovic, D. Bazzacco, P. Bednarczyk, F. Camera, A. Fitzler, A. Gadea, S. Lenzi, S. Lunardi, N. Marginean, O. Möller, D.R. Napoli, A. Paleni, C.M. Petrache, G. Prete, K.O. Zell, Y.H. Zhang, Jing-ye Zhang, Q. Zhong, D. Curien

Lifetime measurements in Pr-134 and chirality in nuclei

Int. J. Mod. Phys., E-Nucl. Phys. 15 (2006) 1531

Tonev, D., P. Petkov, D.L. Balabanski, G. De Angelis, A. Gadea, D.R. Napoli, N. Marginean, A. Dewald, P. Pejovic, A. Fitzler, O. Moeller, K.O.Zell, S. Brant, **S. Frauendorf**, D. Bazzacco, S. Lenzi, S. Lunardi, P. Bednarczyk, D. Curien, C. Petrache, Q. Zhong, Y.H. Zhang, Jing-Ye Zhang

Planar channeling radiation from electrons in quartz

Europhys. Lett. (2007) submitted

Wagner, W., B. Azadegan, L.Sh. Grigoryan, **J. Pawelke**

Photon scattering experiments on the quasistable odd-odd mass nucleus ^{176}Lu

Phys. Rev. C 75 (2007) 034301

Walter, S. F. Stedile, J.J. Carroll, C. Fransen, G. Friessner, N. Hollmann, H. von Garrel, J. Jolie, O. Karg, F. Käppeler, U. Kneissl, C. Kohstall, P. von Neumann-Cosel, A. Linnemann, D. Mücher, N. Pietralla, H.H. Pitz, G. Rusev, M. Scheck, C. Scholl, **R. Schwengner**, V. Werner, K. Wisshak

Synthesis and Biological Evaluation of a New Type of ^{99m}Technetium-Labeled Fatty Acid for Myocardial Metabolism Imaging

Bioconjugate Chemistry 1 (2007) 216

Walther, M., C. Jung, R. Bergmann, J. Pietzsch, K. Rode, **K. Fahmy**, P. Mirtschink, S. Stehr, A. Heintz, G. Wunderlich, W. Kraus, H.-J. Pietzsch, J. Kropp, A. Deussen, H. Spies

Status quo of the Dresden High Magnetic Field Laboratory

J. Phys.: Conf. Series 51 (2006) 619

Wosnitza, J., A.D. Bianci, T. Herrmannsdörfer, **R. Wünsch**, S. Zherlitsyn, S. Zvyagin

Proceedings and Reports

Atanasova, L., D.L. Balabanski, M. Hass, D. Bazzacco, F. Becker, P. Bednarczyk, G. Benzoni, N. Blasi, A. Blazhev, A. Bracco, C. Brandau, L. Caceres, F. Camera, S.K. Chamoli, F.C.L. Crespi, P. Detistov, P. Doornenbal, C. Fahlander, E. Farnea, G. Georgiev, J. Gerl, K. Gladnishki, M. Górska, H.Grawe, J. Grebosz, R. Hoischen, G. Ilie, M. Ionescu-Bujor, A. Iordachescu, A. Jungclaus, G. Lo Bianco, M. Kmiecik, I. Kojouharov, N. Kurz, S. Lakshmi, R. Lozeva, A. Maj, D. Montanari, G. Neyens, M. Pfützner, S. Pietri, Zs. Podolyak, W. Prokopowicz, D. Rudolph, **G. Rusev**, T. R. Saito, A. Saltarelli, H. Schaffner, **R. Schwengner**, G. Simpson, S. Tashenov, J.J. Valiente-Dobón, N. Vermeulen, J. Walker, E. Werner-Malento, O. Wieland, H.J. Wollersheim, g-factor measurements at RISING: the case of ^{127}Sn
Proc. of the XXV Int. WS on Nuclear Theory, Rila Mountains, Bulgaria, 2006, p. 161

Azadegan, B., W. Wagner, J. Pawelke, L.Sh. Grigoryan
Planar channeling radiation from electrons in quartz
"Channeling 2006", Int. Conf. on Charged and Neutral Particles Channeling Phenomena, 2006, Frascati (Rome), Italy, S.B. Dabagov (Ed.), Proc. SPIE, 2007, Bellingham, USA

Bluhm, M., B. Kämpfer, R. Schulze, D. Seipt
Isentronic equation of state of two-flavour QCD in a quasi-particle model
Int. WS on Hot and Dense Matter in Relativistic Heavy Ion Collisions, 2006, Budapest, Hungary

Bluhm, M., B. Kämpfer
Quasi-particle perspective on critical end-point
Critical Point and Onset of Deconfinement, 2006, Florence, Italy

Bluhm, M., R. Schulze, D. Seipt, **B. Kämpfer**
Quasi-Particle Perspective on Equation of State
Quark Confinement and Hadron Spectrum VII, 2006, Ponta Delgada Acores, Portugal

Erhard, M., C. Nair, R. Beyer, E. Grosse, A.R. Junghans, J. Klug, K. Kosev, N. Nankov, G. Rusev, K.D. Schilling, R. Schwengner, A. Wagner
Electromagnetic excitations in nuclei: from photon scattering to photodisintegration
Int. Symposium on Nuclear Astrophysics - Nuclei in the Cosmos - IX , CERN, 2006, Geneva, Schweiz, Trieste: POS Proc. of Science, ISSN 1824-8039, PoS(NIC-IX) 056

Freitag, M., R. Schlenck, **W. Seidel**, U. Willkommen, **R. Wünsch**, B. Wustmann
The partial waveguide resonator of the U100-FEL at FZ Rossendorf
Proc. 28th Int. Free Electron Laser Conf., 2006, Berlin, Deutschland

Gensch, M., J.S. Lee, K. Hinrichs, N. Esser, **W. Seidel**, A. Röseler, U. Schade
Single Shot Intrared Ellipsometry with a Free Electron Laser and its Potential Applications
Proc of 31st Int. Conf. on Infrared and Millimeter Waves and 14th Int. Conf. on Terahertz Electronics, 2006, Shanghai, China, IRMMW-THz 2006, 1-4244-0400-2, 416-416

Hammache, F., D. Galaviz, K. Sümmerer, S. Typel, F. Attallah, M. Caamano, A. Coc, D. Cortina, H. Geissel, M. Hellström, N. Iwasa, J. Kiener, P. Coczon, B. Kohlmeyer, E. Schwab, K. Schwarz, F. Schümann, P. Senger, O. Sorlin, V. Tatischeff, J. P. Thibaud, F. Uhlig, **A. Wagner**, A. Walus
Cross section measurements of the Big Bang nucleosynthesis reaction $D(\alpha,\gamma)^6Li$ by Coulomb dissociation of ^6Li
Proc. of the Int. Conf. on Frontiers in Nuclear Structure, Astrophysics and Reactions, Kos, Greece, 2005, American Institute of Physics, CP831 (2006) 21

Klug, J., E. Altstadt, C. Beckert, **R. Beyer**, H. Freiesleben, V. Galindo, M. Greschner, **E. Grosse, A.R. Junghans**, D. Légrády, B. Naumann, K. Noack, **K.D. Schilling**, R. Schlenk, S. Schneider, K. Seidel, **A. Wagner**, F.-P. Weiss
Development of a neutron time-of-flight source at the ELBE accelerator
Int. WS on Fast Neutron Detectors and Applications, Cape Town, South Africa, 2006, Proc. of Sience, PoS (FNDA2006) 15

Klug, J., E. Altstadt, C. Beckert, **R. Beyer**, H. Freiesleben, M. Greschner, **E. Grosse, A.R. Junghans**, B. Naumann, K. Noack, S. Schneider, K. Seidel, **A. Wagner**, F.-P. Weiss
Development of a neutron time-of-flight source at the ELBE accelerator
Int. WS on Fast Neutron Detectors and Applications, 2005, Pavia, Italy J. Phys.: Conf. Ser. 41 (2006) 296

Lehnert, A., E. Beyreuther, W. Enghardt, E. Lessmann, J. Pawelke, W. Wagner, W. Dörr
RBE of soft X.rays for chromosomal damage determined fpr two human mammary epithelial cell lines
35th Annual Meeting of the Eur. Radiation Res. Society, 2006, Kiev, Ukraine, Book of Abstracts, p. 32

Lehnert, U., P. Michel, **W. Seidel**, J. Teichert, **R. Wünsch**
Laser Gain and Intra-cavity Losses of the ELBE Mid-IR FEL
Proc of 28th Free Electron Laser Conf. 2006, Berlin/Rossendorf, Germany

Michel, P., H. Buettig, F.G. Gabriel, M. Helm, U. Lehnert, Ch. Schneider, R. Schurig, **W. Seidel**, D. Stehr, J. Teichert, S. Winnerl, **R. Wünsch**
The Rossendorf IR-FEL ELBE
Proc. of the 28th Free Electron Laser Conf. 2006, Berlin, Germany

Neyens, G., L. Atanasova, D.L. Balabanski, F. Becker, P. Bednarczyk, L. Caceres, P. Doornenbal, J. Gerl, M. Górska, J. Grebosz, M. Hass, G. Ilie, N. Kurz, I. Kojouharov, R. Lozeva, A. Maj, M. Pfützner, S. Pietri, Zs. Podolyak, W. Prokopowicz, T.R. Saitoh, H. Schaffner, G. Simpson, N. Vermeulen, E. Werner-Malento, J. Walker, H.J. Wollersheim, D. Bazzacco, G. Benzoni, A. Blazhev, N. Blasi, A. Bracco, C. Brandau, F. Camera, S.K. Chamoli, S. Chmel, F.C.L. Crespi, J.M. Daugas, M. De Rydt, P. Detistov, C. Fahlander, E. Farnea, G. Georgiev, K. Gladnishki, R. Hoischen, M. Ionescu-Bujor, A. Iordachescu, J. Jolie, A. Jungclaus, M. Kmiecik, A. Krasznahorkay, R. Kulessa, S. Lakshmi, G. Lo Bianco, S. Mallion, K. Mazurek, W. Meczynski, D. Montanari, S. Myalsky, O. Perru, D. Rudolph, **G. Rusev**, A. Saltarelli, **R. Schwengner**, J. Styczen, K. Turzó, J.J. Valiente-Dobón, O. Wieland, M. Zieblinski,
g-factor measurements on relativistic isomeric beams produced by fragmentation and U-fission: the g-Rising project at GSI
Proc. of the Zakopane Conf. on Nuclear Physics, Poland 2006, in print

Preusche, S., F. Wüst, S. Seifert, **K.D. Schilling**, R. Wenzel, N. Dohn, J. Steinbach
Production of ^{86}Y and ^{56}Co at the Rossendorf CYCLONE 18/9
Proc of 11th Int. WS on Targetry and Target Chemistry, p. 86, 2006, Cambridge, Great Britain

Schwengner, R., G. Rusev, F. Dönau, M. Erhard, E. Grosse, A.R. Junghans, K. Kosev, C. Nair, N. Nankov, K.D. Schilling, A. Wagner
Nuclear-structure and nuclear-astrophysics experiments at the superconducting electron accelerator ELBE
XVI Int. School on Nuclear Physics, Neutron Physics and Nuclear Energy, 2005, INRNE Sofia, Varna, Bulgaria, in print

Shakirin, G., P. Crespo, W. Enghardt
A Method for System Matrix Construction and Processing for Reconstruction of In-Beam PET Data
Nucl. Science Symposium and Medical Imaging Conf., IEEE, 2006, San Diego, USA, in print

Seidel, W., S. Friebel, R. Jainsch, M. Justus, K.-W. Leege, D. Pröhl, D. Stehr, H. Weigelt, S. Winnerl, **D. Wohlfarth**
Remote Controlled IR-Diagnostic Station for the FEL at Rossendorf
28th Int. Free Electron Laser Conf. 2006, Berlin/Rossendorf, Deutschland, JACoW, FEL06

Thomas, R., S. Zschocke, T. Hilger, B. Kämpfer
Hunting Medium Modifications of the Chiral Condensate
44th Int. Winter Meeting on Nuclear Physics, 2006, Bormio, Italy

Thomas, R., B. Kämpfer
Impact of Four-Quark Condensates on In-Medium Effects of Hadrons
Quark Confinement and the Hadron Spectrum VII, 02.-07.09.2006, Ponta Delgado, Azores, Portugal

A. Wagner, M. Erhard, E. Grosse, A.R. Junghans, J. Klug, K. Kosev, C. Nair, N. Nankov, G. Rusev, K.D. Schilling, R. Schwengner
Photodissociation experiments for p-process nuclei
Proc. of the Int. Conf. on Frontiers in Nuclear Structure, Astrophysics and Reactions, 2005, Kos, Greece, American Institute of Physics, CP831 (2006) 16

Winnerl, S., D. Stehr, O. Drachenko, H. Schneider, M. Helm, **W. Seidel**, P. Michel, S. Schneider, J. Seidel, S. Grafström, L.-M. Eng, T. Roch, G. Strasser, T. Maier, M. Walther
FELBE Free-Electron Laser: Status and Application for Time Resolved Spectrocopy Experiments
Joint 31th. Int. Conf. on Infrared and Millimeter Waves and 14th. Int. Conf. on Terahertz Electronics, 2006, Shanghai, China

Posters at Conferences

Crevenna, A.,**S. Madathil, K. Fahmy**, J. Howard
Structural Properties of the Kinesin 'Coiled-coil Break' Region
Annual Meeting of the German Biophysical Society, 2006, Mainz, Germany

Gensch, M., J.S. Lee, K. Hinrichs, N. Esser, **W. Seidel**, A. Röseler, U. Schade
Single Shot Intrared Ellipsometry with a Free Electron Laser and its Potential Applications
Joint 31st International Conference on Infrared and Millimeter Waves and 14th International Conference on Terahertz Electronics, 2006, Shanghai, China

Lehnert, U., P. Michel, **W. Seidel**, J. Teichert, **R. Wünsch**
Laser Gain and Intra-cavity Losses of the ELBE Mid-IR FEL
28th Free Electron Laser Conference 2006, Berlin, Germany

Madathil, S., K. Fahmy
Proton-Regulated Side Chain Lipid Interactions in Conformational Switching by Transmembrane G-Protein-Coupled Receptors
Int. Workshop on Dynamics of Artificial and Biological Membranes, 2006, Gomadingen, Germany

Pönisch, F.
Properties of unflattened photon beams shaped by a multi leaf collimator
AAPM Konferenz, 2006, Orlando, FL, USA

Pollmann, K., M. Merroun, J. Raff, **K. Fahmy**, C. Hennig, S. Selenska-Pobell, T. Hermannsdörfer
Synthesis of metal nanoparticles using bacterial surface layers (S-layers) as biological templates
E-MRS 2006 Spring Meeting, 2006, Nice, France

Shakirin, G., P. Crespo, W. Enghardt
A Method for System Matrix Construction and Processing for Reconstruction of In-Beam PET Data
Nuclear Science Symposium and Medical Imaging Conference, 2006, San Diego, USA

Seidel, W., S. Friebel, R. Jainsch, M. Justus, K.W. Leege, D. Pröhl, D. Stehr, H. Weigelt, S. Winnerl, **D. Wohlfarth**
Remote Controlled IR-Diagnostic Station for the FEL at Rossendorf
28th Int. Free Electron Laser Conference 2006, Berlin, Germany

Freitag, M., R. Schlenck, **W. Seidel**, U. Willkommen, **E. Wünsch**, B. Wustmann
The partial waveguide resonator of the U100-FEL at FZ Rossendorf
28th Int. Free Electron Laser Conference 2006, Berlin, Germany

Talks at Conferences and other Institutes

Azadegan, B., W. Wagner, J. Pawelke, L.Sh. Grigoryan
Planar channeling radiation from electrons in quartz
"Channeling 2006", Int. Conf. on Charged and Neutral Particles Channeling Phenomena, 2006, Frascati (Rome), Italy, S.B. Dabagov (Ed.), Proc. SPIE, 2007, Bellingham, USA

Bemmerer, D.
The Big Bang, our Sun and the $^3\mathrm{He}(\alpha,\gamma)^7\mathrm{Be}$ Reaction
Seminar Nukleare Astrophysik, TU Berlin, Oct. 30, 2006, Berlin, Germany

Beyer, R.
Detection of neutrons with kinetic energy from 24 keV to 1.2 MeV with long plastic scintillators
Workshop on neutron detectors for FAIR and other facilities, July 13-14, 2006, CIEMAT, Madrid, Spain

Beyreuther, E.
Relative biological effectiveness of X-rays
Seminar der AG Umweltbiologie, TU Bergakademie Freiberg, Oct. 05, 2006, Freiberg, Germany

Bluhm, M.
Lattice QCD Based Equation of State - within a Quasi-Particle Perspective
DPG Tagung, March 24, 2006, München, Germany

Bluhm, M.
Lattice QCD Based Equation of State - within a Quasi-Particle Perspective
Int. Workshop on Hot and Dense Matter in Relativistic Heavy Ion Collisions, Apr. 9, 2006, Budapest, Hungary

Bluhm, M.
QCD Equation of State in a Quasi-Particle Perspective
Workshop for Young Scientists on the Physics of Ultrarelativistic Nucleus-Nucleus Collisions, Hot Quarks 2006, May 15-20, 2006, Villasimius, Sardinien, Italy

Bluhm, M.
Quasi-Particle Model for the EOS - critical point imaginary μ
Workshop des Virtuellen Inst., Oct. 16, 2006, Rathen, Germany

Crespo, P., M. Erhard
Strahlungsdetektoren für astrophysikalische Messungen
Lehrerfortbildung 2005/2006 - Astrophysik, Febr. 17, 2006, FZD, Dresden, Germany

Crespo, P.
Monitoring Carbon Ion Tumor Therapy with In-Beam Positron Emission Tomography: Status and Trends
Seminar on Molecular Life Sciences and Imaging, Dr. K. Fahmy, Febr. 28, 2006, FZD, Dresden, Germany

Crespo, P., W. Enghardt, **F. Fiedler**, D. Möckel, J. Pawelke, G. Shakirin
In-beam PET für die Qualitätssicherung der Ionentherapie - Möglichkeiten und Grenzen
DPG Frühjahrstagung, DPG, March 13-15, 2006, Heidelberg, Germany

Crespo, P., T. Barthel, M. Kapusta, K. Heidel, M. Moszyński, J. Pawelke, W. Enghardt
New developments in detectors for in-beam PET
DPG Frühjahrstagung, DPG, March 13-15, 2006, Heidelberg, Germany

Dohrmann, F., R. Kotte, L. Naumann
Testing sub-100ps RPC detectors at ELBE
7th CBM collaboration meeting, GSI, Febr. 28- March 3, 2006, Darmstadt, Germany

Dohrmann, F., invited lecture
Electroproduction of light hypernuclei on Helium
PANDA collaboration meeting Dresden, Inst. f. Kern- u. Teilchenphysik, TU Dresden, March 9-10, 2006, Dresden, Germany

Enghardt, W., invited lecture
In-beam PET for radiotherapy monitoring
Conf. on Clinical and Experimental Research in Radiation Oncology, Jan. 24, 2006, Les Menuires, France

Enghardt, W.
WP1: Development of PET/CT for oncology
BioCare Meeting, EU FP6 Integrated Project Biocare, May 8-9, 2006, Dresden, Germany

Enghardt, W., invited lecture
Der postgraduale Masterstudiengang "Medical Radiation Sciences" in Dresden
XVIII. Winterschule der DGMP. March 14, 2006, Pichel, Austria

Enghardt, W., invited lecture
Visionen der Medizinphysik
12. Jahrestagung der Deutschen Gesellschaft für Radioonkologie (DEGRO), May 25, 2006, Dresden, Germany

Enghardt, W., invited lecture
Der postgraduale Masterstudiengang "Medical Radiation Sciences" und die Ausbildung von Medizinphysik-Experten in Dresden
12. Jahrestagung der Deutschen Gesellschaft für Radioonkologie (DEGRO), May 27, 2006, Dresden, Germany

Enghardt, W., invited lecture
In-beam PET in der Hadronentherapie
37. Jahrestagung der Deutschen Gesellschaft für Medizinische Physik, Sept. 21, 2006, Regensburg, Germany

Enghardt, W., invited lecture
Präzisionsbestrahlung auf der Basis biologischer Daten
5. Leipziger Forum Computer Assisted Surgery, Jan. 7, 2006, Leipzig, Germany

Enghardt, W., invited lecture
Der weiterbildende Masterstudiengang "Medical Radiation Sciences" an der TU Dresden
Techn. Fachhochschule Berlin, Dec. 12, 2006, Berlin, Germany

Fahmy, K.
Molecular switching in GPCRs: FTIR- and Fluorescence-Spectroscopyic Identification of Functional Modules in Rhodopsin
Inst. of Technology Madras, Dec 7, 2006, Chennai, India

Fahmy, K.
DNA-Backbone Dynamics Studied by Time-Resolved Infrared Spectroscopy
Inst. of Education and Research, Dec. 12, 2006, Pune, India

Fiedler, F., invited lecture
Anwendung von PET für die Kontrolle der Tumortherapie mit leichten Ionen
Seminar SF4, Hahn-Meitner-Institut, Apr. 25, 2006, Berlin, Germany

Fiedler, F., M. Sellesk, W. Enghardt
Der Washout der Positronenemitter bei in-beam PET
DPG Frühjahrstagung, DPG, March 13-15, 2006, Heidelberg, Germany

Fiedler, F.
Simulation of positron distributions for carbon and proton beams
Scientific Workshop - For In-Beam PET, May 9-10, 2006, Dresden, Germany

Frauendorf, S., invited lecture
Dynamical and static chirality of rotating triaxial nuclei
Contemporary Frontiers in Nuclear Structure, American Chemical Society Meeting & Exposition, March 26-30, 2006, Atlanta, USA

Frauendorf, S., invited lecture
A closeup of the spinning nucleus
Nucl. Struct. '06, Conf. on nuclei at the limit, Pollard Technology Conf. Center, July 24-28, 2006, Oak Ridge, Tennessee, USA

Frauendorf, S., invited lecture
Emergent phenomena in mesoscopic nuclear systems
Key note talk, Mini-symposium on Nuclei as Mesoscopic Systems, The Annual Meeting of the Div. of Nucl. Phys. of the American Phys. Society, Oct. 25-28, 2006 Nashville, USA

Frauendorf, S.
Emergent phenomena in mesoscopic systems
Colloquium, Nat. Superconducting Cyclotron Lab./Department of Phys., November 17, 2006 , Michigan State University, USA

Grosse, E.
Dipole strength below and above particle thresholds - new data and new ideas
WS Nucl. Astrophys., Dec. 11, 2006, Brussels, Belgium

Junghans, A.R., invited talk
Photodissociation studies p-process nuclei at ELBE
Astrophysics and Nuclear Structure, Int. Workshop XXXIV on Gross Properties of Nuclei and Nuclear Excitations, Jan. 15-21, 2006 Hirschegg, Austria

Junghans, A.R.
Electromagnetic excitations in nuclei from photon scattering to photodissociation
Seminar talk, March 14, 2006, Uni. Konan, Kobe, Japan

Junghans, A.R.
Electromagnetic excitations in nuclei from photon scattering to photodissocaition
Int. Symp. on Nucl. Astrophysics - Nuclei in the Cosmos -IX, June 25-30, 2006, Cern, Switzerland

Kämpfer, B.
Hunting medium modifications of the chiral condensate
Int. Wintermeeting on Nuclear Physics, Jan. 20-Febr. 5, 2006, Bormio, Italy

Kämpfer, B.
D mesons and the chiral condensate
PANDA-Meeting, 2006, TU Dresden, Germany

Kämpfer, B.
1. Electromagnetic probes of strongly interacting matter
2. Medium modifications of hadrons: chiral condensate and more
3. Exclusive virtual bremsstrahlung
HADES-Meeting, Apr. 4-8, 2006, Dresden, Germany

Kämpfer, B.
Quasi-particle model of QCD matter and a family of equations of state
ECT* Workshop, March 21-25, 2006, Trento, Italy

Kämpfer, B.
Physics of high baryon density, Presentation of the chapter "In-medium modifications of hadrons"
ECT* Workshop, May 5- June 2, 2006, Trento, Italy

Kämpfer, B.
Heavy ion reactions at ultrarelativistic energies from hot deconfined matter to hadronic freeze-out
ECT* Workshop, June 26- July 21, 2006, Trento, Italy

Kämpfer, B.
1. Impact of 4-quark condensates on in-medium effects of hadrons
2. Quasi-particle perspective on equation of state and critical end point
Quark Confinement and the Hadron Spectrum VII, Sept. 2-7, 2006, Ponta Delgado, Azores, Portugal

Kämpfer, B.
Dense and hot strongly interacting matter on the universe
Seminar on IST, Sept. 12, 2006, Lissabon, Portugal

Kämpfer, B.
Interpretation of HADES data
Virtual Institute (III): Dense Hadronic Matter and QCD Phase Trasitions, Oct. 15-17, 2006, Rathen, Germany

Kämpfer, B.
Our interest on omega mesons
OMEGA-Workshop, Oct. 19-20, 2006, FZD Dresden, Germany

Kämpfer, B.
Quasi-particle perspective on critical end point
Critical point and onset of deconfinement, July 2-9, 2006, Florence, Italy

Kämpfer, B.
Dense and hot strongly interacting matter on the universe
Seminar FSU Jena, Juni 2006, Jena, Germany

Klug, J.
Development of a neutron time-of-flight source at the ELBE accelerator
International Workshop on Fast Neutron Detectors and Applications, University of Cape Town, South Africa, Apr. 3-6, 2006, Cape Town, South Africa

Kotte, R.
ϕ mesons in C + C collisons at 2 AGeV
Hades collaboration meeting, GSI, Oct 25-28, 2006, Darmstadt, Germany

Lehnert, A. E. Beyreuther, W. Enghardt, E. Lessmann, J. Pawelke, W. Wagner, W. Dörr
RBE of soft X-rays for chromosomal damage determined for two human mammary epithelial cell lines
The 35th Annual Meeting of the European Radiatiton Research Society, European Radiation Research Society, June 22-25, 2006, Kiev, Ukraine

Möckel, D., J. Pawelke, M. Sommer, E. Will, W. Enghardt
Erste Experimente zu in-beam PET mit harter Photonenstrahlung
DPG-Frühjahrstagung, DPG, March 13-15, 2006, Heidelberg, Germany

Möckel, D.
PET and photon therapy
Scientific Workshop for In-Beam PET, May 9-10, 2006, Dresden, Germany

Rusev, G.
Dipole-strength distributions below the giant dipole resonance in ^{92}Mo, ^{98}Mo and ^{100}Mo
Institut für Kern und Teilchenphysik, Oct. 19, 2006, TU Dresden, Germany

Schwengner, R.
Electromagnetic excitations in nuclei: from photon scattering to photodisintegration
Frühjahrstagung der Deutschen Physikalischen Gesellschaft, March 20- 24, 2006, München, Germany

Schwengner, R.
Dipole-strength distributions up to the particle-separation energies and photodissociation of Mo isotopes
2nd Int Conf. on Collective Motion in Nuclei Under Extreme Conditions (COMEX2), June 20-23, 2006, Sankt Goar, Germany

Schwengner, R., invited lecture
Photon-scattering and photoactivation experiments at the electron accelerator ELBE
Workshop AP.G.RA.D(E) 2006, Applications of Gamma-Ray Diffraction, Institut Laue-Langevin, Oct. 26-28, 2006, Grenoble, France

Schwengner, R., invited lecture
Photon-scattering and photoactivation experiments at the electron accelerator ELBE
Departamento de Fisica Teorica, Universidad Autonoma de Madrid, Nov. 6, 2006, Madrid, Spain

Sczepan, M
FEL-induced Reflectivity changes in thin DNA-Films
Inst. für neue Materialien, June 12, 2006, Saarbrücken, Germany

Seidel, W.
First lasing at the U100-FEL
28th Int. Free Electron Laser Conf., Aug. 27- Sept. 1, 2006, Berlin/Rossendorf, Germany

Shakirin, G.
Reconstruction and Corrections in In-Beam PET
Scientific Workshop - For In-Beam PET, May 9-10, 2006, Dresden, Germany

Thomas, R.
Omega, Nucleon, D Spectroscopy: QCD Sum Rules in Vakuum and Nuclear Matter
37. Arbeitstreffen "Kernphysik, March 8, 2006, Schleching, Germany

Thomas, R.
In-Medium Change of Four-Quark Condensates: QCD Sum Rules Evaluation for Omega-Meson and Nucleon
44. Int. Universitätswochen für Theoretische Physik, March 12, 2006, Schladming, Germany

Thomas, R.
In-Medium Change of Four-Quark Condensates: QCD Sum Rules Evaluation for Omega-Meson and Nucleon
Frühjahrstagung der Deutschen Physikalischen Gesellschaft, March 22, 2006, München, Germany

Thomas, R.
In-Medium Properties of Omega.Meson and Nucleon: QCD Sum Rules Approach and Rule of Four-Quark Condensates
Virtual Institute Workshop III, Oct. 16, 2006, Rathen, Germany

Wagner, A.
Kerne und Sterne - Vom Urknall, der Entstehung der chemischen Elemente und Experimenten im FZR
Lehrerfortbildung "Astrophysik", FZD, Febr. 17, 2006, Dresden, Germany

Wagner, A.
Experimental Facilities at ELBE
Seminar, Japan Synchrotron Radiation Research Institute (SPring8), March 17, 2006, Sayo-Gun, Japan

Wagner, A., invited lecture
Dipolstärke in Kernen und der Kernphotoeffekt im Kosmos
Seminar des SFB 634, TU Darmstadt, May 4, 2006, Darmstadt, Germany

Wagner, A.
Die Dipolstärke in Kernen und der Kernphotoeffekt im Kosmos
Physikalisches Kolloquium, TU Dresden, July 4, 2006, Dresden, Germany

Wagner, A., invited lecture
Experiments with real photons for nuclear astrophysics
NuSTAR Seminar, GSI, Jan 24, 2007, Darmstadt, Germany

Talks of Visitors

Dr. Achenbach, P., Univ. Mainz:
Ein neuer Messplatz für die Kaonen- und Hyperkernproduktion an MAMI, Jan. 30, 2006

Dr. Bemmerer, D., INFN Padova, Italy:
Nucleosynthesis studied deep underground at Gran Sasso, Italy, Nov. 29, 2006

Dr. Finocchiaro, P., INFN LNS Catania, Italy:
Single photon sensor arrays and micro-optics, Nov. 7, 2006

Prof. Fuchs, C., Univ. Tübingen:
Transport model interpretation of HADES data, Apr. 4, 2006

Dr. Geithner, O., DKFZ, Heidelberg, Germany:
Monte Carlo Simulations for Heavy Ion Dosimetry, June 23, 2006

Prof. Grigoryan, L., IAPP NAS, Armenia:
Channeling radiation influenced by ultrasound, Dec. 18, 2006

Dr. Gupta, D., Variable Energy Cyclotron Centre, Kolkata, India:
Study of Reactions Induced by Radioactive Beams, Nov. 30, 2006

Dr. Heerklotz, H., Biozentrum, Basel, Switzerland:
Microcalorimetric Investigations of membranes, July 14, 2006

Prof. Lo Iudice, N., INFN Napoli, Italy:
New collective phenomena in spherical and deformed rotating nuclei, May 8, 2006

Dr. Litvinova, E., Physics and Power Engineering Institute, Obninsk, Russia:
Covariant theory of particle vibrational coupling and its application to exotic nuclei, July 28, 2006

Marta, M., INFN Milano, Italy:
Measurements of beam heating effect in a gas target through Rutherford scattering, Dec. 7, 2006

Prof. Mazumdar, I., Tata Insitute of Fundamental Research, Mumbai, India:
Shape Transitions in Hot Nuclei, June 26, 2006

Dr. Molina, R., MPI for the Physics of Complex Systems Dresden, Univ. Complutense de Madrid:
Quantum chaos and 1/f noise, Jan. 16, 2006

Dr. Schrieder, G., TU Darmstadt:
Experimente zur Polarisierbarkeit des Nukleons und zum Protonenradius am S-Dalinac, June 12, 2006

Prof. Weidenmüller, H., MPI Heidelberg:
Random Matrices and Chaos in Quantum Many-Body Systems, March 27, 2006

Prof. Wolter, H., Univ. München:
The symmetry energy in nuclear structure and heavy ion collisions, Oct. 19, 2006

Lecture Courses

Enghardt, W.
Biostatistik
TU Dresden, WS 2005/2006

Enghardt, W.
Physik und Technologie der Nuklearmedizin
TU Dresden, SS 2006

Enghardt, W.
Wechselwirkung von Strahlung mit Materie und Radioaktivität
TU Dresden, WS 2006/2007

Enghardt, W.
Digitale Bildverarbeitung
TU Dresden, WS 2006/2007

Enghardt, W.
Introduction to Biostatistics
TU Dresden, WS 2006/2007

Grosse, E.
Beschleuniger und Detektoren
TU Dresden, SS 2006

Grosse, E., H. Freiesleben
Institutsseminare Inst. für Kern- und Teilchenphysik
TU Dresden, WS 2005/2006, SS 2006

Kämpfer, B.
Kosmologie
TU Dresden, SS 2006

Kämpfer, B.
Theorieseminar Kerne und Teilchen
TU Dresden, WS 2005/2006, SS 2006, WS 2006/2007

Kämpfer, B.
Theoretische Mechanik
TU Dresden, WS 2005/2006

Kämpfer, B.
Standardmodell der Teilchenphysik (Quantenfeldtheorie)
TU Dresden, WS 2006/2007

Pönisch, F.
Dosimetrie für die Strahlentherapie
TU Dresden, SS 2006

Wagner, A.
Nukleare Astrophysik
TU Dresden, WS 2005/2006, WS 2006/2007

Ph.D. Theses

Kaliopi Kanaki
Study of Λ production in C + C collisions at 2 A GeV beam energy with the HADES spectrometer
TU Dresden, Dec. 2006

Gencho Rusev
Dipole-strength distributions below the giant dipole resonance in ^{92}Mo, ^{98}Mo and ^{100}Mo
TU Dresden, Jan. 2007 (submitted Aug. 2006)

Alexander Sadovsky
Investigation of K^+meson production in C + C collisions at 2 A GeV with HADES
TU Dresden, Dec. 2006

Diploma Theses

Benjamin Bannier
Simulations of Dielectron Detection Capabilities of HADES at SIS100
TU Dresden, Nov. 2006

Henry Schade
Dead cone effect for charm
TU Dresden, Oct. 2006

Nicos Stawrakakis
Finite width effects in quasi-particle model
Hochschule Merseburg, March 2007 (submitted Dec. 2006)

Holger Weigelt
Weiterentwicklung und Realisierung der Diagnostik der IR-Strahlung am Frei-Elektronen-Laser
Hochschule Mittweida (FH), March 2006

Meetings organized by the IKH

Topic	Period	Number of Participants
HADES Collaborations Meeting XVI at Dresden	April 4 - 8, 2006	88
Virtual Institute (III): "Dense Hadronic Matter and QCD Phase Trasitions", Rathen	Oct. 15 - 17, 2006	45
OMEGA-Workshop, FZD	Oct. 19 - 20, 2006	20

Departments of the ISP

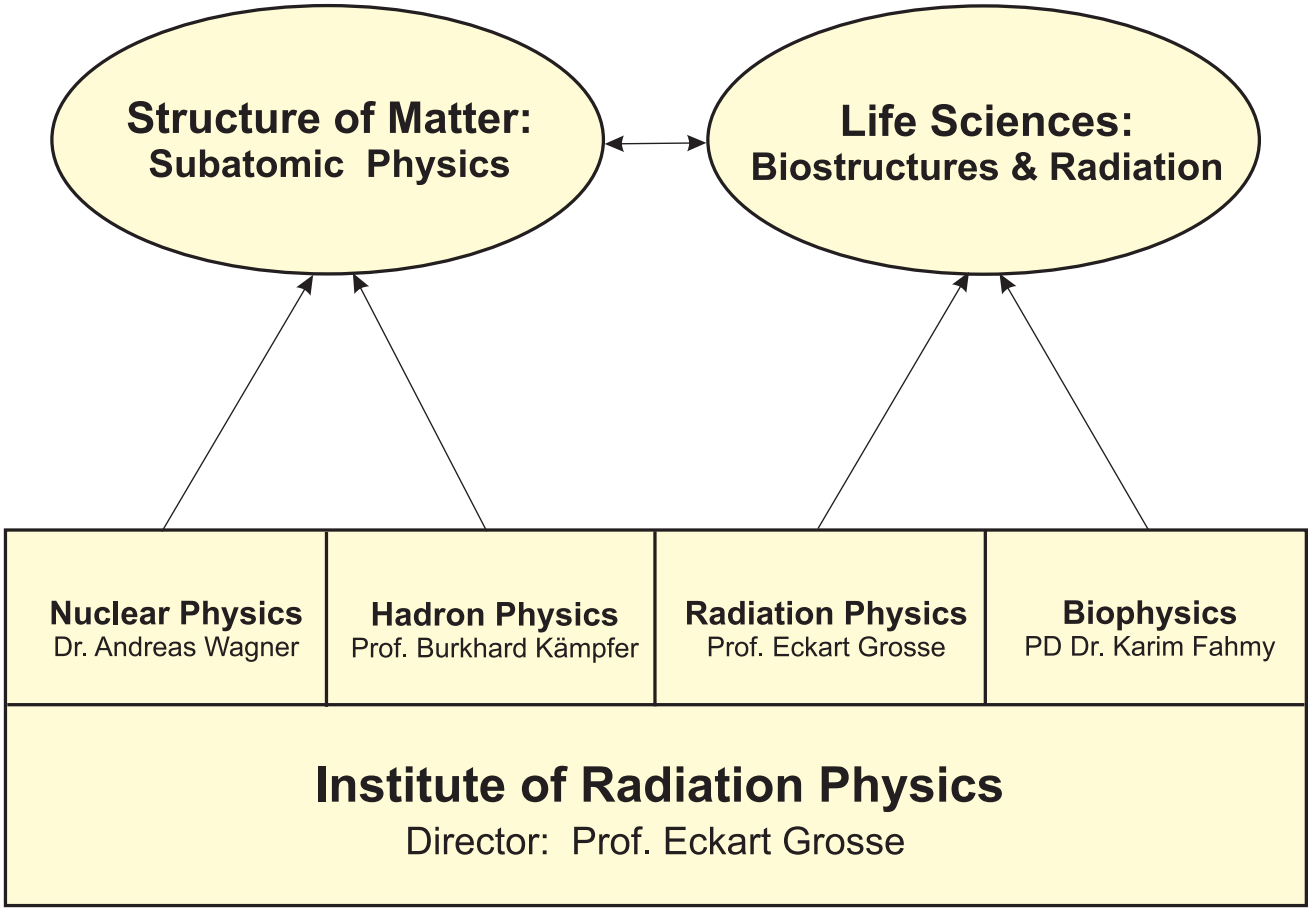

Personnel of the Institute of Radiation Physics

Director: Prof. Dr. E. Grosse [1]

Scientific Personnel

PD Dr. H.W. Barz
Dr. D. Bemmerer
Dr. F. Dönau
Dr. P. Crespo
PD Dr. F. Dohrmann
Prof. Dr. W. Enghardt [1]
PD Dr. K. Fahmy
Prof. Dr. S. Frauendorf [2]
Dr. A. Junghans
Prof. Dr. B. Kämpfer
Dr. J. Klug
Prof. H. Kötzle
Dr. R. Kotte
Dr. A. Lehnert
Dr. H. Müller
Dr. N. Nankov
Dr. L. Naumann
Dr. W. Neubert
Dr. J. Pawelke
Dr. F. Pönisch
Dr. O. Savchuk
Dr. K.D. Schilling
Dr. R. Schwengner
Dr. M. Sczepan
Dr. W. Seidel
Dr. A. Sytcheva
Dr. A. Wagner
Dr. W. Wagner
Dr. R. Wünsch
Dipl. Phys. D. Wohlfarth
Dr. J. Wüstenfeld
Dr. S. Zschocke

PhD Students

B. Azadegan
R. Beyer
E. Beyreuther
M. Bluhm
M. Erhard
F. Fiedler
K. Kanaki
H. Keshbak
K. Kosev
S. Madathil
D. Möckel
C. Nair
U. Reichelt
G. Rusev
A. Sadovsky
G. Shakirin
R. Thomas
P. Zhou

Students

R. Apolle
B. Bannier [3]
M. Fauth
R. Hannaske
T. Hilger
U. Just
V. Katsoulidou
M. Kempe
T. Kluge
A. Müller
H. Schade [3]
R. Schulze [3]
D. Seipt [3]
D. Stach
N. Stawrakikis [3]
T. Würschig [3]
K. Zeil

Technical Personnel

J.U. Berlin
M. Böse
M. Boeck
H. Gude
A. Hartmann
K. Heidel
L. Heinrich
R.R. Hensel
J. Hutsch
K. Krüger
M. Langer
E. Leßmann
A. Liebezeit
M. Paul
J. Philipp
B. Rimarzig
S. Schaller
D. Schich
C. Schneidereit
W. Schulze
A. Seifert
M. Sobiella
J. Steiner
U. Wolf

[1] *also TU Dresden*
[2] *also University of Notre-Dame, Indiana, USA*
[3] *Diploma Student*

Guest Scientists

Barnaföldi, G.	KFKI Budapest, Hungary
Benouret, N.	Univ. Algier, Algerien
Dr. Guber, F.	Institute for Nuclear Research, Moskow, Russia
Prof. Grigoryan, L.	IAPP NAS Rep. of Armenia
Dr. Ivashkin, A.	Institute for Nuclear Research, Moskow, Russia
Dr. Kaptari, L.P.	JINR Dubna, Russia
Dr. Kostov, L.K.	Institute for Nuclear Research and Nuclear Energy, Sofia, Bulgaria
Lantukh, J.	Universität Orenburg, Russia
Prof. Pashkevich, S.	Universität Orenburg, Russia
Dr. Semak, A.	Institute for High Energy Physics, Protvino, Moskow, Russia
Prof. Titov, A.	JINR Dubna, Russia
Usenko, E.	Institute for Nuclear Research, Moskow, Russia
Dr. Wolf, G.	KFKI, RMKI, Budapest, Hungary
Dr. Zschocke, S.	BCPL Bergen, Norway
Zetenyi, M.	KFKI Budapest, Hungary

Index

Alexiev, U. ... 65
Altstadt, E. ... 55, 56
Apostolakis, J. ... 68
Azadegan, B. ... 85–87

Böhl, M. ... 68
Bannier, B. ... 11
Barz, H.W. ... 13, 18
Beckert, C. ... 55, 56
Bemmerer, D. ... 58, 59
Benouaret, N. ... 39, 44
Bernhard, G. ... 71
Beyer, R. ... 39, 49, 54–56
Beyreuther, E. ... 89
Bluhm, M. ... 7, 30–32

CBM-TRT Collab. ... 34
Claussner, J. ... 51
Cohen D.N. ... 69
COSY-TOF Collab. ... 21, 26, 27
Crespo, P. ... 52, 79–82
Crevenna, A.H. ... 69

Dönau, F. ... 41, 42
Dörr, W. ... 88, 89
Date, S. ... 23
Dohrmann, F. ... 9–12, 17–19, 24, 28, 35–38
Dorkin, S.M. ... 33

EDDA Collab. ... 28, 35, 36
Enghardt, W. ... 9, 10, 79–85
Erhard, M. ... 39–41, 49–52

Fahmy, K. ... 63, 65, 67–70
Fauth, M. ... 52
Fiedler, F. ... 80–82
Foerstendorf, H. ... 71
FOPI Collab. ... 20, 25
Frauendorf, S. ... 41
Freiesleben, H. ... 55, 56
Friedrich, M. ... 53
Furlinski, G. ... 67, 70

Gabler, D. ... 90
Galindo, V. ... 55, 56
Greschner, M. ... 55, 56
Grosse, E. 9–11, 17, 18, 37, 39–41, 49–51, 53–57, 80
Gutzeit, H.O. ... 68

HADES Collab. ... 9, 10, 12, 17, 22
Hartmann, A. ... 51, 53
Heidel, K. ... 53, 54, 85
Heim, K. ... 71
Hennig, C. ... 63
Henninger, J. ... 90, 91
Hilger, T. ... 29
Howard, J. ... 69
Hutsch, J. ... 54

Jülich, R. ... 81
Jainsch, R. ... 72
Junghans, A.R. ... 39–42, 49–56
Justus, M. ... 72

Kämpfer, B. ... 7–18, 23, 29–33
Käubler, L. ... 41, 43
Kanaki, K. ... 9, 10, 12, 17
KaoS Collab. ... 18, 19
Kaptari, L.P. ... 14–16, 33
Klug, J. ... 39, 49, 54–56
Kluge, T. ... 84
Kosev, K. ... 39–41, 49, 53
Kostov, L.K. ... 39, 41
Kotte, R. ... 9–12, 17, 20, 22, 25, 38

Légrády, D. ... 54–56
Lange, C. ... 91
Leege, K.-W. ... 72
Lehmann, N. ... 65
Lehnert, A. ... 88
Lessmann, E. ... 88, 89

Möckel, D. ... 84
Müller, H. ... 83
Madathil, S. ... 67–69
Mallion, S. ... 41, 44
Marta, M. ... 58, 59
Merroun, M. ... 63

Nair, C. ... 39, 49–52
Nankov, N. ... 39, 49, 53
Naumann, B. ... 55, 56
Naumann, L. ... 9–12, 17, 18, 21, 26, 27, 34, 38
Neubert, W. ... 85
Noack, K. ... 55, 56

Ohashi, Y. ... 23

Pönisch, F. ... 81
Parodi, K. ... 81, 82
Pawelke, J. ... 81, 84–89
Pfennig, F. ... 68
Pollmann, K. ... 63
Proehl, O. ... 72

Raff, J. ... 63
Rainovski,, G. ... 44
Reichelt, U. ... 90, 91
Rusev, G. ... 39–44, 47–49, 55, 56

Sadovsky, A. ... 9, 10, 12, 17
Savchuk, O. ... 63

Schade, H. 8
Scheinast, W. 18
Schilling, K.D. 39–43, 49–53, 55, 56
Schlenk, R. 55, 56
Schneider, S. 55, 56
Schulze, R. 7, 30, 31
Schwengner, R. 39–47, 49–51
Sczepan, M. 70
Seidel, K. 55, 56
Seidel, W. 70–72, 74, 76, 78
Seipt, D. 7, 30, 31
Selenska-Pobell, S. 63
Sellesk, M. 81, 82
Semikh, S.S. 33
Shakirin, G. 79, 80
Sobiella, M. 51, 53, 54
Sokoll, A. 68
Stach, D. 38
Stehr, D. 78
Steiner, J. 51
Sytcheva, A. 37

Thomas, R. 29
Tietze, S. 68
Titov, A.I. 23

Wünsch, R. 76
Wüstenfeld, J. 9–12, 17
Wagner, A. 39–42, 49–57, 60, 80
Wagner, W. 85–87
Weigelt, H. 72
Weiss, F.-P. 55, 56
Winnerl, S. 74
Winter, A. 76
Wohlfarth, D. 70, 72
Wolf, Gy. 13

Zetenyi, M. 13
Zhou, P. 12
Zvyagin, S. 76